Femtosecond solvation, excited state dynamics, and photophysical properties of chromophores used in polynucleic acids

DISSERTATION

zur Erlangung des akademischen Grades
doctor rerum naturalium
(Dr. rer. nat.)
im Fach Chemie
eingereicht an der
Mathematisch-Naturwissenschaftlichen Fakultät I
der Humboldt-Universität zu Berlin
von
Karunakaran Venugopal, M. Sc.
geboren am 15.04.1974 in Chennai, Indien.

Präsident der Humboldt-Universität zu Berlin:
Prof. Dr. Christoph Markschies
Dekan der Mathematisch-Naturwissenschaftlichen Fakultät I:
Prof. Dr. Christian Limberg
Gutachter:
1. Prof. Dr. Nikolaus P. Ernsting
2. Prof. Dr. Mark Maroncelli (Pennsylvania state Uni., USA)
3. Prof. Dr. Wolfgang Rettig

Tag der mündlichen Prüfung: 30 January 2007

To my ever loving

Amma, Appa, Selvam, Lakshmi, Vijay, Jai and Bhuvana

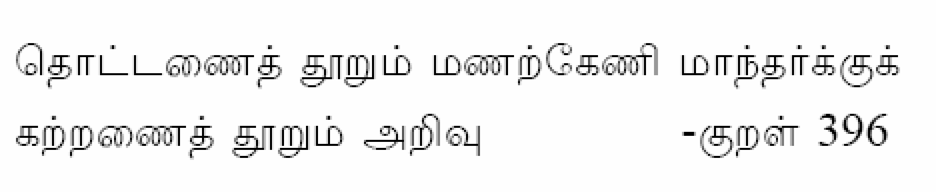

தொட்டணைத் தூறும் மணற்கேணி மாந்தர்க்குக்
கற்றணைத் தூறும் அறிவு -குறள் 396

(The deeper a sand-well is dug the freer is its flow of water. Even so, the deeper a man's learning the greater is his wisdom. ~Thirukural)

Zusammenfassung

Diese Arbeit ist Teil eines Weges, der die Polarisationsdynamik von Polynukleinsäure-Helices (DNA) zum Ziel hat. Die Dynamik kann im Prinzip von innen beobachtet werden, über Femtosekunden-zeitaufgelöste optische Spektroskopie eines Farbstoff-Moleküls anstelle einer Nukleinbase. Der optische Chromophor soll als solvatochrome Sonde der DNA Umgebung funktionieren. Dafür wurde 2-Amino-7-Nitro-Fluoren (ANF) gewählt, welches ideale solvatochrome Eigenschaften hat. Bevor der Einbau des Sondenmoleküls erfolgt, müssen dessen photophysikalischen Eigenschaften in reinen Lösungsmitteln und in Lösungsmittel-Mischungen weitgehend verstanden sein. Dieses Thema bestimmt den größeren Teil der Arbeit.

ANF, aliphatische Derivate, und das entsprechende Nukleosid wurden synthesitsiert. Ihre thermodynamischen Eigenschaften, optischen Spektren, und ps Fluoreszenzlebensdauern werden für eine Reihe von Lösungsmitteln beschrieben. Präferentielle Solvatation in wässrigen Mischungen wird mit optischer Absorptions- und ^{1}H NMR-Spektroskopie untersucht. Inclusionskomplexe mit Cyclodextrinen werden ebenfalls charakterisiert.

Auf diese "klassischen" Studien folgt die fs-transiente optische Absorptionsspektroskopie von ANF und Derivaten. Die transienten Spektren werden zeilegt und die Banden für stimulierte Emission als Funktion der Zeit in den meisten Fällen erhalten. Damit erhält man eine Solvatations-Relaxationsfunktionen C(t) für die meisten Lösungsmittel (50 fs Zeitauflösung). Unterschiede zu bekannten Relaxationsfunktionen für die vieluntersuchte Sonde Coumarin 153 werden diskutiert. Wichtig ist, daß derart C(t) für ein ANF Nukleosid in Wasser existiert. Dies kann mit einer simulierten Kurve für ANF in DNA-Helices verglichen werden. Es folgt, dass gestapelte Chromophore im Innern dynamisch von jenen unterschieden werden können, die in die wässrige Umgebung herausgedreht sind.

Der Cyaninfarbstoff Thiazol Orange (TO) wird von anderen Gruppen verwendet, um die Hybridisierung von DNA-Strängen zu verfolgen. Die Fluoreszenz von TO wird durch schnelle Isomerisation im S_1 Zustand stark gelöscht. In dieser Arbeit wird die entsprechende innermolekulare Verdrillung mit fs-transienter Absorptionsspektroskopie und mit fs-zeitaufgelöster Fluoreszenzspektroskopie (Summenfrequenz-Erzeugung) zum ersten Mal zusammenhängend untersucht. Transiente Spektren in Lösung werden mit stationären Spektren in verschiedenen PNA/DNA Duplex-Konstrukten verglichen. Eine hochfrequente Schwingungsmode ist bei der strukturellen Reorganisation von TO nach $S_1 \leftarrow S_0$ Anregung beteiligt. Zunehmende Aktivität begleitet die Verdrillung. Deshalb sollte die Form der stationären Fluoreszenzbande dazu geeignet sein, das verfügbare freie Volumen in DNA-Konstrukten abzuschätzen.

Stichworte: Solvatochromie, präferentielle Solvatation, fs-transiente Absorption, fs-transiente Fluoreszenz-Summenfrequenzerzeugung, Solvatations-Relaxationsfunktion, ANF, C-153, TO, PNA, DNA.

Abstract

This work is part of an effort to observe the polarization dynamics of duplex polynucleic acids from the inside, through femtosecond time-resolved optical spectroscopy of a dye molecule which has been stacked into the structure at a well-defined site. The dye chromophore should act as a solvatochromic probe of its DNA environment. For a probe, 2-amino-7-nitro fluorene (ANF) had been selected since it has ideal solvatochromic properties. Before being linked into DNA, its photophysical properties in liquids and liquid mixtures should be understood. The larger part of this thesis deals with this topic.

ANF, aliphatic derivatives, and the nucleoside were synthesized. Their thermodynamic properties, optical spectra, and ps fluorescence decay are examined in a wide range of solvents. For preferential solvation in aqueous mixtures, absorption results are compared with ^{1}H NMR spectra. Inclusion properties were also explored.

Femtosecond transient absorption spectroscopy of ANF and derivatives follows after these "classical" studies. The transient spectra are analyzed and, in most cases, the stimulated-emission band can be obtained as function of time. Ultrafast solvation relaxation functions (50 fs resolution) for many solvents are constructed from these data and discussed by comparison with a well-studied probe, Coumarin 153. Most importantly, the solvation relaxation of the ANF nucleoside in water is obtained and compared with a simulated relaxation of the chromophore in a DNA duplex. It follows that chromophores stacked inside DNA can be distinguished from chromophores which extend into the aqueous boundary layer.

The cyanine dye Thiazole Orange (TO) is used by other groups to monitor the hybridisation of DNA strands. Its fluorescence is strongly quenched by intramolecular twisting in the excited state S_1. In this thesis the twisting process is characterized by femtosecond transient absorption and fluorescence upconversion spectroscopy, combined, for the first time. The transient spectra are compared to stationary spectra in a

PNA/DNA duplex where the degree of twisting is restricted. A high-frequency mode is shown to play an important role in the structural reorganisation of TO following $S_1 \leftarrow S_0$ excitation. Its vibrational activity is correlated with twisting. Therefore the shape of the emission band may be used to estimate the available volume in DNA constructs.

Key words: Solvatochromism, preferential solvation, femtosecond transient absorption solvation, femtosecond fluorescence upconversion, solvation relaxation function, ANF, C-153, TO, PNA and DNA.

Contents

1 Aim of the thesis

Deoxyribonucleic acid (DNA) is responsible for genetic propagation of inherited traits. Genomes of an organism are encoded in DNA and the corresponding genetic information is determined by the sequence of base pairs along its length. The information is transferred from DNA into RNA − called transcription − by an RNA polymerase to produce a complementary RNA which in turn translates the genetic code into a functional peptide or protein. The mechanical properties of DNA have a vital role during these processes, and they are related to the molecular structure of DNA, the local mobility, its hydrogen bonding, and electrostatic interaction between the bases. The internal and external mobility of complex DNA can be characterized by a few simple characteristics: the *time* scale of the motions – dynamical events in DNA range from femtosecond to at least seconds; *the amplitude* of the internal motions − small vibrations of individual atom have amplitudes from less than 0.1 Å to large amplitude motions of fragments of polynucleotide chains associated with local unwinding or opening of the double helix; and finally the *energies* or *frequencies* associated with these motion − ranges from 1 to 100 cm^{-1}, somewhat below the frequencies of internal vibrations in isolated small molecules. Theoretical and experimental methods to describe and monitor these motions depend on the desired length- and time scales. Theoretical methods include molecular dynamics simulations, harmonic analysis, the theory of helix-coil transitions and topological concepts such as the rod-like model and the lattice model. Experimental methods for monitoring internal DNA mobility and DNA flexibility are either based on magnetic properties, such as NMR and EPR, on optical properties such as infrared spectroscopy, Raman spectroscopy, transient fluorescence and absorption spectroscopy, and finally on X-ray scattering.

The present work was designed to enable optical monitoring of internal DNA mobility. It starts from the idea that the fluorescence Stokes shift of a specifically designed probe, when linked into DNA, may reflect the structural and polarization dynamics of the surrounding [BMC99]. The time-resolved fluorescence Stokes shift (TRFSS) is used extensively for measuring the polar reorientation dynamics of polar liquids. The latter field is also termed "solvation dynamics"; it has greatly benefited from the advance of femtosecond laser technology and can therefore be extended into more complex environments such as DNA oligomers. But in which way does the fluorescence Stokes shift measure the surrounding dynamics?. Is the time-resolved shift, which occurs on a 50fs- 200 ps time scale, a property of the environment only or does it also depend on the chromophore itself?. Clearly the problem is to find a probe chromophore which is optimal for monitoring DNA dynamics on this time scale. There are several conditions for this choice: (1) The probe must minimally distort the molecular structure of the DNA double helix in which it is embedded, (2) the position of the probe in the helix should be fixed and known, and finally (3) the photophysical properties of the probe must be appropriate for the spectroscopic techniques to be used.

Previously we have measured the femtosecond transient absorption spectra of 2-amino-7-nitro-fluorene (ANF) in acetonitrile [RKE98]. The results showed that the time-resolved Stokes shift of ANF is fully determined by the far-infrard spectrum of the pure polar solvent (acetonitrile). If ANF were intercalated into a DNA duplex, it seems likely that the reorganization of the nearest neighboring base pairs could similarly be obtained, by observing by its shifting fluorescence after ultrafast optical excitation. This idea was tested by preliminary calculations with a molecular model, which predict oscillations caused by the local mobility of the nearest neighbors [FES_ _]. These two observations, taken together, suggest that ANF may be a useful target structure from which solvatochromic DNA probes can be developed for use with femtosecond transient absorption spectroscopy. But if the ANF chromophore is linked into DNA, it will be modified by the linker – usually an aliphatic chain attached to the fluorene body or at a functional group. The question arises how the modifications will influence their physico-chemical properties of the compound. In this work, the properties of ANF derivatives will be studied with stationary and fs time-resolved optical methods.

We prepared derivatives substituted at the amino group, *viz.* the dimethyl (dM-ANF) and dibutyl (dBdP-ANF) derivatives, and also the nucleosides due to ribose (Ri-ANF) and glucose (Gl-ANF). The stationary solvatochromic behavior of these compounds were studied in different solvents varying from polar solvents to non polar solvents from several aspects. Most importantly, the solvation dynamics of these compounds in the excited state have been measured with femtosecond time resolution in different solvents. Gl-ANF is adequately soluble in water, so that the solvation dynamics in water could be measured with this compound.

The aim was to link ANF into a DNA duplex and to measure the solvation dynamics there. This work requires the synthesis of an artificial ANF nucleotide which can be linked into DNA by solid-phase synthesis. That aim was pursued in parallel to this thesis in a bioorganic group of the chemistry department. Unfortunately it could not be reached even at the end of the present thesis even though it is probably attainable. As a consequence, it was not possible to examine the solvatochromic behavior of ANF linked into DNA. Hence only preparatory, comparative work with ANF and related structures can be presented in this thesis. But because DNA is of central interest, we studied a different chromophore linked into the structure, Thiazole Orange (TO), which is also used for DNA diagnostics. This cyanine dye is useful to detect and quantify polynucleotides in variety of techniques which include Polymerase Chain Reaction (PCR) [SSS00], the hybridization of single strands [PMM02], restriction fragments sizing [FAR94] and flow cytometry [HFC94]. Even they were also used as a stain in residual RNA of cells in reticulocyte analysis [LCC86], DNA in agarose gels [RQP90] and capillary electrophoresis [RG095]. The fluorescence quantum yield of the TO is low due to twisting of two heterocyclic moiety. When it is intercalated in to DNA, reduced twisting increases the fluorescence intensity about 3000 fold [LCC86]. The increase in fluorescence intensity is also sensitive to the mismatch of the neighboring pair, so that a DNA target may be distinguished from its base mutant by fluorescence [KS003]. The sensitive of the fluorescence intensity to the DNA environment and its wide application motivate us to know examine the twisting dynamics of TO in neat solvents and the spectroscopic of properties of TO in DNA.

To summarize: the primary intention of this thesis is to characterize the solvatochromic behavior of ANF derivatives in variety of solvents, to obtain solvation dynamics curves of ANF derivatives in selected solvents with femtosecond time resolution, and to compare the shape of the relaxation curves with previously reported ones. In particular, the solvation relaxation curve of an ANF nucleoside was to be measured in water. The latter measurement allows us to compare with a theoretically obtained relaxation curve of ANF in DNA duplex. Thereby we can see which differences must be resolved in ultimate DNA measurements.

In order to gain experience with DNA environments, we also studied the Thiazole Orange. Stationary measurements were carried out with TO linked into various PNA conjugates. Femtosecond time-resolved measurements were performed with TO in neat methanol. Spectral features seen here on a 690 fs time scale are equivalent features which are seen by steady-state spectroscopy in DNA. From a comparison, conclusions about the extent of photochemical isomerization by TO in DNA can be drawn.

2 Background: optical spectroscopy of polar molecular probes

2.1 Electronic spectroscopy in the liquid phase

Solvent effects on electronic spectra contain valuable information about (i) solvent–solute interactions, (ii) solvent structure in the vicinity of the solute, and (iii) solvent dynamics. All three are important for chemical reactivity in liquids and therefore have been the subject of numerous experimental and theoretical studies. The line shape of an electronic absorption or emission spectrum of a dilute solute in a solvent is typically broader and its peak shifted compared with the spectrum in the gas phase. The shift of the spectrum reflects the different averaged interaction energies between the ground and excited states of the solute with the solvent. The width reflects the fluctuations of the solvent–solute interactions in the initial electronic state (S_0 for absorption, S_1 for emission).

2.1.1 **Single vibronic transition** – Gaussian line shape

We consider a single molecular chromophore in a fluid of solvent molecules. In a most simple model the solute chromophore and solvent molecules are treated as spheres, without intramolecular degrees of freedom. When the chromophore is in its ground electronic state denoted as $|0\rangle$, it interacts through pairwise potentials with the solvent molecules. The latter interact among themselves also through a pairwise potential. Thus the Hamiltonian for the system when the solute is in its ground state is

$$H_0 = \frac{\vec{p}_c^{\,2}}{2m_c} + \sum_i \frac{\vec{p}_i^{\,2}}{2m_s} + \sum_i \nu_0(r_i) + \sum_{i<j} \nu_s(r_{ij}) \qquad 2.1$$

where $\vec{p}_c$ is the momentum of the chromophore and m_c its mass, $\vec{p}_i$ is the momentum of the *i*th solvent molecule with mass m_s, $\nu_0(r)$ is the chromophore–solvent pair potential when the chromophore is in its ground state and r_i is the distance between the *i*th solvent and the chromophore, $\nu_s(r)$ is the solvent–solvent pair potential and r_{ij} is the distance between solvent molecules i and j. When the chromophore is excited electronically (in state $|1\rangle$), it interacts with the solvent with a different pair potential, $\nu_1(r)$ and therefore the Hamiltonian for the excited state is

$$H_1 = H_0 + \hbar\omega(\vec{R}) \qquad 2.2$$

where

$$\hbar\omega(\vec{R}) = \hbar\tilde{\omega}_0 + \sum_i \nu(r_i), \qquad 2.3$$

$$\nu(r) = \nu_1(r) - \nu_0(r) \qquad 2.4$$

$\vec{R}$ is the collection of all the chromophore–solvent distances r_i and $\hbar\tilde{\omega}_0$ is the electronic excitation energy of the isolated chromophore. We treat the translational motion of the chromophore and of the solvent molecules classically.

In the inhomogenous limit which occurs at sufficiently slow solvent dynamics, and neglecting the chromophore's excited-state lifetime, the normalized steady-state absorption line shape $I_0(\omega)$ and emission line shape $I_1(\omega)$ are simply given by the equilibrium distribution of transition frequencies for the ground state $P_0(\omega)$ and excited state $P_1(\omega)$ chromophore respectively,

for absorption, $$I_0(\omega) = P_0(\omega) = \left\langle \delta(\omega - \omega(\vec{R})) \right\rangle_0 \qquad 2.5$$

for emission, $$I_1(\omega) = P_1(\omega) = \left\langle \delta(\omega - \omega(\vec{R})) \right\rangle_1 \qquad 2.6$$

$\langle....\rangle_\alpha$ indicates the Boltzmann equilibrium average appropriate for Hamiltonian H_α. It is implicitly assumed that the electronic transition dipole is independent of $\vec{R}$ (Condon approximation). Using the integral representation of the delta function one can write

$$P_\alpha(\omega) = \frac{1}{2\pi}\int_{-\infty}^{\infty} dt e^{-i\omega t} \left\langle e^{i\omega(\vec{R})t} \right\rangle_\alpha \qquad 2.7$$

Under a variety of circumstances it is reasonably good approximation to perform a cumulant expansion [K0062] of the average of the exponential and truncate after second order [SS092]. This leads to the Gaussian distributions

$$P_\alpha(\omega) = \frac{1}{\sqrt{2\pi\Delta_\alpha^2}} e^{-(\omega-\omega_\alpha)^2/2\Delta_0^2} \qquad 2.8$$

where $\omega_\alpha = \left\langle \omega(\vec{R}) \right\rangle_\alpha$, $\Delta_\alpha^2 = \left\langle \Omega_\alpha(\vec{R})^2 \right\rangle_\alpha$, and $\Omega_\alpha(\vec{R}) = \omega(\vec{R}) - \omega_\alpha$

The difference between the absorption and fluorescence maxima is called the Stokes shift, ω_s. If the line shapes are symmetric as in the Gaussian approximation used above, then this is given by $\omega_s = \omega_0 - \omega_1$. These results have been used to obtain approximate analytical formulas for the solvent–induced shift of the absorption and emission peaks.

2.1.2 **Many vibronic transitions** – a spectrum of the molecule

But note that the concept so far referred to a single line in the corresponding gas-phase spectrum, like in atomic spectra, because the internal degrees of freedom were so far neglected. But in molecules the electronic transition $|0\rangle \leftrightarrow |1\rangle$ is distributed over many vibronic sub-transitions. In the simplest case only one vibrational mode is optically active. Then the vibronic transitions $|0;i''\rangle \leftrightarrow |1;j'\rangle$ (i'', j' are vibrational quantum numbers) carry transition dipole moments according to the vibrational overlap (Franck-Condon progression). In a solvent, each vibronic transition is broadened to a Gaussian lineshape as shown before.

2.1.3 **Onsager reaction field theory** – in case of polar interactions

So far we explicitly considered the solvent environment to be molecular. Especially for spheres, as shown in figure 2.1.3-1, the static behavior of the pure liquid is understood (Mean Spherical Approximation, MSA). For a real solute/solvent systems one may assume that the static correlations can also be approximated by the MSA treatment, with a solute sphere carrying a point charge or dipole embedded in a dipolar hard sphere solvent. Next let us consider the time-space average of the solvent motion. Then the solvent can be represented as a smooth dipole distribution, the polarisation, in three dimensional spaces around the solute. The polarisation is caused by the electric field from the solute. The response of the liquid is characterized by the susceptibility ε-1. In the simple continuum model the susceptibility shows no structure around the solute. It is considered to be defined outside of a cavity, to a constant value there. This dielectric continuum is represented as a "yellow sea" in the panel b of the figure 2.1.3-1.

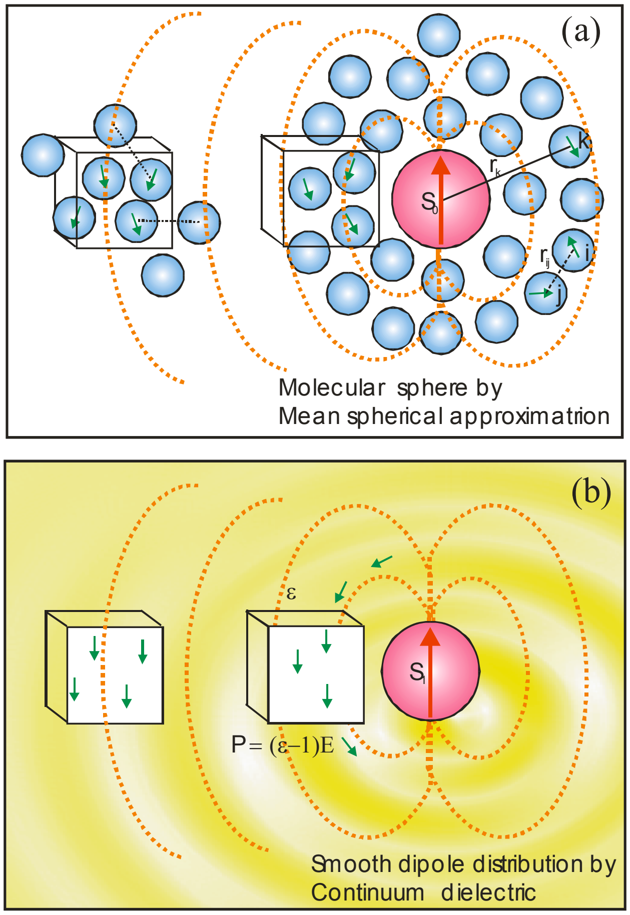

Figure 2.1.3-1. Panel (a) Illustration of the Mean Spherical Approximation (MSA)-molecularity of solvent environment. The real solute is approximated by a hard sphere solute containing a point charge or dipole, and the real solvent is approximated by many hard spheres with a central dipole. Panel (b) Illustration of the Onsager cavity Model. The solvents are treated as a dielectric continuum (yellow). The solute has a point dipole (red arrow). The dipole field (orange lines) creates a smooth polarisation (green arrows) around the solute. The resultant reaction field at the center stabilizes the solute.

Onsager calculated the reaction field and stabilization energy of a point dipole inside a cavity. Now imagine that the molecular chromophore undergoes an excitation that involves a change in the size and orientation of the dipole as well as change in the polarizibility of the chromophore. The spectral shift of the absorption and emission bands can be calculated in terms of the solvent static dielectric constant ε and index of refraction n [M0057]. For parallel solute dipole moments μ_0 and μ_1 the spectral shift (in wavenumbers, cm^{-1}) of the absorption $\Delta\nu_{abs}$ and fluorescence $\Delta\nu_{flu}$ band relative to the gas phase is given by [B0064]

$$\Delta\tilde{\nu}_{abs} = \frac{2\mu_0(\mu_0 - \mu_1)}{hca^3}.\Delta f + const \qquad 2.9$$

$$\Delta\tilde{\nu}_{flu} = \frac{2\mu_1(\mu_1 - \mu_0)}{hca^3}.\Delta f + const \qquad 2.10$$

where a is the radius of the cavity in which chromophore resides, h Planck's constant, c speed of light, and $\Delta f = \frac{\varepsilon - 1}{2\varepsilon + 1} - \frac{n^2 - 1}{2n^2 + 1}$ with ε dielectric constant and n refractive index. If the excited-state dipole is larger, the spectra are red-shifted with increasing solvent polarity ε, which is referred to as positive solvatochromism. Conversely, if the ground state dipole is larger, the spectrum becomes blue shifted (negative solvatochromism).

2.2 Solvent polarity scales

Describing the solvation power of a liquid by a single parameter is quite acceptable when the solvent-solute interactions are non-specific, such as dipolar interactions [MSL97]. This however is not the case if there are also specific effects like donor-acceptor interactions and hydrogen bonding. In order to calibrate specific interactions in addition to the solvent dipolarity and polarizibility (jointly referred as *solvent polarity*), empirical measures are required to derive one or more parameters. So far no unique scale exists which describes the effect of polar solvents on organic solutes. In the following we describe the most important scales of last 50 years, namely Kosower's *Z* [K0058], Brooker's χ_R [BCH65], Kamlet, Abboud and Taft's π^* [KAT77], Dong and Winnick's *Py* [DW084], Dragos's *S'* [D0092], Dimroth and Reichardt's $E_T(30)$ [R0094], and Catalan's *SPP* [CLP95].

a. **Kosower's *Z* scale** [K0058]

The *Z* scale is based on the marked solvatochromism of the 1-ethyl-4-carbomethoxypyridinium iodide ion pair (figure 2.2-1a). It is defined by the position of the maximum of its first absorption band which is due to intermolecular charge-transfer. The transition undergoes a hypsochromic shift as the solvent polarity increases, because of excited state of the chromophore is much less dipolar. *Z* value range from 94.6 kcal./mole for water to 54 kcal./mole for benzene .

b. **Brooker's χ_R scale** [BCH65]

The χ_R ("Red-shifted transition") scale is based on the solvatochromism of several merocyanine dyes (for example figure 2.2-1b), the electronic transition of which is accompanied by charge transfer from the amine nitrogen to a carboxamide group at the other end of the molecule. As the solvent polarity increases, the absorption band is shifted to red since the excited state is more polar than the ground state. The value of χ_R ranges from 50.9 kcal./mol in isooctane to 33.6 kcal./mol in *m*-cresol.

c. **The Kamlet-Abboud-Taft π* scale** [KAT77]

π* scale is so named because it is derived from the $\pi \to \pi^*$ electronic transition of nitro aromatic compounds (figure 2.2-1c) with 70 solvents. In addition to the dipolar/polarizability parameter, it describes hydrogen-bonding by parameters α for acidity and β for basicity. π* values range from -0.08 kcal./mole for n-hexane to 1.09 kcal./mole for water.

d. **The Dong-Winnick *Py* Scale** [DW084]

The *Py* scale is based on the relative intensities I_1/I_3 of the vibronic bands of Pyrene (figure 2.2-1d) fluorescence in 94 solvents and in the vapor phase. The *Py* values range from 0.47 kcal./mole (vapor) to 1.95 kcal./mole (dimethyl sulfoxide). This scale is compared to other scales of solvent polarity, particularly the π* scale of Kamlet and Taft in order to assess the contributions of various factors (dipolarity/polarizability, hydrogen bonding, etc.) to the solute–solvent interaction.

e. The Drago *S'* scale [D0092]

The unified non-specific solvent polarity scale or *S'* scale, was established by Drago. Over three hundred spectral shifts for 30 probe molecules and 31 solvents are fitted to an equation of the form $\Delta\chi = S'P + W$ where *S'* is a *solvent* polarity parameter, *P* is a *solute* (figure 2.2-1e) parameter that represents the susceptibility of the probe molecule to polarity, and *W* is a nonzero intercept at *S'= 0* in n-hexane. Electronic transitions, NMR chemical shifts and EPR hyperfine coupling constants were all fit to the same solvent *S'* values. This universal scale of solvent polarity incorporates the previous scales and considers specific types of interactions which can be described in terms of localized donor-acceptor interactions, involving specific orbitals, by using an electrostatic and covalence parameter. S' values range from 0.15 kcal./mole for n-hexane to 3.53 kcal./mole for water. No scale is valid for the solvating ability in special cases, for example (1) in concentrated solutions of polar probes in non-polar solvents, (2) when specific donor-acceptor interactions exist, and (3) in polar solvents that exist as rotamers which solvate to different extent.

f. The Dimroth-Reichardt's $E_T(30)$ scale [R0094]

Empirical scales $E_T(30)$ (" Transition Energy from dye # 30", figure 2.2-1f) were derived from positively and negatively solvatochromic compounds by UV/vis/near-IR absorption measurements – with emphasis on negatively solvatochromic pyridinium N-phenolate betaine dyes [R0094]. Normalised $E_T^N(30)$ values range from 0.000 kcal./mole for tetramethylsilane to 1.000 kcal./mole for water.

g. The SPP scale by Catalan [CLP95]

The solvent polarity/polarizability (SPP) scale is based on the solvatochromism of 2-(N,N-dimethylamino)-7-nitrofluorene (figure 2.2-1g) and its homomorph 2-fluoro-7-nitrofluorene (figure 2.2-1h); it has been extended to 100 solvents and the gas phase. This scale is normalized to 1.0 kcal./mole for DMSO and 0.0 kcal./mole in the gas phase. This scale is discussed in detail in section 5.1.5.

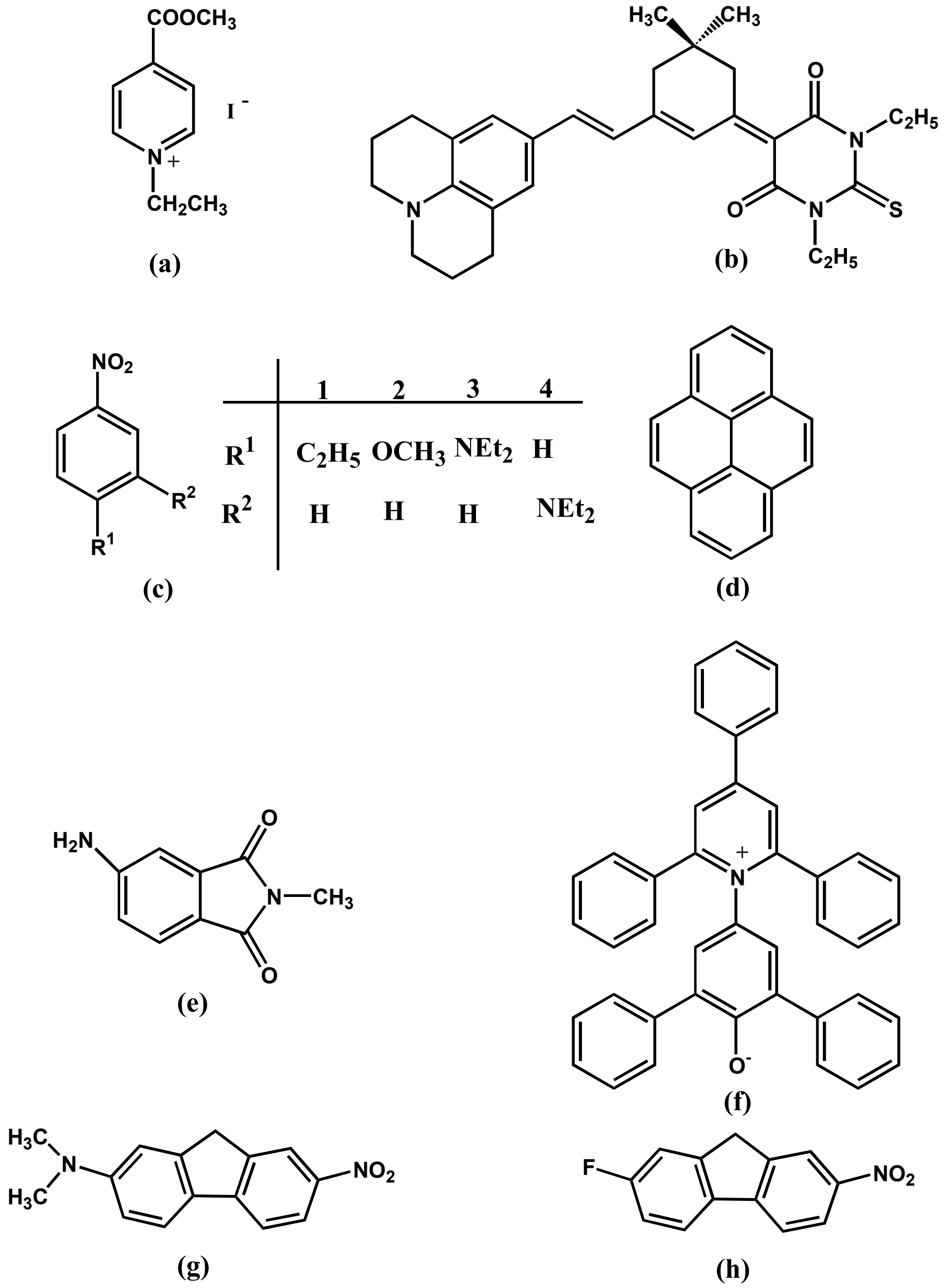

	1	2	3	4
R^1	C_2H_5	OCH_3	NEt_2	H
R^2	H	H	H	NEt_2

Figure 2.2-1 Structures of solvatochromic probes (a) 1-ethyl-4-(methoxycarbonyl)-pyridinium iodide (Z), (b) 1,3-diethyl-5-[5-(2,3,6,7-tetrahydro-1H, 5H-benzoquinolizin-9-yl)-1,3-neopentylene-2,4-pentadienylidene]-2-thiobarbutric acid (χR), (c) nitro benzene derivatives (π*), (d) Pyrene (Py), (e) 5-amino-2-methyl-isoindole-1,3-dione (S’), (f) 2,6-diphenyl-4-(2,4,6-triphenyl-1-pyridiniumyl)phenoxide (ET(30)), (g) 2-(N,N-dimethyl-amino)-7-nitrofluorene, and (h) 2-fluoro-7-nitrofluorene (SPP).

2.3 Solvation Dynamics

2.3.1 Definitions of S(t) and C(t)

The term “solvation” refers to the thermodynamically stable state of the local system consisting of a solute and its surrounding solvent [R0088]. Experiments which address ultrafast solvation dynamics, such as time resolved fluorescence, transient hole burning, transient pump-probe and photon echo experiments, monitor the response of the solvent particles to an optical excitation of the solute which typically involves a sudden change in the solute charge distribution [M0093, MMF89]. The normalized nonequilibrium solvent relaxation function is defined by

$$S(t)=\frac{\overline{\Delta E(t)}-\overline{\Delta E(\infty)}}{\overline{\Delta E(0)}-\overline{\Delta E(\infty)}} \tag{2.11}$$

Here $\overline{\Delta E(t)}$ is the energy gap between the ground and excited states of the solute, which changes with time due to the solvent reorganization. The over-bar denotes the *nonequilibrium* ensemble average after the solute is promoted to the excited state at t = 0. The initial solvent distribution corresponds to the solute in its ground state, and the dynamics after t = 0 evolves according to the solute-solvent interaction potential for the excited state of the solute. The most common approximation in theoretical studies of solvation dynamics is that of linear response [BC089, GC000, JFK94]. In this case S(t) is replaced by the corresponding *equilibrium* solvation time correlation function (TCF),

$$C(t)=\frac{\langle\delta\Delta E(t)\delta\Delta E(0)\rangle}{\langle(\delta\Delta E(0))^2\rangle} \tag{2.12}$$

where the angled brackets now represent the *equilibrium* ensemble average with the solute (either in its ground or excited state) and $\delta\Delta E=\Delta E-\langle\Delta E\rangle$.

In pure dense liquids, S(t) was generally found to agree reasonably well with C(t) [MF088, SR094] although a few exceptions were observed [FL091, HLS03, SL096]. However in liquid mixtures, linear response often fails because changing the solute charge distribution can strongly affect the preferential solvation by one of the components. This phenomenon has been observed in several simulation studies [CBR99, DP099, LP002, LS099] and was analysed theoretically [A0002, CB091, PWS01, YDP98].

Next we consider the time behavior of the polarization in the solvent when the electric field is changed. In the special case of polar solvation, the field in the solvent is altered by changing the solute dipole through optical excitation. The polarization of the solvent can not follow instantly but needs some time to build up. This characteristic time behavior is represented by a frequency-dependence of ε, the dielectric dispersion $\varepsilon(\omega)$ of the medium [SM096]. The most simple dielectric dispersion is given by Debye's

$$\varepsilon(\omega) = \varepsilon_\infty + (\varepsilon_0 - \varepsilon_\infty)/(1 + i\tau_D\omega) \qquad 2.13$$

Here τ_D ("Debye relaxation time") is a characteristic time for the polarization of a macroscopic sample of liquid to return to zero after an external electric field has been turned off. ε_0 and ε_∞ are the static and infinite-frequency dielectric constants of the liquid. In this case we find single-exponential solvation,

$$C(t) = e^{-t/\tau_L}, \tau_L = \varepsilon_\infty \tau_D / \varepsilon_0 \qquad 2.14$$

where τ_L is the observed relaxation time (also called "longitudinal"). The continuum theory for solvation was already depicted in the figure 2.1.3-1. It is considered to be not very accurate in the vicinity of the solute ("molecularity") but capable of providing the correct order of magnitude for the dynamics. In fact continuum theory may be far more accurate than the present literature gives it credit for; [see 2.3.6, LKM05]. The description can be improved by considering the finite size and mass of the solvent molecules [B0089, RKJ88].

2.3.2 Techniques of obtaining solvation curve

The solvation dynamics of a large number of solvents have been reported in the past decade. The experimental techniques can be divided according to method as follows.

(1) By spontaneous emission : With *fluorescence upconversion* techniques, the solvation correlation function has been derived by measuring the time-dependent emission spectrum of a suitable probe upon ultrafast laser excitation. For example,

Maroncelli *et al* [HGP95] studied the solvation of Coumarin 153 (C-153) in 24 different solvents and found the characteristic relaxation time. Ernsting *et al* [SKK01] studied solvation of C-153 and dimethylanilino methyl pyridine in methanol with simultaneous upconversion over a broad range (10,000 cm^{-1}). With the *Kerr-gating* technique, Maroncelli *et al* recently measured the solvation of trans-4-(Dimethylamino)-4'-cyanostilbene [AZM06].

(2) By stimulated emission : *Femtosecond transient absorption spectroscopy* also provided detailed information about the dynamics of solvation [LKM05, RKE98]. It was possible to monitor the solvation dynamics by following the evolution of the stimulated emission of a chromophore in solution on the time scale in which solvent relaxation occurs. If the stimulated-emission band is easily well separated from other features, it is possible to extract it. For example, Ernsting *et al* [LKM05] recently measured the solvation of N-Methyl-6-quinolone in water and methanol. Strong frequency-modulation in the dynamic Stokes shift of the emission band reflects coherent solvent motion which in turn used to probes the local IR spectrum of biochemical environment.

(3) *Three pulse stimulated photon echo peak shift (3PEPS)*: G. R. Fleming *et al* [LOF99, PNJ97] probed the solvation dynamics of tricarbocyanine dye (IR144) as well as *N*, *N*, bis-dimethylphenyl 2, 4, 6, 8, perylenetetracarbonyl diamide in non polar and dipolar solvents.

2.3.3 Components of solvation curve

The ultrafast component in the solvation time correlation function arises from the relaxation in the steep collective solvation potential which involves the total polarization of the system [B0089, BB099]. The component can be roughly defined in to three regions which are mainly based on physical features of solvation as follows; At t = 0 by femtosecond excitation, a dipole is created on the solute. An instantaneous electric field is experienced on the near solvent molecules by this newly created solute dipole. Since there is an interaction between the electric field and solvent permanent dipoles, the free energy minimum of the solvent shifts to a nonzero value of the polarization. Therefore solvent molecules find themselves in relatively high energy configuration initially. With time, the solvent molecules begin to move and rearrange themselves to reach their new equilibrium position. The solvent (nuclear) motion, can be classified into rotational (include hindered rotation, called libration) and translational motions (including intermolecular vibration along hydrogen bonds). The initial solvation relaxation (time constant $t \leq 100$ fs) is mainly dominated by coupled libration and translational motion, since they are high-frequency modes of the solvent with small amplitude. In the intermediate time region (typically $t \leq 0.5$ ps) one finds contributions from critically damped rotational motions or even low-frequency vibrational motions of the solvent molecules. The last part ($t \geq 0.5$ ps) is caused by diffusive rotational and translational motions.

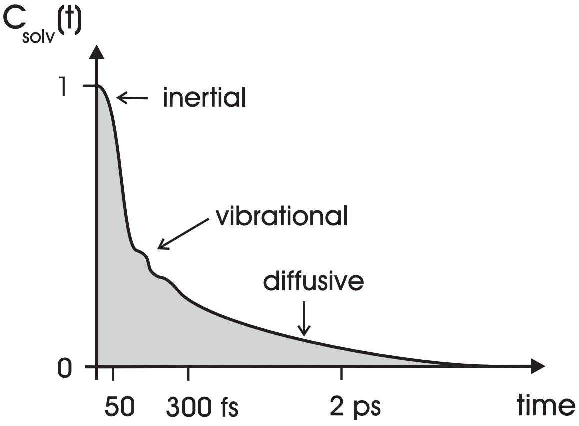

Figure 2.3.3-1 A typical solvation time correlation function for water. The time correlation function exhibits three distinct regions: the initial ultrafast decay until about 50 fs, an intermediate decay of about 300 fs where vibrational motion may lead to oscillatory behavior, and overdamped or diffusive (exponential) decay thereafter.

2.3.4 Solvation in water

Experimental [BJ090, JFK94, JWJ88, KEB98, LKM05, MF088a, SWY98, ZGF97] and simulation studies [ITT05, MC094, NNB91, SB095, SR094] on solvation dynamics of large dye molecules as well as of electrons in water have been repeated for over three decades. The solvation behavior can be related to the dielectric dispersion $\varepsilon(\omega)$ of water which was studied extensively by far-infrared (far-IR) spectroscopy and simulations [BAE89, G0091, H0073, HHF87]. The far-IR spectrum mainly arises from the different intermolecular vibration, libration, and other low-frequency modes. A broad shoulder around 200 cm^{-1} is due to an intermolecular $\mathrm{O \cdots O}$ vibrational mode of the $\mathrm{O-H \cdots O}$ units in the hydrogen bond network, and band at 650 cm^{-1} is caused by the librational motion. From the literature it is known that water has the fastest kinetics among the solvents [JFK94, MF088a]. Barbara *et al* [JWJ88] measured for the first time solvation dynamics of water with 7-(dimethylamino)coumarin-4-acetate by ultrafast fluorescence spectroscopy. The authors modeled the observed microscopic solvation dynamics by a biexponential decay with lifetimes of 160 fs (33%) and 1.2 ps (67%). Fleming *et al* [MF088a] predicted a very fast inertial component with a Gaussian time constant of less than 20 fs by simulation studies. It was found experimentally [JFK94] that the Gaussian component has time constant less than 50 fs and slower biexponential decay occurs with time constants 126 fs (20%) and 880 fs (35%). Huppert and co-worker resolved a biomodal behavior in a study of rhodamine 800 in water, with ultrafast components less than 100 fs [ZGF97]. Bader and Chandler [BC089] theoretically predicted even larger amplitude decay, ~70%−90%, with faster (25 fs) dynamics for the solvation of water. Theoretically predicted dynamics is generally much faster than the experimentally observed dynamics.

2.3.5 **Properties of C(t) –** which kind of curves were observed

In the following we summarize the main results from experimental and theoretical studies of solvation dynamics over last 20 years**.**

(1) The nonequilibrium correlation functions are typically not a single exponential. They include an early very fast (less than 50 fs [JFK94]) inertial (mainly librational motion of the solvent molecules) component, which can account for 60%-80% of the total relaxation in water. This is followed by a multiexponential relaxation on the hundred femtosecond and picosecond time scale owing to the diffusive motions [WJK90].

(2) Molecular details of the solvent are important [S0088], and in many cases, relaxation times can be associated with specific molecular motions such as hydrogen

bonding dynamics or the rotation of solvent molecules [LM098] or of particular functional groups.

(3) Onsager conjectured [O0077] that far-away solvent regions relax first and contribute a large part to C(t). But the solvent response was found to be much more complex than envisioned by this “inverted snowball picture” [PM093]. The source of this complexity lies in the fact that the solvent response can not be usefully thought about in terms of independent contributions from different spatial regions. Even though, simulations show that most of the contribution to polar solvation dynamics comes from the first solvation shell [M0091].

(4) Rotation and translation of the probe molecule can accelerate solvation dynamics, depending on the relative rate of solvent and solute motions. It is also important to consider the influence of solute polarizability on solvation dynamics [KM095]. Higher polarizibility slows down the solvation on a picosecond time scale.

(5) With few exceptions [FL091, FL094, SL096], polar solvent dynamics are in reasonable agreement with linear-response theory, even for large perturbations away from equilibrium. Cases where linear response theory fails involve situation where the equilibrium fluctuations do not sample all regions in which the nonequilibrium dynamics take place [GC000].

(6) Solvation dynamics in liquid mixtures are sensitive to the mixtures composition and may reflect clustering and enrichment of one of the solvents around the solute [CWR97, DP099, LKL02, PWS98, SC000, SL096].

2.3.6 Stokes shift by solvent relaxation − illustration

The dynamic Stokes shift of fluorescence is illustrated with the figure 2.3.6-1. The yellow–red band in the figure images the relaxation of the surrounding solvent in the S_1 state of the solute. Solvent coordinate Q represents the configurational state of the environment and is treated classically. High-frequency motion along internal coordinate q for bond lengths and angles is quantized in vibrational states. Before femtosecond excitation (A) the solute is in the equilibrated ground state S_0 and the (blue) absorption band extends over a Franck–Condon progression for upward optical transitions.

Immediately after excitation (B) the emission overlaps the absorption band at the electronic absorption origin 00. Partially relaxed $E_1(Q)$ (C) corresponds to solvent configurations that have raised $E_0(Q)$. The fluorescence therefore changes from yellow to red as solvation proceeds. After several picoseconds (D) a new equilibrium is reached for the S_1 state. A point dipole in a spherical polarizable cavity represents the solute, while a continuum with dielectric dispersion $\varepsilon(n)$ represents the surrounding liquid.

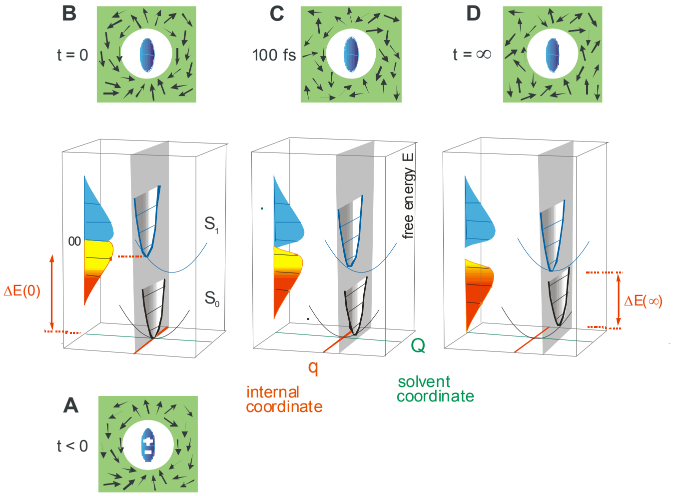

Figure 2.3.6-1 Illustration for the continuum theory of polar solvation. The dynamic Stokes shift of fluorescence images the relaxation of the solute in its S_1 state. Solvent coordinate Q represents the orientational state of the environment and is treated classically. High-frequency motion along internal coordinate q for bond lengths and angles is quantized in vibrational states.

2.4 Ultrafast structural and solvation dynamics of modified DNA

2.4.1 Motivation to study the ultrafast kinetics in modified DNA

Among recent developments, one of the most powerful has been the realization of DNA microarrays and DNA chips for a wide field of applications, from expression analysis to diagnostic chips [P0002]. Reliable detection of genomic sequence variations, mainly point mutations, is critical for the study of population genetics, for the clinical diagnostics of cancer, for the diagnosis and treatment of genetic or viral diseases such as AIDS. Charge transfer in DNA should be suitable for a highly sensitive electrochemical readout on DNA chip, because this process show an extreme sensitivity towards perturbation and interruptions of base stacking that are caused by base mismatches or DNA lesions.

A number of other uses of modified DNAs is driving this field of study.

(1) The local flexibility of DNA must be considered when dynamical models for DNA-drug interactions are developed.

(2) Ultrafast kinetics of modified oligonucleotides might be significant for a comprehensive understanding of sun-light-induced DNA damage.

(3) Modified oligonucleotides and analogues are being pursued as therapeutic agents targeted to human disease.

(4) Modified oligonucleotides are being used in molecular diagnostic strategies for identifying disease-related genes and pathogens.

2.4.2 **Chemical probes covalently attached to DNA** – a brief summary of synthetic work

A variety of fluorescent probes has been covalently attached to DNA sequences with different purposes. For our application, however, we need to incorporate a molecular probe into a DNA duplex with the following considerations: (i) the probe must minimally distort the duplex structure, (ii) the orientation of the probe relative to the helix axis should be fixed and known, and (iii) the photophysical properties of the probe must be appropriate for the spectroscopic technique to be used. Some of fluorophores for this kind of study are briefly discussed here. Many probes are used as free intercalators which bind inside the DNA duplex through electrostatic interaction, and/or “outside” at the end of an oligonucleotide primer. As was mentioned before, our "forced intercalation probes" [KJS05] must fulfill more stringent requirements. The groups which are active in this area or have similar interests are those of Eric T. Kool (Stanford), Hans -A. Wagenknecht (Regensburg), Oliver Seitz (Berlin), Robert S.Coleman (Ohio State), Thomas L. Netzel (Georgia State), Frederick D. Lewis (Illinois), Bernd Giese (Basel), Jacqueline Barton (Caltech), and Thomas Carell (LMU). Here I outline briefly their characteristic research by some recent publications.

a. Eric T.Kool *et al*

They synthesized [CCP05] modified DNA in which multiple individual fluorophores (such as terphenyl, pyrene, terthiophene and fluorescein - figure 2.4.2-1a-d) are incorporated at adjacent positions at the end of a DNA probe. This arrangement acts as an oligomeric fluorescent label for DNA with large Stokes shift and increased emission intensity. The benzo-homologated (x) forms of adenine (xA), thymine (xT), guanine (xG), and cytosine (xC) (figure 2.4.2-1e-h) were also synthesized [GLK05]. It was found that in oligonuclotides, these form right-handed-helical complexes when paired against the natural bases T, A, C, G respectively, with a helical diameter approximately 2.4 Å larger than with natural pairs. All four expanded nucleobases are inherently fluorescent, which makes them potentially applicable as biophysical tools.

Most recently [KK005] a procedure was described for the conversion of toluene, 2, 4-difluorotoluene, 2, 4-dichlorotoluene, 2, 4-dibromotoluene, and 2, 4-diiodotoluene deoxyribosides (figure 2.4.2-1i-m) into suitably protected phosphoramidite derivatives and their incorporation into synthetic DNAs. Thermodynamic studies of hexamer and dodecamer duplexes were carried out in comparison to natural thymine. Thermal melting data with the chromophores in 5' dangling positions showed that all five compounds stack more strongly than thymine, and that the dihalosubstituted compounds stack more strongly than unsubstituted toluene. Stacking correlated with surface area and hydrophobicity, both of which increase along the series mentioned above.

b. Hans-Achim Wagenknecht *et al*

This group synthesized the phenanthiridinium heterocycle (figure 2.4.2-1n) which can function as artificial base in DNA [HAW04]. By combining the fluorescence quenching properties of the chromophore together with DNA-mediated charge transfer, one can detect DNA base mismatches and abasic sites directly [AHW04, VAW05].

Pyrene (Py) was attached to all nucleobases via Suzuki-Miyaura cross-coupling reactions [AW002]. Its fluorescence intensity was studied at different pH, which provides information about the acidity and basicity of photochemically generated DNA base radicals. It was found that electron transfer in 5-(1-pyrenyl)-2'-deoxyuridine (Py-dU,

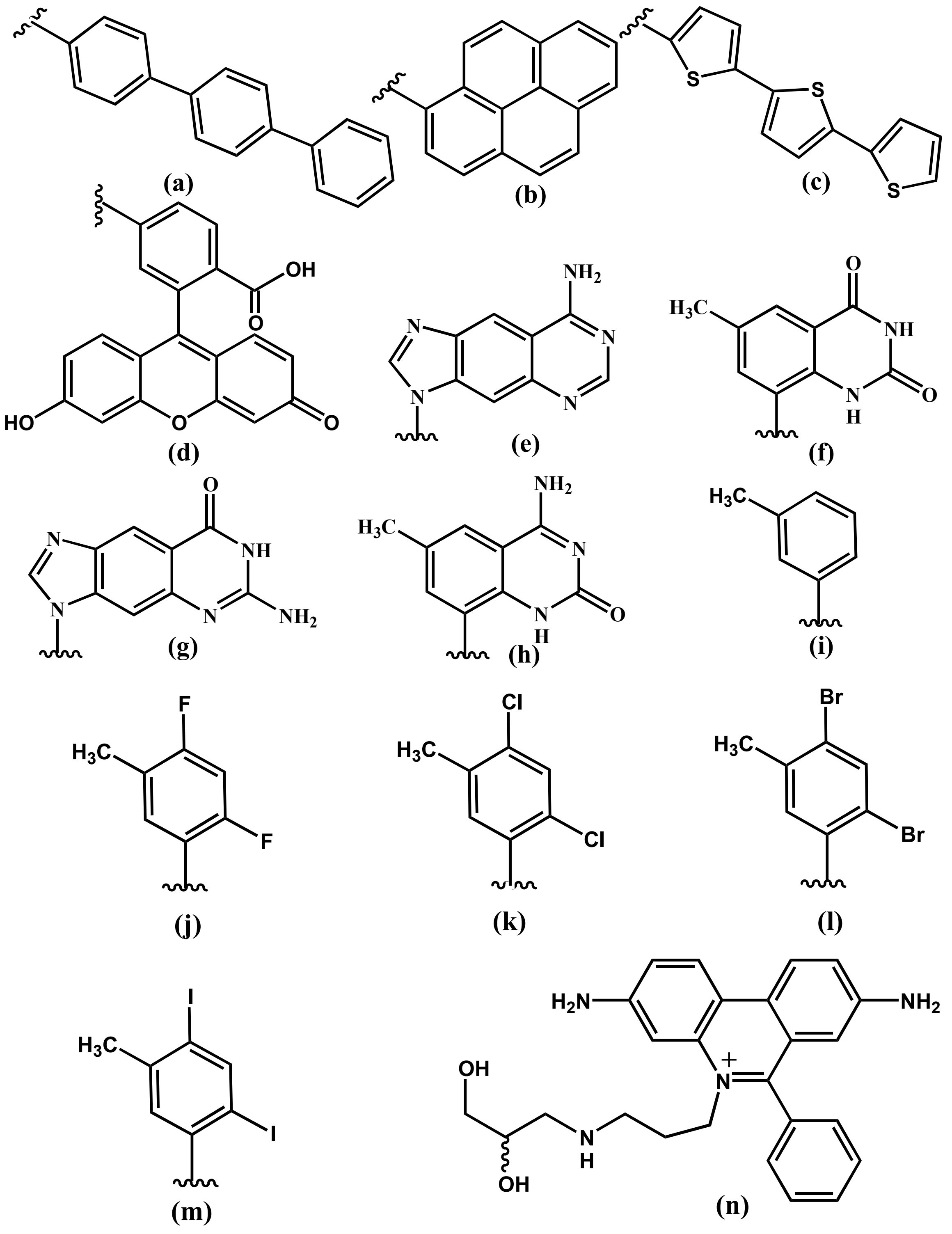

Figure 2.4.2-1 Structures of different chromophores (a) Terphenyl, (b) Pyrene, (c) Terthiophene, (d) Fluorescein, (e) Benzo homologated (Benzo) form of adeinine, (f) Benzo-thymine, (g) Benzo-guanine, (h) Benzo-cytosine, (i) Toluene, (j) difluoro toluene, (k) dichloro toluene, (l) dibromo toluene, (m) diiodo toluene, and (n) Ethidium nucleoside.

figure 2.4.2-2a) and 8-(1-pyrenyl)-2’-deoxyguanosine (Py-dG, figure 2.4.2-2b) are directed in opposite directions. The intramolecular charge transfer in Py-dG generates a cationic nucleoside species ($Py^{\cdot -}$-$dG^{\cdot +}$) which deprotonates at higher pH, whereas charge transfer in (Py-dU) yields an anionic DNA base radical ($Py^{\cdot +}$-$dU^{\cdot -}$) which is protonated at pH >5 [HFW03].

c. Oliver Seitz *et al*

Nonpolar nucleoside analogues containing aromatic chromophores as base, such as pyrene, naphthalene, acenaphthalene, and biphenyl (figure 2.4.2-2c-e) were synthesized by C-glycosylation with organic cupric reagents [BSB03] which are less toxic than cadmium reagents. The aim is to implement this approach for the development of high-affinity binders to other adenine-specific DNA MTases.

Thiazole orange (TO, figure 2.4.2-2f) with an acetate tether to the quinoline ring was synthesized as one of the best peptide nucleic acid (PNA) base surrogates [KJS05]. Their studies and applications were explained in the TO chapter 7. A procedure for solid-phase synthesis of PNA containing thiazole orange was also given [JKS05].

d. Robert S. Coleman *et al*

synthesized a structurally novel photophysical probe, coumarin 2’-deoxy-C-riboside (figure 2.4.2-2g), to be used for ultrafast polar dynamics in and around a DNA double helix [CM098]. The label was always placed opposite an abasic site, with a position varying along the sequence. Structure information on these constructs is not yet available.

e. Thomas L. Netzel *et al*

The synthesis of 5-(2-(pyren-1-yl-ethylenyl)-2'-deoxyuridine (PEdU, figure 2.4.2-2h) was described, based on complete selective reduction of the ethynyl linker in 5-(2-(pyren-1-yl-ethynyl)-2'-deoxyuridine [GN005]. They also established a reliable route to the 1-ethynylpyrenyl intermediate, following many previous attempts with low yield.

A water-soluble, ethynyl-linked AQ-dA conjugate, 8-[(anthraquinone-2-yl)ethynyl]-2'-deoxyadenosine 3'-benzyl hydrogen phosphate (figure 2.4.2-2i), was

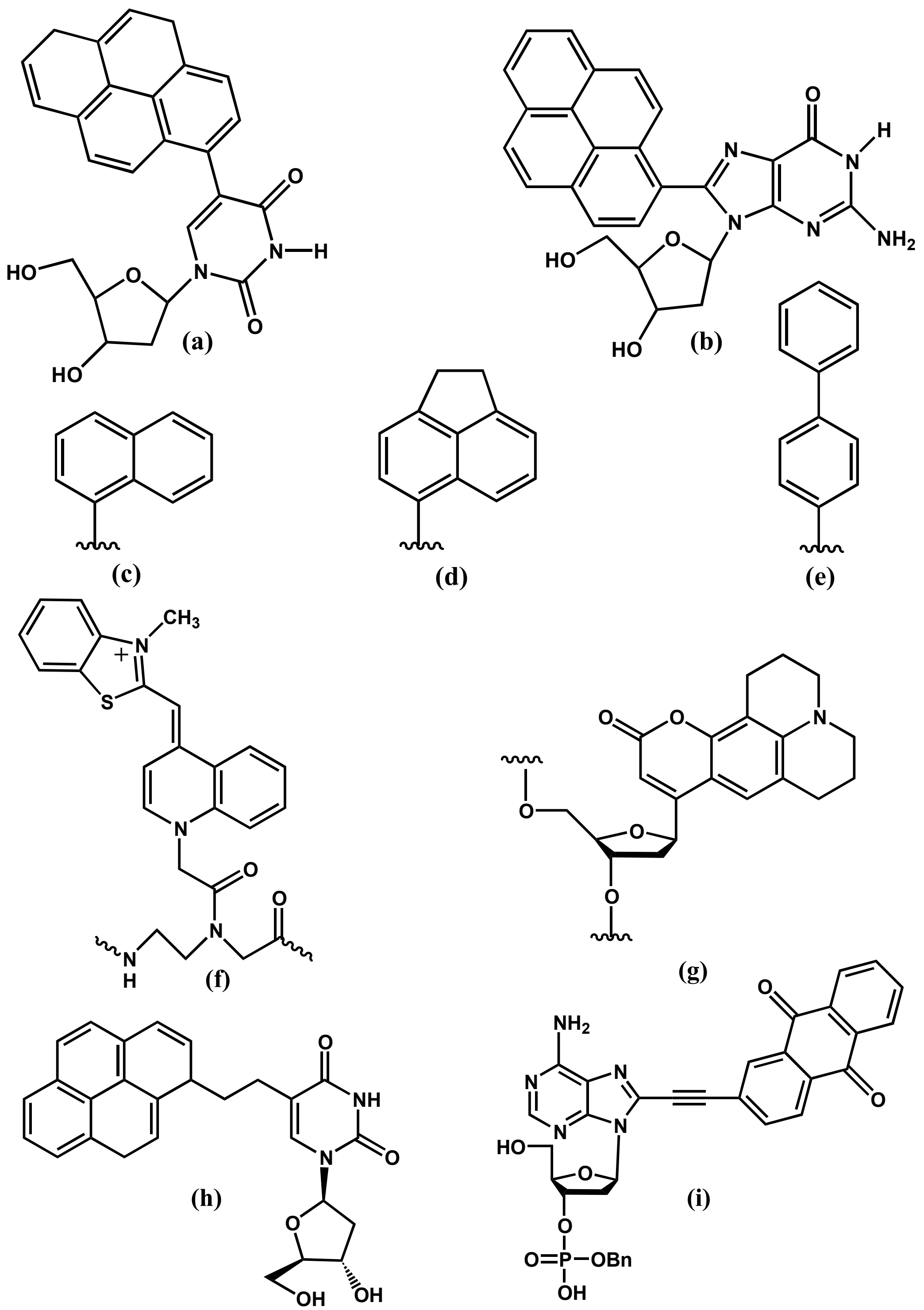

Figure 2.4.2-2 Structures of different chromophores (a) 5-(1-pyrenyl)-2'-deoxyuridine (Py-dU), (b) 8-(1-pyrenyl)-2'-deoxyguanosine (Py-dG), (c) Naphthalene, (d) Acenaphthalene, (e) Biphenyl, (f) Thiazole orange –PNA monomer, (g) Coumarin C-riboside, (h) 5-(2-(pyren-1-yl-ethylenyl)-2'-deoxyuridine (PEdU), (i) 8-[(anthraquinone-2-yl) ethynyl]-2'-deoxyadenosine 3'-benzyl hydrogen phosphate.

described in another paper [AN005]. Its synthesis is based on the initial formation of a 5'-*O*-(4,4'-dimethoxytrityl) (5'-*O*-DMTr) intermediate. But in 5'-*O*-DMTr–protected 2'-deoxyadenosines, if the ethylenyl is reduced by H_2 over Pd/C, then the protecting group is cleaved and multiple side products are precipitated. This work also describes the synthesis of an ethylenyl-linked AQ-dA conjugate, 8-[2-(anthraquinone-2-yl)ethyl]-2'-deoxyadenosine 3'-benzyl hydrogen phosphate, starting with a 5'-O-*tert*-butyldiphenylsilyl protecting group.

f. Frederick D. Lewis *et al*

To study the dynamics of DNA-mediated charge separation and charge recombination, they synthesized hairpin-forming bis(oligonucleotide) conjugates possessing a stilbine-4, 4'-dicarboxamide (figure 2.4.2-3a) linker and a single G-C base pair separated from the linker by a variable number of A-T base pairs [LWZ04]. In the same paper, they use a stilbine-4, 4'-dicarboxamide linker and a stilbenediether positioned at opposite ends of short duplex sequences. The former acts as an electron acceptor and the latter as an electron donor. Circular dichroism spectra and photoinduced electron-transfer dynamics of these hairpin conjugates are reported.

g. Bernd Giese *et al*

synthesized model systems bearing three different redox sites, to study the electron-hole transport in peptides [GNJ05]. These are modified tetrahydrofuran as a charge-injection system, 2, 4, 6-trimethoxyphenylalanine as intermediate charge carrier, and tyrosine as an electron donor (as in the figure 2.4.2-3b). The latter two were separated by oligoproline spacers with variable length. By flash photolysis with nanosecond laser pulses, rate constants were determined for electron transfer from the tyrosine side chain to the 2, 4, 6,-trimethoxyphenylalanine radical cation ($\text{ala}^{\cdot +}$) moiety, which is generated by the flash. It was found that electron-hole transport in peptide radical cations ($\text{ala}^{\cdot +}$) occurs by a hopping mechanism between the aromatic side chains of the amino acids, similar to the long-distance hole transport through DNA.

The following authors used transition metal ions as intercalating agents in a DNA duplex, with the idea of studying duplex stability.

h. Jacqueline K. Barton *et al*

By design, specific sites in DNA are targeted where complexes are formed. This is to be the basis for novel chemotherapeutics aimed at nucleic acids with improper base-pairing motifs, and the approach also provides new tools to probe DNA structure and recognition.

A fluorescent metallointercalator conjugate was synthesized [ZB006] by coupling an organic fluorophore, such as Oregon Green 514, to a bulky Rh intercalator containing the chrysenequinone diimine ligand (figure 2.4.2-3c). This will selectively target DNA base mismatches, which are signalled by a fluorescence increase of the conjugate greater than 300%. Intercalation of the Rh moiety into the mismatched site leads to electrostatic repulsion of the anionic fluorophore away from the DNA phosphate backbone and Rh center. In this state intramolecular quenching of fluorescence is reduced. When such unfolding is not possible, as in the presence of matched DNA or simply in solution, ion pairing between the cationic Rh and anionic fluorophore moieties dramatically quenches the fluorescence.

Long-range photoinduced electron transfer [KHS97] has been systematically examined in a series of small DNA duplexes covalently modified with ethidium and $Rh(phi)_2bpy^{3+}$ through time-resolved and steady-state measurements of fluorescence quenching. Fast fluorescence quenching ($k \geq 10^{10}$ s^{-1}) is observed for this donor/acceptor pair noncovalently bound to DNA, and transient absorption studies allow the assignment of quenching to an electron transfer mechanism. In the duplexes modified with tethered intercalators, intrahelix fluorescence quenching attributed to electron transfer occurs at distances up to 30 Å. Over a donor/acceptor separation of 20 Å, approximately 30% of the ethidium fluorescence is quenched, while at a separation of 30 Å, approximately 10% quenching is observed.

i. Thomas Carell *et al*

describe the synthesis of a DNA metal-base pair based on the N, N'-bis(salicylidene)ethylenediamine (= "salen") ligand in which salicylic aldehyde is connected at the C4 atom to the C1' position of 2'-deoxyribose [CPC05]. Two such

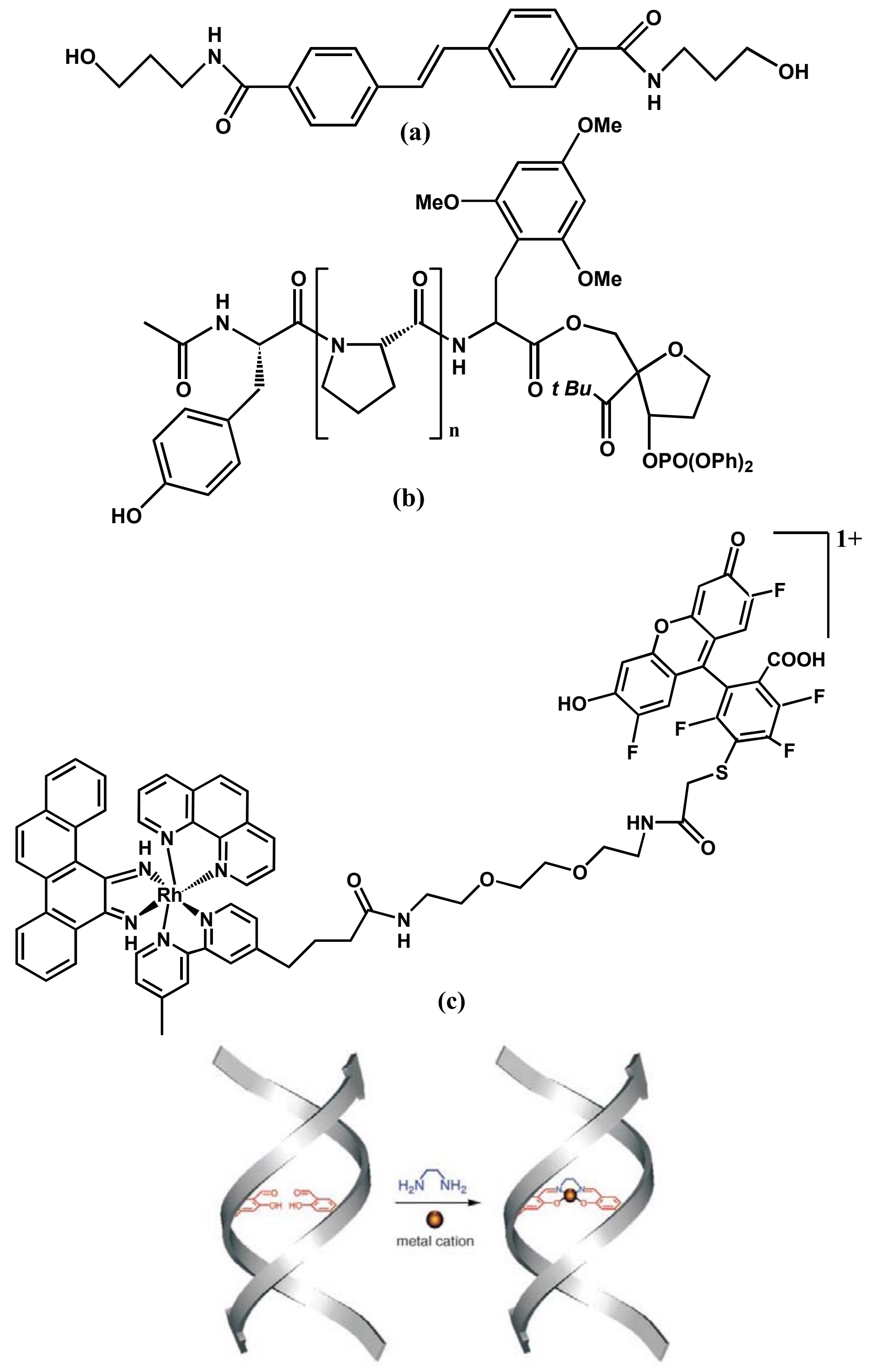

(d)

Figure 2.4.2-3 Structures of different chromophores (a) trans-N,N'-bis(3-hydroxy propyl)stilbene-4,4'-dicarboxamide, (b) Model systems containing modified tetrahydrofuran, 2,4,6-trimethoxyphenylalanine and tyrosine, (c) [Rh(phen)-(bpy) (chrysi)]$^{3+}$ tethered to Oregon Green 514, (d) Depiction of the salicylic aldehyde base pair and assembly of the metal-salen complex inside the duplex.

ligands facing each other in a duplex structure assembled in the presence of copper metal ion (which is located inside the duplex structure) and ethylenediamine to give a metal-salen complex (as in the figure 2.4.2-3d). An increase of melting temperature by more than 40°C is due to reversible cross-linking of the ligand ethylenediamine and additionally, possibly by axial coordination of the metal ion with heteroatoms present in the base pairs below and above the metal-base pair.

To direct the metallization process to specific DNA strands or stretches of DNA, a simple method was recently reported [BGM06], especially for the deposition of Ag(0) around aldehyde-modified DNA. The modification involves incorporation of acetylene-containing nucleotide triphosphates using DNA polymerases on polyacrylamide gel. With this method, Ag(0) deposition can be confined only to the modified DNA. The ability to insert the acetylene labels enzymatically offers the possibility to exploit the arsenal of molecular biological tools to construct conductive DNA nanodevices.

2.4.3 Experimental approaches to DNA dynamics

A number of techniques have been used to look at DNA dynamics at various time and length scales. Information on localized dynamics and short time scales has been the most difficult to obtain. Here we summarize the experimental methods for studying conformational changes or reorganization dynamics in DNA. For each technique only a representative piece of work is cited.

The first two methods concern ultrafast time-resolved spectroscopy.

(1) A single polar charge-transfer chromophore [ALK05] is covalently linked into the base stack, where it replaces a nucleobase. After ultrafast optical excitation a dynamic spectroscopic property is monitored, such as the fluorescence Stokes shift or the shift in the stimulated emission of the chromophore. The surrounding medium responds to the change of the dipole moment of the chromophore. The observable will reflect the polarizibility of the surrounding medium (neighboring base pair, phosphoester backbone, counter anions).

(2) A pair of chromophores [TRB05] is covalently attached to the specific DNA bases, extending from the major groove. The interacting pair will form an excimer with its characteristic spectral property. By studying excimer formation one can infer about the local DNA structure and its dynamics.

The following methods address conformational changes at very long time scales.

(3) Freely intercalating fluorophores [CBR97] have been used in what is known as "optical labeling". For example ethidium bromide was studied both free in solution and bound to DNA at different temperature intervals. From the visible absorption band of the probe as a function of temperature, information on local dynamic properties of the double helix can be obtained. At low temperatures, the DNA double helix presents a rather rigid environment for the bound chromophore. Therefore the conformational heterogeneity is reduced and low frequency motion corresponds to harmonic vibrations, while anharmonic motions are hindered. On the other hand, at higher temperature a large increase of anharmonicity is observed which is attributed to increased "wobbling" of the dye in its intercalation site, in connection with the onset of local opening/unwinding of the double helix.

(4) A number of different NMR techniques may extract dynamical information on DNA, as has been reviewed in detail [G0094, RD095]. In general, the "overall" dynamics corresponding to the rigid-body tumbling motion of an oligomer is well characterized by NMR. In many cases, the total amplitude of motion due to all "internal" motions can be found and is typically in the range 5-30^0. These internal motions comprise both collective, long-range bending and twisting of the helix as well as local motions of the bases and back bone. These motions are typically rapid enough to be strongly averaged in NMR experiments, but in favorable cases the average effective correlation time can be estimated, in the range of tens to hundreds of picoseconds [BLK94].

(5) Single-crystal X-ray diffraction, as function of temperature, may yield the *directions and magnitudes* of translational and rotational mobility of the phosphate, ribose and bases in DNA or RNA [HK084]. An oligonucleotide is divided into several subgroups, in what is termed a "segmented rigid body" model, and the motion of atoms in each is constrained to translate and librate (partially rotate) as a unit.

(6) Molecular dynamics simulations consistently find motion of bases and backbone segments on a time scale of ten to hundred of picoseconds [YJB97].

(7) To study DNA reactions, a new method was developed by *J.K.Barton et al.* These authors assemble DNA duplexes onto gold surfaces with alkane thiols as linkers [BSB02]. An intercalator, Daunomycin, is added as a site specific redox reporter. The films are characterized by various methods, including Atomic Force Microscopy (AFM), Scanning Tunneling Microscopy (STM) and radiative tagging, and are then used as electrodes. Such DNA-modified electrodes can probe DNA mismatches, lesions, as well as protein/DNA interactions and reaction.

Finally, even thermodynamic information may shed light on DNA dynamics because it is connected to the density of states:

(8) Differential scanning calorimetry technique showed that molecular segmental motions of B-DNA and of water attached to it are attributable to a broad distribution of energy barriers between conformational sub states [RHM97].

2.4.4 Observations from structural dynamics of DNA

The following groups are working in the field of ultrafast structural dynamics of DNA, with the explicit purpose to extract the solvation correlation function for DNA: those of Ahmed H. Zewail (Caltech), Mark A. Berg (South Carolina), Torsten Fiebig (Boston), Thomas L. Netzel (Georgia state), Frederick D. Lewis (Illinois) and Jacqueline. K. Barton (Caltech). Here I briefly review their recent characteristic publications in this regard.

a. Ahmed H. Zewail *et al*

This group studied charge-transfer processes in DNA, as they are mediated by the DNA dynamics. In preparatory work [WXB05] they studied 2-aminopurine(AP), a fluorescent isomer of adenine, and daunomycin in complexes with guanine, adenine, and tryptophan. The complexes are either formed by association of the free chromophores in aqueous / buffer solution, or else they are covalently linked as nucleotides. To elucidate the dynamics of these complexes, femtosecond transient absorption and femtosecond fluorescence up-conversion techniques were used. They observe i) a marked difference between transient absorption and transient fluorescence dynamics, ii) the dependence on the free energy gap, iii) an abrupt decrease of the initial fluorescence intensity. From this they derive a model for the general mechanism and obtain rate constants for charge separation, vibrational relaxation and charge recombination. It is proposed that, from the excited state, direct (unequilibrated) nearly barrierless crossing to the charge transfer state could be a major channel that competes with vibrational relaxation and indirect (equilibrated) charge separation. The presence of this pathway is facilitated by strong interaction between the fluorophores and quenchers in the 'stacked' structures of complexes. It is important to account for these 'dark channels' when electron transfer rates are deduced from quantum yield measurements.

In a review [PZ004] important features of biomolecular hydration are addressed, with emphasis on proteins in the native (and denatured) state, and on DNA of two types: synthetic dodecamer duplex and genomic calf thymas. The idea is to obtain the hydration dynamics on the time scale of actual molecular motions of water, which means at the earliest time, by femtoseond time resolved spectroscopy. On this time scale it should be possible to examine the dynamical nature of water in the bulk as compared to water loosely bound in the interfacial layer. Results of biomolecular hydration were obtained from studying the intrinsic amino acid (tryptophan) on the surface of a protein native structure, and the fluorescent probe 2-aminopurine covalently attached in DNA. The dynamics was found to be vastly different from those of bulk water, and lead to identify two types of water molecules at the interface: those which are labile or bulk-like with time constant ~1 ps, and those which are bound to the surface with time constant ~20-40 ps.

b. Mark. A. Berg *et al*

Berg *et al* studied the ultrafast solvation dynamic of DNA by using Coumarin 102 in a 17mer duplex. Time correlated single-photon counting, fluorescence up-conversion, and transient absorption measurements were all linked to this purpose [ALK05]. The time-resolved Stokes-shift was found to increase continuously throughout the 40 fs to 40 ns time range. The authors observed and explained their data by fitting power law kinetics. The fastest components of the solvation in DNA are nearly as fast as the solvation dynamics in pure water. The slower components suggests that motion of other components, such as electrolytic ions, DNA backbone, and DNA bases play an important role in the solvation response.

Another study by the same authors addresses lesions in the DNA structure [SAM04]. Again the time-resolved Stokes shift (TRSS) of Coumarin 102 covalently linked into DNA was monitored between 40 ps and 40 ns. Comparisons are made between 17mers without modification, with a deleted base near the coumarin and with the coumarin placed near the end of the oligomer. In the case of deleted base, the dynamic deviation from the regular behavior begins after 1 ns. This is assigned to the flipping of the abasic sugar between intra- and extrahelical positions. In the case of a chain end, the long time dynamics (i.e after 1 ns) is not altered whereas the amplitude of the dynamics between 40 ps and 1 ns is reduced. The long-term dynamics is assigned to local features of the DNA. The decrease in Stokes shift is suggested that at the chain end, on one side of the probe which before was occupied by DNA is now replaced by water. The relaxation due to water is too fast to be fully seen. This explains the reduced amplitude. The effective polarity of DNA was determined to be 0.69 on the E_T^N polarity scale, from the Stokes shift of coumarin 102 in ethanol as a calibration point.

Acridine Orange (AO) is another interesting fluorescent probe which intercalates into DNA. The binding constant of AO to DNA $\sim 10^4$ M^{-1}. The local dynamics in DNA was studied by measuring the (stationary) Stokes shifts of intercalated AO as function of temperature [BMB98]. Fluorescence excitation and emission spectra have been measured from 100 to 320 K in a 3:1 glycerol-aqueous buffer mixture. The Stokes shift of AO arises from movements of neighboring groups that change the effective volume available to the dye. At lower temperature the interior of DNA shows the diffusive, viscous dynamics characteristics of a fluid, rather than the purely vibrational dynamics of a crystal. At high viscosity the rate of DNA motion is limited by the rate of solvent motion. At room temperature the experiments detected a weak relaxation with time constant of ~100 ps, which was attributed to localised motion of the intercalated dye.

c. Torsten Fiebig *et al*

Fiebig *et al* monitored local structural dynamics in DNA indirectly, by looking at adjacent pyrene molecules which were attached to DNA bases, using femtosecond broadband pump-probe spectroscopy [TRB05]. They found two pathways for electronic coupling. The first is through the base stack, confirmed by observing excited-state absorption within 300 fs even when two chromophores were separated by one AT base pair. Therefore the excitation energy can apparently migrate over ~7Å. The second pathway is through orbital overlap (space), as identified by a pronounced dynamic spectral blue shift. By analyzing the time constant, the local structural motion in DNA is 10 ps if the chromophores are in direct contact, but 2 ns if chromophores were separated by one AT base pair. The latter was assigned to local structural motions in DNA involving the reorientation of at least three base pairs.

The same authors studied the dynamics of reductive electron processes in DNA. Pyren-1-yl-2'-deoxyuridine (Py-dU) was used as electron donor, since photoexcited Py* allows the reduction of C and T, and 5-bromo-2'-deoxyuridine (Br-dU) as electron acceptor [KET02]. Electron transfer processes represent the injection of an electron into the base stack; the injection rate can be obtained from the decay of the transient absorption band of (Py-dU)* at 385 nm. These studies conclude the following. DNA is a flexible medium with a manifold of conformational states exhibiting a wide range of reactivities and rate constants. Since DNA-mediated ET is a multistep processes on various time scales, the electron-injection rates may not necessarily correlate with the strand degradation as the chemical result of DNA-mediated ET. These results provide a lower limit for the rate of reductive ET between single bases in DNA.

In [FWZ02] the femtosecond transient absorption and femtosecond fluorescence upconversion technique was established, for the first time, to study the ultrafast excited state dynamics of 2-amino purine (Ap) with mononucleotides of guanine, adenine, cytosine, thymine, 7-deazaguanine and inosine in buffer solutions. Analyzing the result, the authors suggest that both electron transfer and hydrogen transfer are possible mechanism when Ap is used a probe base in DNA. From the measured rates, they estimated the free energies for both hydrogen transfer to guanine and adenine, and electron transfer to thymine and cytosine. These studies form the foundation for charge transfer in DNA.

d. Thomas L. Netzel *et al*

To understand the photophysics of intramolecular charge transfer (CT) in pyrenyl deoxyuridine nucleoside conjugates, these authors [GHA05] applied femtosecond, picosecond and nanosecond transient absorbance and picosecond emission spectroscopy. They studied the formation and decay dynamics of $Py^{\cdot+}/dU^{\cdot-}$ CT products in three 5-(1-pyrenyl)-2'-deoxyuridine nucleosides, each with different two-atom linkers joining pyrenyl C-1 to uracil C-5. The linkers are respectively -NHCO-, $-(CH_2)$ - and –C ≡ C for PAdU, PEdU and PYdU with varying degrees of free rotation about the linking bonds. For all three nucleoside conjugates, most conformers undergo intramolecular charge transfer from their pyrenyl $^1(\pi, \pi^*)$ excited states to form $Py^{\cdot+}/dU^{\cdot-}$ CT products in ultrashort times: ≤ 0.6 ps for PAdU, ≤ 30 ps for PEdU, and ≤ 100 ps for PYdU. When these nucleoside were studied for excess electron transport in DNA, the lifetimes of the CT products in MeOH lengthened significantly. From these observation the following model has been proposed. The multiexponential emission and TA decays of the pyrenyl $^1(\pi, \pi^*)$ state in both MeOH and MeCN arise from conformational heterogeneity within solutions of the PAdU nucleoside, on time scales of 25 ns or less. In particular, the pyrenyl $^1(\pi, \pi^*)$ states of different conformers undergo intramolecular ET to form the $Py^{\cdot+}/dU^{\cdot-}$ CT state with lifetimes ranging from ≤ 600 fs to 23 ns. The results provide a thorough understanding of the photophysics of intramolecular CT in this series of pyrenyl-dU nucleoside conjugates. They should help to develop nucleoside conjugates with sufficiently long-lived $Py^{\cdot+}/dU^{\cdot-}$ CT. This can be used in duplex DNA as source of an excess electron within the DNA base stack.

The same group [GVE05] studied the lengthened average lifetime of electron or charge transfer, and the enhanced CT emission quantum yield, in hairpins (HP) containing 5-(2-pyren-1-yl-ethylenyl)-2'-deoxyuridine as an electron source nucleotide (U^{PE}) and 5-halodeoxyuridine nucleotides (U^{X}) as a trap, where X = Br or F. The results were compared to HPs lacking UX. The combined results strongly suggested that excess electrons were injected into the DNA stem at any pyrimidine base sites external to U^{PE} as well as through charge separation within U^{PE} itself. Increased CT emission quantum yield implied that externally injected electrons migrated to uracil in U^{PE} (i.e., $Py^{\cdot +}dU$) and thus indirectly formed the emissive $Py^{\cdot +}/dU^{\cdot -}$ state of U^{PE}. These conclusion were tested [GCN05] in DNA duplexes with both a 5-(pyren-1-yl-ethynyl)-2'deoxy-uridine electron source nucleotide (U^{PY}) and a U^F trap nucleotide near U^{PY}, but with zero to three intervening A:T base pairs on the same strand. The motivation for this study was that pyridiniumyl-dU electron traps could be inserted into modified DNA duplexes to provide an optical signal for the arrival of a migrating excess electron at a particular DNA trapping site.

e. Frederick D. Lewis

In his review [L0005] the dynamics of the hole- and electron injection and hole migration processes are explained in detail. The dependence on distance, driving force, and base sequence has been investigated by femtosecond time resolved spectroscopy, with stilbene as chromophore. Using Circular dichroism spectroscopy, the author studied the dynamics of electron transfer processes and exciton coupling between two chromophores which are attached at the both ends of the duplex.

f. Jacqueline K. Barton *et al*

This group [LB005] examined ground state charge transport in DNA films on a Au surface, when a perturbation exists in base-pair stacking. For this purpose a nick was created in one of the duplex strands. Covalently bound daunomycin was used as a redox probe. The electron transfer rates can be estimated through analysis of characteristic splitting of anodic and cathodic peaks as a function of scan rate in cyclic voltametry. While the introduction of one or even two nicks (break between two consecutive strands; at the break, one terminus is a 3'-OH, the other, a 5'-OH) in the sugar-phosphate backbone yields no detectable effect on electron transfer, a CA mismatch significantly attenuates the electron transfer yield. These results confirm that the base pair stack is the pathway for DNA-mediated charge transfer, not the sugar-phosphate backbone.

3 Experimental and analysis methods

3.1 Stationary optical spectroscopy

3.1.1 Absorption

Optical absorption spectra of samples were recorded on a Shimadzu UV-3101 PC spectrometer with 1 nm bandwidth and medium time constant, sampling every 0.2 nm. The wavelength range was 600-250 nm and the wavelength axis of the spectrometer was calibrated to ± 0.02 nm with a Hg lamp and a He-Ne laser. Sample cells of 1 mm, 10 mm, 20 mm and 100 mm were used depending on the solubility of the compound. Before each measurement, both sample and reference cells were filled with the pure solvent and a baseline was recorded. The room temperature during optical measurement was 21°C. In order to record absorption spectra at different temperatures in acentonitrile/water mixtures, we constructed a thermostated compartment for both sample and reference cells. During operation the cell could be rotated from 2 cm to 4 cm path length, for higher and lower acetonitrile mole fraction, respectively. A filter with excess of solid ANF inside was also placed in the sample compartment. The solvent mixture was circulated through it before every temperature measurement and equilibrated for 30 minutes. All solvent mixtures were prepared in weight fraction. They were converted into volume fraction with the help of partial molar volume [M0002].

3.1.2 Fluorescence

Fluorescence was excited at the peak of the absorption band (absorbance ≤ 0.05) and collected from the front face of 1-5 mm cells as well as from the normal face of 10 mm cells. The collected photon flux Φ was dispersed in a double monochromator and registered by photon counting on a modified Spex Fluorolog 212. Background was subtracted from the signal by measuring pure solvent. Photometric calibration was performed with a secondary standard lamp (Optronic) in combination with the fluorescence from a series of dyes [GM098]. In this way the fluorescence quantum distribution $\partial\Phi/\partial\lambda \equiv F(\lambda)$ (normalized to $\Phi = 1$) was obtained in each case. Wavelength axes λ were calibrated with a Hg lamp to ± 0.2 nm for emission. All measurements were performed at ambient temperature

3.2 Fluorescence quantum yields determination

Before determining the fluorescence quantum yield, the following has to be considered: (1) presence of concentration effects, example self-quenching and inner filter effects, (2) effect of the solvent if different for standard and test samples. In that case it is necessary to include the refractive index of the solvent in the calculation. (3) Appropriate selection of the standard sample and accuracy of its quantum yield value. Fluorescence quantum yields of Thiazole Orange (TO) in pure solution, TO incorporated with PNA and its duplex with DNA were determined by comparing with the fluorescence spectrum of a standard of known quantum yield. The integrals over corrected emission spectra were used for the comparison. We used freshly prepared fluorescein in 0.1M NaOH solution as reference with quantum yield of 0.90 [DC071]. Care was taken to have the absorbance of sample and reference nearly at the same value, below 0.05 to avoid the inner filter effect, with absorbance precision of 0.001 at the excitation wavelength. The samples were excited at 485 nm and emission spectra are recorded from 490 nm to 750 nm. The area under the emission spectrum was integrated. The fluorescence quantum yield is calculated using the following equation.

$$Q.Y = \frac{\text{Area}_{\text{sample}}}{\text{Area}_{\text{ref}}} * \frac{\text{abs}_{\text{ref}}}{\text{abs}_{\text{sample}}} * \frac{\eta_{\text{sample}}^{2}}{\eta_{\text{ref}}^{2}} * Q.Y_{\text{ref}} \qquad 3.1$$

where η– refractive index, abs– absorbance, Area– area of the corrected emission spectra from the respective solution.

3.3 Ultraviolet melting experiments

The term "Ultraviolet Melting" always refers to change of absorbance at UV region (260 nm), which inturn monitor the helix → random coil transition in polynucleotides upon varying temperature. Buffer solutions must be chosen carefully [GWW66]. The buffer should have maximum water solubility, it should be as stable as possible and its pK_a should be around 7 since this is the region where DNA melting behavior must be investigated. The absorbance of the buffer around 260 nm should also be very low. Finally, the dependence of pK_a on temperature should be minimal to maintain a stable pH over the temperature range (15-95° C). If the enthalpy of ionization (ΔH_{ion}) and heat capacity change for buffer ionization ($\Delta C_{p\ ion}$) are small, then the changes in K_a with temperature are minor and the pH is kept relatively constant during the course of melting experiments. For many buffers, the temperature dependence of K_a has been published [DEE86, F0089]. All melting studies in this thesis were performed in a phosphate buffer. Sodium chloride was used to adjust the ionic strength and total Na^+ concentration. Melting buffers started with 10 mM NaH_2PO_4 (Merck), 100 mM NaCl (Merck). It was then adjusted to pH = 7.00 by adding 2 M NaOH.

Solutions for the melting (thermal denaturation) studies contained a 1:1 ratio of two complementary oligomers. Duplex concentrations were 1 μmol/L. DNA duplex solutions were degassed by bubbling with a fine stream of nitrogen gas for at least 30 minutes. After the solutions were prepared they were heated to 90 ºC for 5 min and allowed to cool to room temperature for at least 1 hour prior to the melting experiments. Melting studies were carried out in Teflon-stoppered quartz cells (1 cm path-length) in a Varian Cary 300 UV-vis spectrophotometer equipped with a thermo programmer. Optical melting curves were acquired as absorbance at 260 nm *vs* temperature. Absorbance (A_{260}) was measured every 0.2 ºC over the temperature range from 20-90 ºC; the temperature was changed at a rate of 0.5 ºC/min. Both heating and cooling melting curves were collected. At least three heating/cooling melting curves from fresh samples were measured for every duplex. Computer fitting of the curves $A_{260}(T)$ provided the melting temperatures (T_m). In order to find the free enthalpy ΔH_{ass} of complex formation for selected cases, van't Hoff plots of $1/T_m$ of $\ln(C_T/4)$ *vs* $1/T_m$ give slope $\Delta H_{ass}/R$.

3.4 Picosecond time-correlated single photon counting

Fluorescence lifetime measurements were done by time-correlated photon counting. An argon ion laser-pumped, passively mode locked Ti:sapphire laser was used as excitation source. The pulse duration is about 80 fs and the repetition rate 82 MHz. The excitation wavelength ≈ 400 nm was obtained by frequency doubling the fundamental wavelength. Fluorescence decays were detected by a microchannel plate photomultiplier (MCP, Hamamatsu R 1564-U-01) cooled to –30º C, coupled to an emission monochromator (Jobin Yvon II, 10 VIR) by means of quartz fiber optics. The signal from a constant fraction discriminator (CFD, Tennelec 454) was used as the start pulse for the time-to-amplitude converter (TAC, Tennelec TC864) operating in the reverse mode. The excitation pulse was used as the stop pulse. The MCP pulses were amplified by an amplifier (INA 10386) and coupled into the CFD. A multichannel analyser (Fast Comtec MCDLAP) was used for data accumulation. The decays were analysed by the “least squares” iterative reconvolution method on the basis of the Marquardt-Levenberg algorithm, which is implemented in the commercial global analysis program [BGM92]. The instrument response function was obtained by detection of Rayleigh scattered light in pure solvents. It had a width of 50-60 ps at the excitation wavelength and is dominated by the optical path difference in the monochromator. Detection without the monochromator yielded instrument response function (IRF) of 28 ps. The entire equipment and its operation was described in detail elsewhere [VR087, WRD03]. The quality of the exponential fits was evaluated on the basis of reduced χ^2 values.

3.5 Femtosecond transient absorption spectroscopy

Transient absorption spectra (= “TAS”) were measured by pump-supercontinuum-probe spectroscopy. Measurements of ANF derivatives and thiazole orange were performed in two different setups. The basic detection scheme is shown in figure 3.5-1. For ANF and derivatives, a Titanium:sapphire (Ti:sa) laser system (FEMTOLASER) provides basic pulses of 30 fs, 500 μJ at 810 nm with 120 Hz repetition rate. Basic pulses are converted into second harmonic 400 nm, 20 µJ pulses in a β-barium borate crystal (BBO, θ = 29°, d = 0.2 mm). In order to avoid effective time broadening, the group velocity dispersion (GVD) is adjusted by a two-prism compressor. After compression, the basic beam is split into two beams with a 4:1 ratio, for optically pumping the sample and other for probing. The supercontinuum is generated by focusing the pulses of about 10 µJ energy onto a CaF$_2$ plate (1 mm) with a thin lens (f = 200 mm, fused silica). The supercontinuum was filtered through filter soultion to reduce 400 nm light and passed through a pinhole of about 50 µm. This pinhole represents the femtosecond white-light source. The beam emanating from it is split for reference before being imaged on to the sample cell with spot size of about 100 µm.The sample solution typically has an aborbance of 0.7 in a flow cell with internal thickness of 0.3 mm. It is excited by 400 nm pulses of up to 3 µJ (150 µm diameter). Transmitted and reference beams are imaged on to the entrance planes of separate homemade spectrograph, dispersed with a grating and finally registered by photodiode arrays with 512 pixels (S39901-512Q, Hamamatsu) covering the spectral range 270-670 nm.

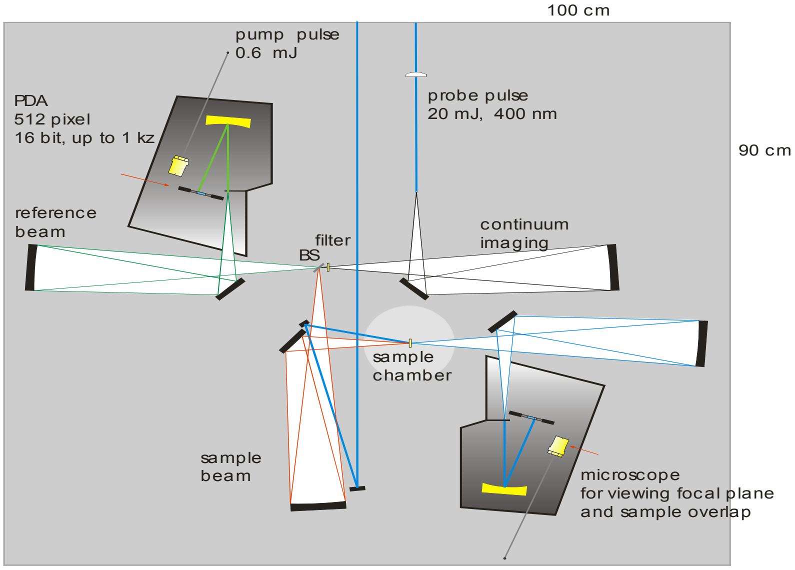

Figure 3.5-1 Experimental setup for femtosecond transient absorption spectroscopy: simultaneous coverage 270-670 nm or 340-1000 nm by the supercontinuum probe pulse, highest time resolution 50 fs, probe spot diameter 50 µm, pump spot diameter 100 µm, sample volume as small as 250 µL, absorbance noise of 10^{-4} rms upon averaging 100 shots.

For Thiazole Orange, a regenerative Ti:sa amplifier (CPA2001, CLARK MXR) provides basic pulses of 150 fs, 0.9 mJ at 775 nm with a repetition rate of 120 Hz. This beam is split in two, one driving a two-stage Nonlinear Optical Parametric Amplifier (NOPA) to generate 530 nm, 20 fs for probing and the other a single-stage NOPA to generate 485 nm, 20 fs for exciting the sample. As above, the supercontinuum is generated by focusing 10 μJ pulses into a CaF_2 plate (1 mm) with a thin lens (f = 200 mm, fused silica). Transmitted and reference beams were imaged on to the entrance planes of separate homemade spectrograph, dispersed with a prism and finally resgistered by photodiode arrays with 512 pixels (S39901-512Q, Hamamatsu). The prism setup alows to cover the spectral range 340-1000 nm.

Measurements of both samples were performed at parallel, perpendicular and magic angle between the pump and probe polarizations. Baseline corrections were applied to every individual set of measurements. Measurements from 50 shots were averaged and the recorded spectra were time corrected for the chirp of the supercontinuum. The pump-probe intensity cross correlation measured over the probe region is described by a 65 fs (fwhm) Gaussian shape. Variations of the pump pulse energy in the range 0.13 −1.0 μJ had no effect on the transient spectral shapes.

The transient absorption spectra of the solvent were subtracted from the respective solute signal. In some cases, the solvent signal was scaled by some factor (~ 0.8) to match it to the resonant measurement. Transient absorption spectra of magic angle polarisation and of anisotropy were obtained with the following formula : $\text{magic} = \frac{I_{11} + 2I_{\perp}}{3}$ and $\text{anisotropy} = \frac{I_{11} - I_{\perp}}{I_{11} + 2I_{\perp}}$, where I_{11} and $I_{\perp}$ are the intensites of vertical and horizontaly polarised measurements respectively.

3.6 Femtosecond fluorescence upconversion spectroscopy

The setup is schematically represented as in figure 3.6-1. A Ti:sa laser (Femtolaser) provides 30 fs, 500 μJ pulses at 810 nm with 500 Hz repetition rate. This is split in to two with a 6:1 ratio. The stronger pulse fraction (430 μJ) are used to pump an optical parametric amplifier (TOPAS, Light Conversion) which provides 50 fs, 60 μJ gate pulses at 1300 nm with horizontal polarization. It passes through a delay stage, the pulse front is tilted are with a prism (SF59) and finally focused onto the nonlinear crystal by lens (f = 109 mm). Alternatively, pump pulses at 450 nm (1 μJ) are also obtained from the TOPAS. Polarization is controlled with a λ / 2 plate, pulse energies are attenuated to 0.2-0.6 μJ, and the pump beam is focused with a lens (f = 200 mm, fused silica) onto the sample cell having 0.40 mm path length. The sample cell is part an axial Schwarzschild objective (see figure). The collected fluorescence are passed through wire-grid polarizer (Moxtec PPL04C, on 700 μm of corning 1737 F glass) which removes unwanted light of horizontal polarization and also through notch filter (Semrock, on 660 mm fused silica). This notch filter reflects the pump light and Rayleigh scatter.

Upconversion is guided by the following principles.

The band width of a nonlinear crystal can be estimated [S0084] as $\Delta\tilde{\nu} = (1/d).\left[\frac{c}{v_U} - \frac{c}{v_F}\right]^{-1}$ for sum frequency mixing $\tilde{\nu}_U = \tilde{\nu}_F + \tilde{\nu}_G$, subscript U, F, and G represent to the upconverted, fluorescence and gate wavenumbers respectively. Here d is the crystal thickness, c is the vacuum light velocity and v the group velocity. With thin and low-dispersion crystals, $\Delta\tilde{\nu}$ can be enlarged. Dispersion also decreases when the gate is shifted to the NIR. As an example, $\Delta\tilde{\nu} \sim 10\,000$ cm^{-1} can be obtained with KDP (type II, θ = 51°, d = 0.1 mm) for λ_G =1300 nm and λ_F = 550 nm. For our measurements of Coumarin 153 in acetonitrile [ZLF05], an upconversion shift by $\tilde{\nu}_G$ = 7700 cm^{-1} it is large enough to separate the signal spectrally from the original fluorescence.

We obtain the best spectra with a noncollinear geometry when the fluorescence and gate beams are focused onto the crystal at an angle of 14°. The crystal can be rotated around its vertical axis for phase matching. The upconverted signal pulses passes through a Glan-Thompson analyzer (Halle) and are imaged dispersion-free, with an off-axis Schwarzschild scheme, onto the entrance slit of a double-prism spectrograph with low scatter. Finally the upconverted spectrum is registered with a CCD camera (DV420 BU from Andor Technology). Photometric correction was effected by similar measurements with standard fluorescence dyes.

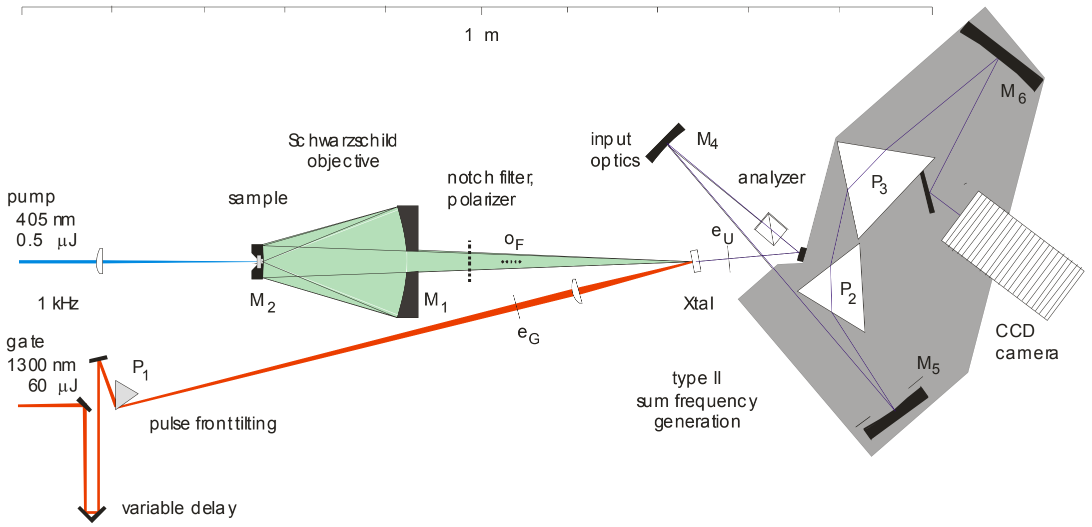

Figure 3.6-1 Experimental setup for broadband FLuorescence UP-conversion Spectroscopy (FLUPS). Spectra are recorded background-free in a noncollinear geometry, with tilted gate pulse fronts, at 80 fs time resolution.

3.7 X-Ray Diffraction

Crystals of 2-amino-7-nitrofluorene (ANF) were obtained from CH_2Cl_2 by air evaporation in the form of red orange platelets. Single crystals were selected under paraffin oil using a polarization microscope. The crystal was mounted on glass fiber and measured at a specific temperature (180 K) on the Stoe Imaging Plate Diffraction System (IPDS) area detector. Mo-K_α radiation was employed with a graphite monochromator (λ = 0.71073 Å). The crystal was measured on the IPDS with rotation and oscillation about the φ-axis. During measurements, the crystal was cooled by an Oxford CRYOSTREAM with the help of liquid nitrogen. The structures were solved with direct methods using SHELXS-97 and refined with SHELXL-97. Non-hydrogen atoms were refined anisotropically. The assignment was confirmed by a decrease in the R_1 and wR_2-factors after a final refinement of the structure. Experimental data for the measurements can be found in appendix 10.1 and the corresponding crystal structure is given in a section 5.1.3

3.8 ^{1}H NMR

^{1}H NMR spectra of ANF in dimethyl sulfoxide (DMSO) (d_6)/H_2O and acetonitrile (ACN) (d_3)/H_2O were measured on a Bruker spectrometer operating at 300 MHz (AM300 NMR). Chemical shifts were determined by external double reference method with a homemade external reference tube: a capillary of 2 mm in diameter which was filled with mixture of 99.5% of CCl_4 and 0.5% of Hexamethyldisiloxane (HMDS) to height of 7 cm, set at the centre of the sample tube which had 5 mm internal diameter. By this method, observed chemical shifts can be corrected precisely for the sample and reference. The solutions were prepared by volume with microsyringes. For example to prepare 0.7 ml solution of volume fraction of water, V_w = 5%, one requires 0.665 ml of ACN (d_3) and 0.035 ml of water. An 0.070 ml aliquot of a stock solution of ANF in ACN (d_3) (1.4096 10^{-2} mol/L) was first pipetted in, after which the remaining 0.595 ml of pure ACN (d_3) were added. Because of the low solubility at higher water content, solutions could only be prepared up to 30% of water volume fraction. The same procedure was followed to prepare solutions in DMSO (d_6)/water mixtures. The measurements were repeated with D_2O in the place of H_2O.

3.9 Terms used in UV-Vis spectroscopy [B0070]

The strength of atomic and molecular transitions is described commonly with several parameters. Those parameters are Einstein A and B coefficients, f values (also called “oscillator strength”), and transition dipole moment, related to strength of transition. It is also necessary to explain for practical purposes, the absorption coefficient-which describe the absorption of a beam of light passing through a medium consisting of the atoms or molecules of interest.

a. Absorption coefficient and absorption cross section

When a monochromatic beam of light of intensity I_i is incident normally on a sample of thickness d (cm), containing q molecules of the absorbing species per cm^3, the intensity I of the emergent beam

$$I = I_i\, e^{-\sigma q d} = I_i\, e^{-\mu d} \qquad 3.2$$

defines the molecular *absorption cross-section* σ (cm^2) and the *absorption coefficient* μ (cm^{-1}). These can be expressed in terms of the *decadic molar extinction coefficient,* defined by

$$I = I_i\, 10^{-\varepsilon [M] d} \qquad 3.3$$

where $[M]$ is the molar concentration (mol/L) of the absorbing species.

$$q = N_A\, [M] \times 10^{-3} \qquad 3.4$$

N_A (= 6.02214×10^{23} mol^{-1}), Avogadro's number, thus the relation between extinction coefficient and cross section is

$$\sigma = \frac{2303\, \varepsilon}{N} = 3.81 \times 10^{-19}\, \varepsilon \ (cm^2) \qquad 3.5$$

b. Einstein coefficients

Einstein identified the three different contributions to an transition between two state levels. These are stimulated absorption and stimulated emission which are quantified by a coefficient B**,** and spontaneous emission which is quantified by coefficient A. Consider a large number of molecules, immersed in a transparent medium of refractive index n, in thermal equilibrium within a cavity at temperature T. The *radiation density* (erg cm^{-3} per unit frequency range) of frequency ν within the medium is given by Planck's black-body radiation law.

$$\rho(\nu) = \frac{8\pi h\nu^3\, n^3/c^3}{\{\exp(h\nu/kT) - 1\}} \qquad 3.6$$

c - velocity of light (3×10^8 ms^{-1}) and h - planck's constant (6.62×10^{-34} Js).

The transition probability known as Einstein coefficient B_{ge} is defined in terms of the rate of the molecules going from ground state "g" to excited state "e" by absorption of radiation

$$\frac{dN_e}{dt} = N_g\, B_{ge}\, \rho(\nu) \qquad 3.7$$

N_g the number of molecules in the ground state, ν the frequency of the transition. The rate at which molecules undergo downward transition, *i.e* from excited state e to ground state g, is given by

$$\frac{dN_g}{dt} = N_e \{A_{eg} + B_{eg}\rho(\nu)\} \qquad 3.8$$

The first term represents spontaneous emission with transition probability A_{eg}. The second term represents stimulted emission $B_{eg}\rho(\nu)$. Here $B_{ge} = B_{eg}$. N_e represents the number density of molecules in the excited state. Since the rates of the absorption and emission transitions are equal at equilibrium, by equating above two equations (3.7 and 3.8) we get

$$\frac{A_{eg}}{B_{eg}} = \left(\frac{N_g}{N_e} - 1\right)\rho(\nu) \qquad 3.9$$

The number of molecules in the two states at equilibrium are related by the Boltzmann distribution law,

$$\frac{N_e}{N_g} = \exp[-h\nu / kT] \qquad 3.10$$

Thus by substituting eqn 3.10 and 3.6 in 3.9, we obtain the relation between the two Einstein coefficient in a medium of refractive index n as

$$A_{eg} = 8\,\pi\,h\,\nu^3 n^3 c^{-3} B_{eg} \qquad 3.11$$

c. Relation between Einstein coefficient and absorption cross section and coefficient

Einstein coefficient, B_{eg} is related to absorption cross section and absorption coefficient as follows

$$B_{eg} = \frac{c}{hn}\int \frac{\sigma(\nu)\,d\nu}{\nu} \qquad 3.12$$

$$= \frac{2303\,c}{hnN}\int \frac{\varepsilon(\nu)d\nu}{\nu} \qquad 3.13$$

where the integrals are over the whole electronic absorption band system.

---

d. Oscillator strength and its relation with other quantity

The oscillator strength is measure of integrated intensity of an electronic or vibronic absorption transition, defined in terms of absorption cross section, coefficient, and Einstein coefficient as

$$f = \frac{m\,c}{\pi\,e^2 n}\int \sigma\,d\nu \qquad 3.14$$

$$= \frac{2303\,m\,c^2}{\pi\,e^2 N\,n}\int \varepsilon\,d\bar{\nu} = \frac{4.39\times 10^{-9}}{n}\int \varepsilon\,d\bar{\nu} \qquad 3.15$$

$$f_{ge} = \frac{mh\nu}{\pi e^2} B_{ge} \qquad 3.16$$

m and e are mass and charge of the electron. ν and $\bar{\nu}$ are the mean frequency and mean wavenumber respectively of the transition.

e. Transition moment

The classical idea is that for the molecule to be able to interact with the electromagnetic field and absorb or emit a photon of frequency ν, it must possess at least transiently, a dipole oscillating at that frequency. This transient dipole is expressed quantum mechanically in terms of *electric dipole transition moment*, a vector quantity between two states as given by their wave functions,

$$\overrightarrow{M}_{g\to e} = \int \psi^*_e\, \vec{\mu}\, \psi_g\, d\tau\,. \qquad 3.17$$

Here $\vec{\mu}$ is the electric dipole moment operator. $\vec{\mu} = \sum_i q_i\, \vec{r_i}$, q_i and $\vec{r_i}$ the charge and the position vector of the *i*th particle. The square of the magnitude of $\overrightarrow{M}_{g\to e}$ is the transition probability; it is related to the Einstein coefficient B_{eg} by

$$B_{eg} = \frac{8\,\pi^3}{4\,\pi\,\varepsilon_0 3\,h^2}\left|\overrightarrow{M}_{e\to g}\right|^2 \qquad 3.18$$

The relation between transition moment and oscillator strength is

$$f_{ge} = \frac{8\pi^2 mc\bar{\nu}}{3he^2}\left|\vec{M}_{g\to e}\right|^2 \qquad 3.19$$

f. Transition moment from stationary spectra [LM098a]

It is necessary to represent the stationary absorption and emission spectral data properly, usually different from how they are obtained from the instruments. Literature describes several methods how the transition moment is reached from absorption and emission spectra. Considering absorption data as first, the transition moment can be found as

$$|M|^2_{g\rightarrow e} = \frac{1}{n}\frac{1}{f(n)}\left[\frac{2303}{8\pi^3}\frac{3hc}{N_A}\right]\int\frac{\varepsilon(\nu)}{\nu}d\nu \qquad 3.20$$

after substituting all constant,

$$|M|_{g\rightarrow e} = 9.584\times 10^{-2}\left[\frac{1}{n}\frac{1}{f(n)}\int\frac{\varepsilon(\nu)}{\nu}d\nu\right]^{1/2} \qquad 3.21$$

(for transition moment in Debye). Similarly for emission data we have

$$|M|^2_{e\rightarrow g} = \frac{1}{n^3}\frac{1}{f(n)}\left[\frac{3hc^3}{64\pi^4}\right]\frac{k_{rad}}{\tilde{\nu}_f^3} \qquad 3.22$$

which can be written as

$$|M|_{e\rightarrow g} = 1.7857\times 10^3\left[\frac{1}{n^3}\frac{1}{f(n)}\frac{k_{rad}}{\tilde{\nu}_f^3}\right]^{1/2} \qquad 3.23$$

where radiative rate k_{rad} is obtained from quantum yield (Φ_f) and lifetime data (τ_f) via $k_{rad} = \frac{\Phi_f}{\tau_f}$ in s^{-1}, $\tilde{\nu}_f^3 = \frac{\int F(\nu)\,\nu^{-3}d\nu}{\int F(\nu)\,d\nu}$ in cm^{-3}, and $f(n) = \frac{9n^2}{(2n^2+1)^2}$ [BGL63].

g. Conversion into wavenumber

For quantitative comparison of band position and shape, the measured absorption spectrum $A(\lambda)$ and the measured fluorescence photon distribution $\Psi(\lambda)$ must be expressed as distributions $f(\tilde{\nu})$ of oscillator strength over wavenumber $\tilde{\nu}$. The oscillator strength for a single vibronic line $|S_0, v = i\rangle \leftrightarrow |S_1, v = j\rangle$ is proportional to the square of the transition matrix element, $M_{ij}^2 = M_{el}^2 FC_{ij}$, where $M_{el} = \langle S_0|\hat{\mu}|S_1\rangle$ is the electronic transition dipole and FC_{ij} the Franck-Condon factor for the vibrational states. In a dye such as Thiazole Orange, many vibronic transitions overlap to produce a smooth spectral distribution. The electronic matrix element is factored out by normalisation and we are left with the distribution of vibrational Franck-Condon factors, $f_{abs}(\tilde{\nu})$ for absorption and

$f_{em}(\tilde{\nu})$ for emission, respectively. It is these distributions or bandshapes which should properly be discussed, for example when mirror symmetry between absorption and emission is examined or when the shape of the emission spectrum in different environments is compared. For absorption we have

$$f_{abs}(\tilde{\nu}) = N_{abs}^{-1} A(\lambda)\,\lambda \qquad 3.24$$

with N_{abs} for normalisation. (Later f_{abs} will also be called g) The measured spectrum $\Psi(\lambda)$ of photon counts is first converted into a quantum distribution over wavenumbers:

$$\Phi(\tilde{\nu}) = 10^{-7}\,\Psi(\lambda)\,\lambda^2 \qquad 3.25$$

where $\tilde{\nu}$ is to be given in cm^{-1} and λ in nm. The probability of spontaneous emission rises with $\tilde{\nu}^3$, and this is why

$$f_{em}(\tilde{\nu}) = N_{em}^{-1}\Phi(\tilde{\nu})/\tilde{\nu}^3 \qquad 3.26$$

(Later f_{em} will simply be called f).

Note that 3.25 and 3.26 imply division of $\Psi(\lambda)$ by $\tilde{\nu}^5$ which drastically alters the appearance of the measured fluorescence spectrum. At this stage all experimental data are available in the desired form.

A smooth interpolation curve to any $f(\tilde{\nu})$ is determined next. For this purpose every oscillator distribution is fitted by a sum of log-normal distributions [SM069] (explained in section 3.11.1). In case of absorption the sum may be divided into a part for the $S_0 \rightarrow S_1$ electronic transition, which is retained, and a part for all higher transitions $S_0 \rightarrow S_n$ which is discarded. In the following we consider only the smoothed bandshapes. For the figures it is convenient to present the absorption spectrum $Abs(\tilde{\nu}) \equiv \tilde{\nu}\, f_{abs}(\tilde{\nu})$ for $S_0 \rightarrow S_1$. The corresponding fluorescence $S_1 \rightarrow S_0$ is rendered as a comparable quantity, as spectrum $SE(\tilde{\nu}) \equiv \tilde{\nu}\, f_{em}(\tilde{\nu})$ for stimulated emission.

3.10 Determination of expected time–zero fluorescence spectrum [FM094]

M. Maroncelli and coworkers used an “Inhomogeneous Kinetic Model” [FMM91] to explain the changes of electronic spectra of solvatochromic probe in solution from that of the vapour phase. The main ingredients are the following. (1) In a polar solvent, molecules occur distributed over a range of local solvation environments; (2) time-dependent fluorescence shifts means that the radiative fluorescence decay rate varies systematically with the solvent-induced spectral shift. It was assumed that individual molecules in different environments are characterized by a frequency shift δ. Absorption spectra of all solute molecules are described by a single line-shape function $g(\nu)$ (to within a site-dependent shift) which accounts for the underlying vibronic structure as well as any homogenous broadening of the spectrum. Thus inhomogeneously broadened absorption spectrum, $A_p(\nu)$, is given by

$$A_p(\nu) \propto \nu \int g(\nu-\delta)\ p(\delta)\ d\delta \qquad 3.27$$

$p(\delta)$ describes the equilibrium distribution of ground state solutes among sites, catalogued according to spectral shift δ. Similarly the corresponding fluorescence spectrum after monochromatic excitation with frequency, ν_{ex}, can be written as based on emission line shape function, $f(\nu)$, analogous to $g(\nu)$,

$$F_p(\nu, t=0, \nu_{ex}) \propto \nu^3\ \nu_{ex} \times \int g(\nu_{ex}-\delta)\, p(\delta)\, f(\nu-\delta)\, k_{rad}(\delta)\, d\delta \qquad 3.28$$

(Remember that, essentially, $\nu_{ex}\ g$ is proportional to the measured absorption spectrum and $\nu^3 f$ proportional to the fluorescence quantum distribution over wavenumbers).

k_{rad} is the radiative rate constant, $f(\nu-\delta)\, k_{rad}(\delta)$ leads to the fluorescence intensity function, and $g(\nu_{ex}-\delta)\, p(\delta)$ to the convolution of the solvent distribution initially transferred to the excited state. This equation describes the fluorescence spectrum observed before nuclear solvent motion or relaxation occurs. Therefore it is clear that following functions are required to determine the expected time zero fluorescence spectrum; $g(\nu)$, $f(\nu)$, $p(\delta)$, and $k_{rad}(\delta)$. The factor of ν is used in the above equations, in order make $g(\nu)$ and $f(\nu)$ directly proportional to Einestein B coefficient for absorption and emission respectively.

In our case, line shape function $g(\nu)$ and $f(\nu)$ can be directly obtained from spectra measured in a non-polar reference solvent such as 2-methyl butane which is nearly equivalent to gaseous spectra.

$$g(\nu) \propto \nu^{-1} A_{np}(\nu), \tag{3.29}$$

and

$$f(\nu) \propto \nu^{-3} F_{np}(\nu) \tag{3.30}$$

A_{np}, absorption spectrum and F_{np}, the steady-state emission spectrum in the non-polar reference solvent. The lineshape function consists of the vibronic structure of the isolated (i.e. vapour phase) molecule together with some broadening due to repulsive and non-polar attractive interactions with the non-polar solvent molecules.

The radiative rate function is calculated with shift δ via

$$k_{rad}(\delta) \propto \frac{\int f(\nu-\delta)\nu^3 d\nu}{\int f(\nu-\delta) d\nu} \tag{3.31}$$

Finally, the site distribution is assumed to be a Gaussian function,

$$p(\delta) = (2\pi\sigma^2)^{-1/2} \exp\left[-(\delta-\delta_0)^2/2\sigma^2\right] \tag{3.32}$$

δ_0, the average shift induced by the polar solvent and σ, the variance of the distribution.

Therefore, the following steps are to be followed in order to calculate the time zero spectrum.

(1) One has to record absorption and emission spectra in a non-polar reference solvent. Alkane solvents are more suitable than aromatic solvents, because the latter will cause some non-negligible Stokes shift.

(2) Reference and polar spectrum have to be recorded at the same temperature because homogenous broadening must be the same in both solvents.

(3) The lineshape functions $g(\nu)$, $f(\nu)$ are determined from the non-polar reference spectra.

(4) The characteristic broadening and shift (σ, δ_0) by the solvent, which enter $p(\delta)$, are then determined as that set which yields the closest match to the polar absorption spectrum when convoluted with $g(\nu)$.

(5) The fitting is done with a non-linear least-squares routine.

Thus finally the estimated time-zero spectrum is computed for any excitation frequency according to the equation 3.28.

3.11 Fitting of spectral data

3.11.1 Spectral analysis

Measured stationary and time resolved spectra were fitted with a sum of log-normal line shape functions [SM069]. The lognormal function has the form

$$F(\tilde{\nu}) = h \begin{Bmatrix} \exp\left[-\ln(2)\,\{\ln(1+\alpha)/\gamma\}^2\right] & \alpha > -1 \\ 0 & \alpha \le -1 \end{Bmatrix} \quad \text{where } \alpha \equiv 2\gamma(\tilde{\nu} - \tilde{\nu}_p)/\Delta \qquad 3.33$$

By this method one can obtain accurate values of the positions and intensities for "buried" or overlapping bands. A log-normal function is an asymmetrized Gaussian with four parameter only: the peak height h, the asymmetry parameter or skewness γ (is the ratio of the distances of the band at $\varepsilon_0/2$ from the mode, which is equivalent to $\gamma \equiv (\tilde{\nu}_b - \tilde{\nu}_0)/(\tilde{\nu}_0 - \tilde{\nu}_r)$), the width parameter Δ and the peak frequency $\tilde{\nu}_p$.

3.11.2 Kinetic analysis

The measured transient spectra which are obtained from the instrument do not directly show the true temporal behavior of the molecular system. Here we assume that the photometric data (i.e. the y-axis) are correctly represented and we focus on the time axis only. The time behavior of the signal can be different at different wavelengths due to group-velocity dispersion of the medium between the light source and the interaction region. A measured kinetic trace $m(t)$ is given by the true kinetics $k(t)$ convoluted with an apparatus function $a(t)$. For the latter the pump-probe intensity cross-correlation function is used. In time-resolved fluorescence k(t) should be, in its simplest form, a step-function multiplied by an exponential decay. The step-function $\Theta(t)$ (= 0 at negative and = 1 at positive time) is necessary to account for the fact there is no fluorescence before excitation of the sample.

Generally, let two functions in the time domain be k(t) and a(t), and their Fourier transforms are $K(\nu)$ and $A(\nu)$ in the frequency domain. The convolution of k(t) and a(t) is defined as

$$\mathrm{m(t)} = \int_{-\infty}^{\infty} \mathrm{k(t)\,a\,(t-t^{'})\,dt}\,. \tag{3.34}$$

Often one also writes symbolically $\mathrm{m(t)} = \mathrm{k(t)} \otimes \mathrm{a(t)}$. The convolution theorem states that convolution $\otimes$ in the time domain (t) corresponds to multiplication in the frequency domain (ν):

$$\mathrm{m(t)} = \int_{-\infty}^{\infty} \mathrm{k(t)\,a\,(t-t^{'})\,dt} \quad \Leftrightarrow \quad \mathrm{M}(\nu) = \mathrm{K}(\nu)\ \ \mathrm{A}(\nu) \tag{3.35}$$

The true kinetic trace in the time domain can be obtained by forming $\mathrm{M}(\nu)/\mathrm{A}(\nu)$ in the frequency domain, followed by inverse Fourier transformation.

3.11.3 Spectral Decomposition

Typical *pump-probe* transient absorption spectra (TAS) have contributions from the following three optical processes: (1) bleach (BL) of absorption because of excitation-induced loss of population in the electronic ground state, (2) excited state absorption (ESA) because population created in the first or higher electronically excited states have absorptive transitions to higher electronic states, and (3) stimulated emission (SE) back to the ground state. The total spectrum consists of an overlap of the above three contributions. In order to obtain the solvation correlation function, C(t), by transient absorption measurements it is necessary to decompose the TAS and to extract the SE component. In principle, spectral oscillations of the BL spectrum could be observed, due to the vibrational coherence of the solute molecules remaining in the ground state. In our case, however, this is not seen because these oscillations are faster than the instrumental response function. Therefore the bleach band can be considered to have a constant shape on the time scale of the measurement. The constant shape of the bands $\sigma_{\mathrm{BL}}(\nu)$ and $\sigma_{\mathrm{SE}}(\nu)$ enable a spectral decomposition as follows. When the spectral evolution has ceased the BL and SE components are given by stationary absorption and emission spectrum respectively. The amplitudes of the two bands are related by the fact that the oscillator strength must be the same:

$$\int_{\mathrm{band}} \sigma_{\mathrm{BL}}(\nu)/\nu \;\, d\nu = \int_{\mathrm{band}} \sigma_{\mathrm{SE}}(\nu)/\nu \;\, d\nu \tag{3.36}$$

Here the absorption cross section $\sigma_{BL}(\nu)$ is proportional to the ground-state absorbance spectrum and the cross section for stimulated emission is obtained from the fluroscence quantum distribution $\mathrm{fqd}(\nu)$ by $\sigma_{SE} \propto \mathrm{fqd}(\nu)/\nu^2$. When BL and SE are subtracted from the transient absorption, the stationary ESA spectrum remains. It is reasonable to approximate the ESA by its stationary form at all times, and in this way one obtains an estimate for the transient SE spectrum. The latter is then fitted by a lognormal line shape function, and the peak frequency $\tilde{\nu}_P$ from the fit is taken as a measure of the free energy gap. The procedure is repeated for every pump-probe delay t. This gives the desired time-resolved Stokes shift $\tilde{\nu}(t)$. With equation 2.12 thus we can derive normalized $C(t)$ in terms of observables.

$$C(t) = \frac{\nu(t) - \nu(\infty)}{\nu(0) - \nu(\infty)} \qquad 3.37$$

where $\nu(0)$ is obtained from expected time zero emission maximum on the basis of the reference nonploar solvent (equation 3.28) and $\nu(\infty)$ is obtained from maximum of the stationary emission spectrum.

3.11.4 Singular Value Decomposition

Singular Value Decomposition (SVD) of a general square or rectangular matrix has been explored for over 60 years [EY039]. It is a widely used technique to decompose a matrix into several component matrices, exposing many of the useful and interesting properties of the original matrix. Using SVD we can determine the rank of the matrix, quantify the sensitivity of a linear system to numerical error, or obtain an optimal lower-rank approximation to the matrix. In the field of physical chemistry, SVD is used to analyze data where the experimental response is a function of two quantities, for example change in absorbance or change in fluorescence intensity as a function of time and wavelength, or as a function of mole fraction of solvent (or ligand) and temperature. SVD gives two sets of eigenvetors, one corresponds (for our example) to time and the other to wavelength, and set of eigenvalues. It is to deduce the number of significant species, N_s, present by inspection of the eigenvectors and eigenvalues. The value of SVD analysis is that a subsequent global fit to the data need be done only on N_s eigenvectors, typically 3-10, rather than the 200 or more wavelengths normally present in the raw data. SVD also has the useful property of separating significant information from noise in the data set. The noise level can also be checked by comparing the original data to data reconstructed from the N_s significant eigenvetors. Henry *et al* has comprehensively discussed the importance of application of SVD to the kinetic data where spectral changes are analyzed as function of time [HH092]. The method of SVD with self modeling was developed and demonstrated in the accurate determination of pure intermediate spectra and kinetics in the dissection of the photocycle of the Asp96→Asn mutant with 3 distinguishable components (K, L and M) [ZKL99].

SVD is based on a theorem from linear algebra which describes that a rectangular matrix A can be broken down into the product of a three matrices: an orthogonal matrix U, a diagonal matrix S, and the transpose of an orthogonal matrix V:

$$A_{mn} = U_{mm} S_{mn} V_{nn}^{T} \qquad 3.38$$

where $U^T U = I$, $V^T V = I$; the columns of U are orthonormal eigenvectors of AA^T, the columns of V are orthonormal eigenvectors of $A^T A$, and S is a diagonal matrix containing the square roots of eigenvalues from U or V in descending order. In our case, matrix $A \equiv \Delta OD(\lambda_i, t_j)$ corresponds to the induced optical density at observation wavelength λ_i ($i = 1, M$) and delay times t_j ($j = 1, N$). Columns of U represent normalized basic spectra, the rows of V^T contain their normalized dynamics, and diagonal S may be presumed to have the weights or singular values $S_{kk} > 0$ arranged in descending order.

3.12 Solvents used

All solvents were obtained from Merck. Those used for steady state and transient spectra were of spectroscopic grades *Uvasol* (purity > 99.9%). The solvents used in this thesis covering from non-polar to highly polar solvents. The absorption and fluorescence spectra of neat solvents were checked before solute measurement to make sure that solvents are free from impurities. For ANF in pure acetonitrile, the solvent was dried and the solution prepared under dry inert gas. The water used for preferential solvation studies were deionised by exchange and its conductivity was ~1µS/cm.

3.13 Sample preparation for absorbance measurements in solvent mixtures

ANF and DMANF solutions in acetonitrile (ACN) / water (W), dimethyl sulphoxide (DMSO) / W and ACN / DMSO mixtures of a desired volume fraction (V_w) were prepared by weight. For example consider an equivalent water weight fraction of 5% in acetonitrile. In this case a water weight of $W_w = 2.5$ g requires the addition of $W_{ACN} = 22.50$ g acetonitrile for total weight of 25 g. An 0.250 mL aliquot of a stock solution of ANF or DMANF in ACN ($1.59\ 10^{-3}$ mol/L) was first pipetted in with a microsyringe, after which pure acetonitrile was added to achieve the target weight for this component. At this stage the actual weight of the acetonitrile component was noted. Then water was added to a final weight which was also noted. For analysis, the weight fractions were converted into mole fractions. The latter were then converted into volume fractions by using the excess molar volume (VE, cm^3/mol) [M0002]. For $V_w > 85\%$, the solubility of ANF and dM-ANF is low and excess solid created some turbidity. This was removed by centrifugation without significantly altering the composition.

4 Synthesis of compounds studied in this thesis

4.1 Synthesis of 2-amino-7-nitro fluorene nucleotide – motivation and hurdles

To obtain the ultrafast structural, polarisation and solvation dynamics of DNA, we chose 2-amino-7-nitro fluorene (ANF) as a probe attached to the 13mer DNA sequences. Sequences and theoretical background are explained in a section 6.1. The ANF nucleotide had to be prepared in a stabilized form with maximum purity before it could be attached to the DNA sequences. Biotez would prepare for the target strands with ANF in the middle position by the solid-phase phosphoramidite method. The overall scheme of synthesis of the ANF nucleotide is illustrated in figure 4.1-1 and each of its steps is discussed successively. In every step, the purity of the sample was checked by high resolution NMR and mass spectrometry. The absorption and fluorescence spectra were measured for the product at every stage in a variety of solvents. The successive products shift to the blue and have nearly the same magnitude of Stokes shift as in ANF. During the synthesis of the 13mer with ANF in the middle position, some other by-product was formed along with the target strand, due to the following reasons:

(1) Because a labile hydrogen atom is present on the amino group of ANF, the addition of the next base sequence can develop from the amino group instead from the 5’-OH group of the sugar.

(2) During process of nucleisation as above, unreacted or excess phosphoramidite can react at the amino nitrogen.

As a consequence, we could not measure the femtosecond transient absorption spectra of the DNA with ANF. Hence it is not reported in this thesis.

<u>Note:</u> The protection of the 5’-OH of deoxy ribose by 4, 4’-dimethoxytrityl chloride and the phosphoramidation were done by Dr.Rainer Mahwald [ME0_ _].

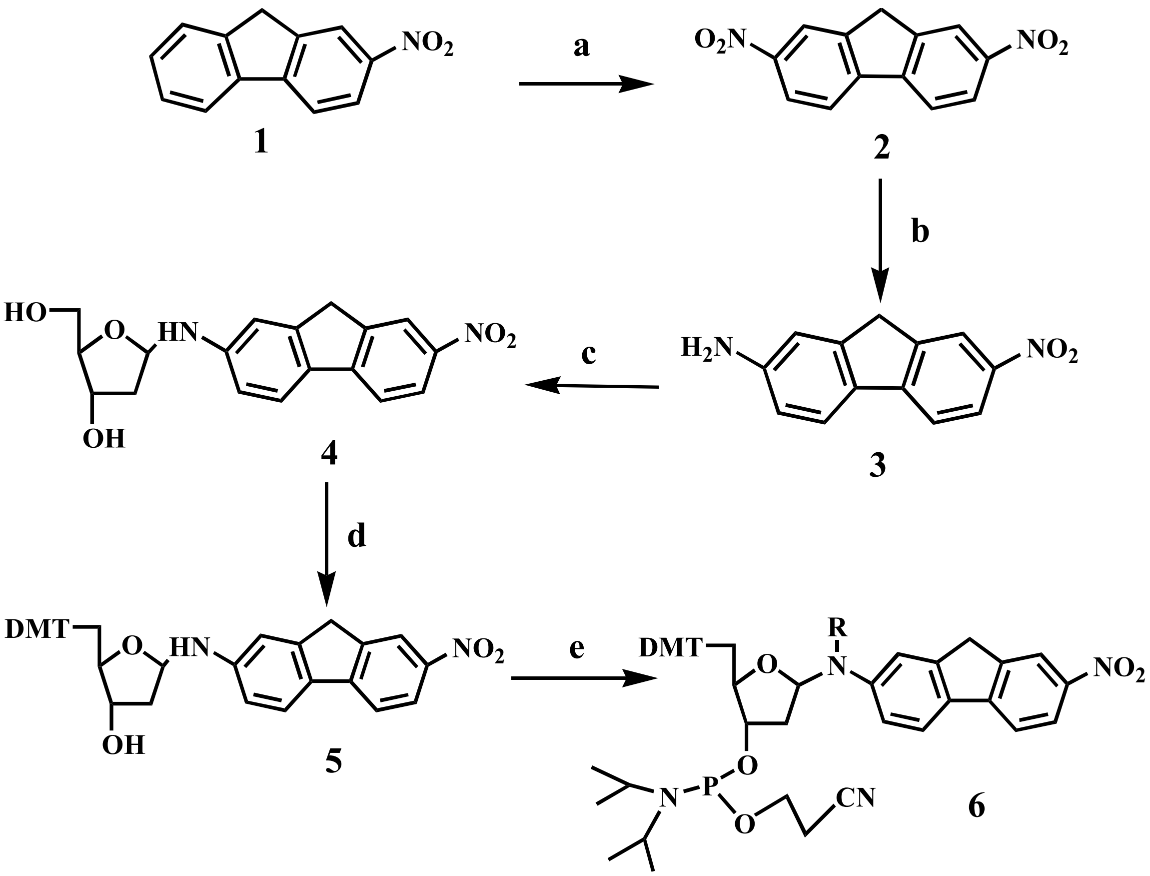

Scheme 1 Synthesis of ANF nucleotide **a**. fuming HNO_3, CH_3COOH, 62%; **b**. Pd/C, HCOOH, NEt_3, 57%; **c**. 2-Deoxy-D-ribose, EtOH , 30%; **d.** DMT-Cl, DIPEA, Pyridine, 79%; **e**. 2-Cyanoethyl N, N-diisopropylchlorophosphoramidite, DIPEA, CH_2Cl_2, 88%. DMT = 4,4'-dimethoxytrityl, DIPEA = N,N-diisopropylethylamine. R = H or 2-Cyanoethyl N, N-diisopropylchlorophosphoramidite.

a) Synthesis of 2, 7-dinitrofluorene (DNF, 2)

2-Nitrofluorene (9 g, 43 mmol), **1** was taken in 90 ml of acetic acid and 90 ml of fuming HNO_3 was added slowly to the mixture by cooling. The mixture was stirred for 2-5 hrs. An yellow solid, **2**, separated was filtered, washed with water and dried to yield crude product of 6.93 g (62 % yield).

b) Synthesis of 2-amino-7-nitro-fluorene (ANF, 3)

A mixture of 2,7-dinitro-fluorene (4 g, 15 mmol), **2**, 10% palladium on carbon (0.25 g) and triethylamine (20 ml, 140 mmol) was placed in a 2 necked round bottomed flask which was equipped with a reflux condenser. The mixture was heated to boiling and formic acid (3.06 g, 2.56 ml, 67 mmol) was added drop wise with stirring. The mixture was boiled about 30 to 45 min. The reaction mixture turned to dark reddish colour after few minutes of addition of formic acid. After, the reaction mixture was cooled, dichloromethane was added and the catalyst was removed by filtration. The solvent and the excess triethylamine were removed under reduced pressure and the reddish residue, **3**, was chromatographed on silica gel with dichloromethane to give bright red solid of 1.94 g (57% yield).

c) Synthesis of 7-Nitro-9H-fluoren-2-ylamine-1'- α/β-deoxyriboside (Ri-ANF, 4)

7-Nitro-9H-fluoren-2-ylamine, **3**, (1.3 g) was taken in 5 ml of ethanol and 2-deoxy ribose (500 mg in 2.5 ml of ethanol) was added slowly to the mixture. Then the mixture is allowed to stir for 24 hrs. Solvents were removed under reduced pressure and the reddish orange colour residue was chromatographed on silica gel with ethyl acetate to give the reddish orange solid, **4**, of 0.39 g (30% yield). (Ethyl acetate is used initially to remove the unreacted ANF, after acetone is used as eluent gradient. All eluent also contained 5% triethyl amine (TEA) to prevent degradation of product). The product is in racemic mixture (α/β).

d) Synthesis of 5'-(4, 4'-dimethoxytrityl)-7-Nitro-9H-fluoren-2-ylamine-1'-α/β-deoxyriboside (TMT-Ri-ANF, 5)

Ri-ANF, (110 mg, 0.32 mmol) was co evaporated with 2x20 ml dry pyridine and then the residue was dissolved in 50 ml dry pyridine. 300 μl DIPEA (1.56 mmol, 6 equiv.) was added in one portion via syringe. 350mg 4, 4'-dimethoxytrityl chloride (1.04 mmol, 4 equiv.) dissolved in 10 ml dry pyridine was transferred to the nucleoside solution via syringe. Reaction mixture was stirred at room temperature for 4 hrs. Solvent was removed under vacuum. The crude product was purified with chromatography to give the product as a red orange solid (150 mg, 79%; the eluent gradient used is hexane: ethyl acetate 2:1 to 100% ethyl acetate; all eluent also contained 3% triethyl amine (TEA) to prevent degradation product).

e. Synthesis of 5’-(4, 4’-dimethoxytrityl)-7-Nitro-9H-fluoren-2-ylamine-1’-α/β-deoxyriboside-3’-O- (cyanoethyl-N,N-diisopropylamino)phosphoramidite (P-TMT-Ri-ANF, 6).

5’-(4,4’-dimethoxytrityl)-7-Nitro-9H-fluoren-2-ylamine-1’-α/β-deoxyriboside (150 mg, 0.23 mmol) was suspended in 15ml dry CH_2Cl_2. N, N-Diisopropylethylamine (DIPEA, 220 µl, 1.26 mmol, 6equiv.) and 2-cyanoethyl N,N-diisopropylchloro-phosphoramidite (140 µl, 0.63 mmol, 3 equiv.) was added via syringe. Reaction mixture was stirred at room temperature for 3 hrs. Solvent was removed under vacuum and the crude product was loaded on to silica column. (150 mg, 79%; the eluent gradient used is hexane: ethyl acetate 2:1 to 100% ethyl acetate).

4.2 ANF derivatives [SPE04]

4.2.1 Synthesis of 2-(dimethylamino)-7-nitro-fluorene (dM-ANF, 7)

To the stirred mixture of 7-nitro-9*H*-fluoren-2-ylamine (100 mg, 0.442 mmol), **3**, and paraformaldehyde (148 mg, 0.005 mmol) in 99% glacial acetic acid (4 ml) at 25 °C under argon was added $NaCNBH_3$ (140 mg, 2.25 mmol) in one portion. The resulting mixture was stirred at 25 °C for 24 h and then poured into cold water. A bright orange-red solid, **7**, precipitated. It was filtered off and recrystallized from MeCN /water: yield 91 mg (81%).

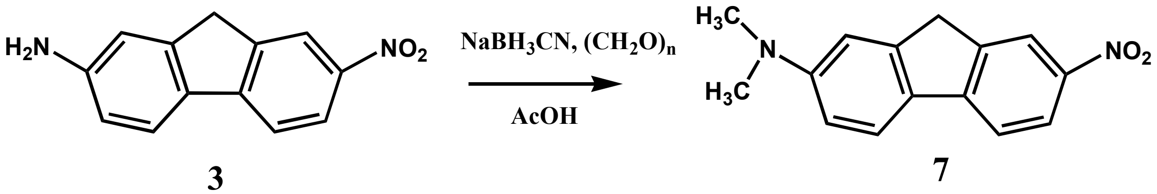

Scheme 2 Synthesis of 2-(dimethylamino)-7-nitro-fluorene (dM-ANF, **7**)

4.2.2 Synthesis of 2-Dibutylamino-7-nitro-9,9-di(n-propyl)-9H-fluorene (dBdP-ANF, 10) – by three steps

1. Synthesis of 2-Bromo-7-nitro-9H-fluorene (8)

To a stirred solution of 2-nitrofluorene, **1**, (8 g, 38 mmol) in dry CH_2Cl_2 (40 ml) was added Br_2 (76 mmol). The HBr, which soon evolved from solution was guided through a trap to a scrubbing solution of NaOH. The mixture was stirred for 5-6 hrs. A yellow precipitate appeared, which was filtered off, washed with 5% $NaHSO_3$ and water and dried with $MgSO_4$. The crude yellowish product was purified from recrystallization from a mixture of DMF and water to yield light yellow material, **8** (7.7 g, 70% yield).

2. Synthesis of 2-bromo-9,9-di(n-propyl)-9-H-fluorene (9)

Mixture of the fluorene, **BrNF,** (1 mmol), n-propyl bromide (2.5 mmol, KI (0.12 mmol) and DMSO 82.2 ml) was stirred at room temperature under argon and powdered KOH or t-BuOK (4.5 mmol) was slowly added. The color of the mixture turned from orange-red to dark green or purple. After stirring for 3-5 hrs, the reaction mixture was poured into water (150 ml). The product was filtered off, **9**, and dried. yield 79% light brown solid.

3. Synthesis of dBdP-ANF (10)

To a solution of 2-bromo-9,9-dipropyl-9*H*-fluorene, **9**, (2 mmol), dibutyl amine (4 mmol), and NaO-*t*-Bu (520 mg, 5 mmol) in dry toluene (16 ml) were added $Pd(OAc)_2$ (26 mg, 1 mmol) and tri-*tert*-butylphosphine (80 mg, 0.4 mmol) under argon atmosphere. The solution was heated to 100 °C under inert conditions for 6 hrs, during which time the color changed to reddish brown. After being cooled to room temperature, the mixture was mixed with AcOEt (50 ml) and washed with brine (100 ml). The organic layer was dried over $MgSO_4$, filtered, and concentrated. The crude product was purified by column chromatography on silica gel with AcOEt/hexanes (1:5) affording the products as crystalline or glassy material. The dark red product, **10** was obtained in 73% yield

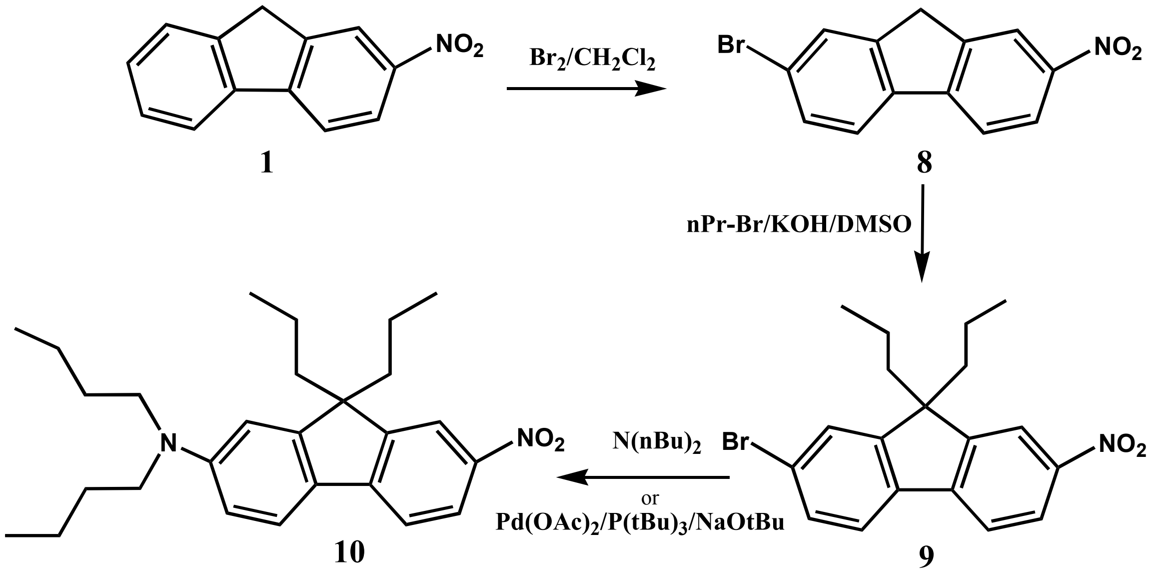

Scheme 3 Synthesis of 2-Dibutylamino-7-nitro-9,9-di(n-propyl)-9H-fluorene (dBdP-ANF, **10**)

4.2.3 Synthesis of 7-Nitro-9H-fluoren-2-ylamine-1'glucose (Gl-ANF, 11)

7-Nitro-9H-fluoren-2-ylamine, **3**, (1.3 g) was taken in 5 ml of ethanol and glucose (500 mg in 2.5 ml of ethanol) was added slowly to the mixture. Then the mixture is allowed to stirr for 24 hrs. Solvents were removed under reduced pressure and the reddish orange colour residue was chromatographed on silica gel with ethyl acetate to give the reddish orange solid, **11**, of 0.39 g (30% yield).

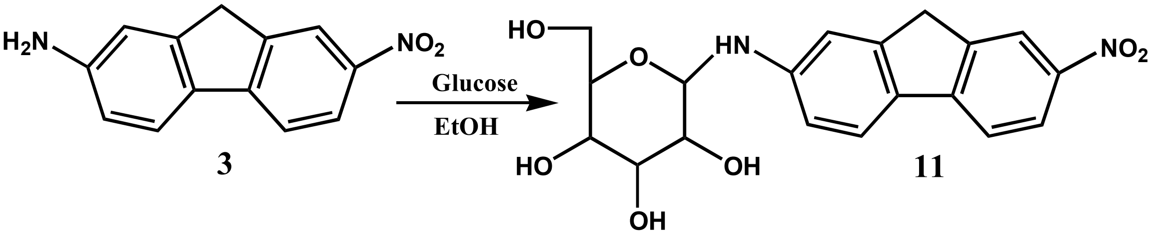

Scheme 4 Synthesis of 7-Nitro-9H-fluoren-2-ylamine-1'glucose (Gl-ANF, **11**)

4.3 Synthesis of Thiazole Orange (TO)

Thiazole Orange dye was provided by our collaborators D. V. Jarikote and Prof. Oliver Seitz, Department of organic and bioorganic chemistry Humboldt university, Berlin. Here a brief description of the synthesis is given.

4.3.1 Synthesis of 2-(1-Carboxy-methyl-1H-quinolin-4-ylidenmethyl)-3-methyl-benzothiazol-3-ium Bromide (TO, 14)

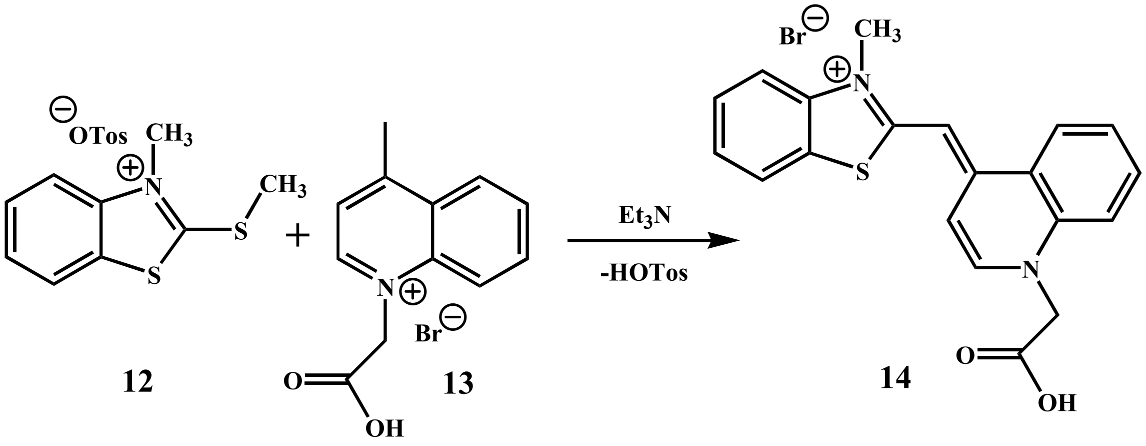

Scheme 5 Synthesis of 2-(1-Carboxy-methyl-1H-quinolin-4-ylidenmethyl)-3-methyl-benzothiazol-3-ium Bromide (**14**)

To 205 mg (0.6 mmol) of 3-Methyl-2-mercaptomethyl-benzothiazol-3-ium Tosylate **12** [SSF85], 158 mg (0.6 mmol) of 1-Carboxymethyl-4-methylquinolinium Bromide **13** [SGS88] was added in 10 ml of dichloromethane. The resulting mixture was stirred for 20 minutes and added 113 mg (1.2 mmol) triethylamine. The mixture was stirred for 48 hrs at room temperature. The resulting solid was dissolved in minimum amount of methanol and water was added until precipitate has formed. The resulting solid was recrystallised at 4°C to achieve the desired thiazole orange derivative.

4.4 Synthesis of Thiazole Orange labeled PNA

All thiazole orange labeled PNA were synthesized by D. V. Jarokote [JKS05].

5 Stationary photophysical studies of ANF derivatives

5.1 An overview of ANF

5.1.1 Properties of ANF

Even though there are many solvatochromic probes available in the field of solution chemistry, we choose 2-amino-7-nitrofluorene (ANF, figure 5.1.1-1) as photophysical probe for DNA. Its usefulness for polar local DNA dynamics is outlined by a summary of a theoretical background study [FES_ _]. In the following we summarize the photophysical properties of ANF, and especially its solvatochromic behavior. ANF is highly sensitive to solvent polarity. The absorption band lies in the visible where all solvents are transparent, and has high extinction (ε_{max} = 18300 L mol^{-1} cm^{-1}). It is reasonably soluble in organic solvents and non reactive with neat solvents.

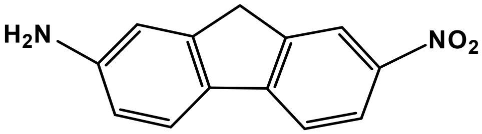

ANF

Figure 5.1.1-1 Chemical structure of 2-amino-7-nitro fluorene (ANF).

5.1.2 Molecular structure of ANF and its studies

The structure of the ANF molecule in the electronic ground state S_0 was calculated [FES_ _] on the DFT B3LYP/6-311G (d,p) level with Gaussian 98 [G0098]. Geometry optimization *in vacuo* gave the structure which is shown in figure 5.1.2-1 and which agrees (~ 0.01 Å standard deviation of bond lengths) with the experimental structure from X-ray diffraction [see section 5.1.3]. The charges were calculated on the MP2/6-31G(d)//B3LYP/6-311G(d,p) level, by fitting partial atomic charges to reproduce the molecular electrostatic potential. The molecule is meant to probe the polarization state of the DNA and its environment by the solvatochromism of the $S_1 \rightarrow S_0$ emission band. In order to simulate this effect one needs the difference charge distribution $q_i(S_1)$-$q_i(S_0)$ when all nuclear modes in S_1 are fully relaxed. Instead we calculated the difference charge distribution at the optimized ground-state geometry using TD B3LYP/6-311G(d,p)/B3LYP/6-311G(d,p) [G0098]. The corresponding change of electrostatic potential energy in the molecular plane is also depicted in the figure 5.1.2-1.

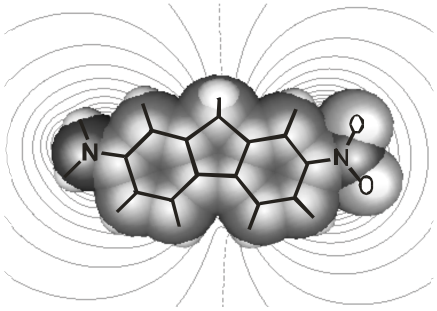

Figure 5.1.2-1 Molecular structure of ANF in its solvent-excluding volume. $S_1 \leftarrow S_0$ optical excitation creates a difference potential (thin lines) which is dipolar in the molecular plane.

Fu *et al* [FFP01] showed that ANF belongs to C_S symmetry on the basis of optimized molecular structure. The chromophore exhibits a large change in dipole moment on excitation to the first excited electronic singlet state. Czekalla *et al* [CLM63] modulated the absorption and emission bands in 1,4 dioxane with an electric field and in this way determined dipole moments, 6.4 D in the electronic ground state S_0 and ~20.3 D in the S_1 ($\pi\pi^*$) excited state. The dipole moment change of 14 D upon excitation explains the large Stokes shift of fluorescence as it depends on solvent polarity. The change in dipole moment results from intramolecular charge transfer upon electronic excitation, from the amino donor at position 2 to the nitro acceptor at position 7. The direction of the dipole moment is essentially kept during the excitation. The aromatic rings of the ANF system are forced in a coplanar configuration and 2nd and 7th positions are therefore strongly resonant. Indeed, the solvatochromism of ANF has been studied since the invention of the solvation field [L0057]. Picosecond time resolved fluorescence spectra of ANF in 2-propanol/benzene mixtures [HT078] showed that rates of Stokes shift and quenching by hydrogen-bonded interactions varied linearly with mole fraction of 2-propanol. The Stokes shift is due to the selective affinity of the highly polar excited state for polar solvent molecules, increasing the microscopic dielectric constant above the macroscopic value. Samantha *et al* [MSS04] observed an excitation-wavelength-dependent shift of the fluorescence spectra from ANF in room-temperature ionic liquids.

This implies a distribution of ground-state molecules differing in their interaction energies with the ionic liquids, and that solvation and /or energy transfer occur on time scales longer than the S_1 lifetime in these media.

Femtosecond studies of ANF were first reported in RKE98. In that work the solvation dynamics of ANF in acetonitrile was followed by observing stimulated emission. For this purpose Pump-Super-Continuum Probe (PSCP) spectroscopy was used. The measured relaxation curve for the maximum of the stimulated emission band is in excellent agreement with the solvation correlation function C(t) obtained from the simple continuum theory of dipolar solvation. In particular, librational coherence was observed in acetonitrile in the intermediate regime, around 300 fs. This observation reflects the far-infrared absorption band in neat acetonitrile which broadly covers that region, with a maximum at 100 cm^{-1}.

5.1.3 Crystal structure of ANF

Crystals of 2-amino-7-nitrofluorene were obtained from CH_2Cl_2 by air evaporation in the form of red orange platelets. Measurements were made on a Nonius Kappa CCD spectrometer and Stoe IPDS instrument using MoK_α radiation, $\lambda = 0.71073$ Å. Bond lengths and angles as well as technical information are given in appendix 10.1. The molecular structure is shown in figure 5.1.3-1.

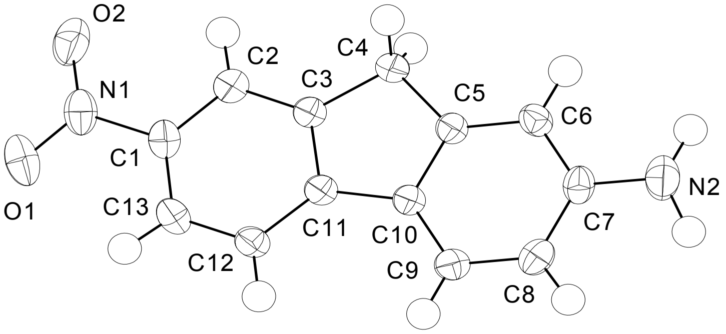

Figure 5.1.3-1 Crystal structure of ANF by X-ray diffraction, which agrees well with calculated on the DFT B3LYP/6-311G(d,p) level with Gaussian 98 [FES_ _]

5.1.4 Derivatives of ANF

Alkylated derivatives of ANF were synthesized in this work by palladium-catalyzed substituted halofluorenes, as described in SPE04. The important derivatives for our purposes are *N*, *N*-dimethyl-(7-nitro-9*H*-fluoren-2-yl)amine (dM-ANF) and 2-dibutylamino-7-nitro-9,9-di(*n*-propyl)-9*H*-fluorene (dBdP-ANF). We have also synthesized nuclosides as 7-nitro-9H-fluoren-2-ylamine-1'- α/β-deoxyriboside (Ri-ANF, 2-deoxyribose attached to amino nitrogen through C1') and 7-nitro-9H-fluoren-2-ylamine-1'glucose (Gl-ANF, glucose is attached through C1'). Their synthesis and characterization of them are explained in the synthesis chapter 4. Chemical structure of all ANF derivatives and nucleosides are schematized in figure 5.1.4-1

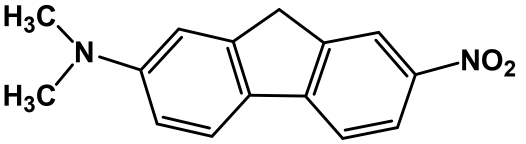

dM-ANF

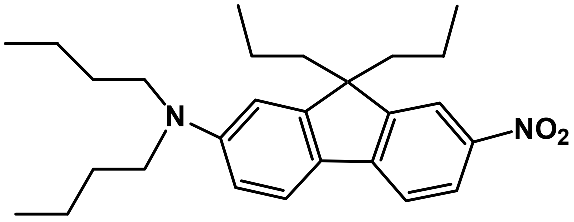

dBdP-ANF

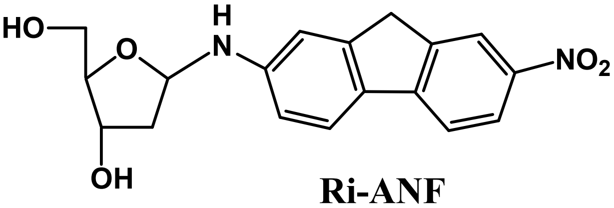

Ri-ANF

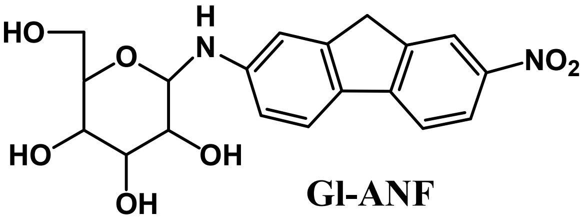

Gl-ANF

Figure 5.1.4-1 ANF derivatives studied in this thesis: *N*, *N*-dimethyl-(7-nitro-9*H*-fluoren-2-yl)amine (dM-ANF) and 2-dibutylamino-7-nitro-9,9-di(*n*-propyl)-9*H*-fluorene (dBdP-ANF). We have also synthesized the nuclosides in the second row: 7-nitro-9H-fluoren-2-ylamine-1'-deoxyriboside (Ri-ANF, 2-deoxyribose attached to amino nitrogen through C1') and 7-nitro-9H-fluoren-2-ylamine-1'-glucose (Gl-ANF, glucose attached through C1').

5.1.5 Importance of dM-ANF

By employing dM-ANF, Catalan *et al* [CLP95] developed a solvent dipolarity - polarizability scale ("SPP") which combines medium dipolarity and polarizibility into a single parameter. For this purpose absorption spectra in more than 100 solvents and in the gas phase were compared. Any solvatochromic probe may show special effects which should be corrected. For example: (1) change of electronic structure upon solvation, (2) hydrogen bonding through some functional group, for example $-NO_2$, Therefore every polarity scale should be validated by one or more homomorphs (similar structure) of the solvatochromic probe compound. Catalan and his group [CLP95] used the UV-visible absorption spectra of 2-(dimethyl-amino)-7-nitrofluorene (dM-ANF) and its homomorph 2-fluoro-7-nitrofluorene (FNF) to establish the SPP scale. dM-ANF has advantages over ANF because dimethyl substitution on amino nitrogen prevents specific solvation there and increases the resonance effect of the electron releasing group. Hence the dipole moment of dM-ANF increases markedly on electronic excitation while its direction remains constant. Therefore it is an excellent solvatochromic probe for measuring non-specific solvent effects. By using the Lorenz-Lorentz function for nonpolar solvents, $\left[f_1\left(n^2\right)=\left(n^2-1\right)/\left(n^2+2\right)\right]$, the maximum absorption in the gas phase is found by extrapolation, to be 28,231cm^{-1}. The SPP and normalized SPP^{N} value for 100 solvent was defined by

$$\mathrm{SPP} = \frac{\Delta\tilde{\mathrm{v}}(\mathrm{solvent}) - \Delta\tilde{\mathrm{v}}(\mathrm{CH})}{\Delta\tilde{\mathrm{v}}(\mathrm{DMSO}) - \Delta\tilde{\mathrm{v}}(\mathrm{CH})} \qquad 5.1$$

$$\mathrm{SPP}^{\mathrm{N}} = \frac{\Delta\tilde{\mathrm{v}}(\mathrm{solvent}) - \Delta\tilde{\mathrm{v}}(\mathrm{gas})}{\Delta\tilde{\mathrm{v}}(\mathrm{DMSO}) - \Delta\tilde{\mathrm{v}}(\mathrm{gas})} \qquad 5.2$$

where $\Delta\tilde{\mathrm{v}} = \tilde{\mathrm{v}}_{\mathrm{FNF}} - \Delta\tilde{\mathrm{v}}_{\mathrm{DMANF}}$ cm^{-1} and gas = gas phase, CH = cyclohexane, and DMSO = dimethylsulfoxide.

From plotting the wavenumber of the first absorption maximum of dM-ANF versus the corresponding value for FNF in different solvents, the following conclusions could be drawn. There is good linear correlation in benzene-derivative solvents. In general, solvents with fluorine substituents and hydroxylic solvents deviate from linearity. It was concluded that dM-ANF solvatochromism is not significantly influenced by specific interactions of the nitro group with hydroxylic solvents. (But note that the solvatochromic plot of dM-ANF gives the two sets of slopes.) The following are the important features of the SPP scale. (1) The portion of the solvent scale below cyclohexane (SPP = 0) is wider (SPP = -1.26 in the gas phase) than the portion for the more polar solvents (SPP = 1.02 for nitrobenzene). (2) The parameters for the alkanes studied encompass a wide portion of the scale (from -0.18 for 2-methylbutane to 0.07 for cyclooctane) and reflect the high sensitivity of their scale to the solvent polarizability. (3) Cycloalkanes are ca.0.1 units more polar than their acyclic analogues. The SPP scale was correlated with other data, from IR, NMR, and UV-Vis absorption, fluorescence, thermodynamics equiquilibria, solvation enthalpy, and kinetics. It was also compared the other polarity scales which have been outlined in the section 2.2.

5.2 Solvatochromism of ANF derivatives

5.2.1 Absorption and emission

Stationary absorption and fluorescence spectra of ANF derivatives, *viz.*, dM-ANF, dBdP-ANF, and ANF were measured in variety of solvents covering non-polar solvent to highly polar solvents. The riboside Ri-ANF and the glucoside Gl-ANF were also examined (given in appendix 10.2 and 10.3). The corresponding results are needed to understand the properties of the chromophore in DNA oligonucleotides; they are also required when determining the solvation correlation function of these compounds. Figure 5.2.1-1 shows the stationary S_1-S_0 absorption and emission bands of ANF, dM-ANF, and dBdP-ANF in 2-methylbutane (*2mb*). Fluorescence distributions were converted into corresponding spectra for stimulated emission $\sigma_{SE} \propto F(\tilde{\nu})/\tilde{\nu}^2$ because these are seen in femtosecond transient absorption experiments, for which the work of this section has been performed. Increasing aliphatic substitution shifts the spectra to the red and enhances vibrational structure. This may be due to the increased charge-transfer character of the excited S_1 state which has stabilizing effect as in coumarin derivatives [GCG98]. For dBdP-ANF a vibrational mode of 1270 cm^{-1} is seen in absorption and emission.

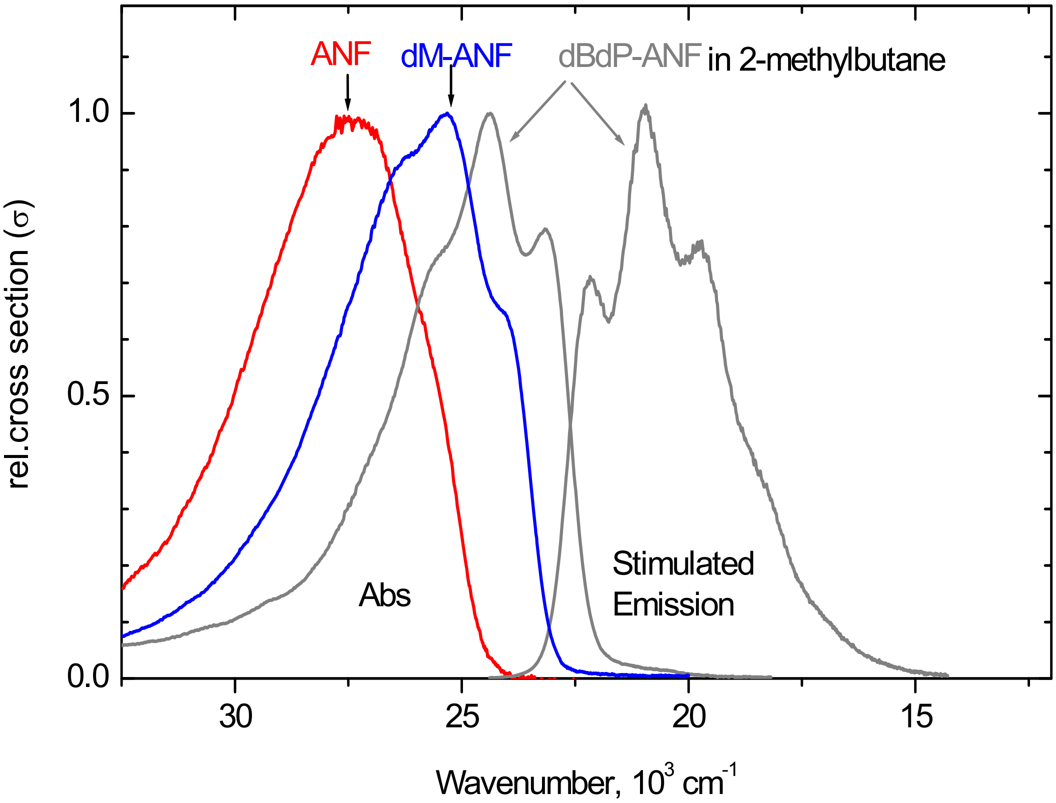

Figure 5.2.1-1 Optical spectra of ANF (red), dM-ANF (blue) and dBdP-ANF (grey) in 2-methylbutane (relative cross section $\sigma(\tilde{\nu})$ of absorption and – for dBdP-ANF – of stimulated emission as derived from fluorescence). All spectra were converted into the corresponding oscillator distributions $M^2(\tilde{\nu}) \propto \sigma / \tilde{\nu}$ and then fitted by lognormal functions.

Figure 5.2.1-2 shows the three compounds in acetonitrile (ACN). Each panel shows the respective stationary absorption spectrum, the stimulated emission spectrum obtained from fluorescence (solid black line), and the calculated time-zero stimulated emission spectra (thick grey line) as explained in the experimental section 3.10. Along with this are shown absorption spectra in 2-methyl butane (*2mb*), shifted such that after Gaussian broadening the respective absorption spectrum is reproduced. In polar solvents vibrational structure is no longer observed because of broadening, and the emission becomes separated from the absorption by a Stokes shift of several 1000 cm^{-1}. For example compare the spectra of dBdP-ANF in *2mb* (gray lines in the figure 5.2.1-1) with those in acetonitrile (lower panel in figure 5.2.1-2). Bands are structured and asymmetric in *2mb* and unstructured, almost symmetric in ACN.

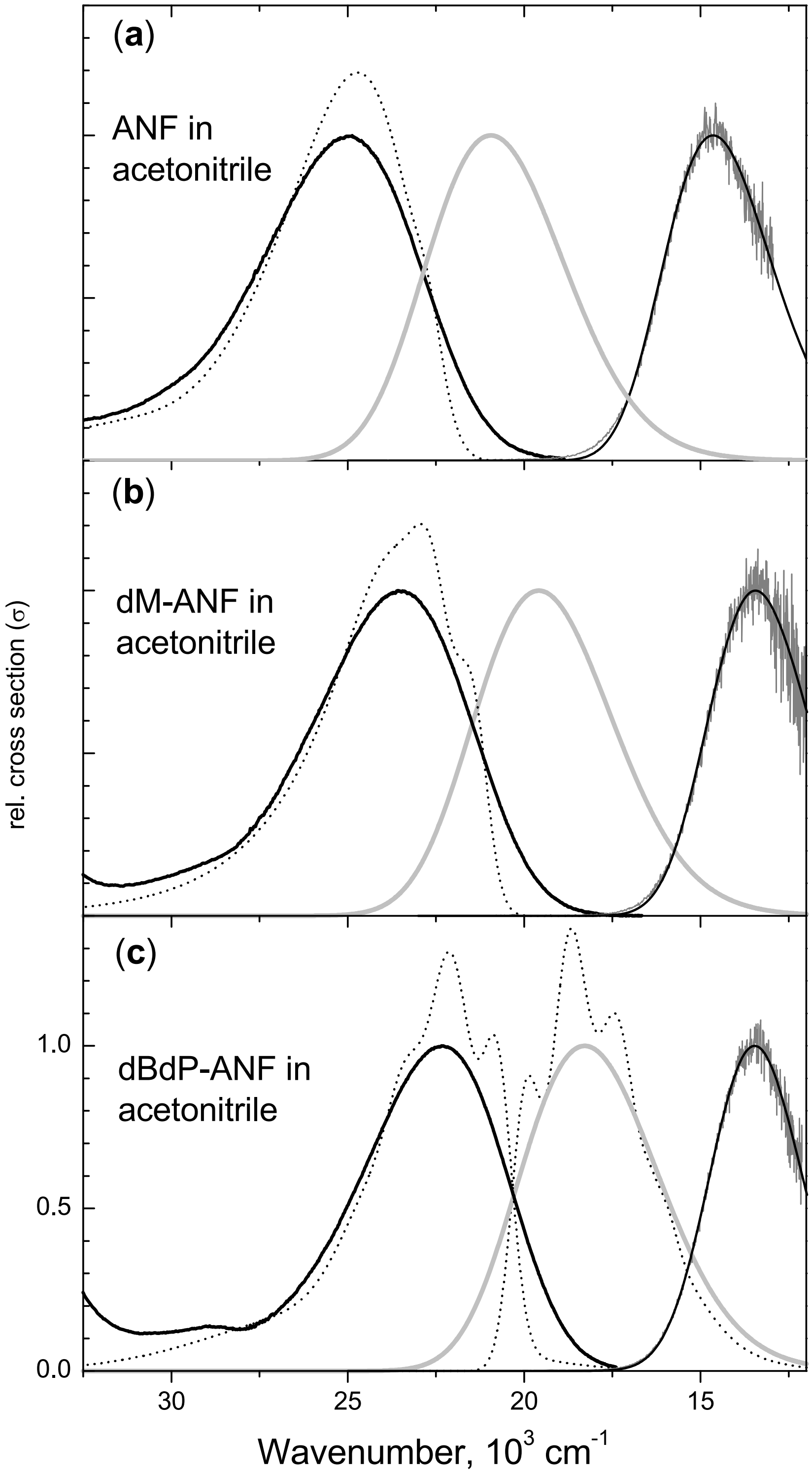

Figure 5.2.1-2 Optical spectra in acetonitrile: *Solid black lines* – stationary absorption and stimulated emission (from fluorescence); *thick gray* – calculated time-zero stimulated emission; *dashed lines* – in 2-methylbutane, shifted such that Gaussian broadening gives the corresponding spectrum in acetonitrile.

5.2.2 Characteristic parameters of spectra

In order to quantify the shift upon going from *2mb* to a polar solvent, the change of shape must be accounted for. In essence, changing shape reflects a redistribution of oscillator strength, and this is why every spectrum must first be converted into the corresponding distribution of oscillator strength – the normalized line shape function – which is for absorption [B0070]

$$g(\tilde{\nu}) \propto \varepsilon(\tilde{\nu})/\tilde{\nu} \qquad 5.3$$

and for emission

$$f(\tilde{\nu}) \propto F(\tilde{\nu})/\tilde{\nu}^3, \qquad 5.4$$

with $1 = \int f d\tilde{\nu} = \int g d\tilde{\nu}$.

Lineshapes were fitted by a sum of lognormal functions [SM069] as explained in experimental section 3.11.1. The needed parameters for solutions in *2mb* are given in table 5.1; those for many solvents are available in the appendix10.4-6.

Table 5.1 Lognormal description of optical spectra (oscillator distributions) for the three chromophores in *2-methylbutane*

dye	**Absorption** $g(\tilde{\nu})$:	$\tilde{\nu}_p$ **/cm^{-1}, Δ /cm^{-1}, γ, h**	**Stat. fluorescence** $f(\tilde{\nu})$
	$S_n \leftarrow S_0$	$S_1 \leftarrow S_0$	$\tilde{\nu}_p$**/cm^{-1}, Δ/cm^{-1}, γ, h**
ANF	38115, 3080, 0.3674, 0.1237 41668, 6435, 0.1362, 0.4203	25380, 854, 0.0048, 0.1225 27309, 4072, 0.4053, 1.0000 34850, 4263, 0.2502, 0.0410	—
dM-ANF	36999, 3275, 0.0978, 0.2803 40035, 4694, 0.4557, 0.2762	23910, 1016, 0.0024, 0.5906 24902, 1174, 0.0047, 0.3560 25986, 3252, 0.6165, 0.8322 26491, 2199, 0.0117, 0.0583	—
dBdP-ANF	35969, 3271, 0.1124, 0.2347 39007, 4579, 0.4709, 0.2165	23021, 996, 0.0024, 0.7066 24292, 1416, 0.0084, 0.8190 25611, 1095, 0.0000, 0.2149 25996, 2759, 0.0023, 0.3668 28050, 5745, 0.0159, 0.0934	22212, 1001, -0.0024, 0.6355 20965, 1225, -0.1020, 0.9629 19621, 1235, 0.0000, 0.7261 18513, 969, -0.0000, 0.3412 17663, 1473, -0.6582, 0.1847

The band position is determined differently for emission $S_1 \rightarrow S_0$ and absorption $S_1 \leftarrow S_0$. In the former case we obtain the first moment directly from the emission lineshape

$$\left\langle \tilde{\nu}^{\mathrm{fls}} \right\rangle = \int \tilde{\nu}\, f(\tilde{\nu})\, d\tilde{\nu} \qquad 5.5$$

The same can not be done for absorption because the corresponding lineshape $g(\tilde{\nu})$ contains contributions from transitions to higher electronic states, $S_n \leftarrow S_0$, which must be separated from $S_1 \leftarrow S_0$ in a consistent way. The absorption of dBdP-ANF in solvent x = acetonitrile (figure 5.2.1-2(c)) serves as an example. It is explained by the lineshape measured in *2mb* and shifted by $-\Delta\tilde{\nu}^{\mathrm{abs}}$ (dashed line in the figure), then broadened by convolution with a Gaussian function $\propto \exp\left\{-\frac{1}{2}\frac{(\delta\tilde{\nu})^2}{\tilde{\sigma}^2}\right\}$ (with fwhm $\tilde{\Gamma} = \tilde{\sigma}\sqrt{8\ln 2}$). By varying shift and broadening $\tilde{\Gamma}$ an optimal fit is sought over a frequency range which extends from the absorption peak by $3\,\Gamma$ to the blue and red. Finally one obtains

$$\left\langle \tilde{\nu}_{x}^{\mathrm{abs}} \right\rangle = \left\langle \tilde{\nu}_{2\mathrm{mb}}^{\mathrm{abs}} \right\rangle - \Delta\tilde{\nu}^{\mathrm{abs}}. \qquad 5.6$$

The emission at time-zero, immediately after excitation but before solvent relaxation, can also be estimated along these lines, in a method devised by Fee and Maroncelli [FM094] (explained in experimental section 3.10). As before one determines the shift and broadening which the absorption lineshape experiences when the chrompohore is transferred from *2mb* to solvent *x*. Subsequently these parameters are used to shift and broaden the emission lineshape $f_{2\mathrm{mb}}$. As a result, the emission lineshape in solvent *x* at time-zero, f_{x}^{0}, is obtained. Such calculations gave the time-zero stimulated emission spectra which are shown as gray lines in figure 5.2.1-2. Here it should be noted that a more detailed treatment applies for excitation at the red edge of the absorption band [FM094]. For reference we use $g_{2\mathrm{mb}}$, $f_{2\mathrm{mb}}$ of dBdP-ANF, because only in this case could $f_{2\mathrm{mb}}$ be obtained. The various $\left\langle \tilde{\nu}_{x}^{\mathrm{abs}} \right\rangle$, Γ^{abs} and $\left\langle \tilde{\nu}_{x}^{\mathrm{fls}} \right\rangle$ constitute the first data set of this work and are summarized in Table 5.2. The peak extinction coefficient of ANF in acetonitrile is $\varepsilon_{\max}$ = 18373 L mol^{-1} cm^{-1}. From our description for the $S_0 \rightarrow S_1$ absorption lineshape we obtain an electronic oscillator strength f_{01} = 0.486 and transition dipole μ_{01} = 6.33 D. Together with the fluorescence quantum distribution (*cf.* appendix 10.4) the predicted radiative lifetime becomes τ_{rad} = 15.3 ns in acetonitrile.

Table 5.2 Mean S_1 — S_0 frequencies $\langle\tilde{\nu}\rangle$ (cm^{-1}) and absorption broadening Γ^{abs} (FWHM of Gaussian, cm^{-1}) for the three compounds in various solvents (*na* = not applied, *nm* = not measured. [a] excess absorption on blue side, [b] positive asymmetry).

Solvent		n	ε	**ANF**			**dM-ANF**			**dBdP-ANF**		
				$\langle\tilde{\nu}^{abs}\rangle$	Γ^{abs}	$\langle\tilde{\nu}^{fls}\rangle$	$\langle\tilde{\nu}^{abs}\rangle$	Γ^{abs}	$\langle\tilde{\nu}^{fls}\rangle$	$\langle\tilde{\nu}^{abs}\rangle$	Γ^{abs}	$\langle\tilde{\nu}^{fls}\rangle$
perfluoro-n-hexane	pfh	1.252	1.57	*nm*	*nm*	*nm*	*nm*	*nm*	*nm*	26010	*na*	19430
2-methyl-butane	mb	1.3509	1.83	28210	*na*	*nm*	26570	*na*	*nm*	25290	*na*	20200
n-pentane	pen	1.3547	1.84	28210	*na*	*nm*	26560	*na*	*nm*	25250	*na*	20320
n-hexane	hex	1.3723	1.88	28100	*na*	*nm*	26400	*na*	*nm*	25190	*na*	20150
n-heptane	hep	1.3851	1.92	28020	*na*	*nm*	26500	*na*	*nm*	25020	*na*	20110
n-octane	oct	1.3951	1.95	27960	*na*	*nm*	26280	*na*	*nm*	25020	*na*	19400
cyclohexane	ch	1.4235	2.02	27810	*na*	*nm*	26110	*na*	*nm*	24910	*na*	19970
carbon-tetrachloride	ctc	1.457	2.24	27220	1370	19260	25620[a]	1480[a]	18630	24420	1180	18130
chloroform	chl	1.442	4.89	26140	2730	15800	24010	2570	14390	22720	2350	14090
1,1,1-trichloro-trifluoro-ethane	tctf	1.356	2.41	27760	1670	*nm*	26020	1600	18490	24760	1320	17970
diethyl ether	dee	1.3495	4.20	26040	2070	16980	25300	1670	16150	24290	1600	16060
dipropyl ether	dpe	1.3780	3.39	26050	2170	16780	25320	1550	15980	24310	1440	15860
dibutyl ether	dbe	1.3968	3.08	26450	2140	18440	25520	1250	18020	24470	1130	17940
tetrahydro-furane	thf	1.4050	7.58	25210	2190	16610	24440	2120	15760	23470	1950	15890
tetrahydro-pyrane	thp	1.4186	5.61	25280	2170	16250	24610	1950	15270	23620	1790	15380
1,4-dioxane	dio	1.4203	2.21	25990	2120	17510	24890	1950	16700	23880	1810	16600
methyl acetate	mac	1.3589	6.68	25700	2430	16280	24660	2280	15220	23650	2120	15760

ethyl acetate	eac	1.3698	6.02	25700	2330	16610	24740	2170	15670	23730	2000	15350
dimethyl-formamide	dmf	1.428	36.71	24100	2730	14190	23580	2710	13320	22540	2570	13520
hexamethyl-phosphoramide	hmpa	1.457	29.30	*nm*	*na*	14850	23500	2430	14130	22520	2380	14200
dimethyl sulfoxide	dmso	1.477	46.45	23620	2850	13840	23190	2850	12930	22200	2660	13020
acetonitrile	acn	1.341	35.94	25500	2870	14070	24130	2900	13020	23010	2680	13220
propionitrile	prn	1.363	28.26	25420	2760	14040	24150	2730	13590	23010	2500	13690
methanol	meoh	1.3265	32.66	25640	3910	13820	24410	3340	*nm*	23270	2940	12980 [b]
ethanol	etoh	1.3594	24.55	25360	3720	14360	24470	2920	11940	23430	2780	13700 [b]
propanol	proh	1.3837	20.45	25370	3840	14790	24480	2940	12370	23450	2800	14020 [b]
butanol	buoh	1.3974	17.51	25370	3790	14880	24520	2920	12670	23480	2780	14240 [b]
benzene	bz	1.4979	2.27	26390	1770	18620	24690	1580	17310	23740	1410	17290
toluene	tol	1.4941	2.38	26440	1650	18800	24800	1460	17640	23860	1320	17550

To take out the effect of solvent polarizability, the average frequencies have been shifted to $\langle\tilde{\nu}\rangle + \Delta(n) \equiv \langle\tilde{\nu}\rangle + 11900\big(f(n) - 0.216\big)$, as if the refractive index were always that of *2mb. na* means that $\langle\tilde{\nu}^{abs}\rangle$ was determined from a lognormal fit of the absorption data directly and not by the shift from the spectrum in *2mb.*

5.2.3 Discussion of solvatochromism

5.2.3.1 with solvent polarity function

In the continuum theory of polar solvation [B0089, CFB88], the solute is represented as a charge distribution in a cavity and the surrounding liquid is treated as a continuum with dielectric constant ε and refractive index n. In a simple version the charge distribution is reduced to a point dipole with moment μ and the cavity is taken to be spherical with radius a. Consider the solute in an initial electronic state i which is in equilibrium with the solvent. The polarized medium creates a reaction field in the center of the cavity

$$\mathbf{R} = B_{or}\,\boldsymbol{\mu}_i + B_{el}\,\boldsymbol{\mu}_i\,. \tag{5.7}$$

where

$$B_{or} = \frac{2}{a^3}\left(\frac{\varepsilon-1}{\varepsilon+2} - \frac{n^2-1}{n^2+2}\right) \tag{5.8}$$

is due to the nuclear (mostly orientational) polarisation in the liquid and

$$B_{el} = \frac{2}{a^3}\left(\frac{n^2-1}{n^2+2}\right) \tag{5.9}$$

comes from the electronic polarisation (Note that forms $\left(\frac{\varepsilon-1}{2\varepsilon+1} - \frac{n^2-1}{2n^2+1}\right)$ are also used in the literature; see below). The free energy for medium polarization is generally $+1/2\,B\,\mu^2$. Therefore the free energy of transfer from the gas phase into the liquid is, after complete equilibration,

$$E_i = -\boldsymbol{\mu}_i(B_{or}\,\boldsymbol{\mu}_i + B_{el}\,\boldsymbol{\mu}_i) + \frac{1}{2}B_{or}\,\boldsymbol{\mu}_i^2 + \frac{1}{2}B_{el}\,\boldsymbol{\mu}_i^2 \tag{5.10}$$

From the solvated state i, only the electronic polarization follows the optical transition to final state f while the nuclear polarization remains at first, so that

$$E_f = -\boldsymbol{\mu}_f(B_{or}\,\boldsymbol{\mu}_i + B_{el}\,\boldsymbol{\mu}_f) + \frac{1}{2}B_{or}\,\boldsymbol{\mu}_i^2 + \frac{1}{2}B_{el}\,\boldsymbol{\mu}_f^2 \tag{5.11}$$

The gas-phase wavenumber $\tilde{\nu}_{gas}^{i\to f}$ is thus shifted to become in solution

$$\tilde{\nu}^{i\to f}_{\mathrm{solvent}} = \nu^{i\to f}_{\mathrm{gas}} - \frac{1}{hc}\left[\left(\boldsymbol{\mu}_f - \boldsymbol{\mu}_i\right) B_{or}\ \boldsymbol{\mu}_i + \frac{1}{2} B_{el} \left(\boldsymbol{\mu}_f^2 - \boldsymbol{\mu}_i^2\right)\right] \qquad 5.12$$

When $\mu_f > \mu_i$ a red-shift is observed when ε or n are increased (positive solvatochromism).

The dispersive second term can be found from the $S_0 \rightarrow S_1$ absorption band in nonpolar solvents as shown in figure 5.2.3.1-1 for the three chromophores. Here the average $\left\langle \tilde{\nu}^{abs} \right\rangle$ is plotted against the polarizability factor $f(n) = \left(n^2 - 1\right)/\left(n^2 + 2\right)$ for three compounds as in figure 5.2.3.1-1. The following figures 5.2.3.1-2 – -4 represents the average frequency dependence of solvent polarity of chromophore *viz.*, ANF, dM-ANF and dBdP-ANF respectively. The average frequency of stationary absorption and emission bands (first moment for the $S_1 \rightarrow S_0$ oscillator distribution) are included in each figure. In the figure 5.2.3.1-3 the peak absorption frequencies reported by Catalan [CLP95] are shown for comparison. dBdP-ANF dissolves well in perfluoro-n-hexane (*pfh*) where spectra almost like in the gas-phase can be recorded. We obtain

$$\left\langle \tilde{\nu}^{\mathrm{abs\,dBdPANF}}_{\mathrm{nonpolar}} \right\rangle / \mathrm{cm}^{-1} = (27870 \pm 140) - (11900 \pm 640)\, f(n)\,. \qquad 5.13$$

Here it is noted that the spectral position of the prominent vibrational band in dBdP-ANF is $\left\langle \nu^{\mathrm{abs\,dBdPANF}}_{\mathrm{nonpolar}} \right\rangle - 990$ cm^{-1}. The slope for dM-ANF is not significantly different and for ANF we find $-(10530 \pm 270)\,\mathrm{cm}^{-1}$. However in both cases we did not record data from solutions in *pfh*, which is why the corresponding slopes should be less accurate compared to that of dBdP-ANF. To take out the effect of solvent polarizability, the average frequencies of table 5.2 have been shifted to $\left\langle \tilde{\nu} \right\rangle + \Delta(n) \equiv \left\langle \tilde{\nu} \right\rangle + 11900\left(f(n) - 0.216\right)$, as if the refractive index were always that of *2mb*.

5.2.3.2 Comparison with literature data

We discuss with the solvatochromism of dM-ANF (figure 5.2.3.1-3) because this dye has been examined extensively by Catalan and coworkers [CLP95]. They determined the peak absorption and emission frequency for many solvents. Their absorption results are shown in the figure as gray points along a gray line, as function of the reaction field

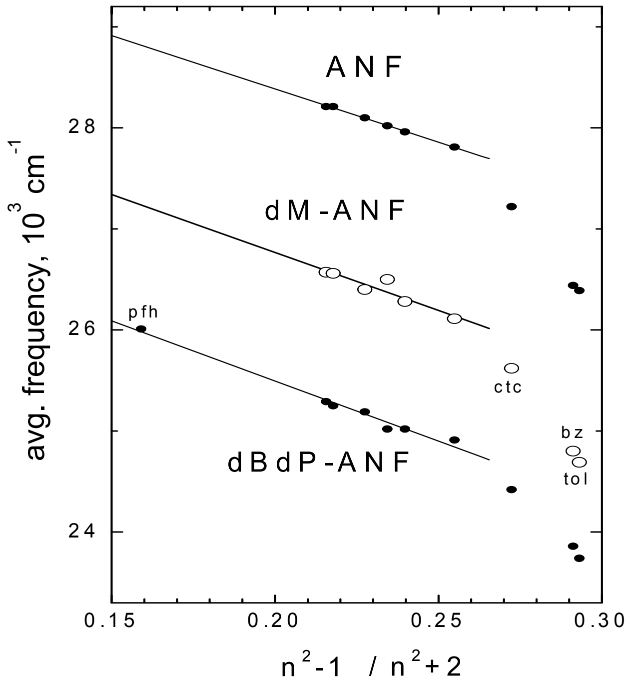

Figure 5.2.3.1-1 Average nonpolar absorption frequency *vs* the solvent polarizability function for the three compounds

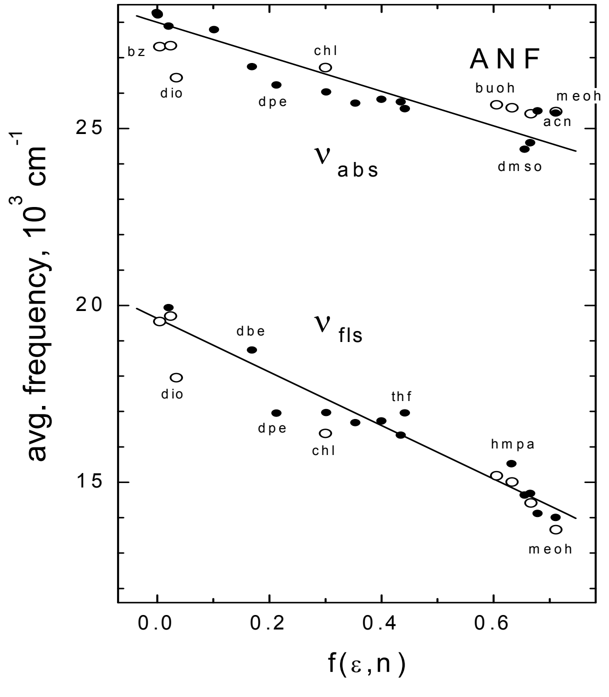

Figure 5.2.3.1-2 Average frequency of ANF steady-state absorption and emission bands (first moment for the $S_1 \leftrightarrow S_0$ oscillator distribution) in a range of solvents, plotted versus the reaction field factor $F(\varepsilon, n)$. The effect of changing dispersion has been removed. Only black dot points were used for regression analysis. For details see text.

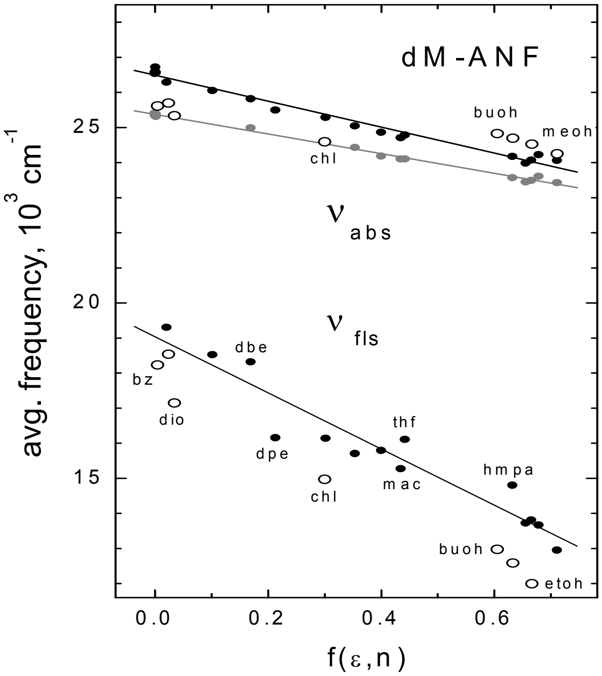

Figure 5.2.3.1-3 Average frequency of dM-ANF steady-state absorption and emission bands in a range of solvents, as in figure 5.2.3.1-2. The peak absorption frequency from ref. CLP95 is shown for comparison (gray points and line).

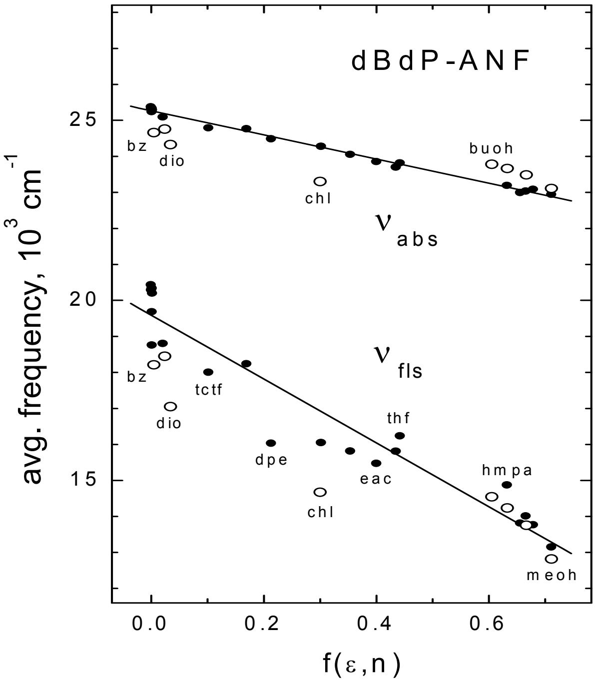

Figure 5.2.3.1-4 Average frequency of dBdP-ANF steady-state absorption and emission bands in a range of solvents, as in figure 5.2.3.1-2.

factor $F(\varepsilon,n)=(\varepsilon-1)/(\varepsilon+2)-(n^2-1)/(n^2+2)$. It should be noted that the reaction field factor has various forms depending on how solute polarizability and dispersion terms are treated. Here we take the form recommended when their contributions are minor [HGP95]. Even though the various factors are highly correlated, their values may differ by > 2, which must be remembered when dipole moments are inferred. Average frequencies are higher because the $S_0 \rightarrow S_1$ absorption band tails towards the blue (*cf.* figure 5.2.3.1-3); the corresponding values from our measurements are entered as black dots and circles. The dots represent all regular solvents, *i.e.* those which can not donate H–bonds and are not multipolar at first order. These points were used to calculate the regression line:

$$\left\langle \tilde{\nu}^{\mathrm{abs\,dMANF}}_{\mathrm{regular}} \right\rangle + \Delta(n) = (26300 \pm 60) - (3330 \pm 130)\,F(\varepsilon,n) \qquad 5.14$$

In the gas phase the extrapolated average for dM-ANF absorption oscillator distribution (*cf.* 5.2.3.1-3) is 29060±500 cm^{-1}; the peak lies 1270 cm^{-1} below at 27780 cm^{-1}. By comparison, Catalan *et al* report 28230 cm^{-1} for the peak absorption in the gas phase. The systematic difference stems from the sensitivity to dispersion, which is slightly smaller when the average frequency is considered rather than the peak frequency. In *2mb* our absorption maximum at 25345 cm^{-1} (calculated from $\tilde{\nu}\, g^{\mathrm{dMANF}}_{2\mathrm{mb}}(\tilde{\nu})$) agrees to 42 cm^{-1} or 0.6 nm with their value. The small deviation comes from our lognormal description which is not perfect for the peak region of a well-defined vibronic band. However this is not essential for the main observation: peak and average shift somewhat differently with increasing polar solvation because the spectrum is transformed from an asymmetrical Franck-Condon progression into a broad lognormal or even Gaussian shape. This can be seen from the different slopes for the two absorption descriptions in figure 5.2.3.1-3.

The fluorescence spectra of dM-ANF are discussed next. The strong dependence of emission frequency on solvent polarity has been explored before [CPL95]. The new aspect here is that the shape of the emission oscillator distribution is also charted (given in the appendix 10.4). Even among the regular solvents, the deviations of the average emission frequency from their regression line are substantial. The regression is

$$\left\langle \tilde{\nu}^{\mathrm{fls\,dMANF}}_{\mathrm{regular}} \right\rangle + \Delta(\mathrm{n}) = (19030 \pm 320) - (7990 \pm 770)\,\mathrm{F}(\varepsilon,\mathrm{n}) \qquad 5.15$$

The pattern of deviations is identical for all three chromophores; for example in tetrahydrofuran (THF) the Stokes shift is always less than expected. Because polar solvation in THF is fast (0.94 ps)[HGP95] compared to the dM-ANF fluorescence lifetime, incomplete relaxation can not be the reason for this irregularity. Possibly the large dipole field in the excited state (see below) causes deviations from linear response in the excited state. The regression parameters for all three dyes are collected in Table 5.3.

Table 5.3 Parameters obtained from the solvatochromic regression analysis.

Dyes	$\left\langle \tilde{\nu}^{\mathrm{abs}} \right\rangle + \Delta(\mathrm{n}) =$	$\left\langle \tilde{\nu}^{\mathrm{fls}} \right\rangle + \Delta(\mathrm{n}) =$
ANF	$(28000 \pm 150) - (4880 \pm 400)\,\mathrm{f}(\varepsilon,\mathrm{n})$	$(19630 \pm 320) - (7560 \pm 660)\,\mathrm{f}(\varepsilon,\mathrm{n})$
dM-ANF	$(26300 \pm 60) - (3330 \pm 130)\,\mathrm{f}(\varepsilon,\mathrm{n})$	$(19030 \pm 320) - (7990 \pm 770)\,\mathrm{f}(\varepsilon,\mathrm{n})$
dBdP-ANF	$(25270 \pm 25) - (3355 \pm 60)\,\mathrm{f}(\varepsilon,\mathrm{n})$	$(19590 \pm 230) - (8870 \pm 590)\,\mathrm{f}(\varepsilon,\mathrm{n})$

5.2.3.3 Broadening and shift

It is interesting to compare broadening $\tilde{\sigma}$ to absorption shift $\Delta\tilde{\nu}^{\mathrm{abs}}$ as the solute is transferred from 2-methylbutane to a polar solvent. Linear response of solvation implies

$$\frac{\tilde{\sigma}^2}{\mathrm{k_B T / hc}} = 2\,\Delta\tilde{\nu}^{\mathrm{abs}} \qquad 5.16$$

where $\mathrm{k_B T}$ is the thermal energy, h Planck's constant, and c the light velocity. This relationship was first demonstrated for the well-known dye Coumarin 153 [HGP95], in which case the full dynamic Stokes shift was used in place of $2\Delta\tilde{\nu}^{\mathrm{abs}}$. Figure 5.2.3.3-1 shows the quantity on the *l.h.s.* of eqn. (5.16) plotted against $\Delta\tilde{\nu}^{\mathrm{abs}}$ for our three amino-nitro-fluorenes in the "regular" solvents. The slope of a regression line through the origin is 1.95 ± 0.07, thus confirming the validity of linear response in the electronic ground state, even though the correlation (R = 0.85) is not as strict as with C153 (R = 0.95).

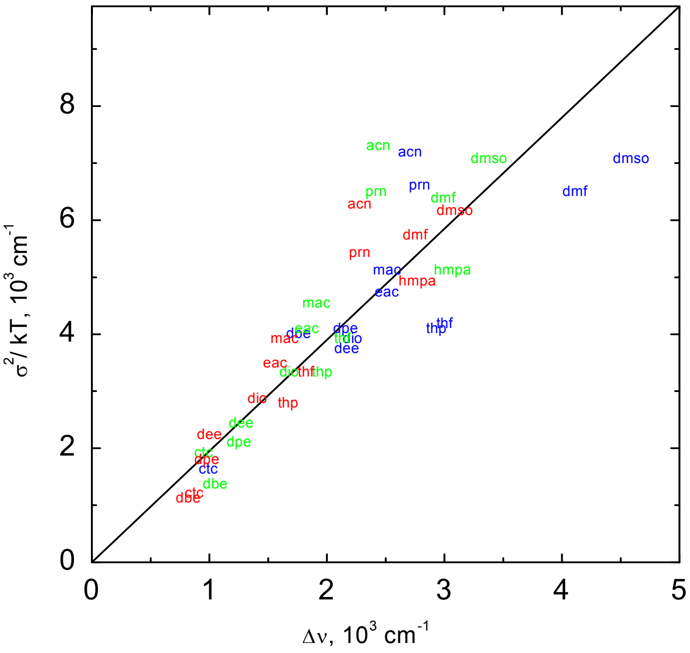

Figure 5.2.3.3-1 Test of the linear response relationship between the absorption shift $\Delta\tilde{\nu}^{abs}$ upon transfer from 2-methylbutane to a solvent, and the corresponding Gaussian broadening $\tilde{\sigma}$ (see text). ANF – blue, dM-ANF – red, dBdP-ANF – green.

Finally for this section, the dipole moment change $\Delta\mu$ upon $S_0 \rightarrow S_1$ excitation is estimated in the context of simple continuum theory, from

$$\frac{d}{dF}\left(\left\langle\tilde{\nu}^{abs}\right\rangle - \left\langle\tilde{\nu}^{fls}\right\rangle\right) = \frac{2(\Delta\mu)^2}{hca^3} \tag{5.17}$$

The quantity on the *l.h.s.* is determined to 4664±650 cm^{-1} from the data of dM-ANF, which we take to be applicable to ANF also. The Connolly excluded-solvent volume of the ANF chromophore is calculated to be V = 170 Å^3 and the corresponding spherical radius becomes 3.5 Å. General experience with molecular dynamics simulations suggest an empirical correction factor 1.5 [HGP95] so that a ≈ 5.2 Å, hence $\Delta\mu$ = 8 ± 0.6 D (Note that with $F(\varepsilon,n) = (\varepsilon-1)/(2\varepsilon+1) - (n^2-1)/(2n^2+1)$ one finds $\Delta\mu \approx 13$ D). The dipole moment for the ground state was calculated by us to be $\mu_0 = 7.8$ D. With these estimates at hand, it is instructive to visualize the various electrostatic contributions to the free energy which are involved in the stationary absorption or fluorescence process (eqns. 5.10, 5.11, figure. 5.2.3.3-2).

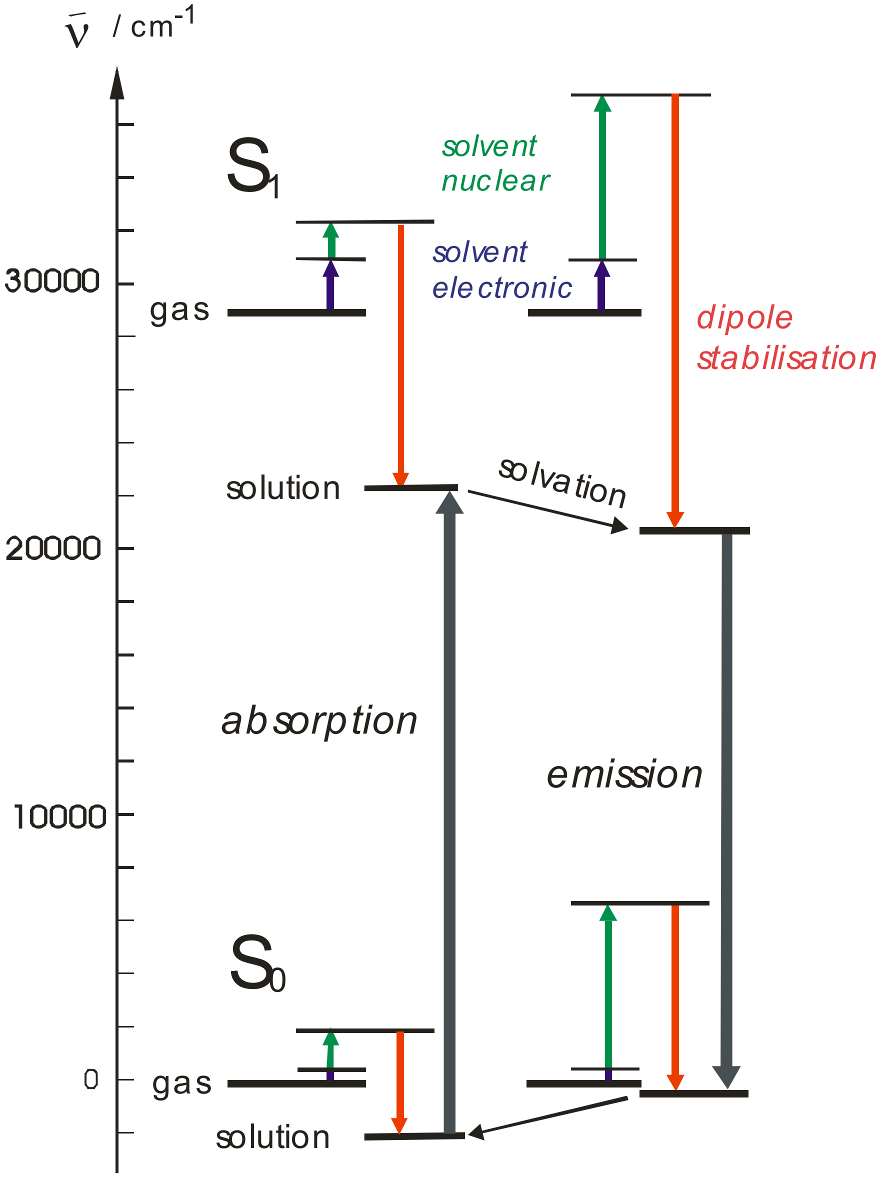

Figure 5.2.3.3-2 Electrostatic contributions to the free energy which are involved in the stationary absorption or fluorescence process. For this qualitative illustration of simple continuum theory, ANF in acetonitrile is assumed to have a dipole moment change $\Delta\mu = 8$ D.

5.3 Preferential solvation

5.3.1 by NMR

^{1}H NMR spectroscopy may also be used to monitor solvation. The chemical shifts of amino protons in ANF are shown in figure 5.3.1-1 (solid dots) where the results from CD_3CN / H_2O and $(CD_3)_2SO$ / H_2O solvent mixtures are combined. When the water volume fraction (V_w) in CD_3CN / H_2O mixture is increased from 0 to 0.1, the chemical shift moves from $\delta H_{(N)} = 5.1205$ to 5.1908 ppm; it then turns around and decreases with higher V_w. The other protons in ANF move upfield, *i.e.* to smaller chemical shifts, with increasing V_w in a perfectly linear manner. This is shown for the low-field line of the $\delta H_{(C5)}$ doublet (proton of the 5th carbon atom in the ANF moiety is presented as circles; data were shifted for this representation). In $(CD_3)_2SO$ / H_2O the behaviour is qualitatively different as can be seen in the lower portion of the figure. Now the amino protons move monotonously upfield with V_w. The slope is greater than for the reference $\delta H_{(C5)}$ line initially, and it increases with V_w. NMR data were drawn so that they can be directly compared with the optical results from the aqueous solvent mixtures (figure 5.3.2). The chemical shift of the other protons of ANF *vs* volume fraction of water in both deuterated aqueous solvent mixtures are given in the appendix 10.7 and 10.8.

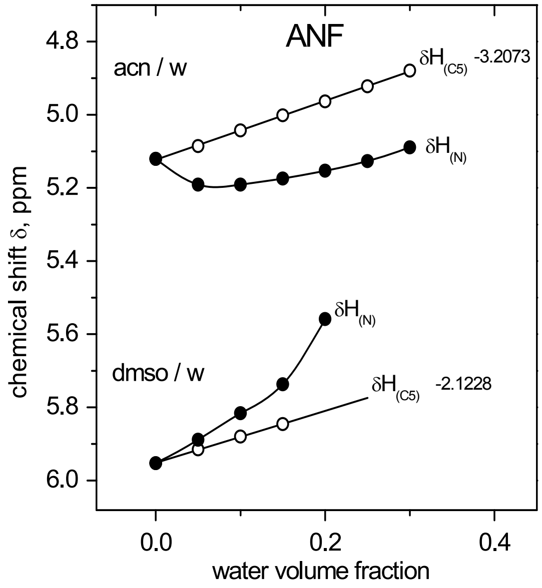

Figure 5.3.1-1 ^{1}H-NMR chemical shift $\delta H_{(N)}$ of amino protons in ANF as function of water volume fraction in CD_3CN and $(CD_3)_2SO$. In either solution, the behaviour of a $\delta H_{(C5)}$ resonance is shown for comparison.

5.3.2 by optical absorption

Aqueous solvent mixtures may help to understand how a chromophore will function in a biopolymer. For example in DNA oligonucleotides (*cf.* figure 6.1-3 in solvation section) the ANF molecule is not accessible by water when it is perfectly stacked between neighbouring base pairs, but it should be solvated partially when it is hinged around the sugar-phosphodiester backbone. In this case solvation is microheterogeneous, with strongly bound water in the minor groove close to the amino tail and bulk-like water near the nitro head [PZ004]. Similar situations may also arise upon preferential solvation of ANF and its derivatives in solvent mixtures. Hints of such effects may be seen in the unusual retention of the fluorenes in liquid chromatography [ME0_ _]. To mimick partial or preferential solvation in DNA, we therefore studied the solvatochromism in several mixtures.

Hydrogen bonding and preferential solvation were studied by measuring the absorption band in solvent mixtures as a function of composition. The results are shown in figures 5.3.2-1 and -2. For example ANF has a mean absorption at 25500 cm^{-1} in acetonitrile (ACN) which is a weak H-bond acceptor, and at 23620 cm^{-1} in dimethyl sulfoxide (DMSO) which can accept H-bonds from the amino group. The red-shift is explained as follows. In the excited state, electron density on the amino group is reduced because of intramolecular charge transfer to the nitro group, thereby strengthening the H–bond relative to the ground state. As net result, the absorption band is therefore observed at lower energy when compared to solution in ACN, even when the change of polarity and polarizability of the solvent is taken into account. In more detailed experiments the fraction of the second solvent component is increased gradually and the corresponding small absorption shift is noted. (for example green line in figure (5.3.2-1). In ideal mixtures the optical properties of a solute depend linearly on volume fraction V_x of the second component [TDB94, VS098], which is therefore generally adopted as a measure for the composition. The results from such experiments, however, are best represented after dispersive contributions to the shift have been factored out, and for this reason they

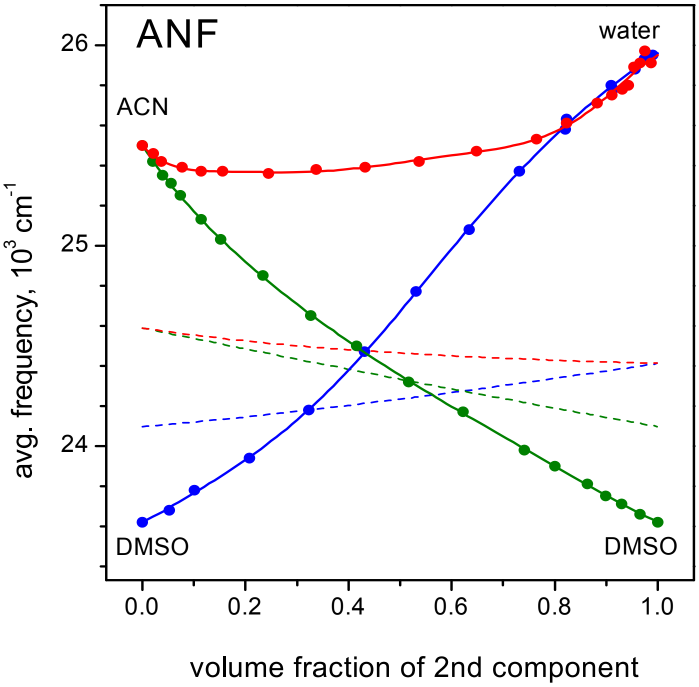

Figure 5.3.2-1 Average frequency of the steady-state absorption band of ANF in solvent mixtures, as function of volume fraction of the second component. Dashed lines connect the points for the pure solvents, as expected from the solvatochromic regression analysis.

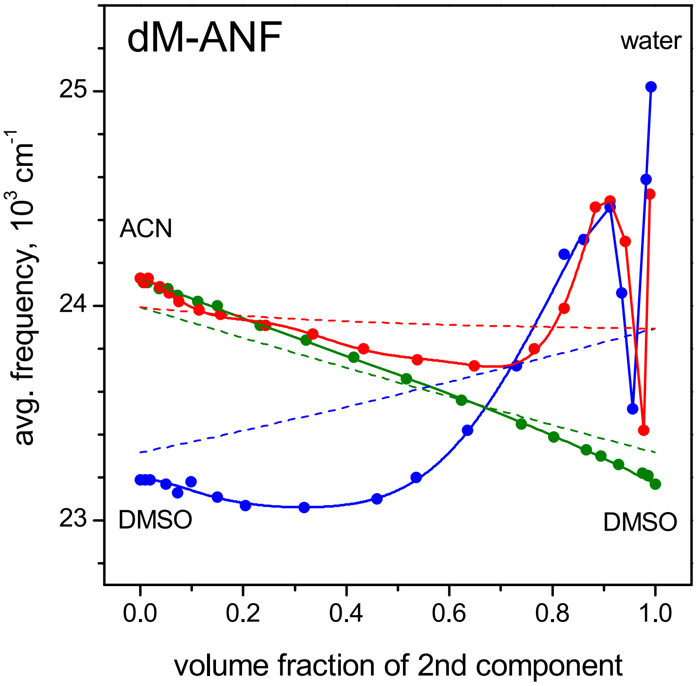

Figure 5.3.2-2 Average frequency of the steady-state absorption band of dM-ANF in solvent mixtures, as in figure 5.3.2-1. Dashed lines connect the points for the pure solvents, as expected from the solvatochromic regression analysis. The unusual excursion to the red near water rich region corresponds to the unbalanced formation of clusters by cosolvent around one end of the solute, or to the formation of solute dimers.

will be shown (figure 5.3.2-1 and -2) after the discussion of solvatochromism in pure solvents. Figure (5.3.2-1 and -2) shows the average absorption frequency ANF and dM-ANF as function of the volume fraction V_x of the second component. The mixtures were ACN/water (red dots and solid red line), DMSO/water (blue), and ACN/DMSO (green). Dashed lines connect the points at $V_x = 0$ and $V_x = 1$ which can be read off the absorption regression lines in figure 5.3.2-1 and 5.3.2-2, respectively, for the pure solvents. They represent the expected frequencies when only unspecific solvation is active (through solvent polarity and polarizibility) according to simple continuum theory. For the interpolation it was assumed that ε and n change linearly with V_x.

The behavior of dM-ANF in figure. 5.3.2-2 is discussed first, and for a start we consider the ACN/DMSO series (green). Dimethyl sulfoxide is slightly less polar ($F(\varepsilon,n) = 0.656$) than acetonitrile (0.711) and for this reason the absorption band should shift to higher frequencies by about 180 cm^{-1} as V_{DMSO} is increased from 0 to 1. But at the same time n increases from 1.341 to 1.477 and the net expected change becomes -680 cm^{-1} (dashed green line). The observed frequency falls initially above the expected line and then goes below. Hydrogen bonds can not be formed between dM-ANF and DMSO; therefore the systematic deviations of ± 90 cm^{-1} must be ascribed to molecularity of solvation [MF087] which can not be captured by a continuum model.

When water ($F(\varepsilon,n) = 0.757$) is added to ACN, simple theory predicts a small linear decrease of the absorption frequency (dashed red line), mainly because of the polarity change in this case. The observed absorption frequency (solid red dots and line) first moves gradually more to the red, reaches a minimum at $V_w = 0.69$, then turns around and moves to the blue by more than 1300 cm^{-1} in the end. In DMSO/ water (blue) similar behavior is seen. One possibility to consider is preferential solvation [A0002], for example retention of methyl-containing solvent molecules near the hydrophobic solute in excess of the bulk fraction ($1-V_w$). Preferential solvation is usually conceived as an enrichment of one component over the other in the first few solvent shells, *i.e.* in terms of radial distribution only. It leads to an effective frequency which falls between those for the pure solvents. The initial slope should therefore be positive or zero, as for example if

DMSO were completely retained. The observed small decrease in DMSO / water as V_w is raised to 0.4 is still consistent with this view, since the deviation (100 cm^{-1}) is of the same size which earlier had to be ascribed to molecularity.

At the other end a water-rich mixture has ACN or DMSO as cosolvents. The strong blue shift as $V_w \rightarrow 1$ must be explained by weakened interaction in the excited state. The only mode available for this is a donated H–bond to the dimethyl amino group. Upon $S_0 \rightarrow S_1$ excitation, electronic charge is drawn from the amino group and the interaction strength thereby reduced.

The most interesting feature is a narrow frequency dip as methyl-containing cosolvent is added to a solution of dM-ANF in (nearly) pure water. The compositional range was scanned in finer steps with DMSO/water (not shown) and the maximal effect is located around $V_w \approx 0.94$, corresponding to a DMSO mole fraction of 0.016. Figure 5.3.2-3 shows the absorption band at this composition. Compared to solution in pure DMSO, the distribution of oscillator strength at $V_w \approx 0.94$ has opposite asymmetry, i.e. it slopes towards the red. Thus a significant contribution to the oscillator strength comes from molecules which absorb at lower frequencies than in pure DMSO. Here, the background due to Mie scattering of remaining particles could not be fully controlled in these experiments. This is why the absorption center frequency in this region is determined only approximately, and quantitative analysis must be deferred. At this stage we can only speculate on the underlying cause of the narrow frequency dip which is also seen in ACN/water but at slightly different composition. Two possibilites are (i) preferential solvation, not only regarding the radial distribution but also distinguishing between the dimethyl amino and nitro caps of the molecule [J0086] and (ii) dimer formation [HMT96]. In either case, multiple equilibria between single dM-ANF molecules, water, and cosolvent must be involved which are controlled by the thermodynamic properties of the bulk solvent mixture. The two aqueous solvent systems are interesting because the cosolvent disrupts the hydrogen-bonded water network [GH070, ÖV006]. This is indicated by unusual thermodynamic properties. For example, dilute dimethyl sulphoxide in water contracts its partial molar volume to 96% of pure dmso and has strongly negative excess entropy of mixing, in partial molar terms $\partial(TS^E)/\partial x'_{DMSO}$ = -12.68 kJ/mol [M0002]. Taken together it follows that differently absorbing species may depend highly nonlinearly on solvent composition, allowing for the observation of sharp absorption features when varying $V_w \approx 1$.

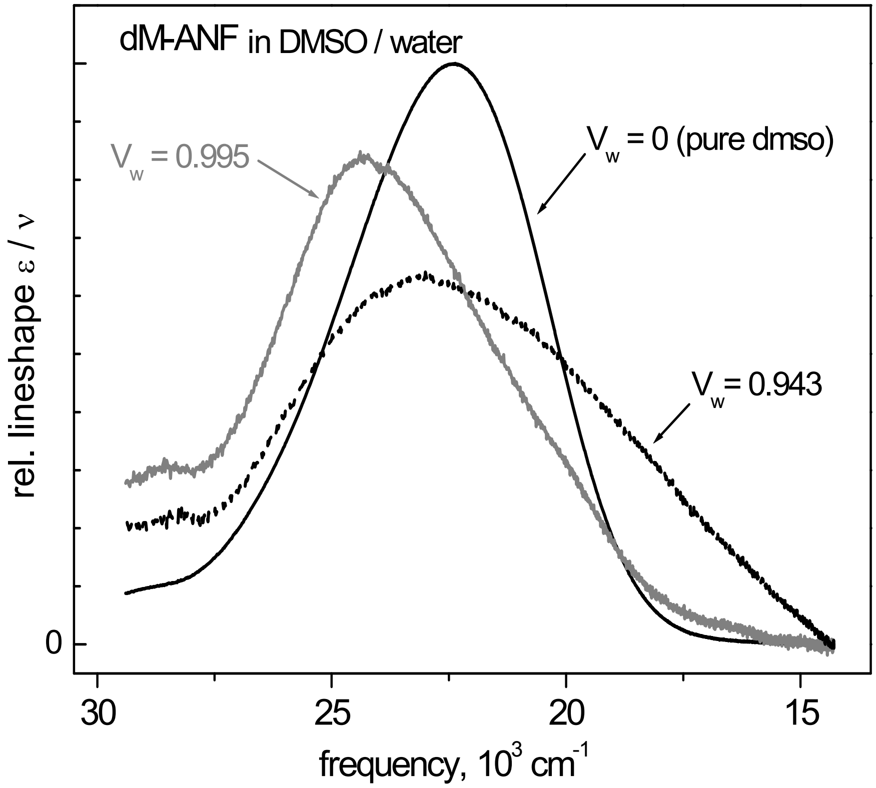

Figure 5.3.2-3 Aqueous dM-ANF absorption with dmso cosolvent. In a sharp compositional region around volume fraction $V_w \approx 0.94$ (dashed line), an absorption contribution appears to the red of band in pure dmso, probably due to preferential solvation or dimer formation.

5.4 Fluorescence lifetimes of ANF derivatives

The fluorescence lifetimes of ANF, dM-ANF and Ri-ANF were measured with a time-correlated single-photon counting spectrometer as described in the experimental section 3.4. Different solvents were used: acetonitrile (ACN), methanol (MeOH), dimethyl sulfoxide (DMSO), ethyl aceatete (EA), 1,4-dioxane, Diethyl ether (DEE), carbon tetrachloride (CCl_4), cyclohexane (CHex) and 2-methyl butane (2mb). The chromophores were excited at 387 nm with an average power of 20.3 mW at a repetition rate of 81 MHz. Fluorescence decays were fit with a biexponential function for solutions in CHex, CCl_4 and 2mb, and to a monoexponential otherwise, and the corresponding χ^2 value was ≤ 1.2. A representative measurement (ANF in ethyl acetate) with fit is shown in figure 5.4-1. The upper panel a shows the measured instrument response function (green), the sample decay (black) and the fitted decay (red). The fluorescence lifetime is found to be 1.7 ns. The residual trace in panel b demonstrates the quality of this fit, which has χ^2 of 1.11. Results are given in appendix 10.9. The lifetime of dM-ANF is longer than that of ANF in all solvents. The lifetime of all the three compounds is very short in ACN, DMSO and MeOH, < 50 ps and practically immeasurable by photon counting. On the other side, lifetimes in ethyl acetate and 1,4-dioxane are relatively long, in the range of 2.5 ns. The fluorescence lifetime parallels the observations which were made by transient absorption.

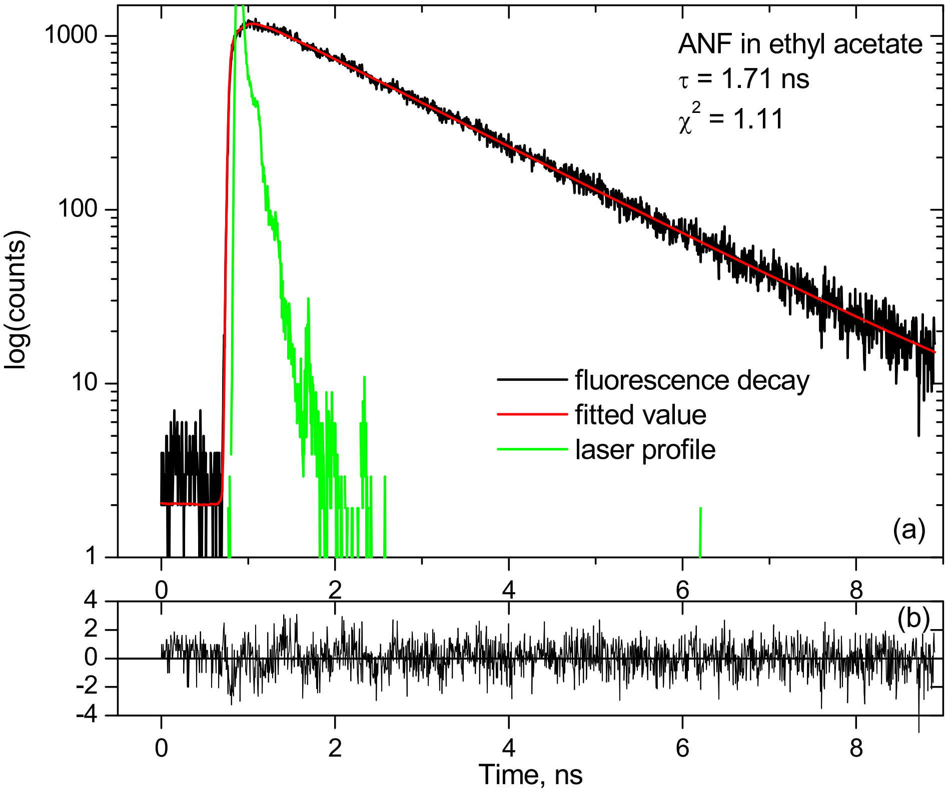

Figure 5.4-1 The upper panel a shows the measured fluorescence decay from ANF in ethyl acetate (black), the instrument response function (green), and the fitted decay (red). The residual trace in panel b represent demonstrates the quality of the fit.

5.5 Solubility of the ANF in aqueous solvent mixtures

A saturated solution of ANF was prepared in an acetonitrile (ACN) / water (W) mixture of various compositions, by adding excess of solid ANF at ambient temperature (21°C). The composition of the mixture ranged from 0% to 99% of water by weight. The excess of solid was then removed by centrifugation and the absorption spectrum of the solution was measured. For lower concentrations we used a cell of 10 cm path length while for higher concentrations a 1mm cell was used. The weight fraction is converted into volume fraction with the help of the excess molar volume [M0002]. Figure 5.5-1 shows a plot of the concentration *vs* volume fraction of water.

Let us consider the standard Gibbs energy change $\Delta G^0_{\mathrm{dissolv}}$ upon transferring the ANF molecule from its standard state in the solid (S) to its standard state in an aqueous solvent (W)[B0082]. We have from elementary considerations

$$\Delta G_{\mathrm{dissolv}}{}^0 = -\mathrm{RT}\ln\{f_c C\} \qquad 5.18$$

where C is the ANF concentration and f_c is the associated activity coefficient. We standardize at infinite dilution ($C \to 0$) and treat $f_c = 1$ throughout. Therefore the change of the Gibbs energy upon dissolving into the mixture (writing C_{sat} for the concentration in equilibrium) is

$$\Delta G^0_{\mathrm{dissolv}} = -\mathrm{R\,T}\ln(C_{sat}) \qquad 5.19$$

The dependence of $\Delta G^0_{\mathrm{dissolv}}$ on the volume fraction of water V_W is shown in figure 5.5-2. There seems to be a linear region from $V_w = 0$ to ~0.3, after which a nonlinear range is entered. There aforementioned microheterogeneity is expected. This was cross checked with the shape and width of the absorption spectra in this region, which is described in the preferential solvation section. The value of absorbance, concentration and change of free energy of the ANF for the corresponding volume fraction of water are given in table 5.4.

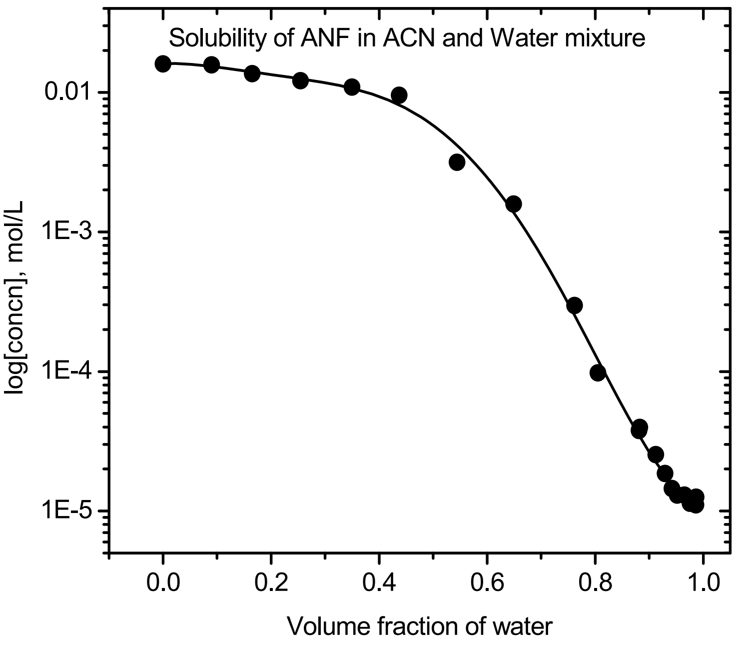

Figure 5.5-1 The plot of concentration of dissolved ANF_{satd} in ACN/W mixture *vs* volume fraction of water.

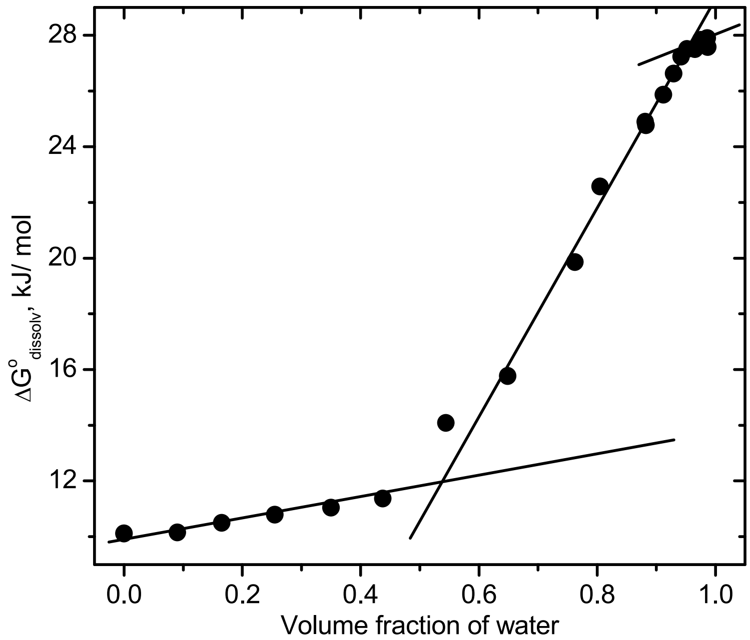

Figure 5.5-2 The change of Gibbs free energy (ΔG^0) for transferring ANF from ACN to water. After linear behavior in the range of water volume fraction $V_W = 0–0.3$, nonlinear change may indicate the onset of micro heterogeneity.

Table 5.4 The absorbance, concentration of dissolved ANF and Gibbs free energy in ACN/W mixture are given.

Volume fraction of water (V_w)	Absorbance of ANF_{satd} /cm	Concentration mol/L	ΔG_t^0 kJ/mol
0.0000	293.745	0.01599	10.1093
0.0901	288.855	0.01572	10.1504
0.1653	250.320	0.01363	10.5003
0.2547	222.865	0.01213	10.7843
0.3499	200.735	0.01093	11.0399
0.4375	175.315	0.00954	11.3709
0.5442	57.84 0	0.00315	14.0814
0.6489	29.065	0.00158	15.7634
0.7622	5.447	0.0002965	19.8562
0.8050	1.793	0.0000976	22.5712
0.8813	0.694	0.0000377	24.8918
0.9419	0.266	0.0000144	27.2345
0.9863	0.203	0.0000110	27.8930

5.6 Temperature studies of ANF

Absorption spectra of ANF were measured in acetonitrile (ACN) and water(W) mixtures at different temperatures. Proportions of 8%, 4%, 3%, 2% and 1% of ACN in W were prepared by weight. The temperature ranged from 20° to 50° by increments of 5° C. Since ANF is hydrophobic, measurement was started with the 1% ACN/W mixture. The sample compartment and path lengths were described in the experimental section 3.1.1. The solution was always in equilibrium with solid ANF at the same temperature (equilibration took more than 30 min). Since the solubility of ANF increases with temperature, the absorbance increases correspondingly. The same is observed when increasing the acetonitrile fraction. For comparison, absorption spectra of ANF in 4 % and 1 % of ACN/W at different temperature are shown in figures figure 5.6-1 and figure 5.6-2, respectively.

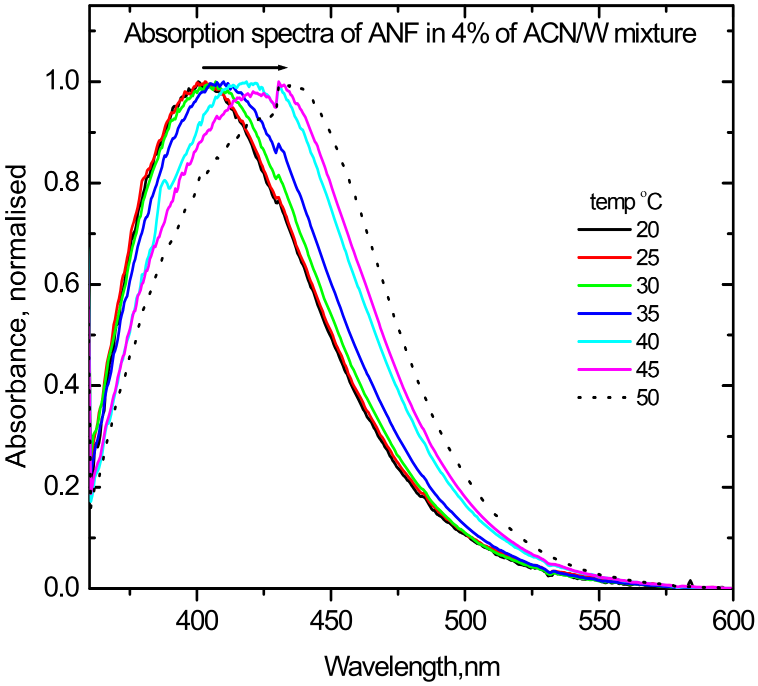

Figure 5.6-1 Normalized absorption spectra of ANF in 4% (by partial volume) of ACN/W mixture at different temperature. A red shift of absorption and increased broadening are observed with increasing temperature. Various temperatures are shown in different colour from 20° to 50°C (Since maximum absorbance is noted to calculate the concentration of dissolved ANF, dip at 425 nm does not affect our ΔH value).

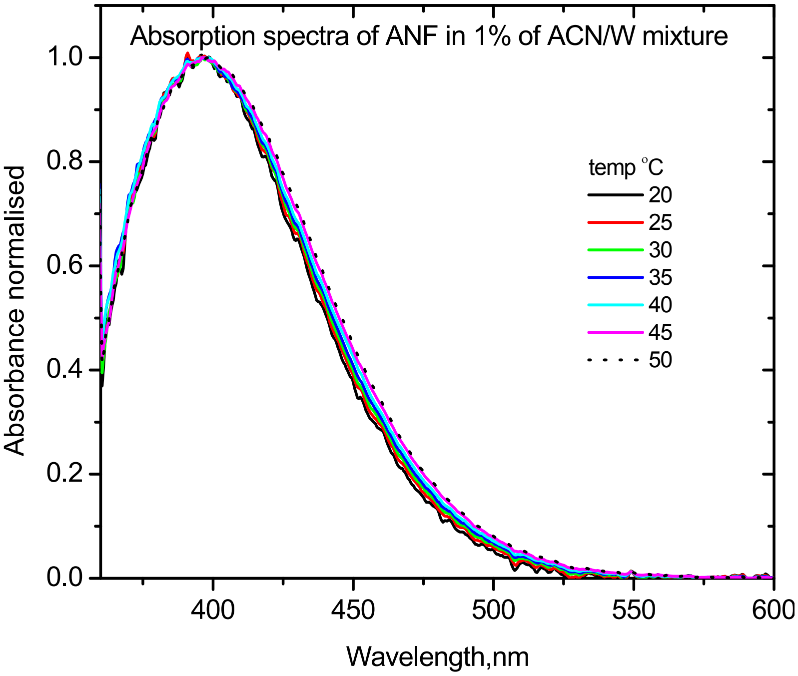

Figure 5.6-2 Normalized absorption spectra of ANF in 1% of ACN/W mixture at different temperatures as shown in figure 5.6-1. Red shift and broadening are less pronounced with increasing temperature.

Upon increasing temperature, the absorption shifts from 402 nm to the red and broadens. This effect is clearly seen in 3% and 4% of acetonitrile, where the shift goes to 430 nm, whereas shift and broadening are less pronounced in the 1% and 2% ACN mixtures.

The transfer of ANF from the solid into the liquid can be described by considering the equilibrium $\mathrm{ANF_s} \overset{\mathrm{K_{eq}}}{\Leftrightarrow} \mathrm{ANF_l}$. The standard Gibbs free energy change of solvation, ΔG°, is given by $\Delta G^\circ = -\mathrm{R\,T} \ln \mathrm{K_{eq}}$. The solvation Gibbs energy relates to the change in enthalpy and entropy through $\Delta G^\circ = \Delta H^\circ - T\Delta S^\circ$. Combining the two equations we have

$$\ln \mathrm{K_{eq}} = -\frac{\Delta H^\circ}{R}\left(\frac{1}{T}\right) + \frac{\Delta S^\circ}{R} \qquad 5.20$$

$\mathrm{K_{eq}}$ is given by $\mathrm{K_{eq}} = \frac{[\mathrm{ANF_l}]}{[\mathrm{ANF_s}]}$. Since $[\mathrm{ANF_s}]$ is constant, $\mathrm{K_{eq}}$ is determined by $[\mathrm{ANF_l}]$ alone, which in turn is obtained from the absorption of the solution using Beer's law, $[\mathrm{ANF_l}] = \frac{A}{\varepsilon\ l}$. Therefore, enthalpy and entropy of solvation are obtained from a plot of $\ln[\mathrm{ANF_l}]$ vs $\left(\frac{1}{T}\right)$ by linear regression. A representative plot, of ANF in 3% ACN, is shown in figure 5.6-3 below. Values of solvation enthalpy, entropy, and standard Gibbs free energy are given in the following table 5.5.

With decreasing ACN fraction, the enthalpy of solvation increases whereas its entropy decreases. The values are plotted against the weight of water separately and shown in the following figure 5.6-4 and -5. In general the Gibbs solvation energy increases with increasing water concentration; therefore the solvation equilibrium is strongly moved to the left by water. But ΔG^0 deviates from this trend at 4% of acetonitrile in water, which points to some special effect at this composition. Note that with dM-ANF a strong red shift of the absorption spectrum is observed near this composition even at room temperature (*cf.* preferential solvation section 5.3). The solvation entropy of ANF is more negative in this range when compared to mixtures with higher ACN content. We can only speculate

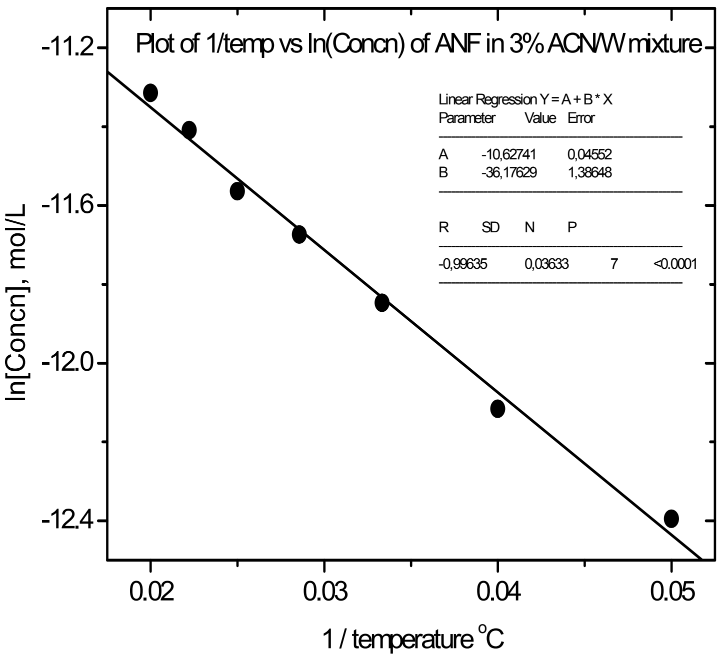

Figure 5.6-3 Solvation enthalpy and entropy are obtained by fitting the plot of logarithmic concentration of ANF *vs* inverse temperature. For example, experimental data are shown for a 3% ACN/W mixture.

Table 5.5 Change in enthalpy and entropy solvation of ANF are given for volume fraction of ACN. Enthalpy of solvation increases and entropy decreases with decreasing V_{ACN}

Volume fraction of ACN, V_{ACN}	Enthalpy of solvation (ΔH°) kJ.mol^{-1}	Entropy of solvation (ΔS°) J. K^{-1}.mol^{-1}	Std.Gibbs free energy (ΔG°) kJ.mol^{-1}
8.007	276.3882 ± 12.58	-85.8136 ± 0.40	301.9606
4.005	270.0575 ± 13.77	-88.5699 ± 0.44	296.4505
3.002	300.7696 ± 11.52	-88.3562 ± 0.37	327.0997
2.014	382.9723 ± 31.31	-88.1234 ± 1.02	409.2330
1.017	417.5930 ± 25.57	-88.2551 ± 0.83	443.8930

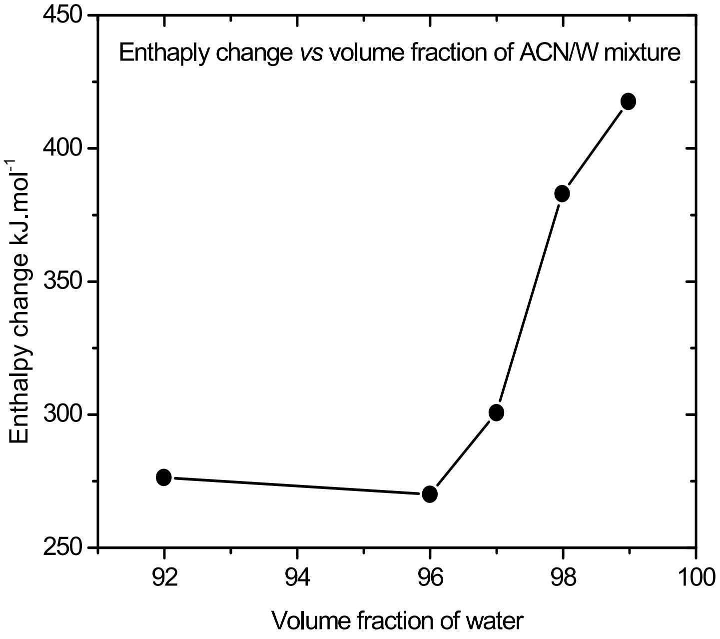

Figure 5.6-4 Solvation enthalpy of ANF *vs* volume fraction of water. Increase with water content reflects that the solvation equilibrium moves towards the solid by adding water.

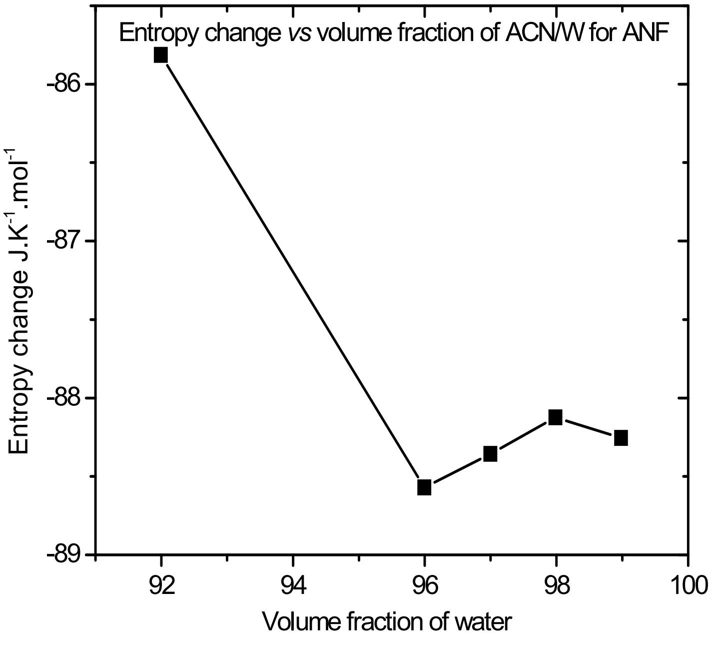

Figure 5.6-5 Solvation entropy *vs* volume fraction of water. It decreases with the water fraction and is more negative at 4% ACN. This suggests that clusters of the co-solvent are formed, or dimer of the solute.

about the reasons here, and this is done with the help of figures 5.6-6 and 5.6-7. Figure 5.6-6 shows the solvation of ACN in water. Large clusters can be formed when the ACN mole fraction is about 4% or larger (left panel), whereas smaller clusters or possibly single acetonitrile molecules exist at lower ACN mole fractions [GH070]. Chains of water H-bonds are being broken when acetonitrile is added, and this is why the excess entropy of mixing is strongly negative, so that (in partial molar terms) $\partial(TS^E)/\partial x_{ACN} = -7.899$ kJ/mole at room temperature. Now imagine that ANF is introduced from the solid into the mixture (figure 5.6-7). The dye molecules are preferentially solvated by ACN. At 4% or more of ACN it can be surrounded completely by the organic cosolvent (left panel) and no additional H-bonds need be broken. At lower ACN content, however, preferential solvation may not cover the fluorene dye, parts of which make contact with water molecules. In this case additional water chains are broken, which shows up as more negative ΔS_{solv} for solvation.

5.7 Inclusion studies of 7-Nitro-9H-fluoren-2-ylamine-1’-deoxyriboside– Ri-ANF

Our aim is to follow the solvation dynamics of DNA, by probing the shift of the stimulated emission of ANF in water. In this context it is interesting to see the Transient Absorption Spectrum (TAS) of the corresponding nucleoside, *i.e.* ANF attached to 2-deoxy ribose (abbreviated Ri-ANF), and possibly of the nucleotide also. In this section we discuss Ri-ANF only. Unfortunately the solubility of Ri-ANF in water is low, with absorbance of 0.408 (λ_{max} = 392 nm) in 1 cm, which is not enough for femtosecond TAS. Therefore we tried to increase the solubility of Ri-ANF by using cyclodextrins (CD). The absorbance reaches 1.3117 with ß-CD in mM concentration. Still this is not high enough for fs TAS which needs an absorbance of about 0.6 in 0.4mm at the pump wavelength (400 nm). But we observe a large Stokes shift and an increase of fluorescence intensity. This motivated us to study the inclusion properties of the Ri-ANF with different CDs.

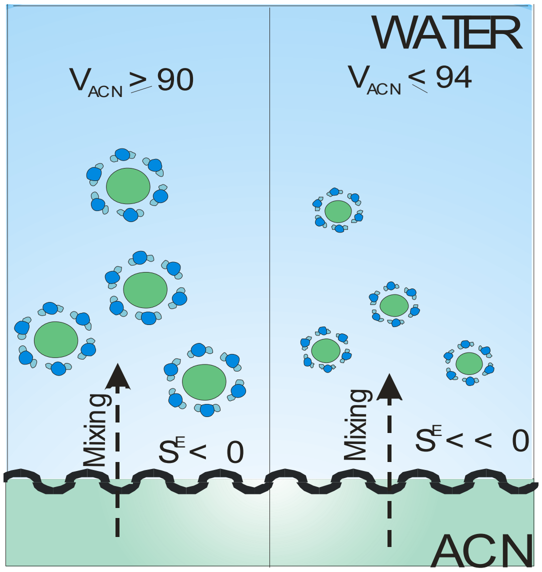

Figure 5.6-6 The transfer of ACN into water is illustrated here. ACN is indicated by green and water by blue colors. At $V_{ACN} \geq 90$, large clusters of ACN are formed and the excess entropy of mixing less than zero. At $V_{ACN} \leq 94$, smaller clusters are formed and entropy of mixing is more negative, since more chains of water H-bonds are being broken when the acetonitrile concentration is increased.

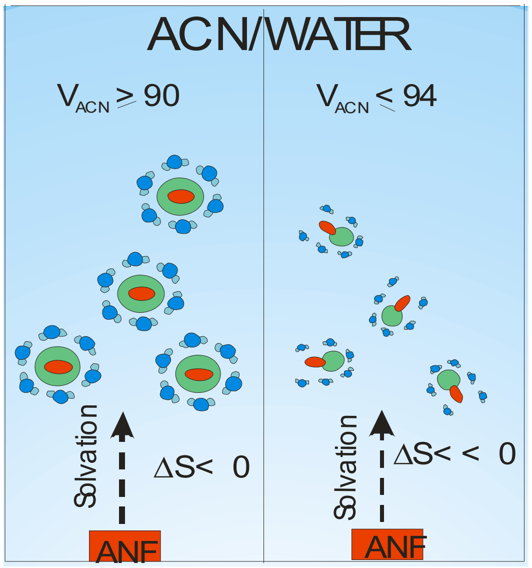

Figure 5.6-7 Transfer of ANF in ACN/W mixtures, as in Fig. 5.6-6. At $V_{ACN} \geq 90$, ANF is solvated preferentially and completely by acetonitrile clusters, hence no additional H-bonds need be broken. However at $V_{ACN} \leq 94$, the ANF molecule can not be completely solvated by acetonitrile clusters as they are too small. Therefore additional water chains must be destroyed which yields a more negative of entropy of solvation

5.7.1 Absorption and emission with different cyclodextrins (CD)

Inclusion studies of Ri-ANF were performed with three different CDs, viz α, ß,and γ cyclodextrins. The hydrophobic cavity diameters of α, ß, and γ -CD are 5.7 Å, 7.8 Å and 9.5 Å respectively [S0098]. The optimized configuration of Ri-ANF from semiempirical AM1 calculations is represented in figure 5.7.1-1. The whole molecule may be viewed as a cylindrical tube with diameter 7.3 Å and length 17.6 Å. By considering the sizes, it should be difficult for Ri-ANF to get in to the α-CD when compared to ß- and γ-CD. The absorption and emission spectra of Ri-ANF with the three cyclodextrins were measured, with the concentration of the CDs in the mmolar range and Ri-ANF saturated with excess of solid. Excess of solid is removed by centrifuge. The normalized absorption spectra and fluorescence spectra are shown in figure 5.7.1-2. The absorption maximum of Ri-ANF is shifted from 392 nm to ~ 405 nm in all CDs. Spectral broadening follows the order α > γ > ß. It should be noted that the oscillator strength of the UV band (with peak near 275 nm) increases when the inclusion complex is formed. The emission spectrum of Ri-ANF with ß-CD is red shifted from 537 to 749 nm with increasing intensity, but a shoulder at 537 remains. With γ-CD the red shift extends to 665 nm only and shows remarkable shoulder at 537 nm. In α-CD the emission is shifted to 706 nm and the 537 nm shoulder is not seen clearly. These observations are explained on the basis of CD cavity diameters and hydrophobic attraction.

First we will consider γ-CD. Since the cavity diameter of γ-CD is greater than the cylindrical diameter of Ri-ANF, the host molecule (-CD) has a possibility to form a loose (unbound) and/or tight (bound) complex with the guest molecule(-Ri-ANF) as shown in figure 5.7.1-3. This effect was already seen for *trans*-stilbene with ß-CD by N. J. Turro *et al* [DSE89] who found clear biexponential fluorescence decay. Our observations are supported by the fluorescence changes with increasing γ-CD concentration, as explained in next section. Therefore we assign the shoulder at 537 nm to free or loosely bound Ri-ANF and the red-shifted emission at 665 nm to the tight complex.

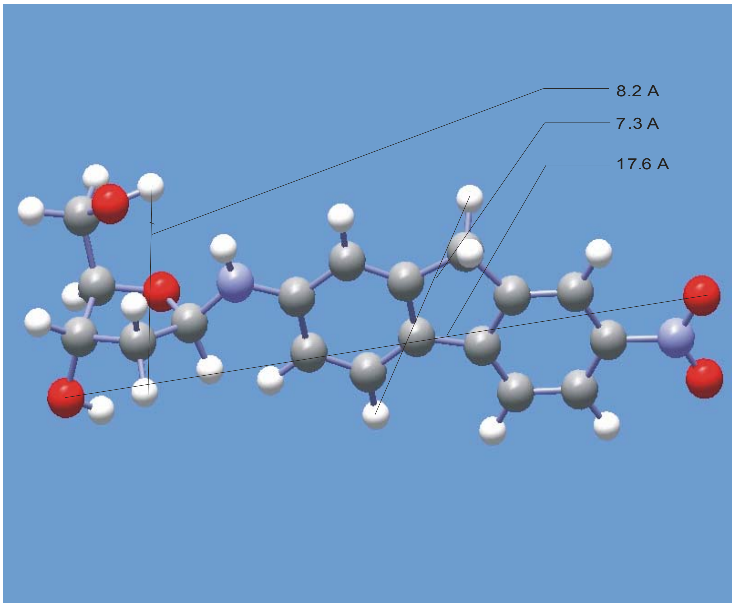

Figure 5.7.1-1 Optimized configuration of Ri-ANF from semiemprical AM1 calculation [FE0_ _]. Its outer shape can be approximated as a tube with diameter 7.3 Å and length 17.6Å.

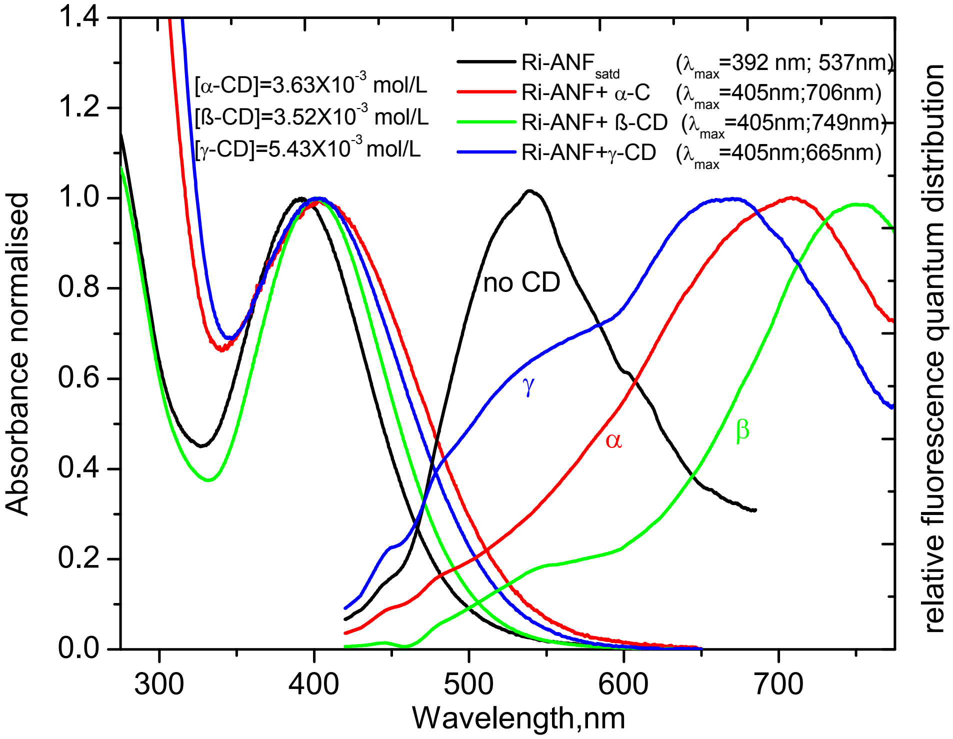

Figure 5.7.1-2 Absorption and fluorescence spectra of Ri-ANF(black) in three different cyclodextrins (CD), α–CD (red), ß-CD (green) and γ-CD (blue) respectively. Shifts are explained in the text.

There is competitive interaction between loose and bound complex with further increase of the CD concentration.

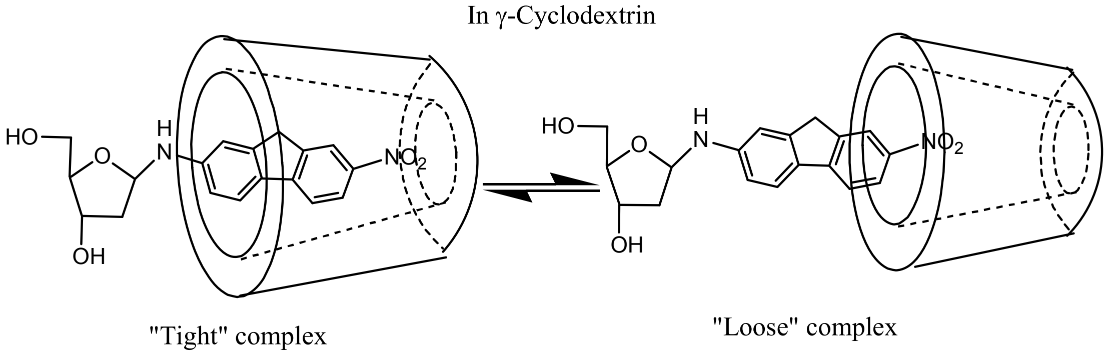

Figure 5.7.1-3 Illustration of the formation of a “tight complex” and “loose complex” of Ri-ANF in γ-CD.

In case of ß-CD, the cavity diameter and the diameter of Ri-ANF are nearly matched. The strong red shifted emission at 749 nm with increased fluorescence intensity are an indication of strong interaction. The shoulder at 537 nm is now weak, meaning that only few free or loosely bound complexes are formed. It follows that Ri-ANF forms a tight complex with ß-CD as in figure 5.7.1-4.

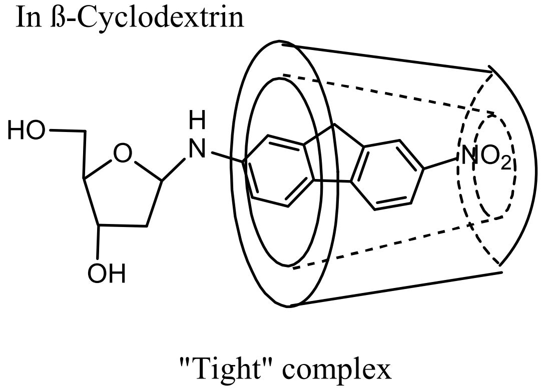

Figure 5.7.1-4 Illustration of the formation of the “tight complex” of Ri-ANF in ß-CD.

Finally we discuss α-CD which should not be wide enough to accommodate the ANF moiety. Even though, red shifted emission at 749 nm is observed, but not strongly. We assigned this shift mainly to hydrophobic interaction, and illustrated as figure 5.7.1-5, since the inner cavity of CD and ANF are hydrophobic in nature. A shoulder is not observed, implying that all chromophores have the same environment.

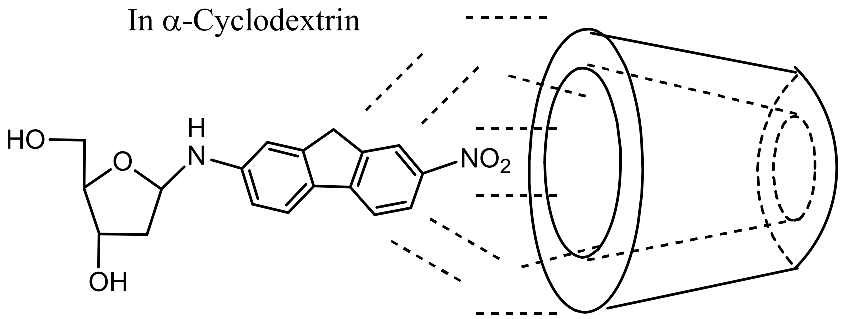

Figure 5.7.1-5 Illustration for the formation of a complex by the hydrophobic interaction of Ri-ANF with α-CD

5.7.2 Concentration effect of γ-cyclodextrin

Absorption and fluorescence spectra were measured for Ri-ANF with concentrations of γ-CD varying from 0.2 to 10 mM. The solubility of Ri-ANF in water is small, but it increases as γ-CD is added. First consider absorption spectra. For concentrations up to 0.5088 mM there is an increase of absorbance, very little broadening, and an absorption red shift. Further increase of concentration, absorption band shifts noticeably more to the red, until the peak reaches 412 nm. For lower concentrations an isosbestic point appears at 345 nm, showing the presence of two components. Thus there is an equilibrium between loose and tight complexes, and probably the 1:1 complex between Ri-ANF and γ-CD is formed. At higher concentration, the equilibrium seems to be shifted to the tight complex.

Next we discuss the fluorescence spectra measured at different concentrations of γ-CD. Since the fluorescence quantum yield of Ri-ANF is low and the sensitivity of our fluorimeter is weak in the near IR region, the red part of the spectra is more noisy. As the γ-CD concentration is increased to 0.5 mM, the fluorescence intensity at 532 nm increases, which shows the formation of the loose complex. Further increase shifts the fluorescence peak to 632 nm and the intensity increases even more. This confirms that the tight complex is being formed at higher concentrations.

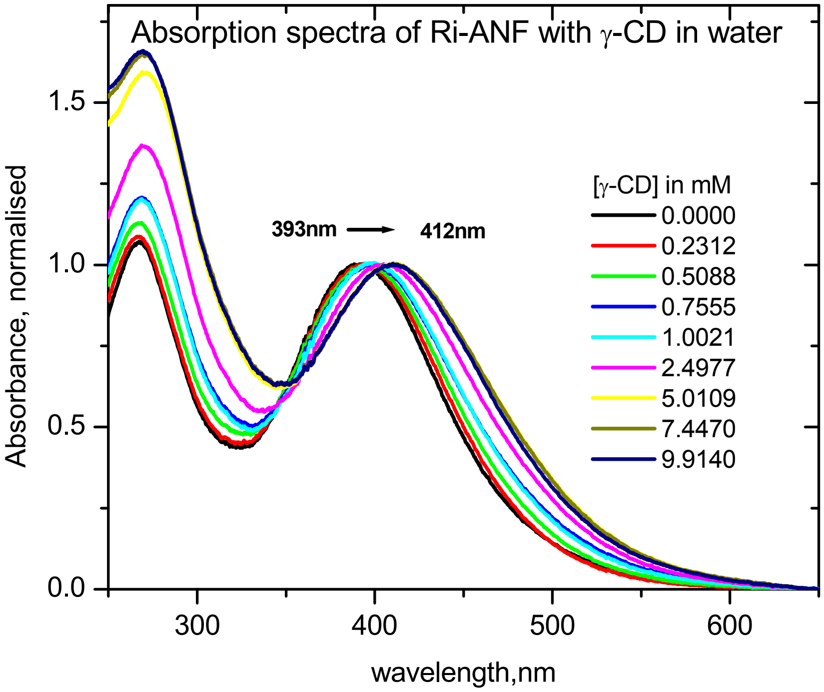

Figure 5.7.2-1 Normalized absorption spectra of Ri-ANF for various concentration of γ-CD in water. Different concentrations are distinguished by color. With increasing concentration, a red shift of absorption is observed.

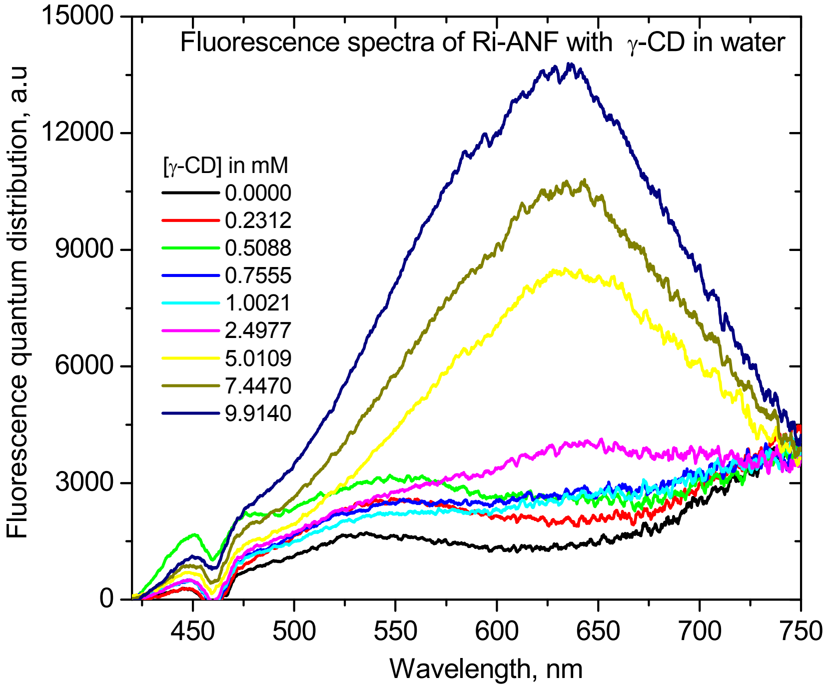

Figure 5.7.2-1 Fluorescence spectra of Ri-ANF in various concentrations of γ-CD in water. Different concentrations are distinguished by color. With increasing concentration, the fluorescence intensity at 632nm increases.

5.7.3 Concentration effect of ß-cyclodextrin

In this case the ß-CD concentration range was also 0.2–10 mM. When the concentration is increased from 0.2 mM, the absorption maxima shifts from 393 nm to 403nm and the band broadens simultaneously. Unlike with γ-CD, and isosbestic point is not observed with ß-CD. The normalized absorption spectra are shown in figure 5.7.3-1. The emission spectra of the above solutions are shown in figure 5.7.3-2 . With increasing ß-CD concentration, the peak intensity at 740 nm increases, while shoulder at 537 nm remains up to 2.325 mM. Upon further increase (up to 10.1149 mM) the shoulder at 537 nm and peak at 740 nm increase in parallel. At this higher concentration, there is a also the possibility of forming a 1:2 complex. This situation will be examined below in terms of binding curves.

5.7.4 Determination of association constant

Most of the complexation studies in the literature assumed a 1:1 stoichiometry between CD and the guest molecule of interest. Interpretation of the results in studies involving complexation may vary significantly depending on the stoichiometry. For a single 1:1 complex, the equilibrium and equilibrium constant can be written as

$$\mathrm{Ri\text{-}ANF} + \mathrm{CD} \Leftrightarrow \mathrm{RCD} \qquad 5.21$$

and

$$K = \frac{[\mathrm{RCD}]_{eq}}{[\mathrm{Ri\text{-}ANF}]_{eq}\,[\mathrm{CD}]_{eq}} \qquad 5.22$$

When we substitute the initial concentration of the CD and Ri-ANF,

$$K = \frac{[\mathrm{RCD}]_{eq}}{\left([\mathrm{Ri\text{-}ANF}]_0 - [\mathrm{RCD}]_{eq}\right)\left([\mathrm{CD}]_0 - [\mathrm{RCD}]_{eq}\right)} \qquad 5.23$$

becomes

$$K = \frac{[\mathrm{RCD}]_{eq}}{\left([\mathrm{Ri\text{-}ANF}]_0 - [\mathrm{RCD}]_{eq}\right)\left([\mathrm{CD}]_0\right)} \qquad 5.24$$

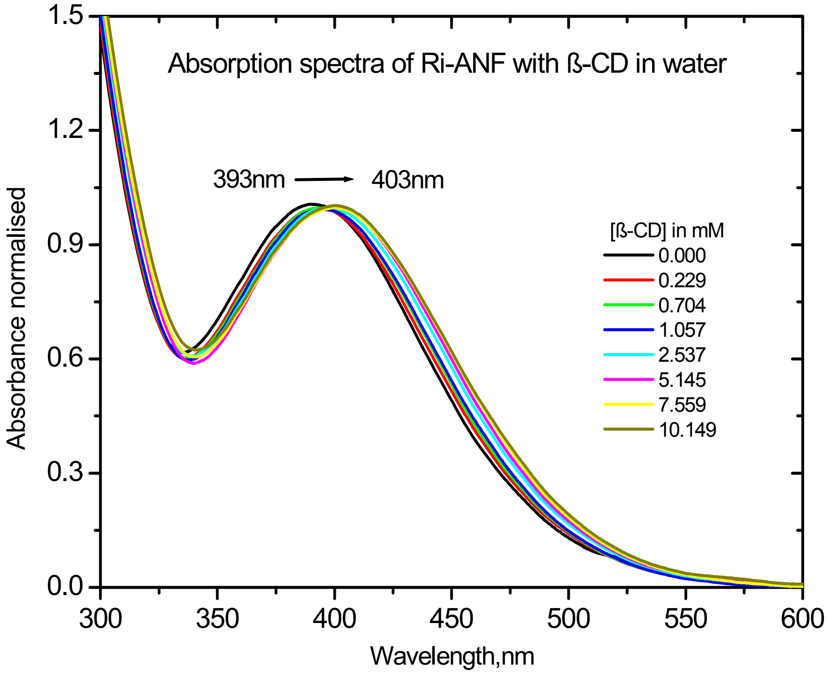

Figure 5.7.3-1 Normalized absorption spectra of Ri-ANF for various concentrations of ß-CD in water. With increasing concentration, the red red shift is less pronounced compared to the previous figures.

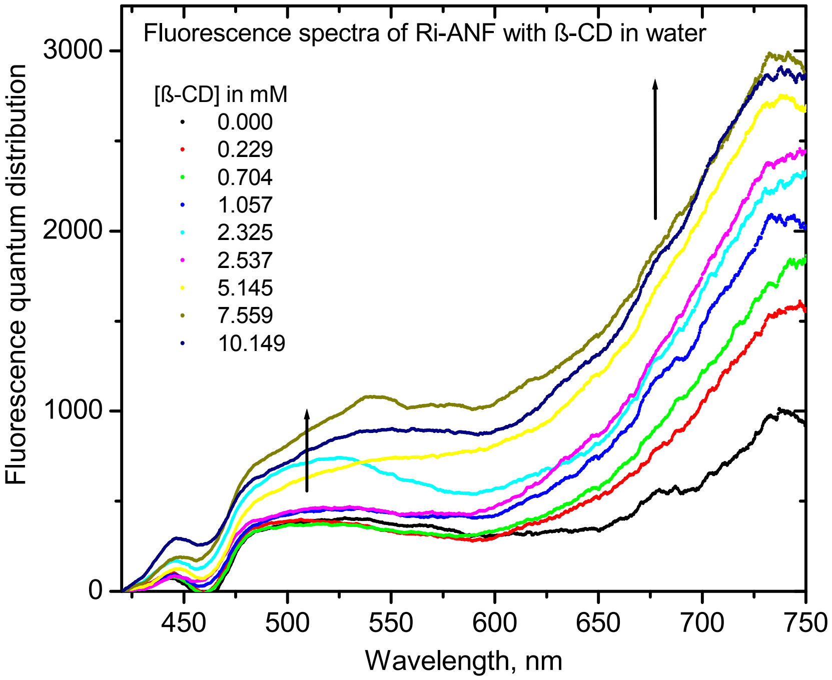

Figure 5.7.3-2 Fluorescence spectra of Ri-ANF in various concentration of ß-CD. Different concentrations are shown in different color. For all increasing concentration, intensity at 640nm increases considerably whereas shoulder around 537 nm starts to increase from 2.5 mM.

since $[\mathrm{CD}]_{\mathrm{eq}} >> [\mathrm{RCD}]_{\mathrm{eq}}$.The total fluorescence intensity observed from the measurement is weighted average of the intensity from the free Ri-ANF and complexed molecule. Thus

$$\frac{[\mathrm{RCD}]_{\mathrm{eq}}}{[\mathrm{Ri\text{-}ANF}]_0} = \frac{I_0 - I}{I_0 - I_1} \qquad 5.25$$

where I_0, I, and I_1 denote the fluorescence intensity of only Ri-ANF, at a given CD concentration, and when all Ri-ANF molecules are complexed with CD forming the 1:1 complex. Combining the above two equation one obtains

$$\frac{1}{I - I_0} = \frac{1}{K(I_1 - I_0)} \frac{1}{[\mathrm{CD}]_0} + \frac{1}{I_1 - I_0} \qquad 5.26$$

With this equation, a Benesi-Hildebrand plot [BH049] can be obtained by plotting $\frac{1}{(I - I_0)}$ versus $\frac{1}{[\mathrm{CD}]_0}$. From the slope and intercept respectively from the straight line we extract K and I_1.

5.7.4.1 with ß-CD

The experimental data of Ri-ANF in the presence of ß-CD are shown as a Benesi-Hildebrand plot in figure 5.7.4.1-1. Clearly the plot can not be fitted by a single straight line, but it seems to consist of two linear segments. It follows that the situation there is not only the formation of 1:1 complex. The initial portion corresponds to higher ß-CD concentration where a 1:2 complex might exist, whereas the later portion corresponding to lower ß-CD concentration might reflect a 1.1 complex. With linear regression, the experimental data are not weighted properly, since data points are widely spaced at lower concentration compared to higher concentration. Therefore if nonlinear least-squares regression analysis is used to find the binding constant, the above equation 5.26 must be rearranged assuming 1:1 complexation at lower concentration [ND096, SPK04]

$$I = \frac{I_0 + I_1 K_1 [\mathrm{CD}]_0}{1 + K_1 [\mathrm{CD}]_0} \qquad 5.27$$

The initial values of I_0 and I_1 given to analysis are the experimental values and K_1 is obtained. Since we consider the formation of 1:2 complex at higher concentration, we

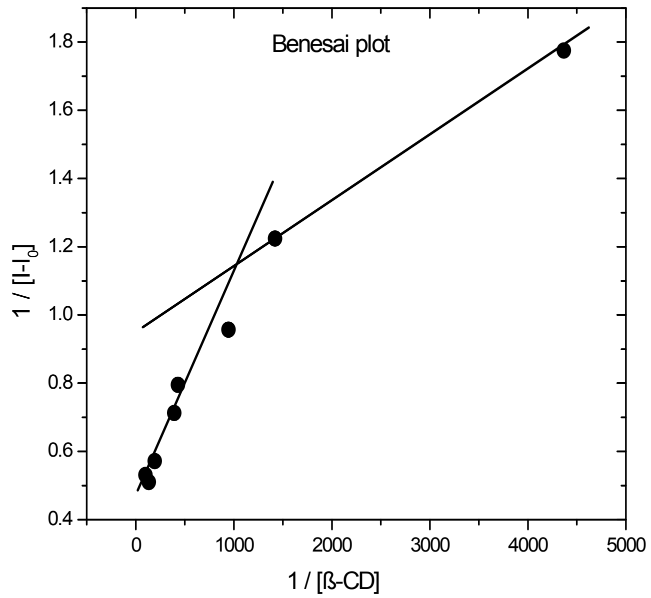

Figure 5.7.4.1-1 Benesi-Hildebrand plot for Ri-ANF in ß-CD, *i.e.* 1/[ß-CD] *vs*1/[I-I$_o$] (see text). Data can not be fitted by single straight line.

have the following additional stepwise equilibrium $\mathrm{RCD} + \mathrm{CD} \Leftrightarrow \mathrm{R(CD)_2}$. From this equilibrium, we obtain the following equation by linear regression,

$$\frac{1}{I - I_0} = \frac{1}{(I_2 - I_0)\, K_1\, K_2}\, \frac{1}{[\mathrm{CD}]_0^{\,2}} + \frac{1}{(I_2 - I_0)} \qquad 5.27$$

where K_2 is the stepwise association constant of $G(CD)_2$. Since this equation did not give the exact binding constant, more reliable values of the binding constants are obtained by using *matlab programme* from the following equation.

$$I = \frac{I_0 + I_1\, K_1\, [\mathrm{CD}]_0 + I_2\, K_1\, K_2\, [\mathrm{CD}]_0^{\,2}}{1 + K_1\, [\mathrm{CD}]_0 + K_1\, K_2\, [\mathrm{CD}]_0^{\,2}} \qquad 5.28$$

The line drawn in this figure 5.7.4.1-2 is the fit to the data which yield correlation coefficients of 0.96. From this non linear regression analysis, the binding constants K_1 (= 4101.5 dm^3mol^{-1}), K_2 (= 154.1 dm^3mol^{-1}) were obtained along with the fluorescence intensities of the inclusion complexes. This treatment suggests that a stepwise 1:1 followed by a 1:2 complex is formed in this case. The 1:2 binding constant is much lower than the 1:1 constant.

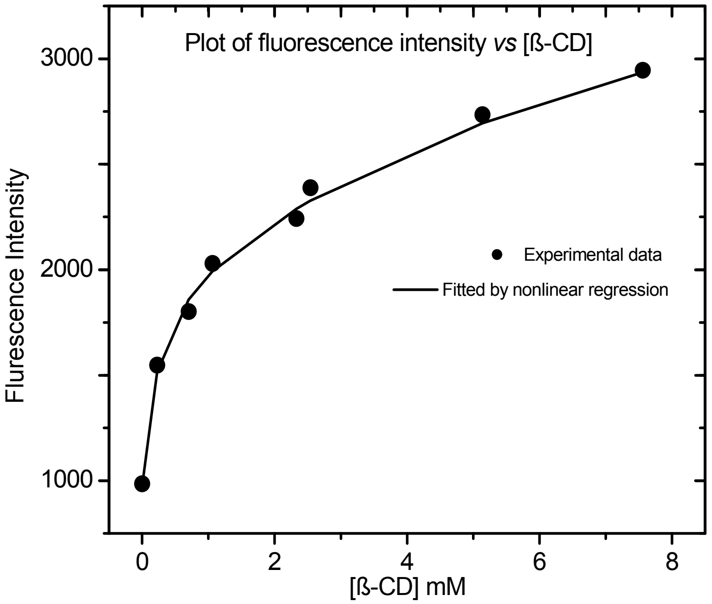

Figure 5.7.4.1-2 Plot of the fluorescence intensity I from Ri-ANF *vs* [ß-CD]. The full line is the nonlinear regression fit of eq. 5.28 to the experimental points.

5.7.4.2 with γ-CD

The same procedure was also tried for γ-CD to check whether the 1:2 complexes is formed at high γ-CD concentration. In figure 5.7.4.2-1 the experimental data are shown directly. The observed linearity suggests that only a 1:1 complex is formed and its binding constant as 1215.6 dm^3 mol^{-1}.

To conclude: in ß-CD a tight complex 1.1 complex is formed first, at lower concentration, to be followed by a loose 1:2 complex at higher concentration. The fluorescence spectrum of the tight complex peaks at about 730 nm. The loose 1:2 complex has a fluorescence spectrum which peaks much further in the blue, around 530 nm, as if the chromophore were in an unpolar environment. This suggests that the chromophore is fully shielded from water in the 1:2 complex.

From the binding constants and with the equation, $\Delta G = -RT \ln K$, we find ΔG ≈20.33 kJ and 17.36 kJ for ß-CD and γ-CD respectively. Compared with ΔG from solubility measurements of ANF in ACN/water mixtures, these values correspond to volume fraction of acetonitrile at 0.24 and 0.32 respectively. In other words, the dissolving power of ß-CD on Ri-ANF is equivalent to that of 0.24 volme fraction of acetonitrile on ANF in water.

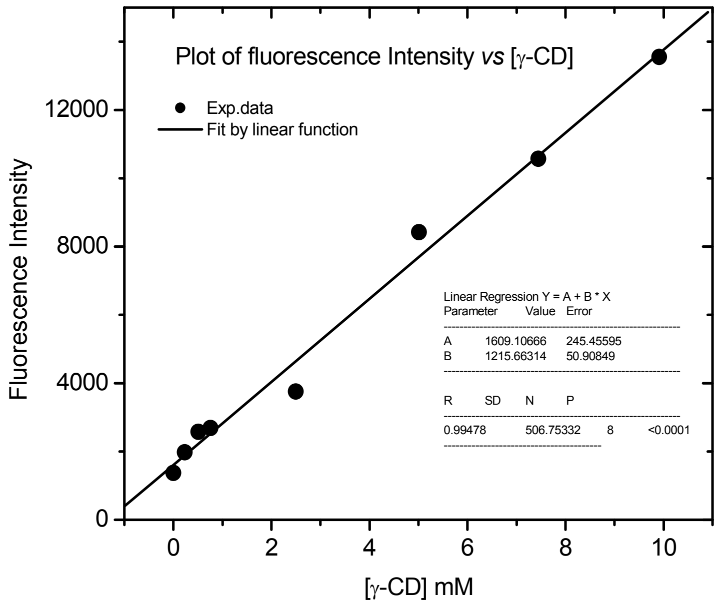

```
Linear Regression Y = A + B * X
Parameter       Value       Error
------------------------------------------------------------
A          1609.10666     245.45595
B          1215.66314     50.90849
------------------------------------------------------------

R          SD          N           P
------------------------------------------------------------
0.99478          506.75332      8          <0.0001
----------------------------------------
```

Figure 5.7.4.2-1 Plot of the fluorescence intensity I from Ri-ANF *vs* [γ-CD]. The full line is the linear regression fit to the experimental data points.

6 Femtosecond time resolved photophysical studies of ANF derivatives

6.1 Expected solvation dynamics of ANF in DNA from molecular modeling

The ultrafast structural [AD091, B0003, NB002, ORA99, PLK98, PSC94, S0000] and electronic properties of DNA [CG003, GK004, RM003, SW001] have attracted the attention of many photophysicsts and photochemists. DNA is a complex medium whose internal dynamics ranges on time scales from 10^{-13} to 10^{2} seconds, over 15 orders of magnitude [C0004, M0096]. Various organic dyes have been attached covalently to oligonucleotides (some of them were described in the section 2.4.2) and applied as probes for the local environment and its dynamics. By observing the fluorescence Stokes shift of Coumarin 102, Berg *et al* [BMC99, SAM04] derived the effective polarity of DNA and the characteristic time scale for polar reorganization dynamics. The Stokes shift reflects the polarizibility of the DNA environment which responds to the change of dipole moment of the probe upon excitation. In the same fashion, we intended to use 2-Amino-7-Nitro-Fluorene (ANF) as a polarity probe in studies of DNA dynamics. Modified ANF is an excellent solvation probe in a variety of environments because of its strict bipolar nature and large Stokes shift. The question arises if it can be used in DNA also, and for this purpose theoretical studies were carried out (by Dr. V. Farztdinov) [FES_ _] which will briefly be outlined here. The following base sequences were simulated

5’-G C G C A A F T T C G C G-3’(AFT)
3’-C G C G T T _ A A G C G C-5’(T_A)

5’-G C G C T A F A T C G C G-3’(AFA)
3’-C G C G A T _ T A G C G C-5’(T_T)

5’-G C G C A A F T T C G C G-3’(AFT)
3’-C G C G T T C A A G C G C-5’(TCA)

Here F represents the ANF chromophore which is attached to C_1' of the corresponding deoxyribose through the amino group and it is shown in figure 6.1-1.

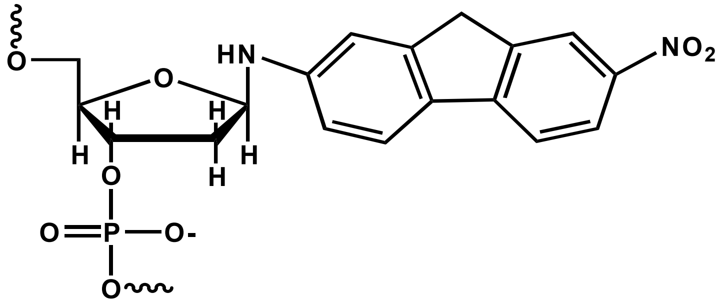

Figure 6.1-1 Chemical structure of ANF nucleotide.

To either side 6 nucleobases were attached as shown above. The opposite strand had the central nucleobase deleted so that the ANF chromophore occupies an abasic site. Structures were preoptimised with the JUMNA algorithm and then subjected to Monte Carlo (MC) simulation. The force field was AMBER 95 with appropriate parameters for the artificial nucleobase. After 10^6 cycles the free energy sampled over the last 1000 configurations was found to be constant, and properties were always calculated from such equilibrated ensembles. The following figure 6.1-2 represents the structure of the labeled 13mer AFT/T_A (see above) at minimum potential energy (a) and typical fluctuations (b, c) corresponding to the average energy.

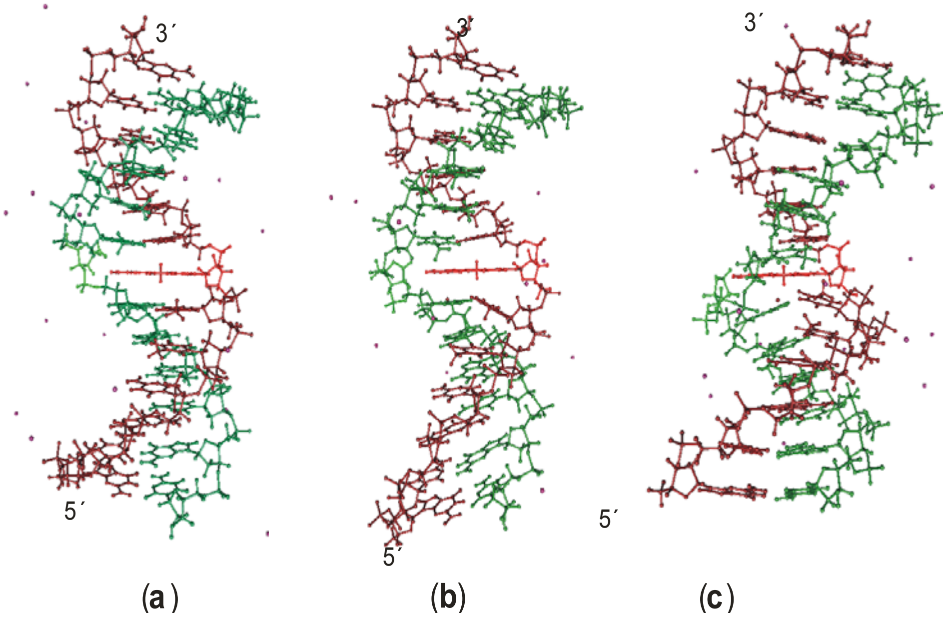

Figure 6.1-2 Structure of the labelled 13mer AFT/T_A (see text) at minimum potential energy (a) and fluctuations (b,c) corresponding to the average energy (taken from [FES_ _]). ANF(pink) is oriented in the middle of the DNA duplex.

It is possible to derive the solvation dynamics from such Monto-Carlo simulations, as will be explained in the following:

For each momentary structure of the MC ensemble, the infrared spectrum ω_j was calculated and the normal coordinates q_j were obtained. Also calculated was the electric interaction energy H_{el} of the chromophore with the DNA duplex. The coupling constant is given by $\left(\frac{\partial H_{el}}{\partial q_j}\right)^2$. Plotting the coupling constant against frequencies ω_j and summing over the ensemble gives the solvation spectral density $\rho_{solv}(\omega)$. From there, the solvation correlation function is obtained by

$$G(t) = k_B\,T\int d\omega \rho_{solv}(\omega)\ \cos(\omega\,t) \qquad 6.1$$

then

$$C_{\Delta E}(t) = 1 - \left\langle(\delta\,\Delta E)^2\right\rangle^{-1}\int_0^1 (t-\tau)\,G(\tau)\,d\tau \qquad 6.2$$

The results are shown in figure 6.1-3.

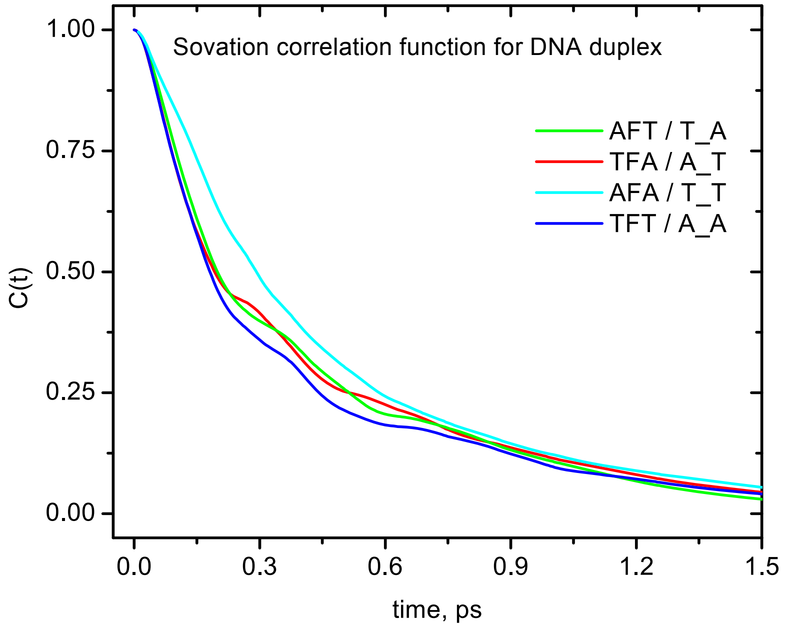

Figure 6.1-3 Solvation correlation function for different DNA duplexes, derived from the corresponding solvation spectral densities (from [FES_ _]).

The calculations predict different relaxation functions for the various neighborhoods in the duplex. (They can be distinguished even better if the solvation spectral density is viewed which, however, is not shown here.) If the ANF nucleotide can be synthesized and incorporated into DNA, this is what we expect to see in the femtosecond experiments. As steps in this direction, the solvation behavior of the chromophore ANF itself and of derivatives should be studied by themselves. The bulk of the femtosecond work in this thesis therefore concerns solvation of ANF and derivatives in pure solvents. This topic and corresponding results will be presented in the following sections.

6.2 Femtosecond transient absorption spectra of ANF derivatives

In this section the spectral evolution of the amino nitro fluorene derivatives were presented and described qualitatively (the extraction of the solvation correlation function from the evolution will be treated in the next section). Femtosecond Transient Absorption Spectra (TAS) of the derivative dM-ANF and of the glucosylated Gl-ANF were recorded with our pump-super continuum probe setup. The compounds were synthesized and purified as described in the section 4.2. Solvents were methanol, ethanol, dimethyl sulfoxide (DMSO), tetrahydrofuran (THF), ethyl acetate (EA), acetonitrile (ACN), 1,4 dioxane (DIOX) and water. They cover a polar to medium-polar range of the polarity scale and generally were of UV grade (Merck UVASOL). The chromophore was excited at 470 nm or 400 nm with pulse energy of 0.5 μJ at a repetition rate of 60 Hz. The pathlength of sample cell was 0.35 mm and the optical density was 0.65 at the absorption maximum corresponding to a concentration of about 2.3×10^{-4} mol/L. The pump-induced transient absorption signal $\Delta OD(t,\lambda)$ was monitored by supercontinuum probe pulses covering the spectral range $270 \leq \lambda \leq 688$ nm or $360 \leq \lambda \leq 775$ nm. The TAS of Gl-ANF in highly polar solvents are different from the spectra in weakly polar solvents and each of them is explained. Since the spectral evolutions of dM-ANF and ANF are nearly the same, dM-ANF is taken to be representative of the two in the following.

6.2.1 dM-ANF in acetonitrile (ACN)

We start with the measurement of dM-ANF in acetonitrile. Early pump-probe spectra of dM-ANF in ACN from 0 to 250 fs with steps of 12 fs, excited at 400 nm, is shown in figure 6.2.1-1. Positive induced optical density ΔOD corresponds to excited state absorption (ESA) and negative ΔOD at longer wavelength to stimulated emission (SE), which is similar to the stationary fluorescence spectrum. Negative ΔOD at shorter wavelength corresponds to bleaching (BL). The direction of the spectral evolution is shown by arrows. Bleach at wavelengths $\lambda \leq 295$ nm corresponds to the second, near-UV peak of the ground state stationary absorption spectrum. Between 295 and 507 nm the transient spectra are dominated by ESA and for $\lambda \geq 507$ nm by SE. At early time, while pump and probe pulses are overlap, the transient signal consists in general three components. The first is stimulated resonant Raman scattering of the pump at 400 nm. The coherent contribution should follow the pump/probe cross correlation. The other two components are due to the "particle" (population) in the excited state and to the corresponding "hole" (lack of population) in the ground state. Particle and hole are created by optical pumping at 400 nm, which selects chromophores with favorable solvent configurations for the interaction. But also the solvent, by itself, contributes to the coherent signal. Thus at 0 fs, the small positive peak at 357 nm corresponds to inverse stimulated Raman scattering by a CH stretching mode (2900 cm^{-1}) of pure acetonitrile. The same mode gives the stimulated Raman signal (negative peak) at 426 nm. But let us return to the solute chromophore. Until ~85 fs, the sequential or population signal increases, since it follows the time-integral of the apparatus function. Afterwards the SE shifts dynamically towards the deep red with a large Stokes shift of about 5700 cm^{-1}. Simultaneously the ESA shifts to blue to a smaller extent, by about 2000 cm^{-1}. We also observe two isosbestic points, at 294 nm between BL and ESA for all times and at 487 nm between ESA and SE from 80 fs onwards.

Figure 6.2.1-2 shows the evolution from 240 fs to 1.5 ps in steps of 180 fs. The SE shifts completely to red and from 500 fs BL starts to appear around 464 nm. As time increases, this BL region begins to increase in intensity and shifts slightly to the blue, where the

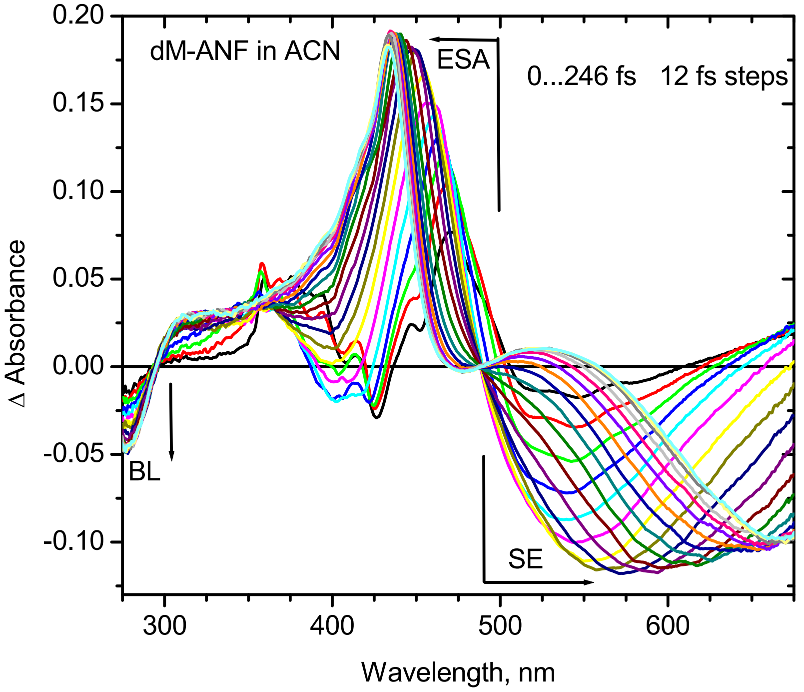

Figure 6.2.1-1 Transient absorption spectra of dM-ANF in acetonitrile from 0 fs to 246 fs in time steps of 12 fs after excitation at 400 nm. Negative ΔOD corresponds to Stimulated Emission (SE) or Bleach (BL), and positive ΔOD corresponds to Excited State Absorption (ESA). Arrows indicate the direction of the spectral evolution.

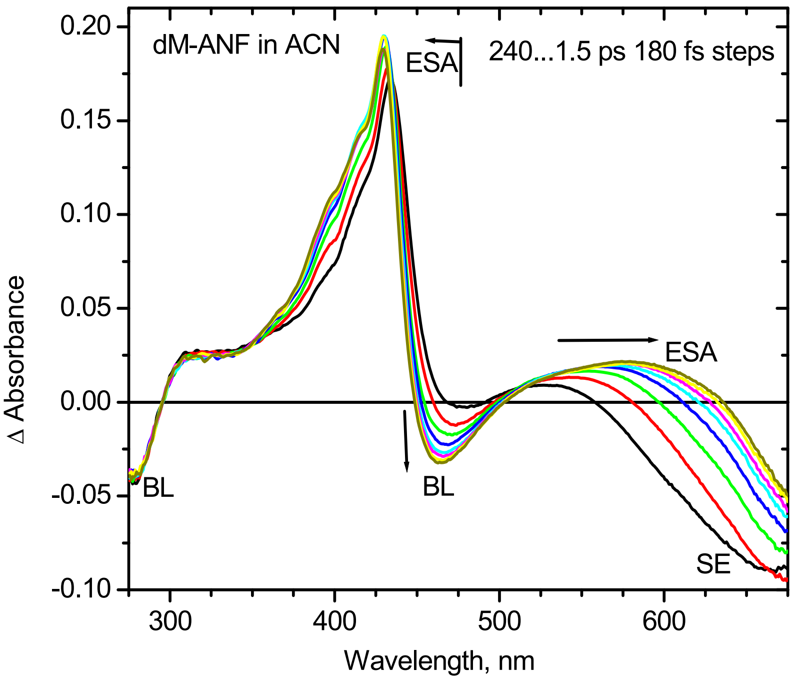

Figure 6.2.1-2 Transient absorption spectra of dM-ANF in acetonitrile from 240 fs to 1.5 ps, in time steps of 180 fs. Arrows indicate the direction of the spectral evolution.

stationary absorption spectrum is located. From 240 fs onwards positive absorption (ESA) appears around 525 nm but shifts to red with time. The blue shift of ESA and BL at 464 nm, and the red shift of SE and ESA at 520 nm reflect the solvation processes. Note that to cover the blue BL region, the spectrograph was adjusted to the range 260 – 688 nm. Additional measurements covering the range 360 – 775 nm were also obtained. As an example, TAS of dM-ANF in ACN covering full SE region at different scale are given in appendix 10.10.

The next figure 6.2.1-3 shows the evolution from 2.5 ps to 20 ps. There is no significant spectral shift, only a small decrease of amplitude is observed. The spectral evolution of dM-ANF in methanol and DMSO is qualitatively the same as in acetonitrile and therefore not shown here. Only the solvation dynamics is different, of course, as will be seen from the solvation curve for these solvents in next section 6.4.

6.2.2 dM-ANF in 1, 4-dioxane

Femtosecond transient absorption spectra of dM-ANF in 1,4 dioxane are shown below (figure 6.2.2-1) from -12 fs to 120 fs in steps of 12 fs. The time evolution is again indicated by arrows. In all spectra presented here, the solvent signal has already been subtracted. In 1,4-dioxane the (coherent) solvent signal is stronger than the signal from the solute, and its subtraction may introduce systematic errors. At early time during optical pumping, the transient spectra reveal structure which reaches maximal contrast at zero delay and disappears after 60 fs. SE is observed from 490 nm to 640 nm, and two regions of excited-state absorption are seen: ESA1 between 420–510 nm and ESA2 for $\lambda > 630$ nm. The latter may correspond an optical transition $S_n \leftarrow S_1$ where the terminal S_n state is the one which is seen in the stationary absorption spectrum at 260 nm. We will see later that there is a strong oscillation of ESA1 and SE amplitudes on this time scale.

The next figure 6.2.2-2 shows the spectral evolution from 160 fs to 1.06 ps in time steps of 100 fs. Here the spectral shift of ESA1 to the blue, and of SE to the red are clearly seen.

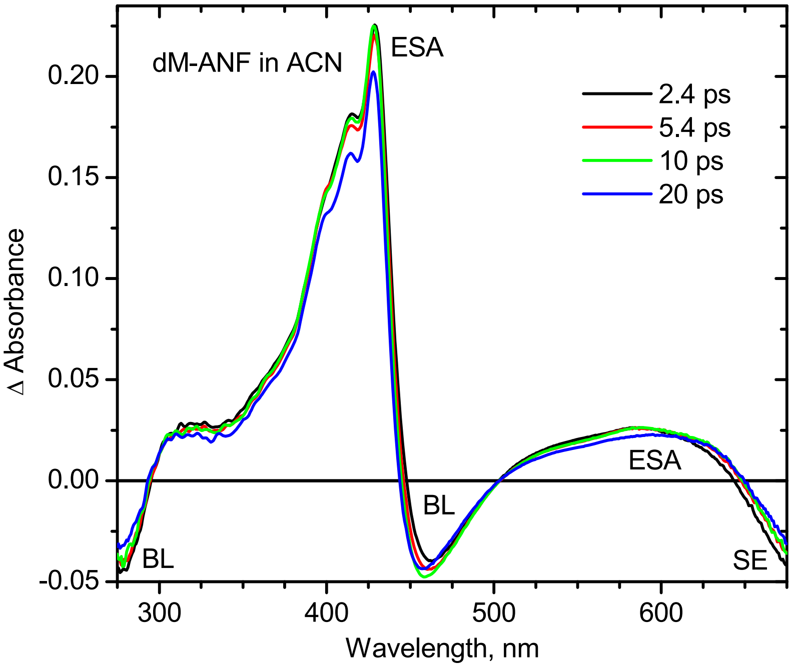

Figure 6.2.1-3 Transient absorption spectra of dM-ANF in acetonitrile at delays of 2.4, 5.4, 10 and 20 ps. Spectral evolution is largely completed.

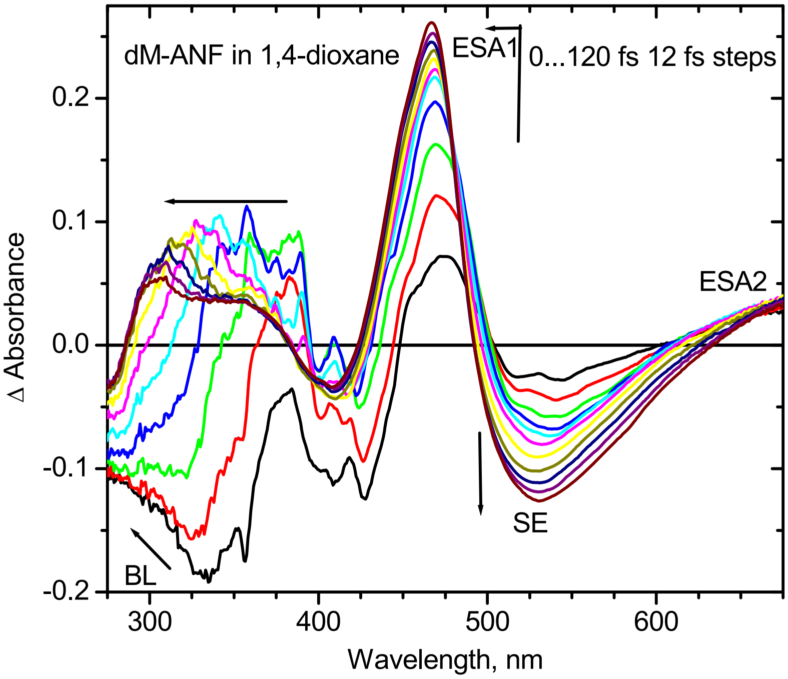

Figure 6.2.2-1 Transient absorption spectra of dM-ANF in 1, 4-dioxane from 0 fs to 120 fs in time steps of 12 fs after excitation at 400 nm. Arrows represent the direction of spectral evolution. Two excited state absorptions are observed − ESA1 at 420-510 nm and ESA2 at $\lambda > 630$ nm. The latter corresponds to an optical transition $S_n \leftarrow S_1$ which may correspond to the $S_n \leftarrow S_0$ band seen by stationary absorption around 260 nm. On this time scales, SE and ESA1 show a clear oscillation.

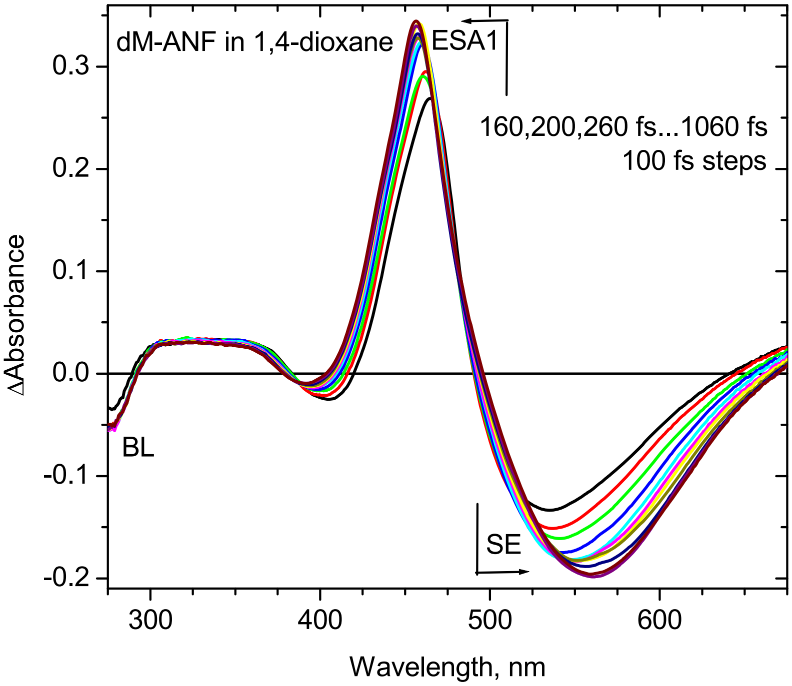

Figure 6.2.2-2 Transient absorption spectra of dM-ANF in 1, 4-dioxane from 160 fs to 1060 fs with time steps of 100 fs. Again, arrows represent the direction of spectral evolution.

The next figure 6.2.2-3 shows the further spectral evolution from 2 ps to 10 ps in steps of 1 ps. Here the SE continues to shift to the red and reaches the stationary fluorescence spectrum; a change of peak value may be balanced by corresponding changes of width. The amplitudes of ESA1 and BL remain nearly constant. ESA2 has been obliterated by the stimulated emission in this region.

Over the period 10 −100 ps (figure 6.2.2-4) the solvation process is no longer active, and the amplitudes of ESA1 and SE decrease simultaneously with time. Since the spectral evolutions for dM-ANF in ethyl acetate and tetrahydrofuran are nearly as same as 1,4-dioxane, they are not shown here.

6.2.3 Gl-ANF in acetonitrile

The nucleoside Ri-ANF (ANF as base surrogate attached to deoxyribose at C_1’) was synthesized in order to measure its transient absorption spectrum. However the

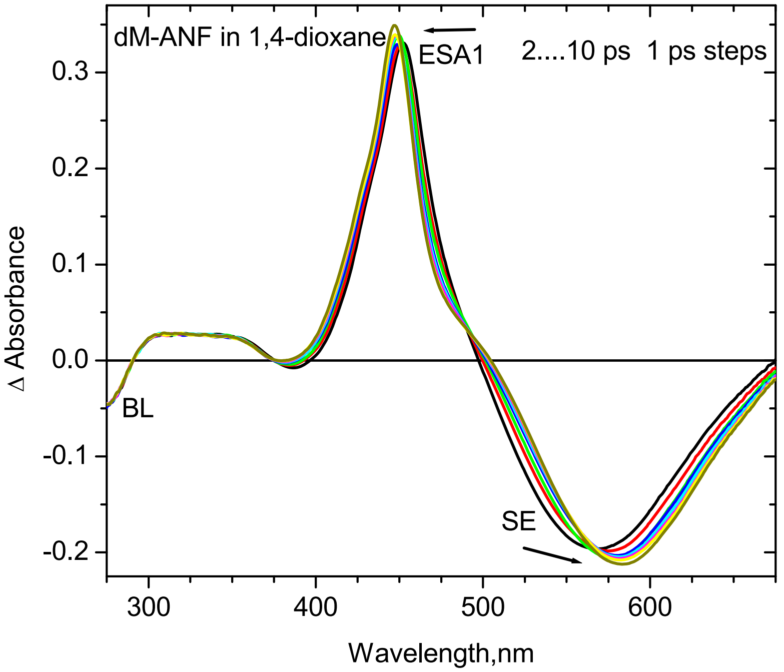

Figure 6.2.2-3 Transient absorption spectra of dM-ANF in 1,4-dioxane from 2 ps to 10 ps with time steps of 1 ps.

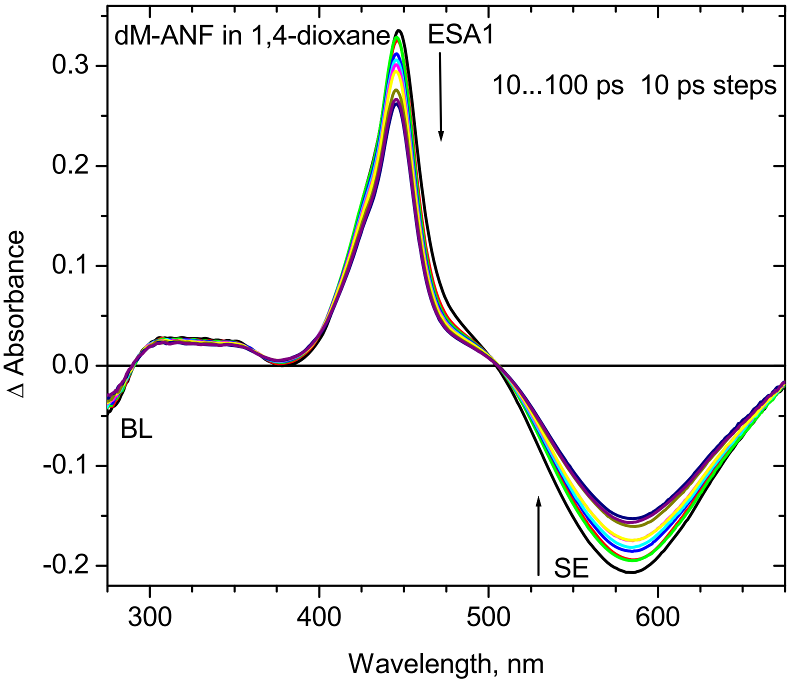

Figure 6.2.2-4 Transient absorption spectra of dM-ANF in 1,4-dioxane from 10 ps to 100 ps in time steps of 10 ps. The SE peak corresponds to the maximum of the stationary fluorescence spectrum.

solubility of Ri-ANF in water is insufficient for fs-time resolved measurements and this is why a higher homologue of the sugar moiety, glucose (Gl-ANF) was synthesized. The solubility of the compound Gl-ANF in water is explained elsewhere (section 6.2.5). The spectral evolution for Gl-ANF is quite different in ACN, THF and water, therefore the results for each of the solvents are presented separately.

First we consider the Gl-ANF in acetonitrile. Figure 6.2.3-1 shows the spectral evolution from -18 fs to 78 fs in steps of 12 fs. SE is seen for $498 < \lambda < 612$ nm and BL for $\lambda < 315$ nm (remember that solvent signal has always been subtracted). The transient spectra have more structure at early time around $t = 0$ which vanishes after 40 fs when the pump/probe overlap is over. With time, early SE appears and simultaneously shifts to red. BL is observed only in the region of the second ground-state absorption band around 280 nm. The main feature seems to be that excited-state absorption is relatively strong throughout the observation window.

The next figure 6.2.3-2 shows the evolution in acetonitrile from 0.1 to 1 ps (100 fs steps). On this time scale the intensity of ESA1 increases slightly and shifts to blue whereas ESA2 decreases somewhat. The most important observation is that SE has maximum amplitude at 200 fs and rapidly decays afterwards while shifting slightly to the red. Here it should be noted that the broad ESA contribution seems to remain nearly constant. Since both ESA and SE are governed by the same population in the excited state, such behavior clearly indicates a transient decrease of the oscillator strength for SE. By 300 fs, SE has completely disappeared and the region from 485 nm to 657 nm becomes positive throughout. This kind of behavior is not observed with the other ANF derivatives in acetonitrile. It is difficult to explain by solvation; we speculate that some dark state exists at this time, i.e. some excited form of Gl-ANF which is not coupled radiatively to the ground state.

The evolution until 100 ps is shown in figure 6.2.3-3. Interestingly, weak SE grows in slowly (note the varying time steps in the figure). By 100 ps negative ΔOD around 650 nm clearly corresponds to the stationary emission spectrum.

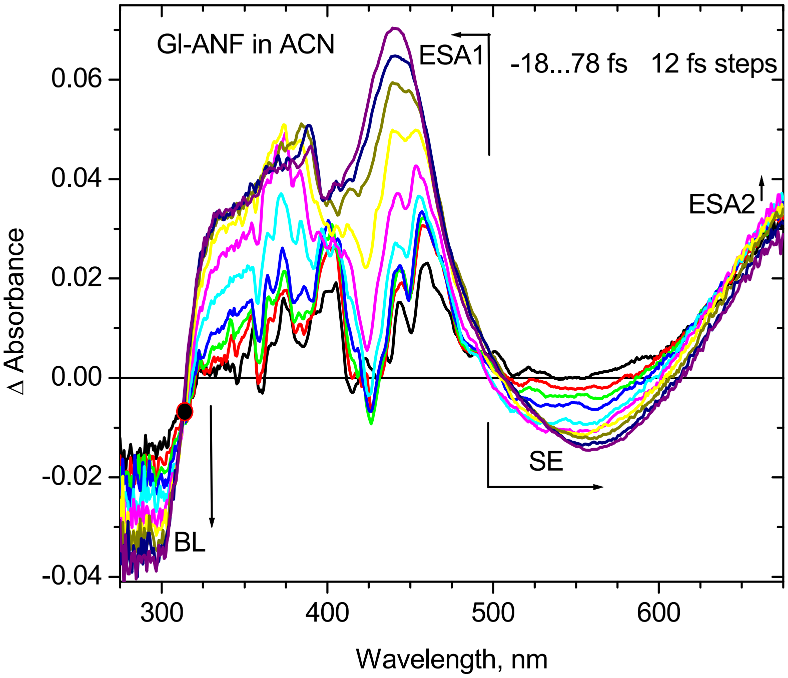

Figure 6.2.3-1 Transient absorption spectra of Gl-ANF in acetonitrile from -18 fs to 78 fs with time steps of 12 fs after excitation of 400 nm. The transient spectra have more structure at early time, which vanishes after 40 fs when pump/probe pulses are over.

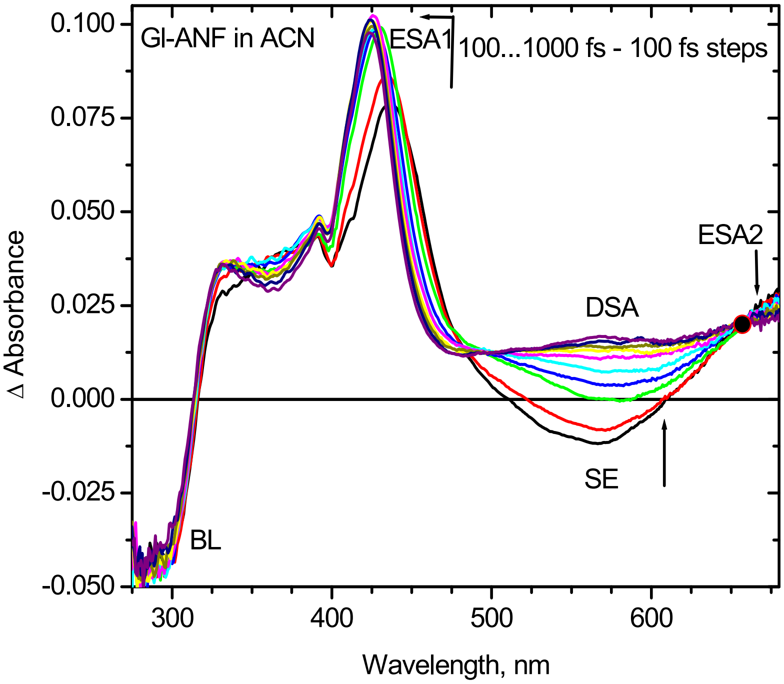

Figure 6.2.3-2 Transient absorption spectra of Gl-ANF in acetonitrile from 100 fs to 1 ps with time steps of 100 fs. The SE decays very fast and after 300 fs, a dark-state absorption (DSA) dominates in the SE region. For details see text.

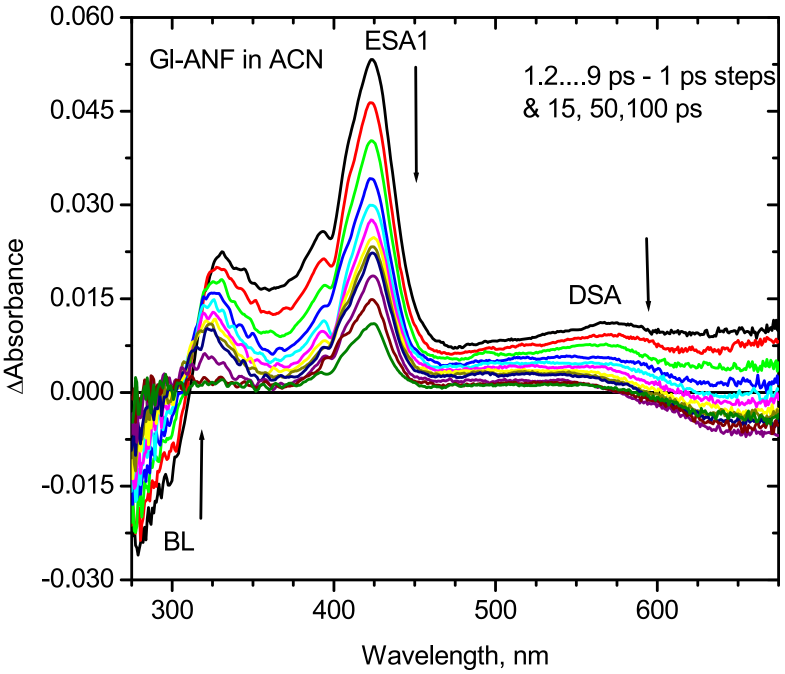

Figure 6.2.3-3 Transient absorption spectra of Gl-ANF in acetonitrile from 1.2 ps to 9 ps with time steps of 1 ps, and at 15 ps, 50 ps and 100 ps after excitation. At 100 ps, all spectral evolution is completed and the spectrum around 650 nm corresponds to the stationary fluorescence spectrum.

6.2.4 Gl-ANF in tetrahydrofuran (THF)

In tetrahydrofuran the intermediate "dark state" is not seen. Figure 6.2.4-1 shows the spectral evolution of Gl-ANF in THF. In this figure the time runs -36 fs to 84 fs in steps of 12 fs. The solvent Raman signal is strong in the UV region because of near electronic resonance. Its subtraction from the signal measured with the sample can therefore be problematic in the near-UV (see experimental section 3.5). Even if the subtraction is optimal at some delay time, for example for t = 0, there remains Raman structure from the solvent at other delay times. We find negative ΔOD for $488 \leq \lambda \leq 619$ nm due to stimulated emission and for $\lambda \leq 333$ nm due to bleach. Excited state absorption occurs at two positions (as in acetonitrile): at $333 \leq \lambda \leq 488$ nm (ESA1) and for $\lambda \geq 640$ nm (ESA2). On the whole, the development on this early time scale is similar to that in acetonitrile.

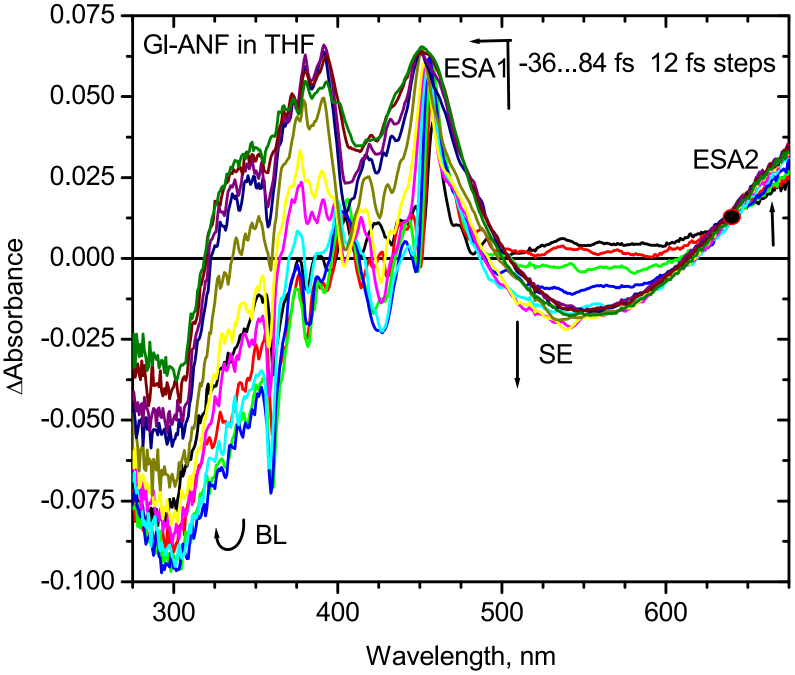

Figure 6.2.4-1 Transient absorption spectra of Gl-ANF in tetrahydrofuran from -36 fs to 84 fs with time steps of 12 fs after excitation at 400 nm. Spectra are more structured at negative delay because of Raman solvent signals are strong – see text

The difference with Gl-ANF in ACN comes in when the middle time scale, from 120 fs to 1.2 ps, is considered (figure 6.2.4-2). In THF the evolution is normal, i.e. similar to dM-ANF in 1,4-dioxane which was shown earlier (figure. 6.2.2-2). Mainly we see a small red shift of the SE and a corresponding blue shift of ESA1. This behavior is continued at later times, after 2 ps, as seen in figure 6.2.4-3. The maximum of SE at 565 nm corresponds to that of the stationary emission spectrum. A decrease of all amplitudes is seen over 100 ps.

6.2.5 Gl-ANF in water

The solubility of Gl-ANF in water is poor: an absorbance of only 1.13 at the peak wavelength in 1cm is reached. But in fs transient absorption experiments the sample thickness must be much smaller in order to achieve the desired time resolution. We used a sample thickness of 0.35 mm throughout, so that the maximum ground-state absorption was 40 mOD. Transient induced spectra were on the order of 10 mOD or below. At this signal level it is dangerous to subtract the signal from the pure solvent. Therefore the

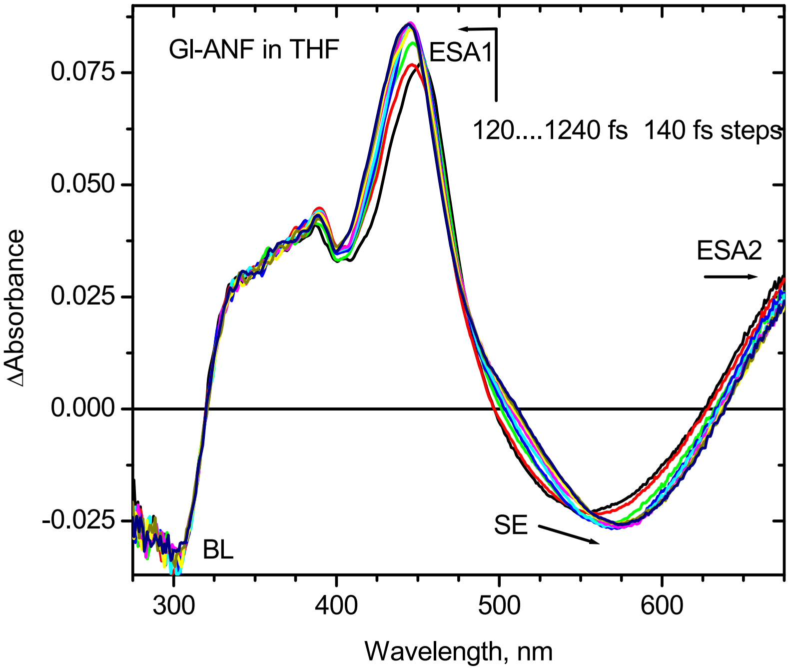

Figure 6.2.4-2 Transient absorption spectra of Gl-ANF in tetrahydrofuran from 120 fs to 1240 fs with time steps of 140 fs. The spectral evolution is similar to dM-ANF in 1,4 dioxane (figure 6.2.2).

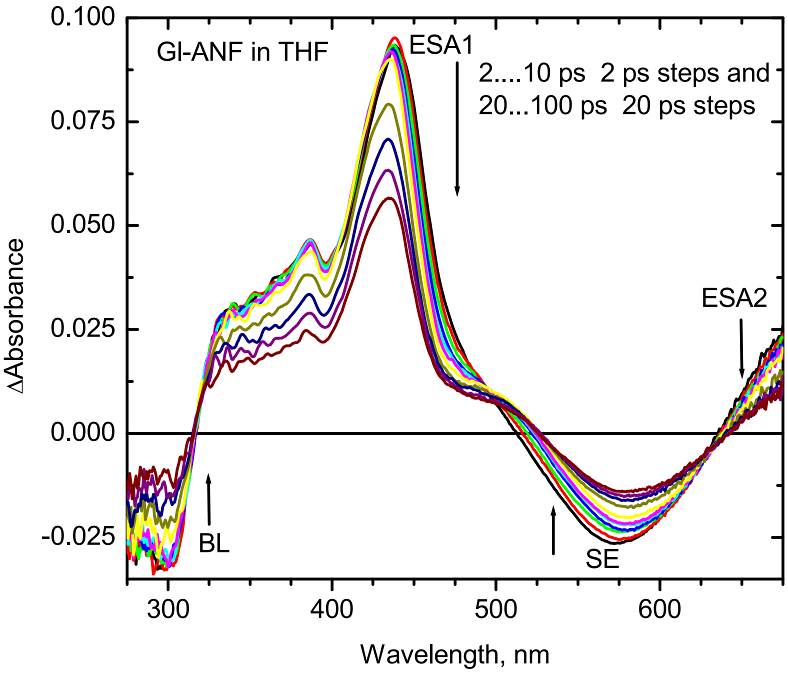

Figure 6.2.4-3 Transient absorption spectra of Gl-ANF in tetrahydrofuran from 2 ps to 10 ps with time steps of 2 ps and with time steps 20 ps from 20 ps to 100 ps. At 100 ps, the spectrum around 575 nm looks similar to the stationary fluorescence spectrum.

direct measurements (time corrected but without solvent subtraction) are being shown (figures 6.2.5-1−3). In figure 6.2.5-1, panel *a* shows the early spectra for pump-probe delays from -48 fs to 0 fs with 12 fs steps. The signals grow in uniformly on this time scale. In panel *b* the evolution is shown from 6 fs to 48 fs. The passing of the Raman signal is evident, after which we are left with the weak contribution by the excited Gl-ANF in water. Simultaneous growth and decay of the Raman peaks in different spectral regions reflects our quality of the time correction. For our measurements reported here, time resolution is better than ± 10 fs. The negative Raman peak at 464 nm (21551 cm^{-1}) is caused by the O-H (3430 cm^{-1}) stretching mode of the water. The same mode gives anti-Stokes absorption of probe light, as positive peak at 352 nm (28409 cm^{-1}). The position of the pump wavelength (400 nm) can be indirectly determined from the position of Stokes and anti-Stokes peaks.

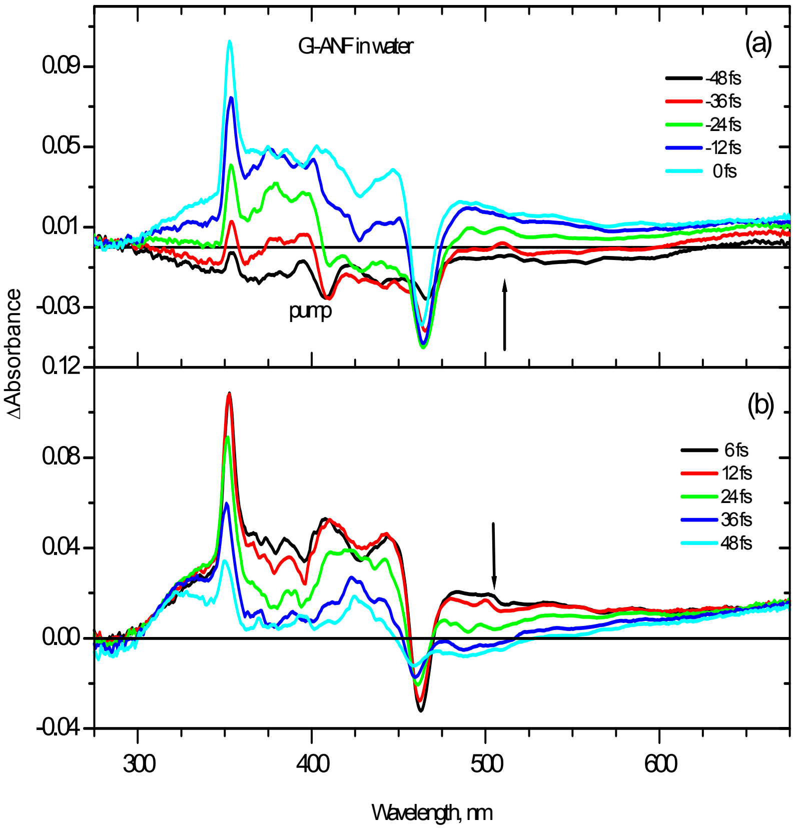

Figure 6.2.5-1 Panel (a) transient absorption spectra of Gl-ANF in water from -48 fs to 0 fs and panel (b) from 6 fs to 48 fs with time steps of 12 fs after excitation at 400nm. Simultaneous growth and decay of Raman signal shows the quality of our time correction. The negative Raman peak at 464 nm (21551 cm^{-1}) is caused by the O–H (3430 cm^{-1}) stretching mode of the water. The same mode gives an anti-Stokes absorption of probe light, as a positive peak at 352 nm (28409 cm^{-1}).

The next figure 6.2.5-2 shows the evolution from 54 fs to 84 fs in steps of 6 fs. Right after the pump pulse is over, at 54 fs time delay, SE is clearly seen around 487 nm. It decays extremely fast, and by 72 fs there is no negative induced absorption left around 487 nm. On this time scale the intensity of ESA1 increases with a small blue shift. The bleach in the near-UV also seems to be increasing, although the noise is much higher in this region and definite conclusions should not be drawn. After 72 fs the dark state begins to appear.

Until 1 ps (figure 6.2.5-3) the broad dark-state absorption dominates the transient spectra. Comparing with the previous figure 6.2.5-2, it looks as if the excited-state absorption in the deep red decreases somewhat. In summary, the evolution in water bears strong resemblance to that in acetonitrile, only it is much faster.

The evolution from 1 ps to 10 ps is shown in figure 6.2.5-4. On this time scale all spectral evolution has ceased, only amplitudes are decreasing. We do not observe stationary SE at late times (compare figure 6.2.3-3 for Gl-ANF in acetonitrile).

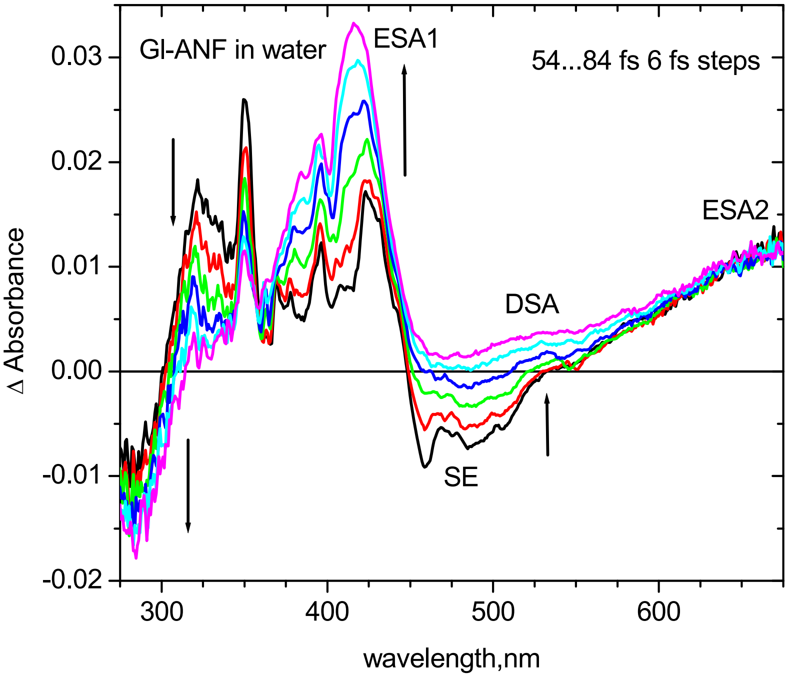

Figure 6.2.5-2 Transient absorption spectra of Gl-ANF in water from 54 fs to 84 fs with time steps of 6 fs. SE decays very much faster as compared to ACN solutions. At 72 fs, dark state absorption (DSA) appears and there is no negative absorption contribution.

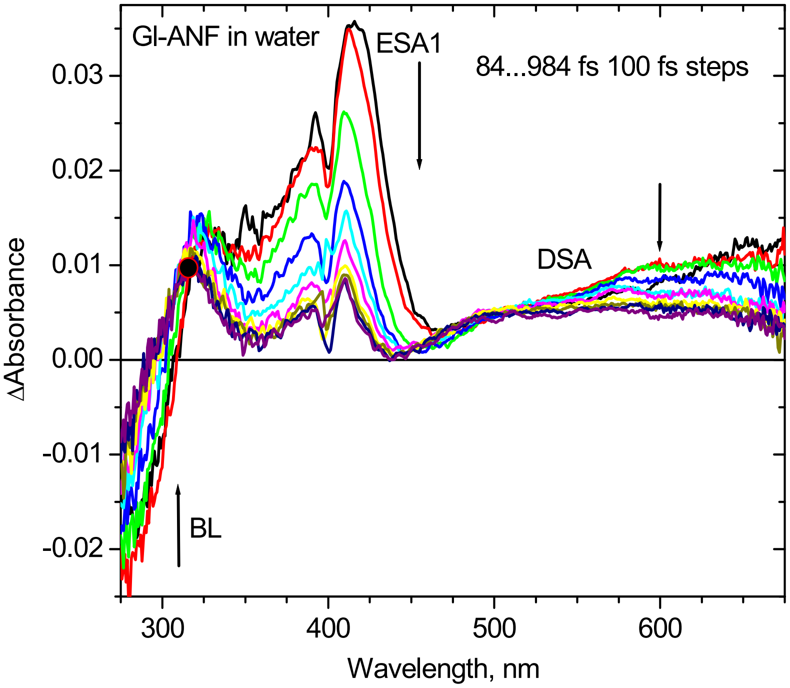

Figure 6.2.5-3 Transient absorption spectra of Gl-ANF in water from 84 fs to 984 fs with time steps of 100 fs. The amplitudes of ESA1 and DSA started to decrease on this time scale.

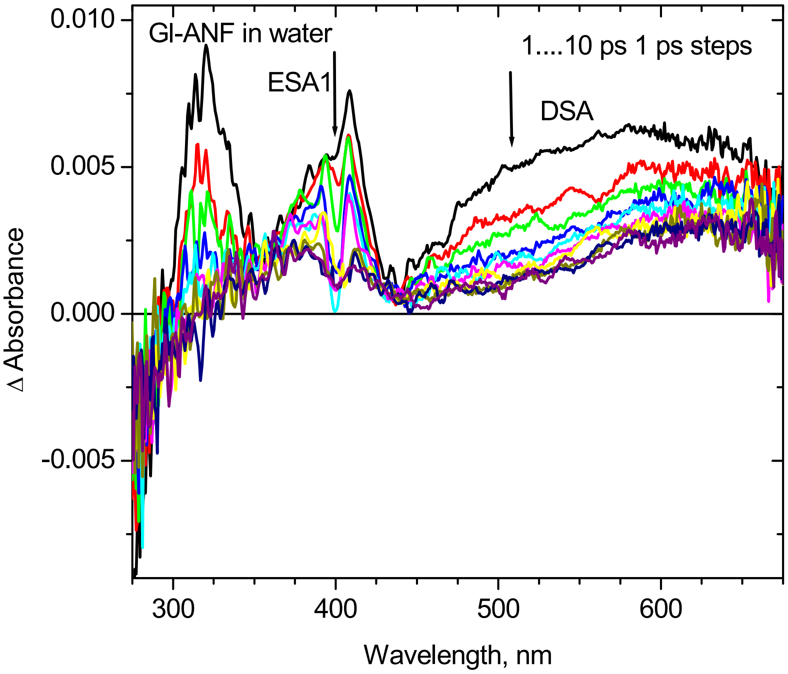

Figure 6.2.5-4 Transient absorption spectra of Gl-ANF in water from 1 ps to 10 ps with time steps of 1 ps. All spectral evolution is completed by now.

6.3 Dynamics in the excited state: possible explaination

The transient stimulated emission and transient absorption spectra by the excited chromophore in a solvent can be used to gain insight into *inter*molecular relaxation of the solvent − i.e. solvation − or into *intra*molecular rearrangement such as vibrational relaxation, isomerisation, intramolecular charge transfer, intersystem crossing, or H-abstraction from solvent. The difference between the two types of processes are explained by scheme 1 and 2 in figure 6.3-1. The scheme 1 represents the solvation process. The chromophore is pumped in a vertical $S_1 \leftarrow S_0$ transition by ultrafast pulses, preferably without excess vibrational energy. After the excitation, the induced transient spectra show features which can be assigned to excited-state absorption (ESA) $S_n \leftarrow S_1$ and to simulated emission (SE) $S_1 \rightarrow S_0$ from the evolving S_1 state. When the configuration of the solvent evolves around the S_1 state, this is reflected in the red shift of the SE as shown in scheme 1 (dynamic Stokes shift). It may be the case that the equilibrium solvent configuration of a higher excited state S_n is not much different from that of the S_0 state, as is also shown in scheme 1. In this case the ESA $S_n \leftarrow S_1$ would simultaneously shift to the blue. The scheme 2 explains the situation when other, intramolecular processes occur in addition to solvation. For example the excited solute molecules may relax nearly horizontally (wavy arrow) to another minimum of the potential surface. If that state has no dipole coupling to the ground state, stimulated emission is not seen and the corresponding state might be termed a "dark state" (DS). However it is quite possible that this dark state is seen by excited-state absorption, which is here termed "dark-state absorption" (DSA). With time, the excited molecules after reaching the DS may relax to the ground state by internal conversion. In most cases both solvation and intramolecular processes will occur at the same time. For example there are indications of intramolecular reorganisation in C153 in parallel with solvation [A0090, KRE97].

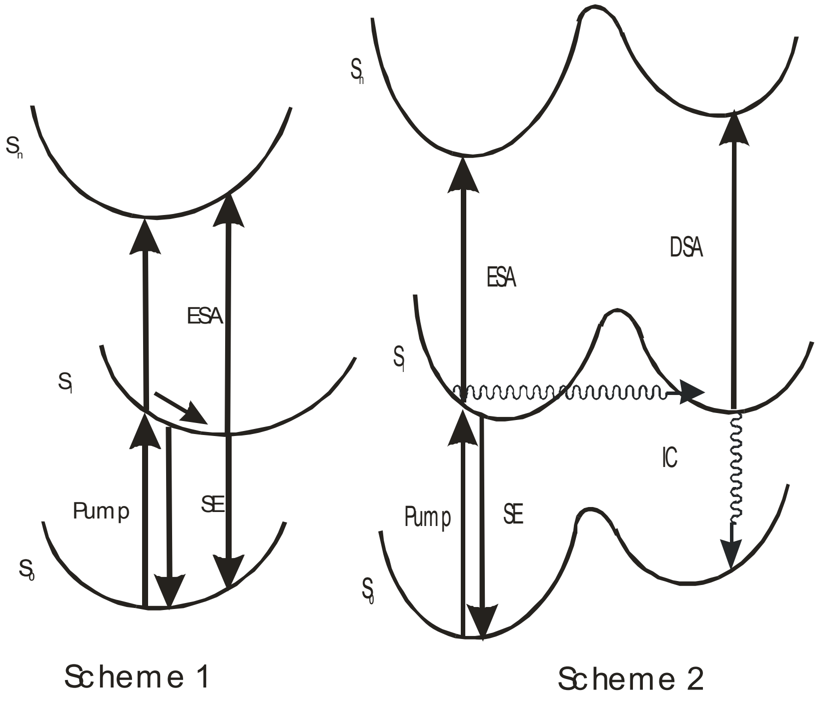

Figure 6.3-1 Scheme 1 explains the solvation dynamics, while Scheme 2 refers to an intramolecular process (leading to a "dark state") in addition to solvation dynamics. For an explanation see the text.

These schemes will now be related to the transient absorption spectra of dM-ANF and Gl-ANF. At first consider the solvent acetonitrile for both cases. The behavior of the transient absorption spectra of ANF derivatives and Gl-ANF are different here, mainly for SE. With dM-ANF the SE shifts towards the red from 525 nm to 650 nm during 1ps, at the same time exposing a bleach at 450 nm. The band shape and width of SE does not change during this process which suggests that there is no intramolecular process on this time scale. Also the prominent ESA band at 425 nm moves slightly to the blue, which results in an apparent blue shift of the bleach also. Taken together, it appears that only solvation is active here and dM-ANF follows scheme 1. On the other hand, with Gl-ANF the stimulated emission is no longer observed after 300 fs. It may still be present, but the net absorbance in the fluorescence region has turned positive so that excited-state absorption dominates. When increasing time the positive OD even increases and there is no recognizable shifts. There is also no bleach in the region of the first absorption band. On the whole, ESA is much more pronounced compared to the previous case, without spectral evolution. It follows that some other process apart from solvation takes place. To sum up, we have:

1. Fast decay of SE and slower decay of ESA, similar to observations with *p*-nitroaniline and dimethylamino-*p*-nitroaniline [FKS00].
2. Temporary isosbetic points are seen at 487 nm (at 494 nm before 80 fs, blue shifting with time) and at 657 nm (see figure 6.2.1-1)

Hence we propose that Gl-ANF might follow scheme 2. Note that the difference of behavior, of Gl-ANF vs dM-ANF in acetonitrile, is maintained in the solvents methanol and DMSO. It must arise from the glucose unit which is attached to the ANF moiety. It is seen most clearly by examining kinetic traces at two characteristic wavelengths as shown in figure 6.3-2 (at 464 nm in the bleach region) and in figure 6.3-3 (at 630 nm in the fluorescence region). In figure 6.3.2, Gl-ANF has positive contribution which corresponds to ESA, whereas in dM-ANF has negative contribution after 250 fs which corresponds to bleach. In figure 6.3.3, Gl-ANF has positive contribution up to 5 ps after that stationary fluorescence appears, whereas in dM-ANF, SE has seen up to 1 ps after that ESA dominates.

Next we will consider the transient absorption spectra in THF, ethyl acetate and 1,4 dioxane. In these solvents the "dark-state" absorption is not seen with Gl-ANF, which therefore resembles the dM-ANF behavior in these solvents. The trend of the spectral evolution of dM-ANF and Gl-ANF in 1,4-dioxane is shown in the following figure 6.3-4, and 6.3-5 again at 464 nm and 600 nm. The ESA appears more to the red in these solvents compared to the previous solvents, exactly on the bleach which is completely filled up so that only positive absorption remains in this region. We assign the excited-state reaction to scheme 1 for both chromophores in these solvents. In each figure both chromophore have same contribution, but with different time constants.

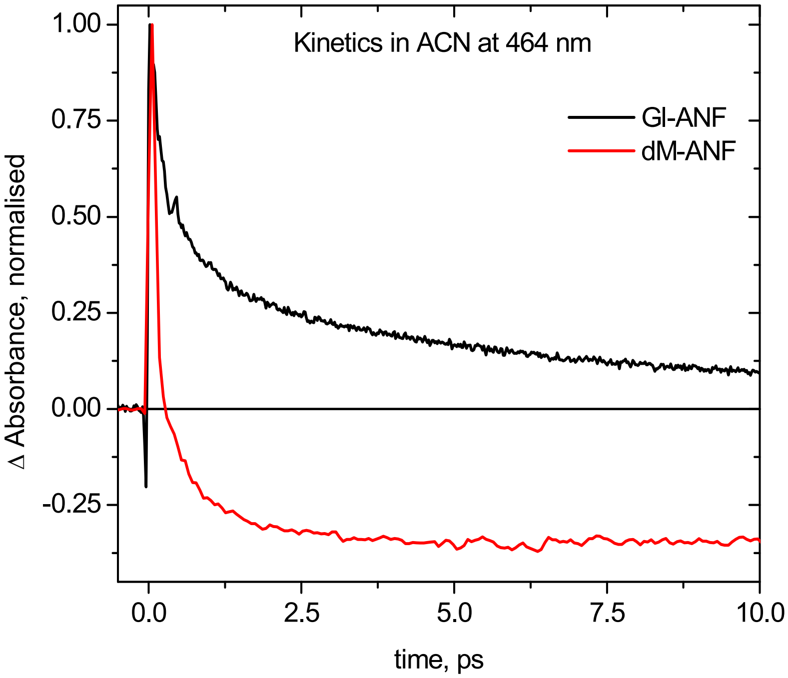

Figure 6.3-2 Kinetic traces of Gl-ANF (black) and dM-ANF (red) in acetonitrile at 464 nm. Gl-ANF shows a positive contribution and dM-ANF a negative contribution.

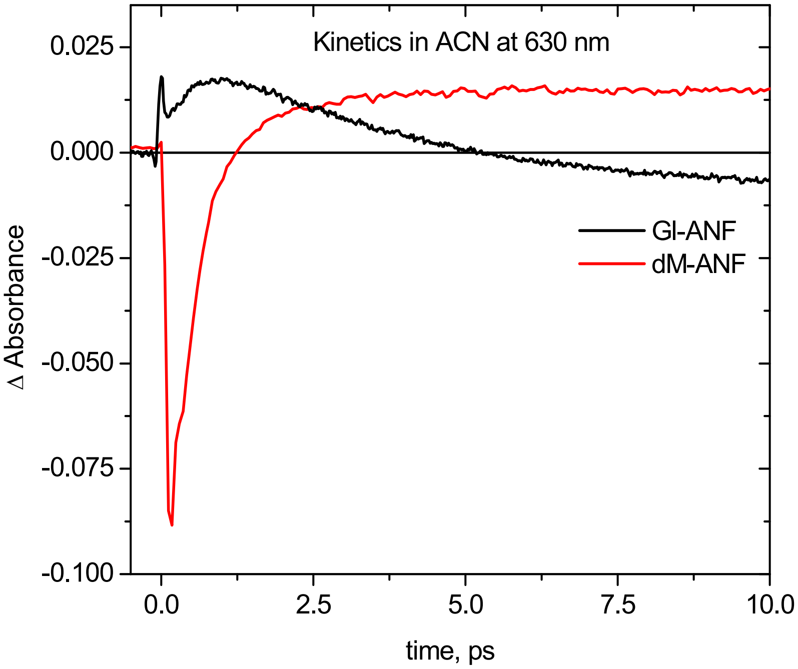

Figure 6.3-3 Kinetic traces of Gl-ANF (black) and dM-ANF (red) in acetonitrile at 630 nm. The Gl-ANF transient absorption trace is initially positive, with a peak at 1.25 ps, whereas dM-ANF shows negative stimulated emission at the same time.

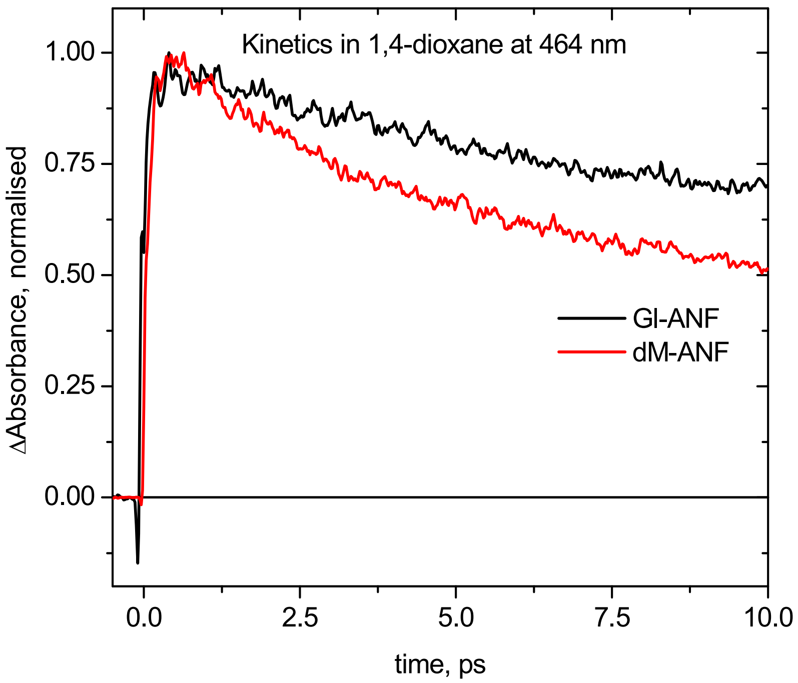

Figure 6.3-4 Kinetic traces of Gl-ANF and dM-ANF in 1,4-dioxane at 464 nm. Both Gl-ANF and dM-ANF show dominant excited-state absorption at all time scales here.

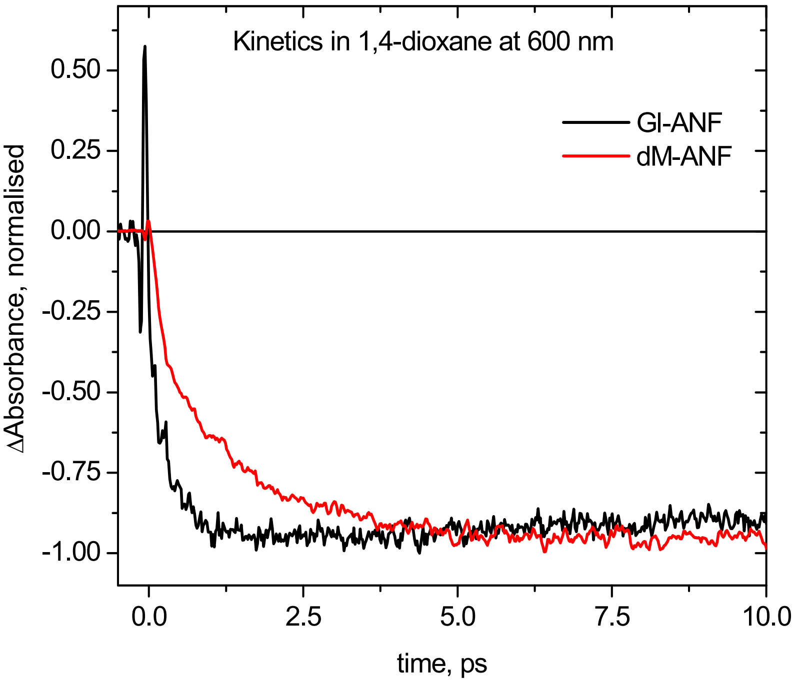

Figure 6.3-5 Kinetic traces of Gl-ANF and dM-ANF in 1,4-dioxane at 600 nm. Both Gl-ANF and dM-ANF show negative contribution after 200 fs

6.4 Solvation relaxation curves

6.4.1 Spectral decomposition

The detailed procedure for decomposing the transient absorption spectra into Bleach (BL), Excited State Absorption (ESA), and Stimulated Emission (SE) spectra was already explained in the experimental section 3.11.3. A representative spectral decomposition for dM-ANF in 1, 4-dioxane, at 119 ps, is shown in figure 6.4.1-1. Results for Gl-ANF in THF at 100 ps are shown in figure 6.4.1-2.

Then for a given spectral evolution the SE(t) spectra and hence the peak frequency $\tilde{\nu}(t)$ is obtained. Figure 6.4.1-3 – -5 show the curve $\tilde{\nu}(t)$ of individual compounds in various solvents. By referencing to $\tilde{\nu}(\infty)$ from stationary measurements and to the average emission frequency $\tilde{\nu}(0)$ at time-zero we reach the experimental, normalized solvation relaxation function C(t) (see eqn. 3.37 on p. 50). The main difficulty of this procedure is to find $\tilde{\nu}(0)$; we use the value derived from time-zero analysis as described in section 3.10 (*cf.* eqn. 3.2.8). The C(t) curves for ANF, dM-ANF, and Gl-ANF in different solvents are explained in the following section. With Gl-ANF one has to take into account that broad ESA (which was ascribed to a dark state) dominates over SE – in fact the latter can not even be recognized. In this case we obtain an empirical relaxation function by monitoring the blue shift of the prominent ESA band. C(t) were fitted with a multiexponential function

$$C(t) = \sum_{i=1}^{n} a_i \exp(-t/\tau_i) \qquad 6.3$$

with $a_i \geq 0$ and $\sum_{i=1}^{n} a_i = 1$, and the resulting time constants and their amplitudes are given in table 6.1 – 6.3 for different chromophores. C(t) can never be fitted by single exponential. Solvation relaxation curves in acetonitrile and THF were fitted with biexponential function while others were fitted with triexponentials. A representative fit with a biexponential is shown in figure 6.4.1-6 for Gl-ANF in acetonitrile.

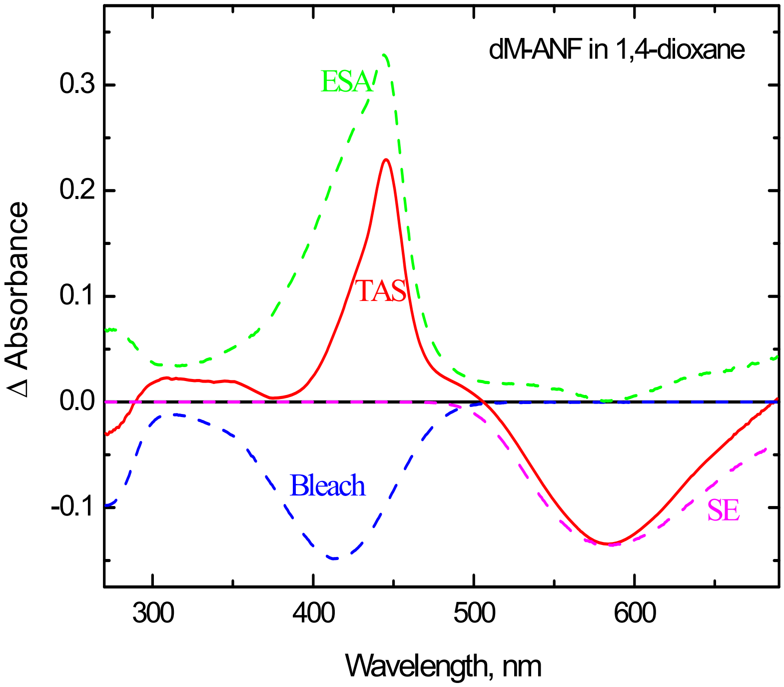

Figure 6.4.1-1 Spectral decomposition of transient absorption spectra of dM-ANF (TAS, red-line) in 1,4-dioxane at 119 ps. The decomposition yields the positive contribution of excited-state absorption (ESA, green-dotted) and the negative contributions of bleach (BL, blue-dotted) and stimulated emission (SE, magenta-dotted). The SE band is described by a lognormal distribution.

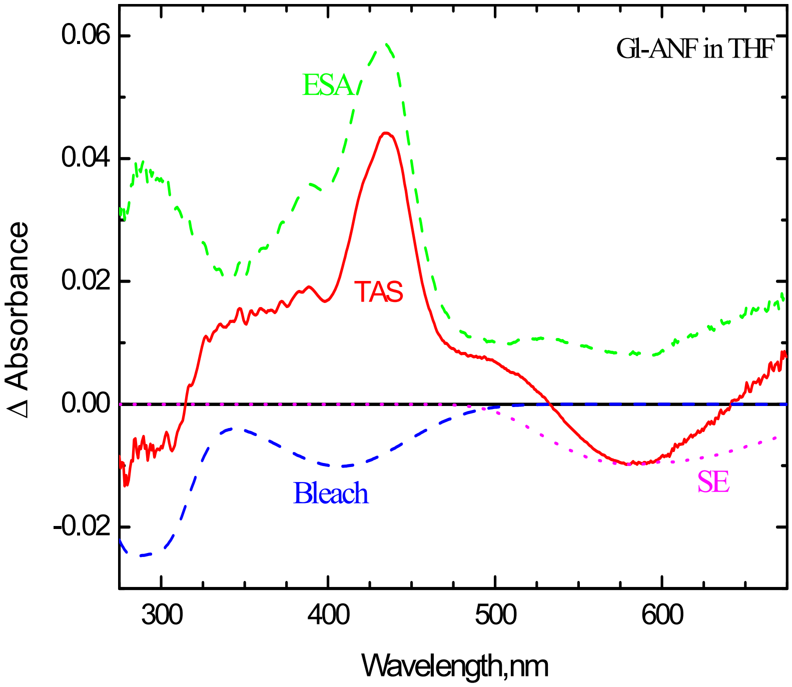

Figure 6.4.1-2 Spectral decomposition of transient absorption spectra of Gl-ANF in tetrahydrofuran at 100.5 ps as shown in the figure 6.4.1-1.

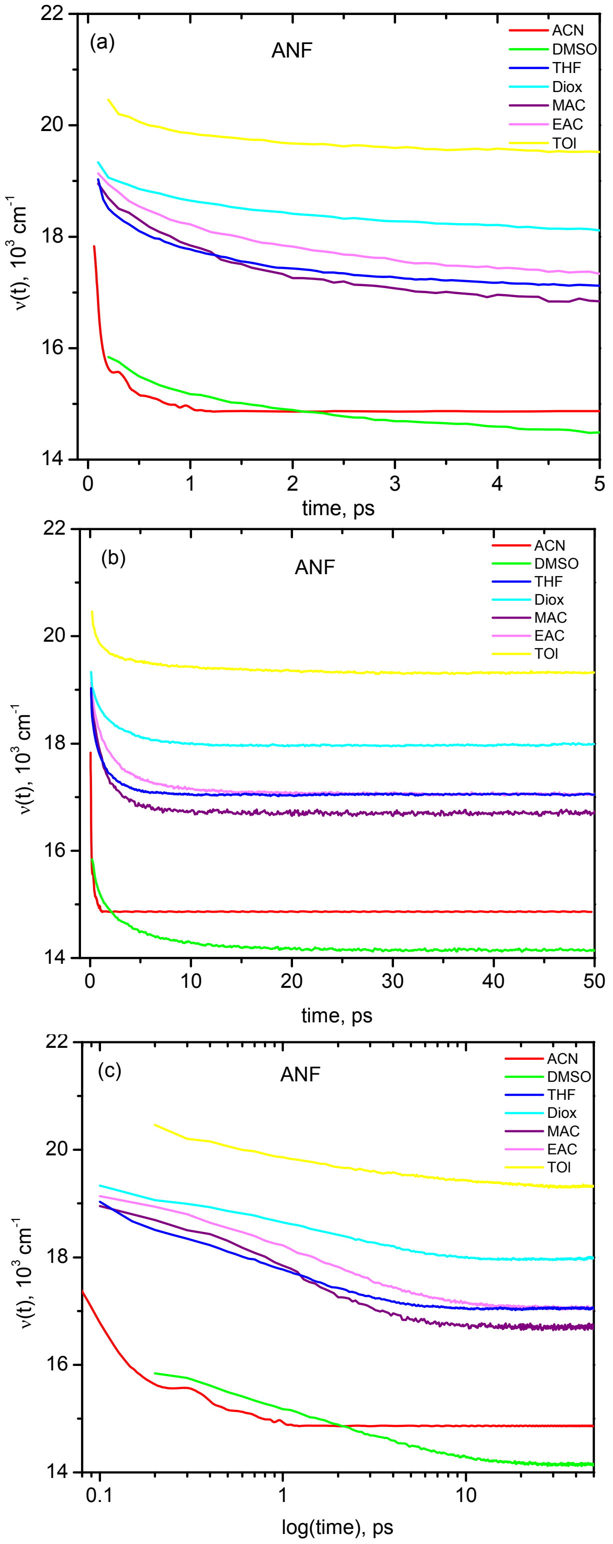

Figure 6.4.1-3 Solvation relaxation curves derived from peak frequency of stimulated emission, of ANF in various solvents. Different solvents are shown in different colors. Two different time scales are shown: (a) until 5 ps, (b) until 50 ps, while (c) runs until 50 ps on a logarithmic scale.

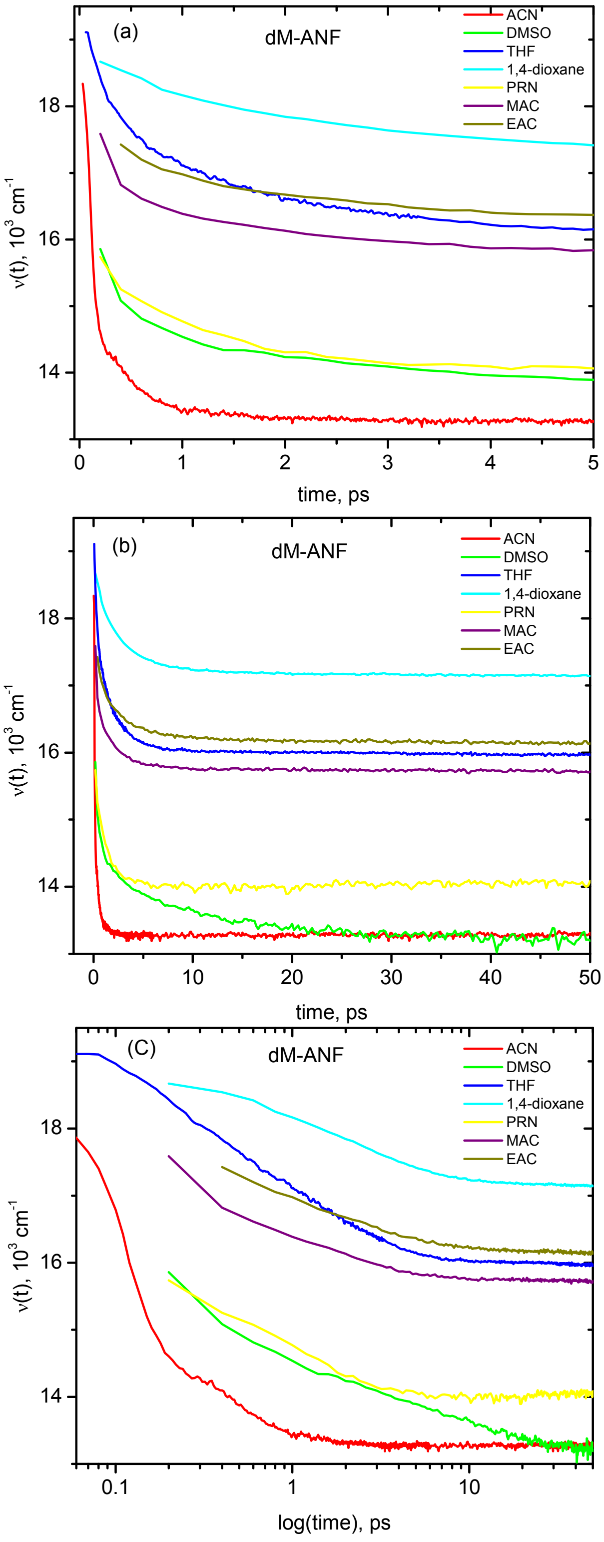

Figure 6.4.1-4 Solvation relaxation curve derived from peak frequency of SE from dM-ANF in different solvents. The scales are as in the previous figure.

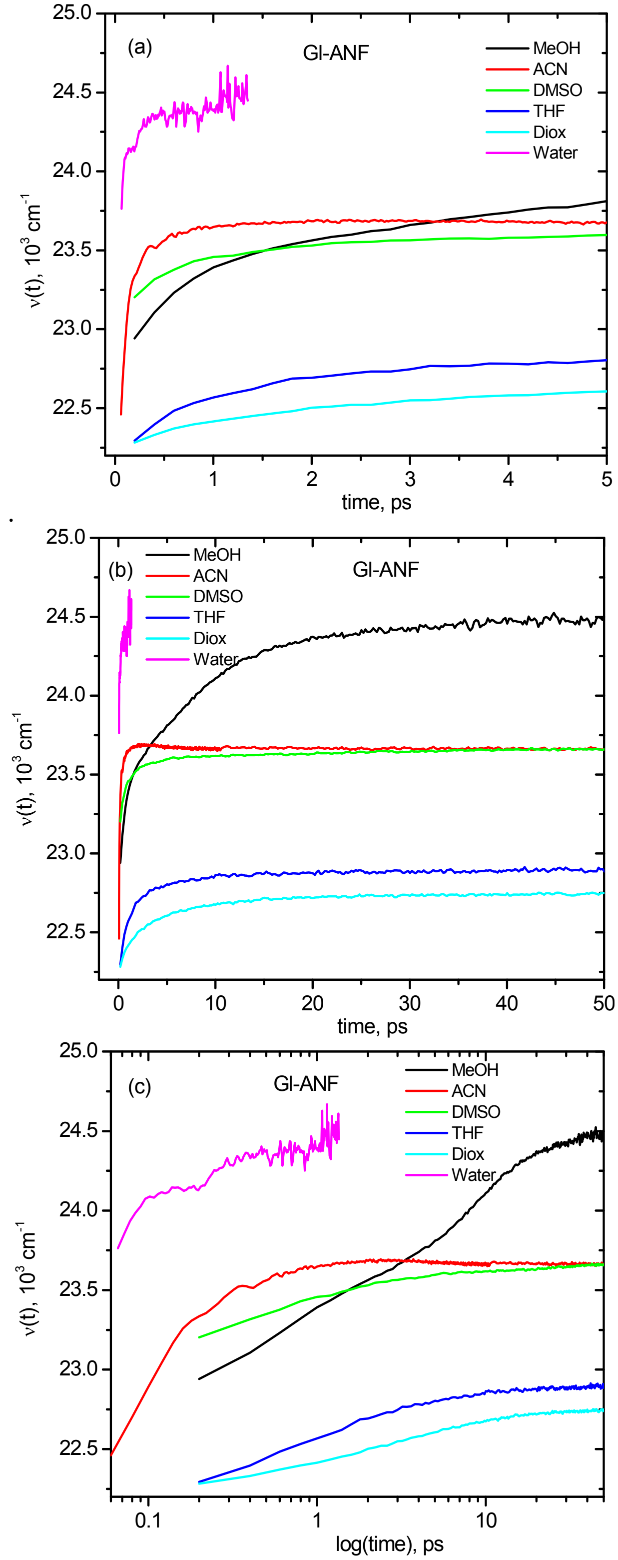

Figure 6.4.1-5 Solvation relaxation curve derived from peak frequency of ESA of Gl-ANF in different solvents.

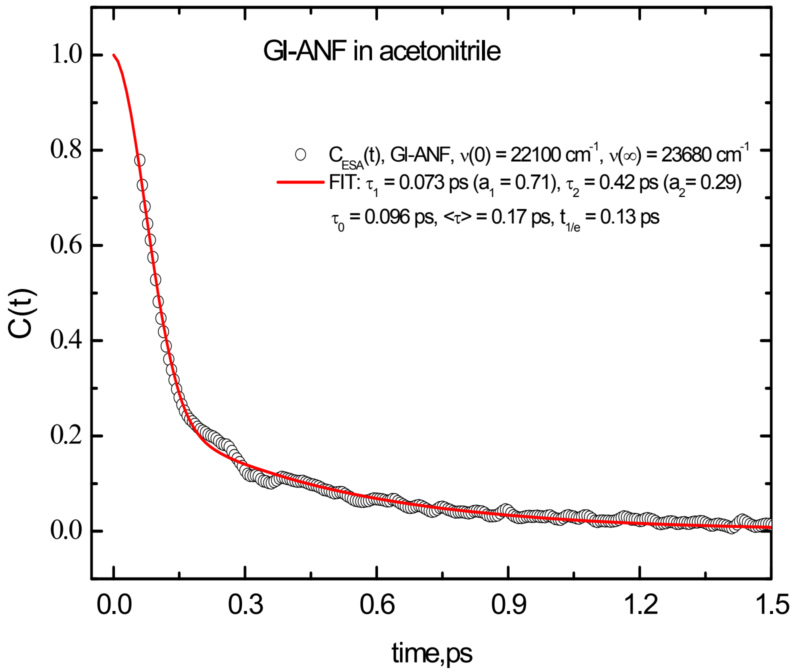

Figure 6.4.1-6 A representative biexponential fit to normalized solvation relaxation points from Gl-ANF in acetonitrile. From the fit, the initial time constant τ_0, the correlation time or average time constant $\langle\tau\rangle$, and the time $t_{1/e}$ required for to reach 1/e = 0.368 are obtained.

The solvation relaxation function can be characterized by the following three time parameters: (a) the initial time constant τ_0, where

$$\tau_0^{-1} = \sum a_i \tau_i^{-1} \tag{6.4}$$

is the negative slope of C(t), (b) the correlation time or average time constant

$$\langle\tau\rangle = \sum a_i \tau_i , \tag{6.5}$$

which is the area under C(t), and (c) the time $t_{1/e}$ required for to reach 1/e = 0.368. Of course, for a single-exponential function all of these times are equal.

Table 6.1 Summary of spectral response functions for ANF

Solvent	**Wavenumbers, cm^{-1}**		**Multiexponential fit parameters**						**Characteristic time**		
	ν_0	ν_∞	a_1	τ_1 (ps)	a_2	τ_2 (ps)	a_3	τ_3 (ps)	τ_0 (ps)	$t_{1/e}$ (ps)	$\langle\tau\rangle$ (ps)
Acetonitrile	19230	14622	0.66	0.065	0.34	0.60	-	-	0.09	0.24	0.10
Methanol-ESA	22400	24560	0.25	0.082	0.49	1.13	0.26	12.05	0.29	1.49	3.71
DMSO	18980	14145	0.56	0.087	0.19	0.42	0.25	4.29	0.14	0.23	1.20
1,4-dioxane	20486	18000	0.58	0.100	0.37	2.15	0.05	15.00	0.17	0.41	1.62
THF	19926	17043	0.51	0.105	0.49	1.63	-	-	0.19	0.49	0.85
Methyl Acetate	20645	16670	0.36	0.040	0.53	0.99	0.11	5.90	0.09	0.66	1.19
Ethyl Acetate	20634	17041	0.40	0.047	0.36	1.18	0.24	5.03	0.11	0.91	1.65
Toluene	21035	19300	0.56	0.260	0.25	1.39	0.19	10.25	0.42	0.70	2.44
Dibutyl Ether	20789	18981	0.59	0.133	0.41	17.59	-	-	0.22	1.84	7.26

where $\nu(0)$ is obtained from expected time zero emission maximum on the basis of the reference nonploar solvent (eqn. 3.28) and $\nu(\infty)$ is obtained from maximum of the stationary emission spectrum. Parameters of multiexponential fit of $C(t)$ are obtained according to eqn. 6.3. The characteristics times listed here are the initial time τ_0, the 1/e time, and the average or correlation time $\langle\tau\rangle$ defined by eqn. 6.4 and 6.5. ESA – the values are obtained by following the shift of the excited state absorption peak with time, otherwise with stimulated-emission peak shift.

Table 6.2 Summary of spectral response functions for dM-ANF

Solvent	**Wavenumbers, cm^{-1}**			**Multiexponential fit parameters**					**Characteristic time**		
	ν_0	ν_∞	a_1	τ_1 (ps)	a_2	τ_2 (ps)	a_3	τ_3 (ps)	τ_0 (ps)	$t_{1/e}$ (ps)	$\langle\tau\rangle$ (ps)
Acetonitrile-ESA	21400	23333	0.80	0.073	0.20	0.48	-	-	0.09	0.12	0.15
Methanol-ESA	21300	24360	0.23	0.062	0.51	1.30	0.26	9.64	0.24	1.61	3.18
DMSO	18762	13180	0.64	0.078	0.18	1.26	0.18	12.70	0.12	0.19	2.56
1,4-dioxane	20,030	17126	0.43	0.080	0.52	2.06	0.05	22.21	0.18	1.04	2.34
THF	19652	15964	0.51	0.227	0.49	1.98	-	-	0.40	0.70	1.09
Methyl Acetate	18630	15700	0.50	0.110	0.45	1.31	0.05	17.00	0.20	0.46	1.49
Ethyl Acetate	18800	16120	0.30	0.086	0.52	0.98	0.18	7.98	0.25	0.90	1.97
Propionitrile	17860	14020	0.56	0.071	0.44	1.17	-	-	0.12	0.22	0.55

as in the table 6.1

Table 6.3 Summary of spectral response functions for Gl-ANF

Solvent	**Wavenumbers, cm^{-1}**		**Multiexponential fit parameters**						**Characteristic time**		
	ν_0	ν_∞	a_1	τ_1 (ps)	a_2	τ_2 (ps)	a_3	τ_3 (ps)	τ_0 (ps)	$t_{1/e}$ (ps)	$\langle\tau\rangle$ (ps)
Acetonitrile-ESA	22100	23680	0.71	0.073	0.29	0.42	-	-	0.09	0.17	0.13
Methanol -ESA	22300	24500	0.10	0.054	0.36	0.36	0.54	9.56	0.34	3.67	5.30
DMSO- ESA	22600	23683	0.62	0.100	0.30	1.15	0.08	27.15	0.15	0.23	2.60
1,4-dioxane	21700	22740	0.43	0.080	0.24	1.33	0.33	5.80	0.18	1.19	2.27
THF	18100	17046	0.66	0.230	0.34	3.38	-	-	0.34	0.50	1.30
Water-ESA	23500	24600	0.22	0.055	0.45	0.11	0.33	1.44	0.12	0.53	0.19

as in the table 6.1

6.4.2 Solvation relaxation curves for organic solvents

Acetonitrile: Relaxation curves for the investigated chromophores in acetonitrile are shown on linear time scales in figure 6.4.2-1a, b and on a logarithmic scale in figure 6.4.2-1c. The curves begin typically at 50-70 fs, at a delay time when the stimulated emission spectrum can be first recognized and fitted. The corresponding curve for Coumarin 153 (C-153) [HGP95] was added for comparison (in this case a first entry is shown at 60 fs, well inside the stated time resolution of 120 fs [HGP95]). For all compounds, relaxation in ACN shows a steep decline at earliest time followed by a small hump, or shoulder, at 300 fs. The latter had already been assigned quantitatively to a librational wave packet in the solvent [RKE98]. It is most pronounced with ANF but it is just recognized with dM-ANF and Gl-ANF on the logarithmic time scale. The relaxation processes in all are completed before 1.5 ps.

Dimethyl sulfoxide: Relaxation curves of the three ANF derivatives in DMSO is shown in figure 6.4.2-2. for 1.5 ps (a) and 20 ps (b,c) respectively. For all compounds, relaxation in DMSO declines as steeply as in ACN until 300 fs. By this time about 25% of C(t) remains which is relaxing much more slowly. The second solvation component of ANF is faster (τ_2= 420 fs) than that of others (dM-ANF τ_2= 1.26 ps, Gl-ANF τ_2= 1.15 ps). In Gl-ANF oscillations around 300 fs are clearly seen, with peaks at 236 and 440 fs and a trough at 335 fs. The time structure and width is different from that in acetonitrile, however. The relaxation is completed at 10 ps in DMSO.

1,4 dioxane: C(t) curves in 1,4-dioxane are shown in figure 6.4.2-3, where the relaxation is seen to persists up to10 ps for all compounds. For C153, this observation was assigned to the large quadrupole moment arising from the presence of two polar groups CH_2−O−CH_2. Note that the chromophores have large Stokes shift even though 1,4-dioxane is considered as a nondipolar solvent. With Gl-ANF an oscillation was observed with maxima at 158 and 363 fs and a minimum at 270 fs. The relative amplitude of the initial, fastest component is larger for ANF compared to the other chromophores.

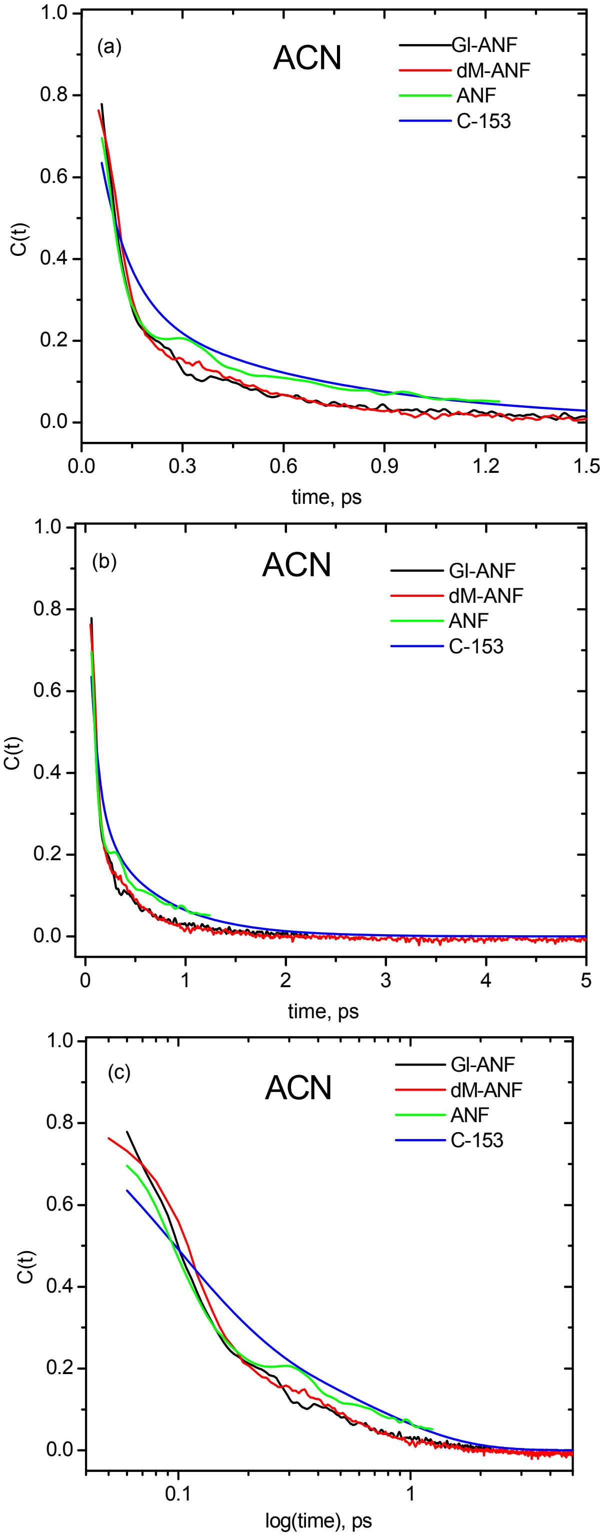

Figure 6.4.2-1 a, b & c Normalized relaxation curves based on eqn. 3.37 for ANF(green), dM-ANF(red), Gl-ANF(black) and Coumarin 153(C-153, blue) [HGP95] in acetonitrile. Compared are again on linear time scales (a and b) and on a logarithmic scale (c).

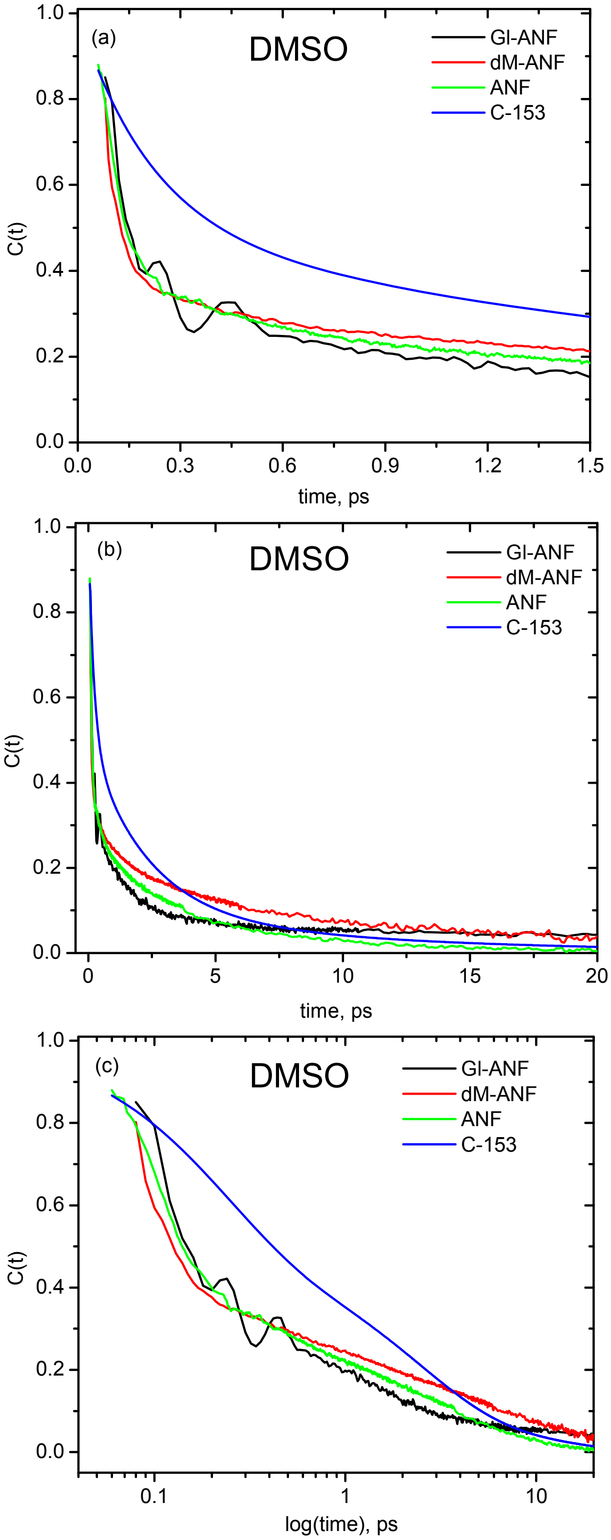

Figure 6.4.2-2 a, b & c Normalized solvation curve for the ANF derivatives and C-153 in DMSO, as in figure 6.4.2-1.

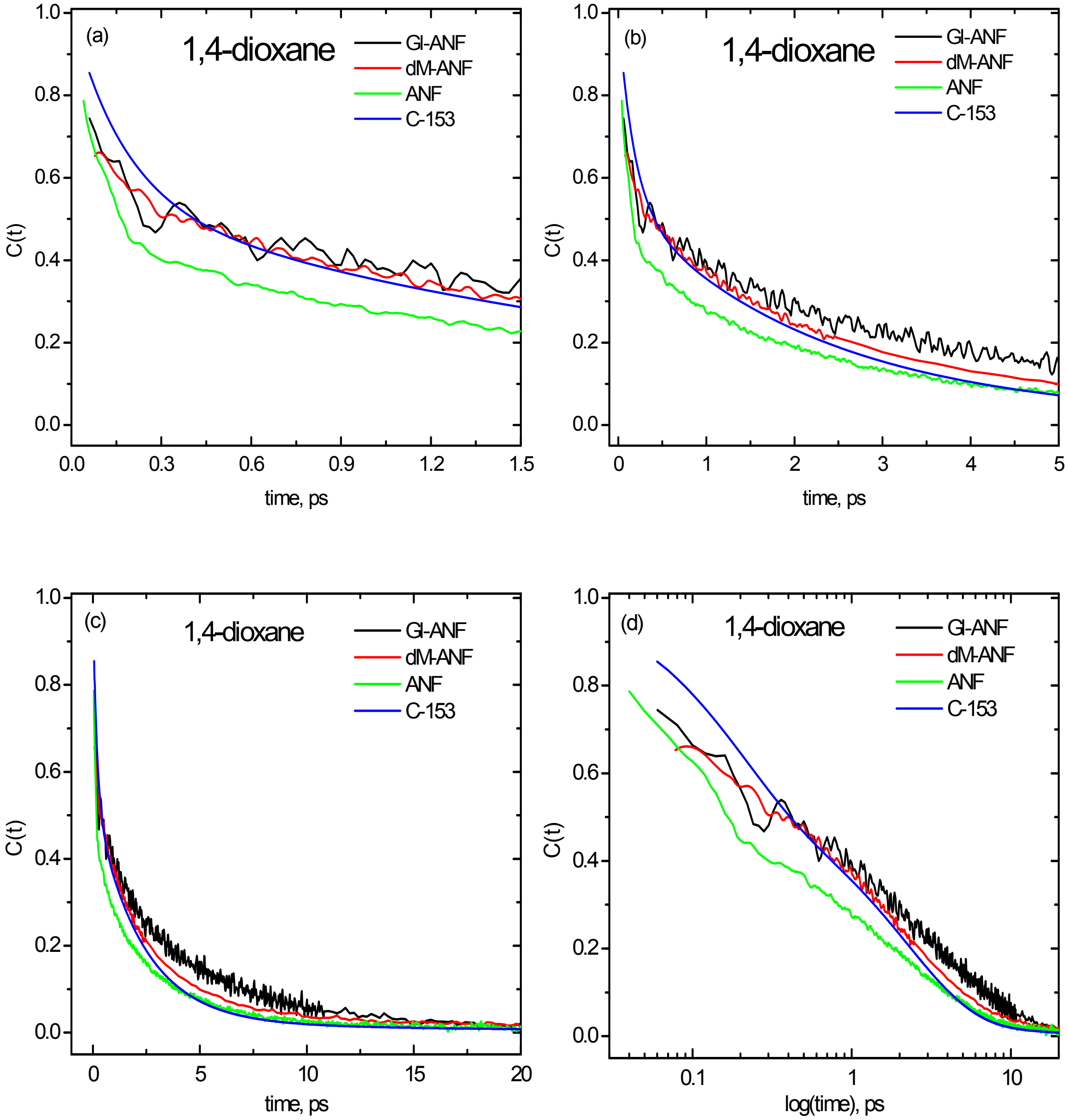

Figure 6.4.2-3 a, b, c & d Normalized solvation curves for ANF derivatives and C-153 in 1,4-dioxane, as in figure 6.4.2-1.

Over all, the initial part of the solvation has time constant of ~100 fs and constitutes the 42-57 % of the relaxation.

Methanol: Here relaxation curve for all chromophores were obtained by following the ESA shift. Because in transient absorption spectra, the stimulated emission region has noise. The results are shown in figure 6.4.2-4. Now $\tilde{\nu}(0)$ must be obtained from the initial excited-state absorption spectrum. This value can be found unambiguously because the ESA is sharp and dominant around 440 nm. Relaxation is seen until 25 ps in methanol, after which time stationarity seems to have been reached. The initial fast components observed ($\tau_1 \approx 80$ fs) is nearly same for all chromophores − mainly of O−H librational character [FL094] where as Gl-ANF has large amplitude of slower components. The latter effect may arise from interactions of glucose hydroxyl groups with methanol. The relaxation behavior of ANF and dM-ANF is quite similar.

Tetrahydrofuran: Figure 6.4.2-5 shows the C(t) curves in THF, which looks similar for all chromophores. Again, Gl-ANF shows oscillations, with peaks at 105 and 236 fs and a trough at 176 fs.

Methyl and Ethyl acetate: C(t) for methyl and ethyl acetate are given in figure 6.4.2-6, where results with the ANF (green lines) and dM-ANF (red) chromophore are shown together. The initial part of the curve is different for both chromophores, as can be seen clearly up to 300 fs. The first stimulated emission spectrum that could be recorded with ANF, at 50 fs, appears more to the red than the spectrum at this time with dM-ANF. This behavior is reflected by the first time constant and its amplitude. For example in methyl acetate, the amplitude and time constants of ANF are $a_1 = 0.36, \tau_1 = \underline{0.04\text{ ps}}$ and $a_2 = 0.53, \tau_2 = 0.99$ ps, while for dM-ANF we find $a_1 = 0.50, \tau_1 = \underline{0.11\text{ ps}}$ and $a_2 = 0.45, \tau_2 = 1.3$ ps.

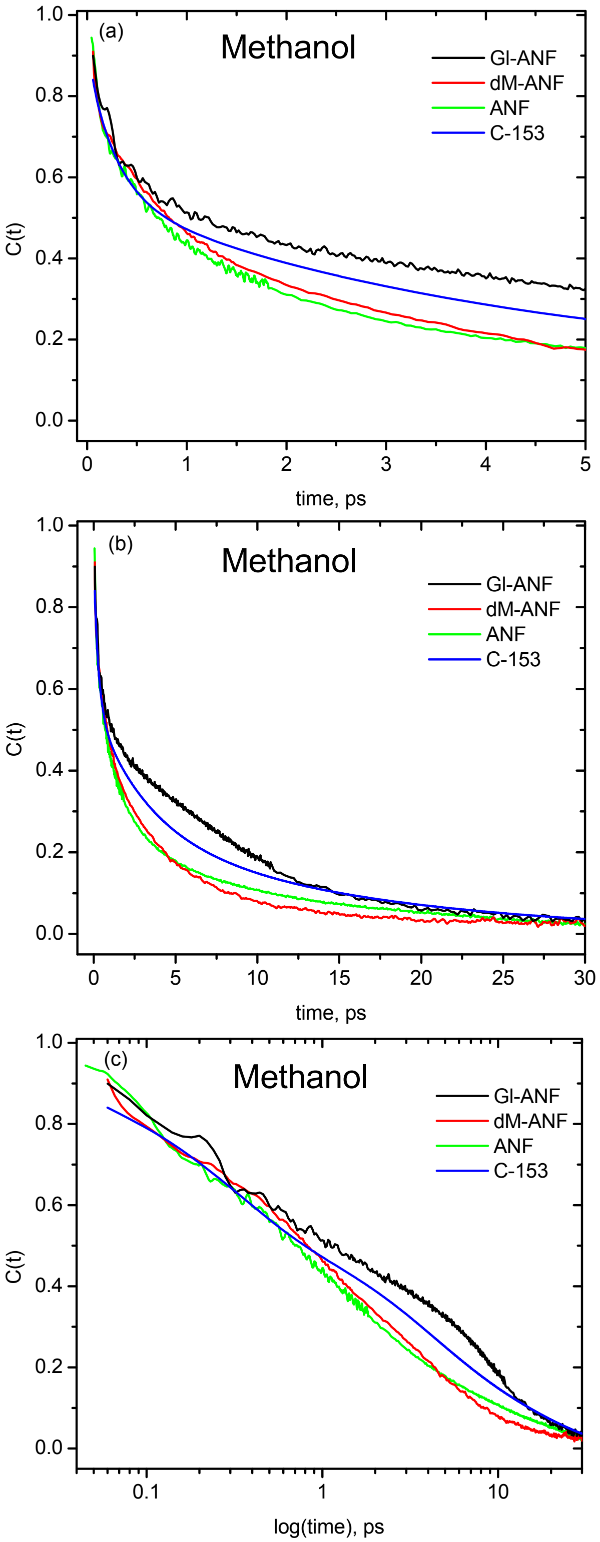

Figure 6.4.2-4 a,b & c Normalized solvation curve for ANF derivative and C-153 in methanol. In this case, C(t) was calculated from ESA shifts for all ANF derivatives.

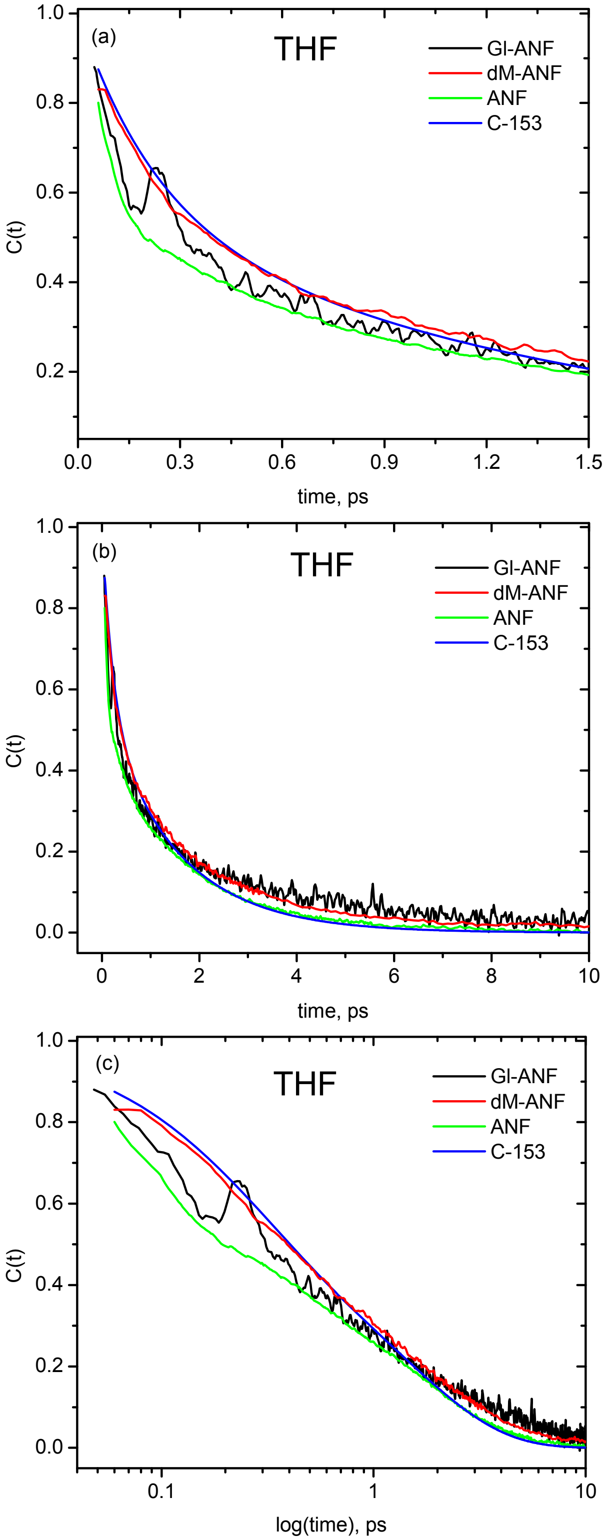

Figure 6.4.2-5 a, b & c Normalized solvation curve for ANF derivative and C-153 in tetrahydrofuran C(t) was calculated on the basis of SE shifts for all ANF derivatives.

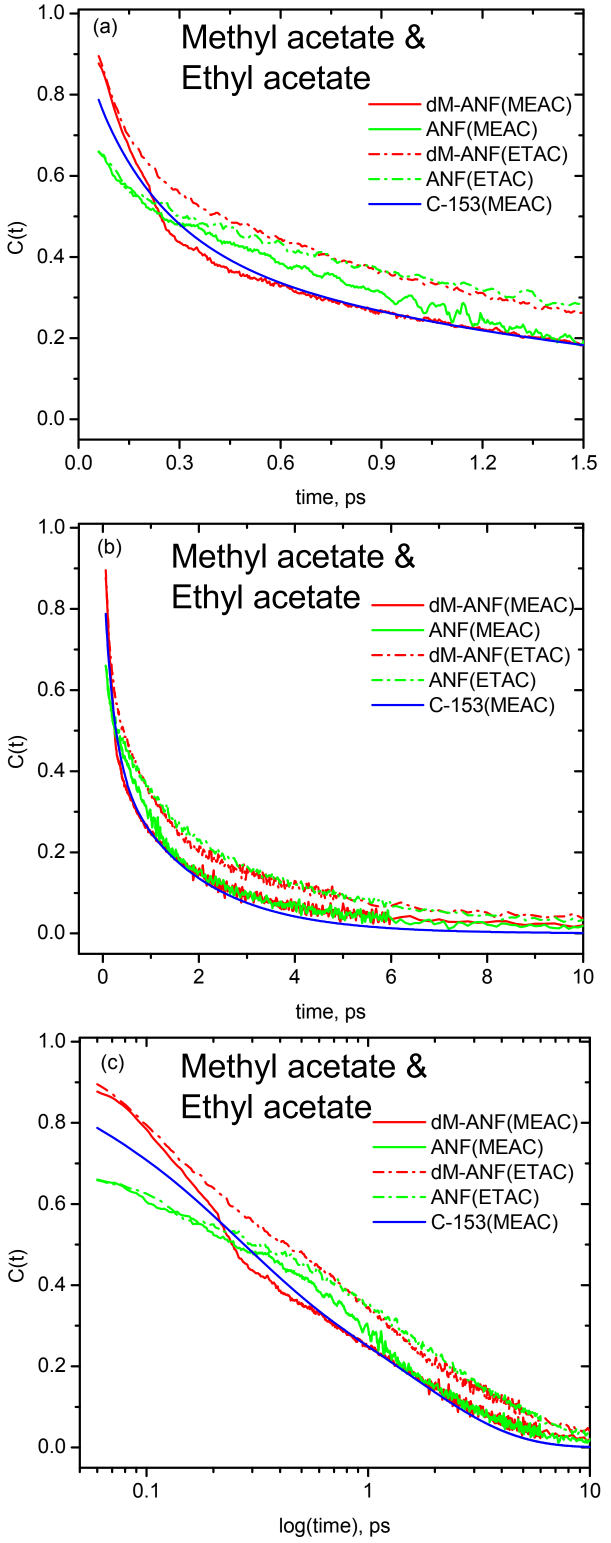

Figure 6.4.2-6 a, b & c Normalized solvation curve for ANF, dM-ANF and C-153 in methyl (MEAC, line) and ethyl acetate (ETAC, dotted), as in figure 6.4.2-1.

6.4.3 Summary and comparison with Coumarin 153 (C-153)

Summarizing all experimental results, we observe the following:

We obtained spectral relaxation curves using transient absorption spectroscopy, by monitoring the shift of the stimulated emission band. In all measurements, the pump-probe temporal cross correlation width is about 60 fs. The transient behavior of Gl-ANF differs from that of the other fluorene derivatives due to intramolecular electronic processes. But with ANF and dM-ANF the stimulated emission band is well defined and the corresponding relaxation functions are at least of the same quality as those reported for C153. Comparison yields the following:

In *acetonitrile* the C(t) curves for ANF and dM-ANF agree well – i.e. on all time scales – with the C(t) curve for C-153. Differences can be attributed to better time resolution for the fluorene curves, by which oscillations become noticeable in acetonitrile. In *dimethyl sulfoxide*, the C(t) of the fluorene derivatives strongly deviates from the relaxation curve of C-153 at all time scales. In *1,4-dioxane,* the shape of the curve of dM-ANF and C-153 agree well until 2 ps, while ANF and C-153 relaxed in similar fashion after 4 ps. In *methanol* the initial fast components of all the chromophore are nearly the same; relaxation curves are identical until 1ps. Afterwards, until about 5 ps, the fluorene derivatives relax faster than C-153. After 5 ps we can not draw definite conclusions because C(t) < 0.1 and a noisy region is entered. The difference between C153 and the substituted fluorenes may arise from the different specific hydrogen bonding behavior of solutes with the solvent. In *THF,* C(t) of dM-ANF and C-153 are in excellent agreement from the beginning until 1.5 ps. The curve for ANF matches the C-153 curve after 2 ps. This means that the second exponential time components of the ANF and C-153 are identical, while dM-ANF is relaxing slower. In *methyl acetate*, it is interesting to note that all the three chromophores are relaxing in similar fashion until 3ps. Afterwards, the fluorene derivatives are relaxing slower than the C-153. Note however that here one is entering the last fraction of C(t) which is bound below by noise.

We may speculate the reasons for the observed differences between fluorene derivatives and C-153. A critical discussion must take into account differences due to technique and method (“artifacts”) and should aim to identify differences in solvent-solute interaction (the “molecularity” of solvation).

Possible Artifacts: There may be errors in finding the peak frequency ν(t) when not enough spectral width or monitoring wavelengths are seen. When the shape of the stimulated emission band changes with time, C(t) constructed from the peak frequency may differ from a curve which is based on mean frequencies. The most serious error is probably associated with finding the initial (peak or mean) ν(0) position. The latter enters into normalization, and errors in determining ν(0) propagate onto C(t) accordingly. However note that all of the problem discussed so far affect equally the transient absorption spectra as well as transient fluorescence spectra which were constructed from kinetic curves. The most serious challenge which, in addition, transient absorption presents is that of partitioning the measured spectra into their BL, ESA, and SE components (cf. section 3.11.3). When the SE band is overlapped significantly with a prominent ESA band it may be impossible to separate the two uniquely, causing and equivalent error in the relaxation curve.

Molecularity: If excess vibrational energy is deposited in the solute molecule, vibrational relaxation may contribute to the very early parts of C(t), probably before 200 fs. For the fluorene solutes, however, excess energy is not of concern because excitation took place at the band maximum or at its red flank. Isomerization along low-frequency modes may also contribute to C(t), but again, for ANF and derivatives this complication may be excluded because the main chromophore structure is rigid and planar. Rather, conformational changes could complicate the C-153 relaxation curve because several conformers are possible for the julolidine group [A0090, GCG98]. We conclude that the ANF and dM-ANF relaxation curves depend only on *non*-specific solvation, on hydrogen bonding with solvents, and (in case of mixtures) on preferential solvation.

In order to understand solvation molecularity one has to perform molecular dynamic simulations, which are not part and purpose of the present study. The emphasis here is on an empirical description of measured relaxation curves with various polar probes.

6.4.4 Comparison of C(t) curves obtained from ESA and SE shift

Solvation curves were obtained by monitoring the SE band and/or an ESA band. In several cases either band can be used to construct a relaxation curve. An example is given by dM-ANF in ACN and Gl-ANF in THF, for which the two kinds of $C(t)$ are shown in figure 6.4.4-1 and -2, respectively. In figure 6.4.4-1 the two curves are nearly identical, except at 300 fs where an oscillation is more pronounced in the "ESA curve" compared to the "SE curve". The common oscillation suggests that the two transition energies $S_n \leftarrow S_1$ (for ESA) and $S_1 \rightarrow S_0$ (for SE) are correlated, which reflects the same type of potential is operative in the terminal S_n and S_1 states. Since these potentials are due to polar solvation, then ESA blue-shift indicates that dipole moment of higher states is less than that of the first excited state $\mu_n < \mu_1$ [RKE98]. The blue-shift of the ESA and the red-shift of the SE band are fully correlated in this way.

For Gl-ANF the situation is different (shown in figure 6.4.4-2). Even though the trend of the shape of the curve of SE and ESA band are similar to the previous case, the clear oscillation appears with a different time structure and SE and ESA seem to have opposing amplitude (or the phase between them is 180°). For SE a trough is seen at 170 and peak at 237 fs while for ESA a trough is seen at 260 and peak at 340 fs. This means that the *red*-shift of the ESA band is now correlated with the red-shift of the SE band. In other words, both bands oscillate in the same direction. This is an indication that the ESA and SE bands are not completely separable here, and that some overlap of the SE band exists with the ESA band which was not properly treated.

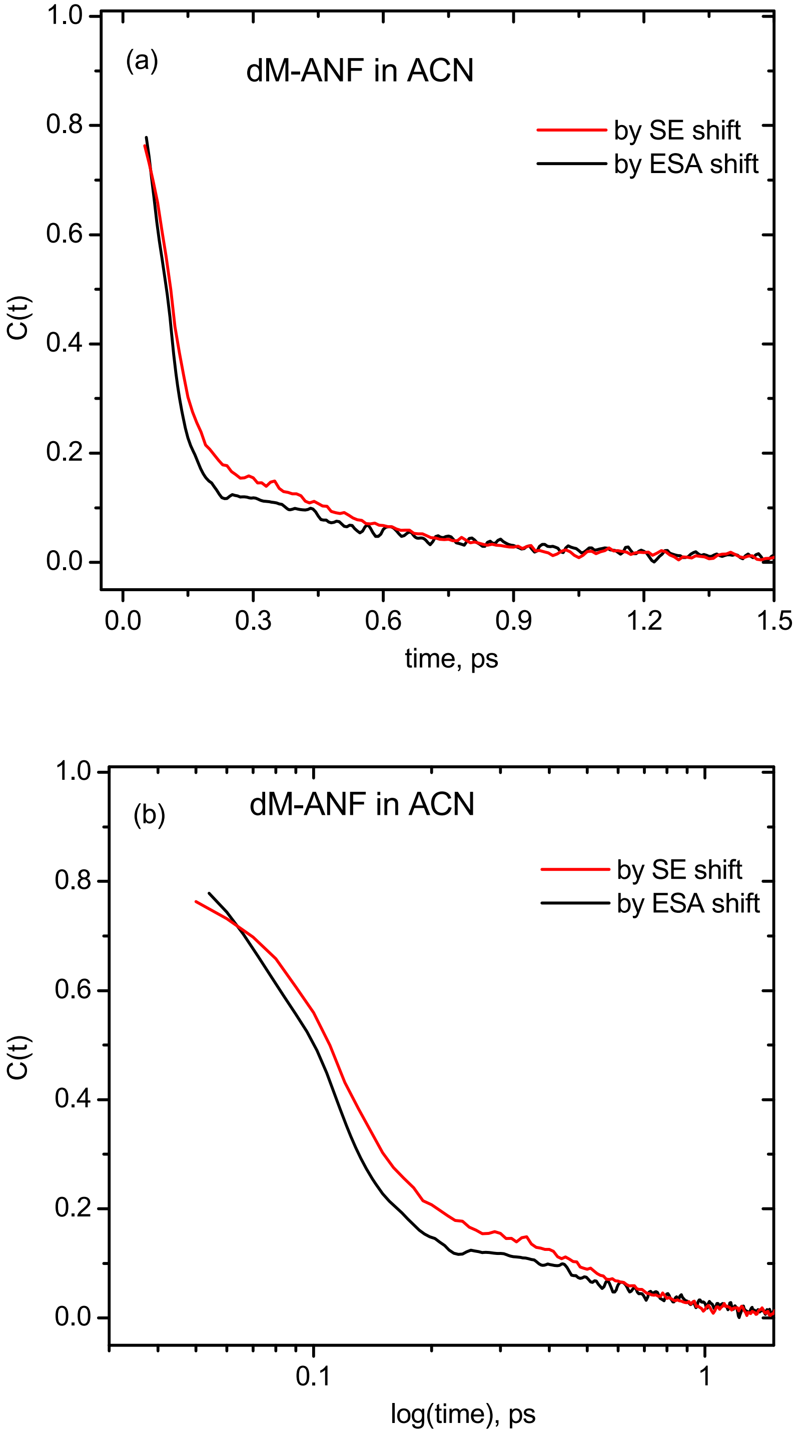

Figure 6.4.4-1 Comparison of solvation curves obtained from SE shift (red) and ESA shift (black) for dM-ANF in acetonitrile. The oscillation is more pronounced in the ESA curve. (a- for linear time scale and b- for logarithmic scale). The common oscillation is due to a librational wavepacket in the surrounding liquid [RKE98].

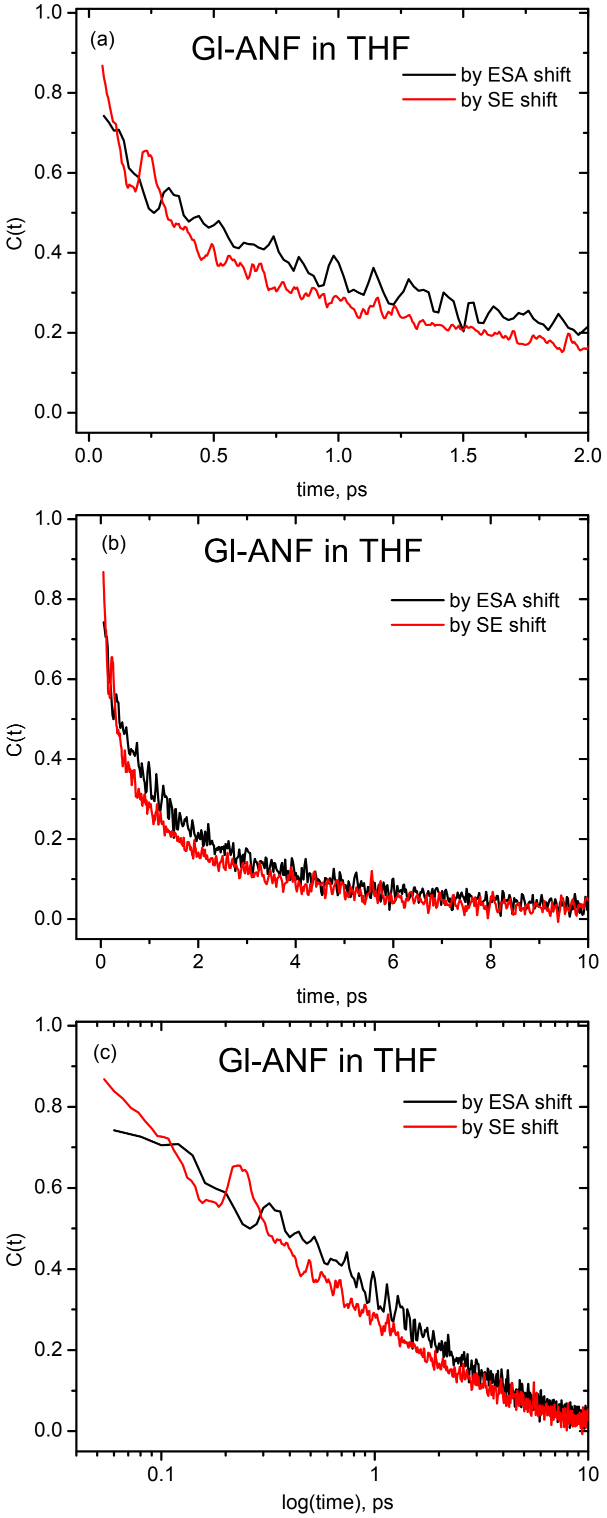

Figure 6.4.4-2 Comparison of solvation curves obtained from the SE shift (red) and from the ESA shift (black), for Gl-ANF in acetonitrile. Again (a) and (b) have a linear time scale while (c) redraws the latter data on a logarithmic time scale. An early oscillatory feature appears with different phase, indicating overlap of the ESA band with SE band; for details see text.

6.4.5 Solvation curve for water

In this section we stay mainly with Gl-ANF, but this time we concentrate on its solvation by water. Figure 6.4.5-1 shows the relaxation curve in water of Gl-ANF, C-153 and methyl quinoline [LKM05]. Since the spectral evolution combined with electronic change is fast for Gl-ANF in water, it was not possible to observe SE. An empirical relaxation function was therefore constructed from the ESA shift. That function is compared to the solvation relaxation function calculated for dipole solvation in water within the continuum model (figure 6.4.5-2). It appears that the two curves are nearly identical. The Gl-ANF curve is fitted with a tri-exponential function and the corresponding time constants are τ_1 = 0.055 ps (22.4%), τ_2 = 0.11 ps (45.3%) and τ_3 = 1.44 ps (32.3%), comparable to value in the ref. JFK94.

Finally let us compare the experimental solvation curve of Gl-ANF in water and the theoretically determined solvation curve of ANF in a DNA duplex. For example consider the TFT/A_A construct; the calculated relaxation curve is also shown in figure 6.4.3-3. Of course, the two curves correspond to different environments and should therefore not be compared in terms of molecular processes. But a comparison is interesting in terms of spectral and time resolution which will be needed to distinguish DNA process from pure solvation in water. We find that the relaxation in DNA is significantly slower than in water. Therefore it should be possible to distinguish the chromophore when it is stacked inside DNA, compared to when it is twisted around the sugar-phosphate backbone and extents into the aqueous boundary layer.

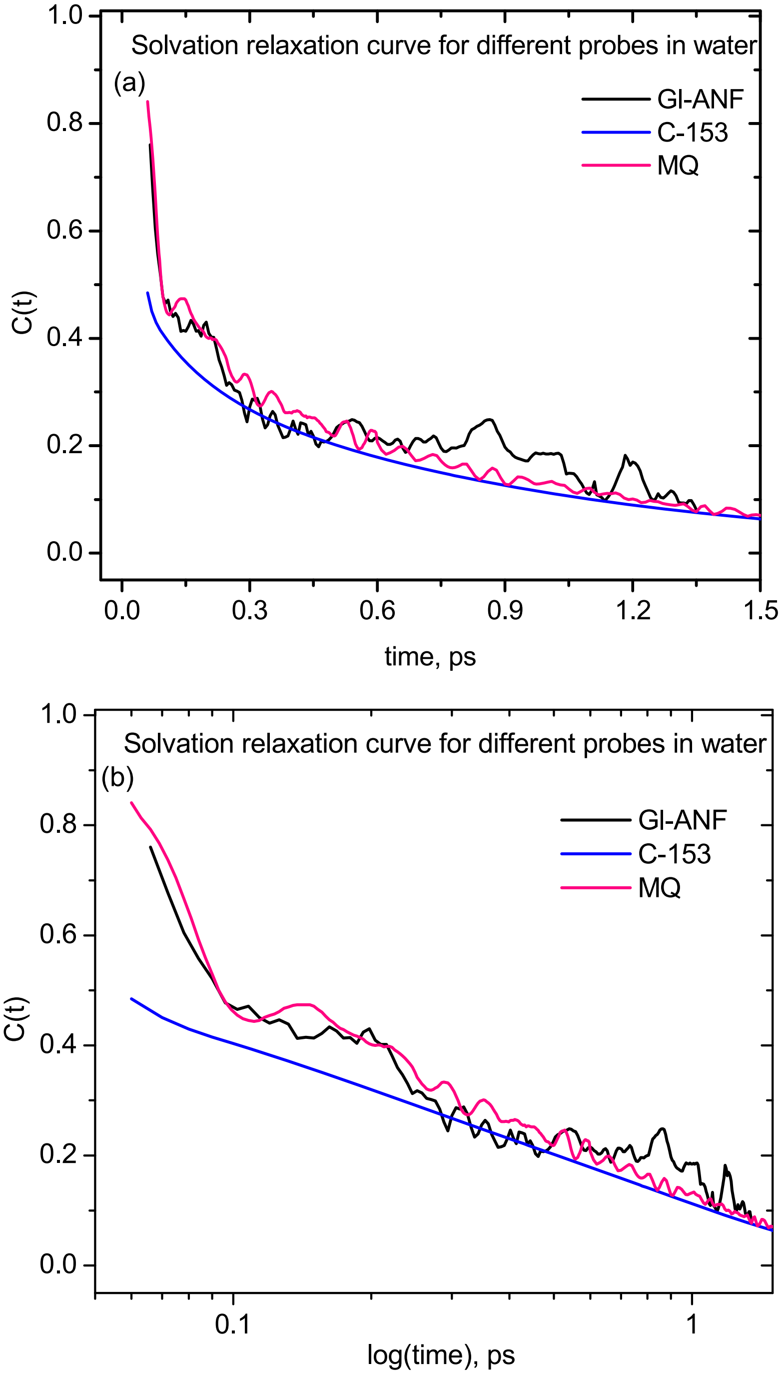

Figure 6.4.5-1 Solvation relaxation curve for Gl-ANF, Methyl Quinoline (MQ) and C-153 in water. For Gl-ANF, excited-state absorption was used to construct the (black) curve. MQ and C-153, on the other hand, gave stimulated emission which lead to the corresponding solvation curves (pink and blue, respectively).

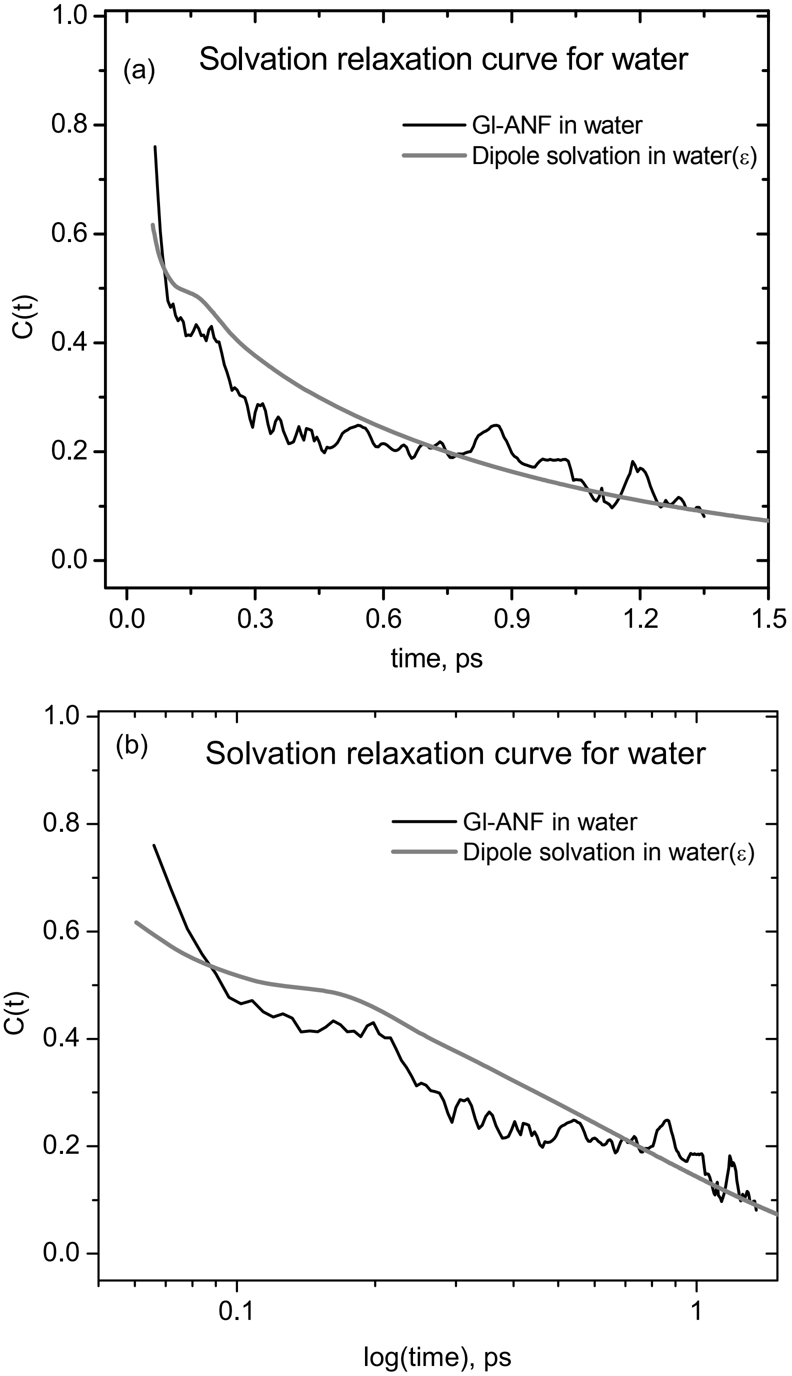

Figure 6.4.5-2 Comparison of solvation relaxation curve for Gl-ANF in water, and dipole solvation in water based on continuum model [LKM05]. The oscillatory hump at 200 fs seems to be similar in both types of curves.

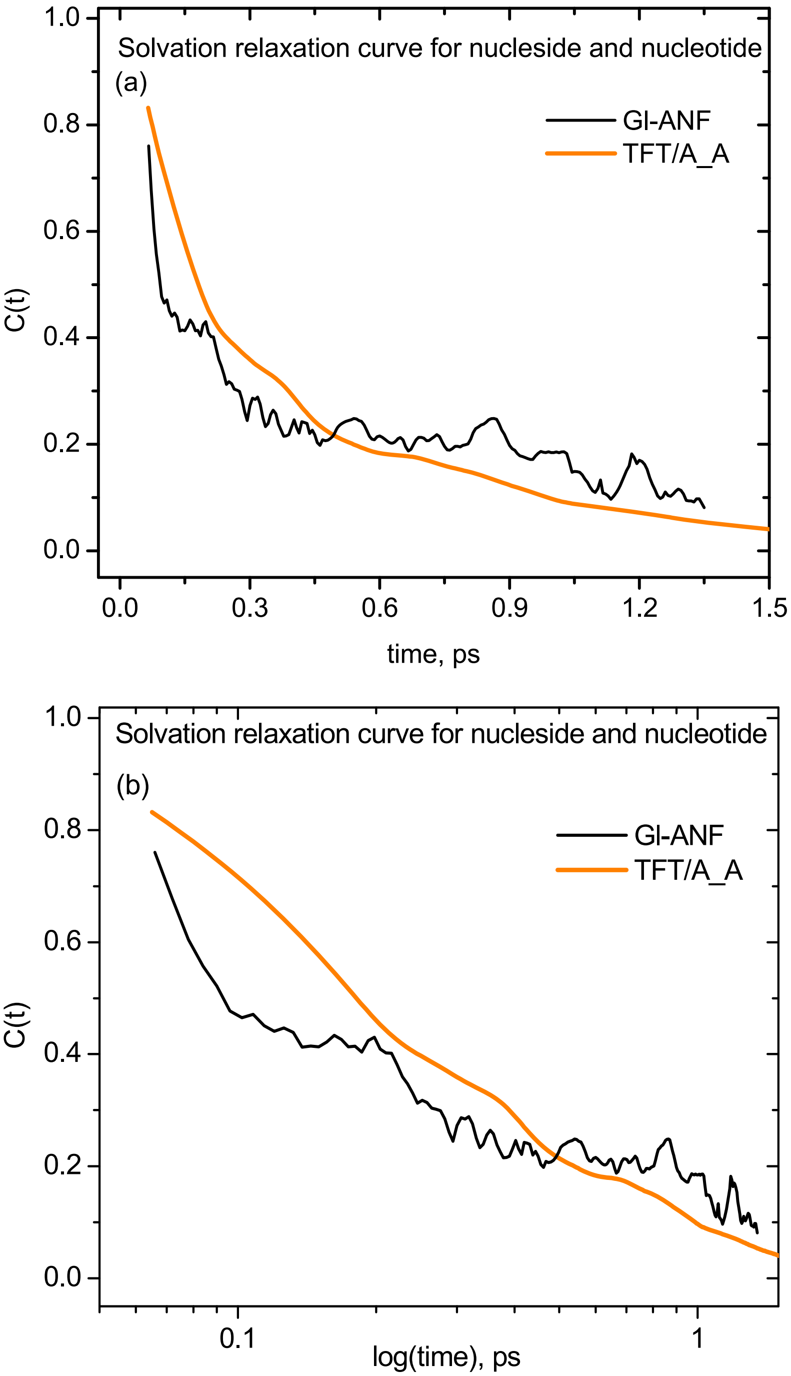

Figure 6.4.5-3 Comparison of experimentally observed solvation curve of nucleoside (Gl-ANF) and theoretically simulated curve for nucleotide (DNA duplex as TFT/A_A) in water. Relaxation in DNA is expected to be significantly slower than in water. Therefore it will be possible to distinguish ANF protruding outside from ANF stacked in DNA.

7 Excited state dynamics of Thiazole Orange

7.1 An overview of cyanines

Cyanine dyes were first reported more than 150 years ago [W0056]. They are characterized by two heterocyclic components connected by a polymethine bridge having an odd number of carbons. When the heterocyclic components and bridge length are changed, the absorption and emission maxima shift across the visible and near-infrared spectrum. Cyanines exhibit large extinction coefficient ($\varepsilon_{\max} > 10^4\,\mathrm{M}^{-1}\mathrm{cm}^{-1}$) and have very low fluorescence quantum yields. These properties give rise to widespread applications. They are employed extensively as spectral sensitizers in photographic systems [S0077] and for photodynamic therapy [DT080, KR093], as active dye laser media or mode-locking dyes in dye lasers [MGA79], as initiators in photopolymerization reactions [CDG90], IR absorbing films in optical-disk recording systems [M0090], probes of micelle structures [GLT85], membranes or model membrane systems [W0076], as stains, and as fluorescent labels [MBB00].

7.2 Photophysical and photochemical properties of cyanines

7.2.1 Aggregation

Cyanines are the best-known self-aggregating dyes. Their aggregation has been studied extensively for the last 40 years [ECR67, KS097], and the photophysics of the aggregates was studied in detail [HMT96, KS097]. The aggregates are used as light-harvesting arrays in artificial photosynthetic systems [MNT89] and have potential as nonlinear optical materials [CWP92]. Aggregation is caused by strong intermolecular van der Waals attractive forces between molecules; it is reflected by distinct changes in the band shape, a large spectral shift compared to the monomeric species, and not least by significant deviations from Beer’s law. The tendency of dye molecules to aggregate depends on the structure of the dye and also on the environment, such as micellar, micro emulsion, pH, ionic strength, concentration, solvent polarity, electrolyte, and temperature parameters. Generally, dye self-association in solution depends directly on dye concentration, added electrolyte, and inversely on the temperature. The following kinds of aggregates are formed. (1) **H**-aggregates (for hypsochromic, the dye molecule aggregate in a parallel way by plane to plane stacking to form a sandwich-type, with head to head arrangement) exhibit a broader blue-shifted absorption band. (2) **J**-aggregates (for Jelly who found this effect, the dyes aggregate by end-to-end stacking, with head-to-tail arrangement) in the aqueous solution have a very intense, narrow, red-shifted absorption band. (3) The dimer [WP065] exhibits a strong blue-shifted band and a variably intense red-shifted band relative to the monomeric band. It is generally agreed that they form as two-dimensional dye crystals. The aggregation is explained with molecular exciton coupling theory (figure 7.2.1-1), *i.e.* coupling of optical transition moments of the constituent molecules. Dimers may be considered as the first step of aggregation and the simplest associates in the course of the formation of higher aggregates, which are formed when the dye concentration is increased. It is difficult to interpret the results because equilibria exists always between aggregates of different compositions including those with monomers. Literature reports [HMT96, and reference there in] also proposed that **J**- and **H**-aggregates in solution exist as one-dimensional dye assemblies that could espouse a brick work, a ladder, or a staircase-type arrangement (shown in figure 7.2.1-2). Depending on the angle of slippage 'α' (α angle between the line-of-centres of a column of dye molecules and the long axes of any one of the parallel molecules) in the staircase architecture, (α < ~ 32°) **J**- and (α > ~ 32°) **H**- aggregates are observed.

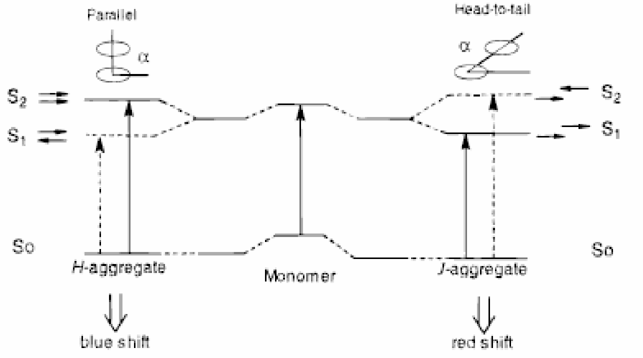

Figure 7.2.1-1 Schematic representation of the relationship between chromophore arrangement and spectral shift based on the molecular excition thorey [KIO97].

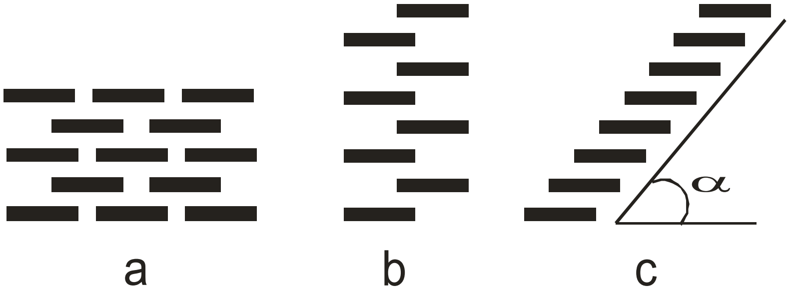

Figure 7.2.1-2 Schematic representation of the different arrangement of cyanine dyes. (a) brick work arrangement, (b) ladder structure and (c) staircase arrangement. α is the angle of slippage [HMT96].

In water the aggregation occurs easily compared to organic solvents (for example, methanol), even if the latter has high dielectric constant. Strong dispersion forces are associated with the high polarizabilty of the chromophore. Since water has high dielectric constant, it reduces the repulsive force between the similarly charged dye cations or anions in the aggregate. In organic solvents on the other hand, even with high dielectric constant, solvation interferes with aggregation and in such solvent the aggregates are stable only at low temperature under the conditions of high viscosity. Therefore, we did not observe aggregation of the dye in methanol which will be used in our work.

7.2.2 Isomerization by twisting

Isomerization of carbocyanines and other polymethine dyes has been extensively studied [ASG86, GH083, H0085, LZR87, and VWF83]. The photoisomerization process is illustrated in figure 7.2.2-1. In the ground state, most cyanine dyes are in a trans configuration. Optical excitation leads to a region on the S_1 potential-energy hypersurface; the two moieties begin to twist around their connecting bonds, so that fluorescence is effectively avoided. This twisted molecule converts to the ground state to form the *cis* isomer or it returns to the thermodynamically stable *trans* isomer [ANR94, LNA85]. The isomerziation involves tremendous molecular movement, it can be an activated process in its later stage, and is much influenced by temperature, viscosity, and/or polarity of the medium.

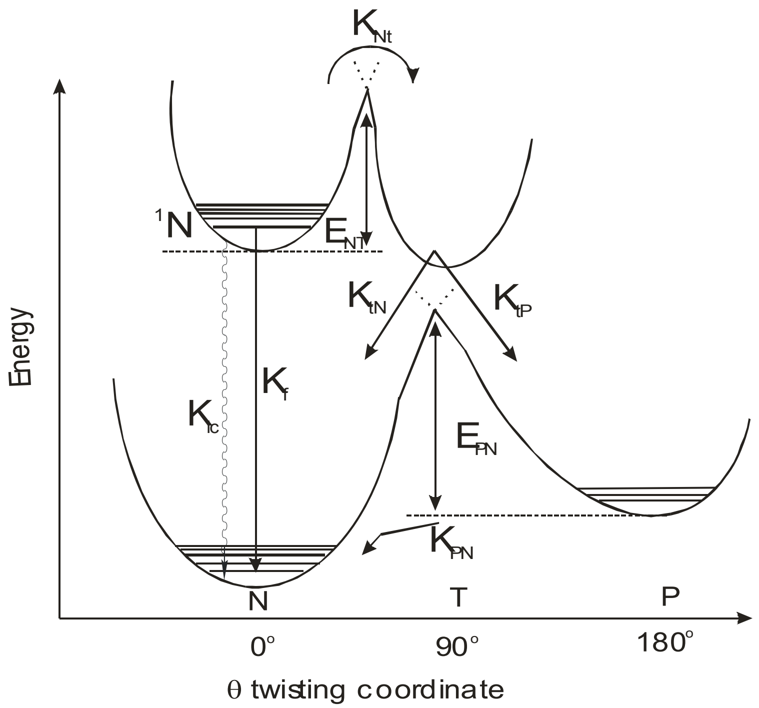

Figure 7.2.2-1 Potential energy surface diagram for cyanine photoisomerization: N, thermodynamically stable normal trans form; t, non spectroscopically partially twisted intermediate excited state; P, photo cis isomer. θ is the twisting coordinate responsible for the isomerization. Following light absorption, the dye isomerizes from the first excited singlet state ^1N to a ground state photoisomer; P which has cis form. k_i and E_i are rate constants and energies of the corresponding states.

Recent computational studies are given by [HR005, IS005, SHR00]. Hunt *et al* [HR005] examine a model trimethine cyanine. They find that nonadiabatic transition takes place over a complete range of twist angles from *trans* to *cis* isomer and not just at the minimum energy point on the conical intersection seam. Thus, radiationless decay occurs along the extended conical intersection seam. This is contrast to the simpler model by Sundström *et al* [YAA95], “sand flowing through a funnel”, which assumes that internal conversion occurs only after the system evolved to the excited-state minimum on the S_1 potential surface. The presence of an extended low-energy seam might be useful for coherent control experiments. Wavepackets with major components near the high energy region of the CI seam result in *trans* isomers, while wavepackets with low-energy components should propagate along the torsion reaction path, resulting in the *cis* isomer. Robb *et al* [SHR00] investigated the ultrafast photoisomerisation of three symmetric cyanine dye models of different chains length based on CASSCF quantum chemical calculations. The main results will be explained in 7.4.

Ultrafast time resolved measurements on barrierless isomerisation of cyanines were performed extensively by V. Sundström *et al* [AYÅ98, ÅÅA94, YAÅ95]. Transient absorption of 1,1'-diethyl-4,4'-cyanine (1144C) was studied [AYÅ98] at different temperatures and viscosities to investigate temperature dependence in the excited state. They observed the reaction crossover rate from a negative temperature dependence at low viscosities to a positive temperature dependence at higher viscosities. This agrees with BFO theory [BFO83, explained below] according to which the temperature dependence of the decay in barrierless isomerization is controlled by the competition between motion to the sink and removal of population from the sink region. They [YAÅ95] also measured the fluorescence dynamics of 1144-C in alcohol solutions by fluorescence up-conversion. A fast decay in the blue part of the fluorescence band was observed and a fast rise at longer wavelength. This is consistent with an overdamped wavepacket motion indicating the twisting of quinoline rings, slower internal conversion, and no contribution from intermolecular vibrational relaxation or Frank-Condon non-active transitions or solvation dynamics. These viscosity dependent studies were in good agreement with transient absorption studies. The same authors [ÅÅA94] compared transient absorption results with Monto Carlo simulations and also treat the process with the Smoluchowski equation. They suggest that bond twisting is reflected as a delayed onset of ground state recovery and very fast spectral shifts of stimulated emission and excited state absorption. The same type of process should occur in isomerization reactions of bacteriorhodopsin and rhodopsin.

Excited-state absorption of many symmetrical cyanines was recorded by Y. H. Meyer *et al* [MPP98] using sub picosecond time resolution. Absolute values of the excited state or photoisomer cross sections of polymethine carbocyanines are evaluated by global spectral analysis. The spectral position of the main $S_1 \rightarrow S_n$ bands can be empirically predicted with a few structural parameters, such as length of methine chain, end-group nature, choice of solvent, and substitution by electron donating or withdrawing group.

A theoretical model of barrierless relaxation dynamics in the case of large amplitude motion was provided by Bagchi, Fleming, and Oxtoby [BFO83]. This important contribution is known as BFO theory. The radiationless relaxation from the S_1 to the S_0 state is represented by a coordinate-dependent internal conversion funnel, the sink, centered at the position where the energy difference between the excited and ground-state potential surfaces is minimum. The radiative relaxation is represented by a position-independent sink distributed along the whole excited state potential surface. BFO further assume a one-dimensional harmonic potential surface that drives the molecules from reactant to product under the influence of solvent friction, and they describe the relaxation dynamics using a modified Smoluchowski equation. Processes such as intermolecular vibration relaxation (IVR), intermolecular vibrational cooling (IVC), and solvent dynamics are not considered; therefore this model might present a slightly oversimplified description of the bond-twisting reaction.

7.2.3 Intercalation with DNA and PNA

Studies of intercalation – interaction between DNA and cyanine dyes are useful for the design of new dyes which will have more effective binding at a specific base or sequence of bases. This intercalation will play a role in the development of dye-based methodologies to detect / monitor DNA mutation or damage. A large number of studies was carried out for binding of a cyanine with DNA, and as well as with PNA. Some of the recent papers are reviewed here.

7.2.3.1 with DNA

J. C. Scaiano *et al* [MCS05] studied the interaction between the cyanine, Pico Green and single stranded DNA homopolymers such as poly(dG), poly(dC), poly(dC) and ploy(dT). It was noticed that poly(dA) and poly(dG) appear to bind very strongly as monomer with dramatic increase in fluorescence, whereas poly(dC) and poly(dT) bind only weakly and seem to promote dye aggregation. Molecular dynamics calculations suggest that intercalation in poly(dA) involves the quinoline rings between two bases in a way that favors π-stacking. This is confirmed by a shift of the stationary absorption maximum, by single-exponential decay of strong fluorescence, and similar effects in induced circular dichroism.

S. M. Yarmoluk *et al* [OLK01] studied the changes of absorption, emission and excitation spectra of Thiazole Orange (TO) and Cyan 13, when it is added to calf thymus DNA. In water, the free dyes form self-aggregates with a sandwich-like structure. At low concentration, free dye molecules interact with DNA, while at higher concentration, free dye molecules aggregate with those that are already bound at DNA. The latter are observed easily by an anomalously large fluorescence Stokes shift of about 100 nm. The large Stokes shift suggests that the π-electron systems of the aggregate undergo substantial changes in the excited state upon DNA binding. This is explained by the "half intercalation" model: only one of the heterocycles of the dye intercalates between DNA base pairs while the other heterocycle, placed outside the inter-base space, is available for aggregation with free dye molecules.

P. Vigny *et al* [PDV99] studied the photophysical properties and did quantum-chemical calculations of thiazole orange derivatives with two different side chains *viz*, ($-(CH_2)_3-N^+(CH_3)_3$ and $-(CH_2)_6-I$) linked to the nitrogen of the quinoline ring of the thiazole orange, with single and double stranded DNA. These dyes have fluorescence quantum yields of 8×10^{-5} and 2×10^{-4} respectively, in buffered aqueous solution without DNA, 7×10^{-3} to 3×10^{-2} in single strand or short nucleotides, and 0.2 and 0.3 in double stranded DNA. The significant increase of quantum yield in single strands is interpreted as a folding of the strand around the dye, which reduces the internal rotation of the two heterocycles.

Netzel *et al* [NNZ95] reported fluorescence quantum yield, emission enhancement and emission lifetime measurements of Thiazole Orange and Yellow Orange derivatives complexed to calf thymus DNA (CT-DNA), $(dAdT)_{10}$, and $(dGdC)_6$ duplexes. Enhancement of emission by factors 200 to 1800 are observed with DNA when compared with free dye solution. All of the dyes exhibit either bi- or tri-exponential emission decay kinetics reflecting the different dye/ds DNA modes of binding. The lifetime of bichromophores bound to ds DNA is 5.1 ± 0.8 ns. These results suggest that binding-induced restriction of twisting about the central methane bridge is responsible for the large emission enhancements. Relative rates for electron transfer (ET) quenching of emission from the excited dye were determined as a function of free energy using redox data for cyanine dye analogs of the DNA-staining dyes. Electron transfer efficiency should correlate with base content, but there is no variation of average lifetime for these dyes on $(dAdT)_{10}$ and $(dGdC)_6$ duplexes. Therefore ET emission quenching is not an important process in this case. There is distinct difference between pyridinium dyes which have 4-fold greater emission yields on $(dAdT)_{10}$ duplexes and quinolinium dyes which have 2-fold greater emission yields on $(dGdC)_6$ duplexes. This suggests that pyridinium associates selectively with AT- and quinolinium associate selectively with GC-rich region, when bound to CT-DNA.

Kumar *et al* [KTA93] distinguished groove binding and intercalative binding with DNA by observing changes of fluorescence yield. Changes of the absorption, fluorescence intensity, quantum yield and lifetime, were monitored when styrylcyanine dyes were added to DNA. It is suggested that groove binding inhibits the non-radiative deactivation of the dye's excited state, owing to the geometric restriction imposed by the narrow minor groove of the DNA helix, resulting in enhanced fluorescence yields and lifetimes. The addition of salt or a strong electrolyte to the solution releases the DNA-bound dye cations from the groove and causes a decrease in the fluorescence quantum yield. These results are quite useful in the staining of DNA gels and for detection of very low concentrations of DNA.

7.2.3.2 with PNA

What are **P**eptide **N**ucleic **A**cids (PNA)? − Modification of bases and the deoxyribose phosphate backbone of DNA offer the possibility to increase the nuclease stability and cell membrane permeability, and to probe DNA-DNA and DNA-protein recognition. Peptide nucleic acids are DNA analogs where the four nucleobases, adenine

(A), thymine (T), guanine (G), and cytosine (C) are linked to a N-(2-aminoethyl)glycine backbone instead of the negatively charged deoxyribose phosphate backbone of DNA. A methylenecarbonyl linker is used for this purpose. Such a backbone is homomorphous with the deoxyribose phosphate backbone of DNA with a high degree of constrained conformational flexibility due to the two amido groups per unit. A schematic comparison of DNA and PNA is given in figure 7.2.3.2-1.

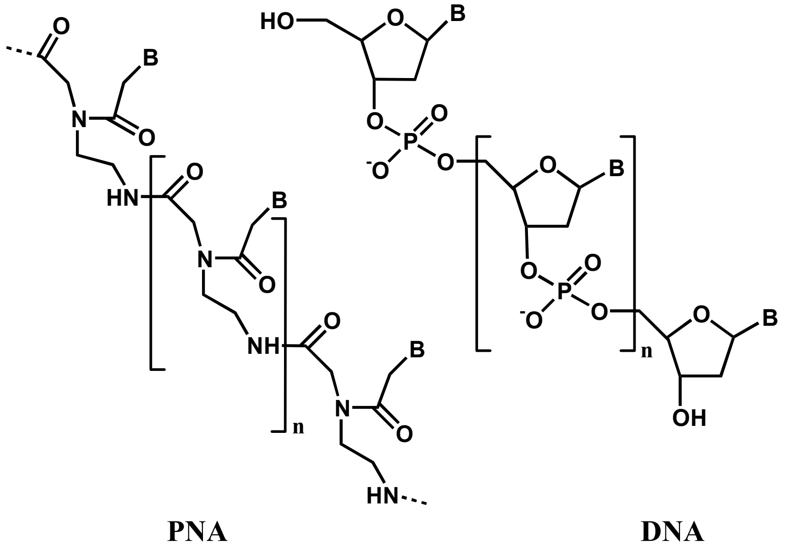

Figure 7.2.3.2-1 Schematic chemical structures comparing PNA and DNA. The deoxyribose phosphodiester backbone in DNA has been changed to N-(2-aminoethyl)glycine in PNA.

PNA synthesis is more versatile than that of the oligonucleotide, allowing the facile design of a chiral backbone and relatively large-scale production. The lack of negative charges along the PNA backbone permits high-affinity hybridization to complementary DNA and RNA sequences [EBC93] even for targets that have competing secondary or tertiary structure [A0003]. Hence PNA is used as antisense agent, as hybridization probe for diagnostics, and as capture strand for purification of nucleic acids. Interaction of cyanine dyes and PNA is one of the growing research field in biochemistry and some of the recent studies are explained here.

P. E. Nielsen *et al* [SN006] compared purine and pyrimidine based asymmetric PNA/DNA duplexes. They showed that purine-rich PNA strands are more stabilized with regard to thermal melting temperature, free energy, enthalpy and are relatively less entropically disfavored. The difference in stability is obtained by finding the difference in counter ion binding, hydration or single strand conformation. They also observed an unexpected, significant increase in both binding enthalpy and entropy for PNA/DNA duplexes containing a pyrimidine-rich PNA strand in organic solvents, which implies that these duplexes are relatively enthalpically disfavored in water. Their results point to enthalpic contributions both within the duplex structure as well as from bound water molecules as the reason for the different stabilities. The same group [RHT00] characterized the binding affinity and sequence specificity of mixed sequences of matched PNA/DNA duplexes and single mismatched PNA/DNA duplexes using melting curves and isothermal titration calorimetry. The overall observation concludes the following.

(1) Strong enthalpy-entropy compensation in matched duplexes. (2) Weakening of the H-bonds between the strands is compensated by a less rigid structure upon forming less perfect sequence-matched duplexes in mismatched duplexes. (3) These are due not only to changes in base pair formation and stacking but also to rearrangement of solvent molecules and ions.

F. P. Schwarz *et al* [SRB99], by measuring the thermodynamics with isothermal titration calorimetry (ITC), proved that most PNA sequences exhibited tighter binding affinities than the corresponding DNA sequences, resulting from smaller entropy changes in PNA/DNA hybridization reactions. For example, the binding constant for PNA(GA)/DNA is 4.15×10^7 M^{-1}, whereas for DNA(GT)/DNA the binding constant is 2.9×10^5 M^{-1}. The highest PNA binding affinities occur with a large number of purine bases in the PNA sequence.

B. A. Armitage *et al* [SOA99] proposed that symmetrical cyanine dyes recognize the minor groove of a PNA/DNA duplex, a PNA/PNA duplex and a bisPNA/DNA triplex, and that the dye molecules form a helical aggregate there using the duplex as a template. This was reflected by visible color change and improved hybridization of PNA with the complementary DNA strand, by optical spectroscopy and molecular dynamics simulations, respectively. This helical aggregation is confirmed [DMS05] by the addition of isobutyl groups to the PNA backbone which hinders the aggregation, because the substituents project into the minor groove. The effect is less when they are directed out of the groove.

O. Seitz *et al* [KJS04, KS003] studied the fluorescence enhancement of TO labeled PNA, when it is hybridized with DNA. Their studies were described in detail in next section.

7.3 Intrinsic nature of Thiazole Orange

In this thesis, the asymmetric cyanine Thiazole Orange(TO) was studied. This 2-[1-Carboxy-methyl-1H-quinolin-4-ylidenmethyl]-3-methyl-benzothiazol-3-ium Bromide consists of quinoline and benzothiozole ring connected by one methine group, as shown in figure 7.3-1. The compound is essentially nonfluorescent in aqueous solution (fluorescence quantum yield is 0.0002 [NSK98]). Since the chromophore is cationic, it intercalates with high affinity into double stranded DNA with an association constant of about 3.3×10^5 M^{-1}. When it intercalates into DNA, its nonradiative decay channel is closed and the fluorescence quantum yield increases to between 0.1 and 0.4 in double stranded DNA. Lee *et al* [LCC86] postulated that the fluorescence enhancement upon

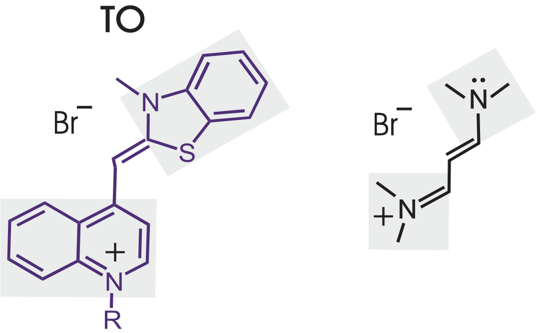

Figure 7.3-1 Thiazole Orange (TO) in its most stable conformation in the electronic ground state. R = $-CH_2-COOH$. The lowest isomer (10 kcal/mole above, from AM1 calculations [FE0_ _]) has the thiazolyl group rotated by 180°. The photoreaction of TO involves torsional motion of the two moieties (*gray rectangles*) around the central methine bridge. Structural changes will be illustrated with a small model cyanine (*right*). For simplicity only one VB structure is shown in each case.

nucleic acid binding of TO (which exhibits approximately 3000-fold enhancement on RNA) is due to the change in the relative orientation of the benzothiazole and quinolinium rings from skewed to coplanar. The charge and structure of the dyes influences the strength of its interaction with DNA and the affinity towards double-stranded *(ds)* DNA can be raised with positively charged side chains of the dye [PBR00] or by linking two chromophores through a tether which carries multiple positive charges [GR092]. Therefore, TO and similar type of dyes like Pico Green (PG) [CFM00], and Yellow Orange (YO) [SAS98] are useful to detect and quantify polynucleotides in a variety of techniques. Some of the techniques are the polymerase chain reaction [SSS00], the hybridization of single strands [PMM02], restriction fragment sizing [FAR94], and flow cytometry [HFC94]. These cyanine dyes are used in reticulocyte analysis to stain residual RNA of blood cells [LCC86], and to stain DNA in agarose gels [RQP90] and capillary electrophoresis [RG095, ZCB94]. The selectivity of binding of the PG to DNA was examined by J. C. Scaiano *et al* [SS003] with fluorescence lifetime measurements and by circular dichroism. They demonstrated that binding of PG to dsDNA preferentially occurs by intercalation between alternating GC base pairs. O. Seitz *et al* showed that TO behaves as an artificial universal base, and that it stabilizes the duplex with DNA when it is linked to PNA sequences. Specificity by design was achieved when a TO peptide conjugate was linked into a single-stranded sequence [KJS04]. Hybridization was possible with every natural base paired against the chromophore, it could be monitored by a 20-fold increase of fluorescence, and the increase is sensitive to the mismatch of a neighboring pair [KS003]. The latter observation suggests that a DNA target may be distinguished from its base mutant by fluorescence directly, and thus could be of use in real time quantitative PCR analysis, array technology, and live-cell analysis. These aims motivated our present study.

7.4 Photoreaction of the cyanine in S_1 based on Robb's model [SHR00]

The mechanism which governs the interaction of TO with neighboring nucleotides is crucial for applications. It is based on the photochemistry of cyanines in pure solvents, which were studied extensively [ASG86, GH083, H0085, LZR87 and

VWF83]. The structural and electronic changes along the S_1 reaction path were examined recently in computational studies of symmetrical model carbocyanines [HR005, IS005 SHR00]. The results for the trimethine cyanine [HR005, SHR00] (figure 7.3-1) are summarized in figure 7.4-1. In this figure δ and ε measure the deviation of the bridge dihedral angles from their initial *trans* conformation in the directions shown. Twisting of the moieties against each other is thus described as conrotary, $\delta = \varepsilon$, toward the perpendicular conformation at $\delta = 45°$. However, different high-frequency modes are predicted to be active along the way (this is indicated by vibrational parabolas which are oriented in orthogonal directions).

Initially, excitation $S_1 \leftarrow S_0$ is accompanied by symmetric expansion of the bridge bonds which continues on the S_1 hypersurface until $\delta \approx 20°$ (process 1). For symmetric cyanines, the positive charge should so far be distributed equally over the two moieties. Then asymmetric distortion sets in, and the positive charge becomes localized. During this process (2), the asymmetric displacement in S_1 increases strongly with twist angle until the perpendicular conformation is reached (note a corresponding displacement “wedge” in the figure). The scheme implies a wide FC progression in a high-frequency mode for fluorescence at large twist angles provided there is sufficient radiative coupling. Next, while keeping the perpendicular form, the plane of the bridge turns to become coplanar with the charged moiety (described by disrotary motion 3) along a more gentle slope of the S_1 surface, and the global minimum is thus reached. From here, a conical intersection (CI) can be accessed by asymmetric stretching so that internal conversion is an activated process (4), partly to the *cis* isomer and partly back to the original *trans* form [SG082]. The intersection is accessible at all torsional angles so that the S_1 minimum may not be reached at all or at least be of little importance for the dynamics [HR005].

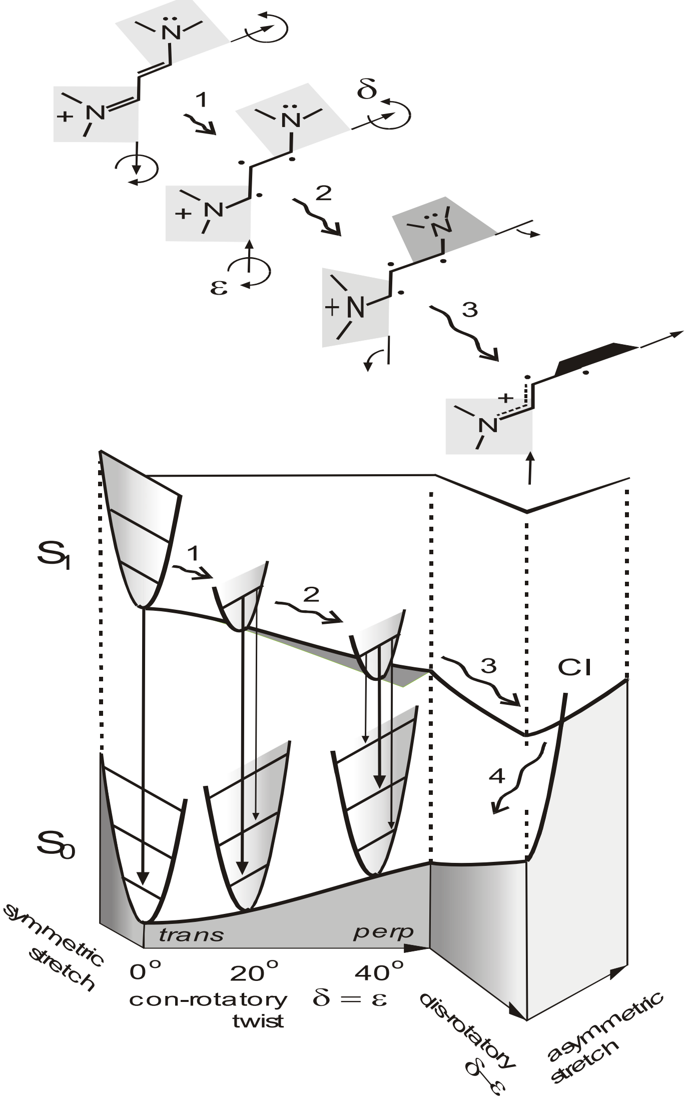

Figure 7.4-1 Electronic and structural changes of cyanine based on Robb's model [HR005, SHR00]. Photoreaction in S_1 as calculated for a symmetric model cyanine, for twist angles δ, ε from the all-*trans* conformation of S_0. Optical absorption $S_1 \leftarrow S_0$ initially causes symmetric expansion and conrotary twisting (1) until $\delta = \varepsilon \approx 20°$. Then asymmetric distortion sets in, strongly increasing with further conrotation (2), and the positive charge becomes localized. After the perpendicular conformation is reached the bridge plane turns coplanar with the charged moiety (described by disrotary motion 3). Internal conversion (4) is an activated process involving asymmetric stretching from the global minimum to a conical intersection (CI).

7.5 Stationary measurements

7.5.1 Absorption and fluorescence of Thiazole Orange

The stationary absorption and emission spectrum of Thiazole Orange in methanol is shown in figure 7.5.1-1.

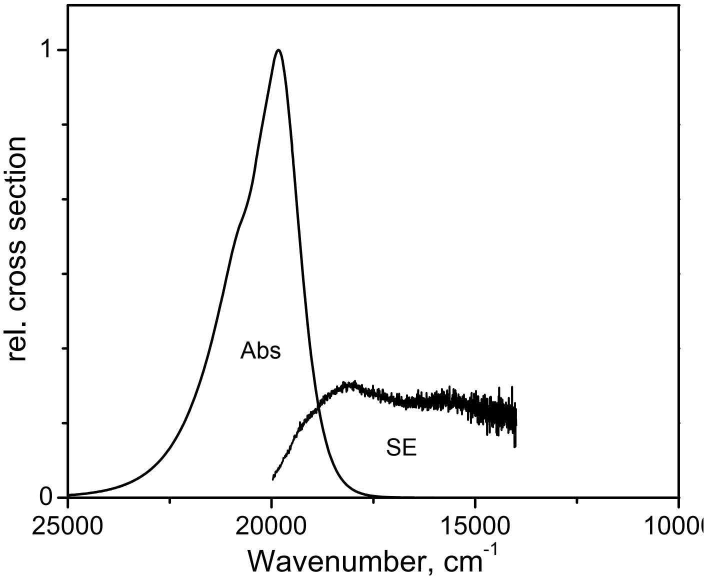

Figure 7.5.1-1 Stationary absorption and emission spectra of TO in methanol. The measured fluorescence quantum distribution (λ_{exc} = 480 nm) was converted into cross sections for stimulated emission SE, only relative values are given.

The absorption band of $S_1 \leftarrow S_0$, due to the $\pi \rightarrow \pi^*$ transition has maximum at 19,990 cm^{-1} with extinction coefficient value of 79 ± 3 × 10^3 L mol^{-1}cm^{-1} and a blue shoulder represents vibrational activity. The electronic oscillator strength is estimated to be $f_{abs} \approx 0.72$ (see equation 3.15) and the radiative lifetime is $\tau_{rad} \approx 6.2\,\mathrm{ns}$. Fluorescence spectra are usually represented in terms of the fluorescence quantum distribution (FQD). Since in transient absorption measurement one observes the spectrum of stimulated emission, here fluorescence is given in terms of cross sections for stimulated emission. The observed emission band does not mirror the absorption spectrum; instead it is broadened and extended to the red. The absorption spectrum of Thiazole Orange at various concentrations in methanol were also recorded from 5.1 × 10^{-6} to 2.55 × 10^{-4} mol/L. The results are presented in figure 7.5.1-2. Normalization of all spectra shows that there is no systematic change of band shape or absorption maximum as the concentration is increased. It follows that there is no aggregation in this range of concentrations. For comparison, the absorption spectrum of Thiazole Orange in water at various concentrations is shown in figure 7.5.1-3, where the concentration ranges from 0.652×10^{-6} to 7.826×10^{-5} mol/L. The band shape of the spectrum clearly shows the dimer formation [WP065].

7.5.2 Absorption and fluorescence of TO in PNA

Thiazole Orange labeled PNA (TOPNA), also with an abasic site adjacent to thiazole orange (TOAPNA), were prepared by the procedure described in [JKS05]. Both PNA sequences were hybridized separately with various DNA strands which differ at an adjacent position to the site opposite of TO (8th position towards 5' hydroxyl group of sugar). According to the scheme below, the DNA strands are called *matched* DNA (MDNA), *mismatched* DNA (MMDNA) and *abasic* DNA(ADNA).

PNA sequences are

N'-g c c g t a-aeg(TO)-t a g c c g-gly-coNH_2 (TOPNA)

N'-g c c g t a-aeg(TO)-_ a g c c g-gly-coNH_2 (TOAPNA)

DNA sequences are

3'-C G G C A T T A T C G G C-5' (MDNA)

3'-C G G C A T T _ T C G G C-5' (ADNA)

3'-C G G C A T T C T C G G C-5' (MMDNA)

Hybridizations were done by heating the mixed solution of TOPNA (or TOAPNA) and respective DNA (1:1 ratio) in buffer, to 85°C (5 °C/min) for 20 min

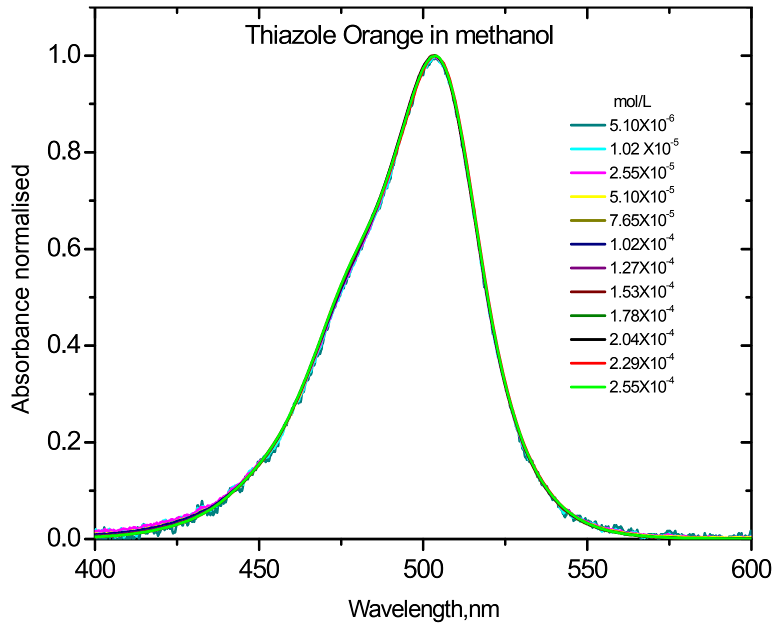

Figure 7.5.1-2 Normalized absorption spectra of TO in methanol at various concentration from 5.10 × 10^{-6} to 2.556 × 10^{-4} mol/L. Different concentrations are shown with different colors. There is no change of band shape and maximum, proving that aggregation plays no role at these concentrations.

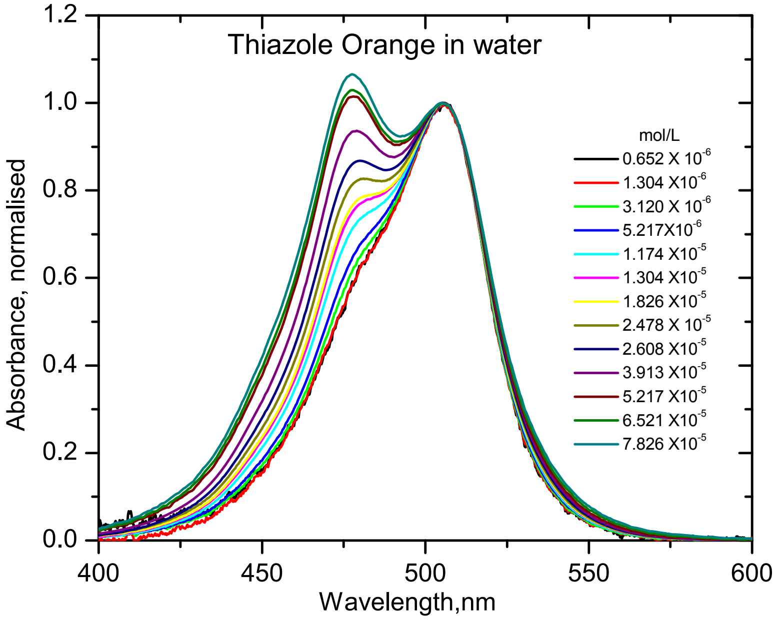

Figure 7.5.1-3 Normalized absorption spectra of TO in water at various concentration from 0.652 × 10^{-6} to 7.826 × 10^{-5} mol/L. Different concentrations are shown with different colors. The band shape of the spectrum reflects the formation of a dimer with increasing concentration.

followed by cooling to 25 °C (1 °C/min). The buffer solution contains 100 mM NaCl and 10 mM NaH_2PO_4 and is adjusted to pH 7.0 with 2M NaOH, finally it is degassed for 30 minutes. The concentration of duplex solutions were 1.5 μmol/L. The absorption and fluorescence spectra were recorded for all hybridized solution at room temperature. In order to compare quantitatively the band positions and shapes, the measured spectra are converted in to distribution of oscillator strength over wavenumber. This means that absorption spectra are converted in to oscillator strength and fluorescence spectra are converted in to stimulated emission spectra (as in the section 3.9 g). The results are shown in figures 7.5.2-1 and 7.5.2-2. Every oscillator distribution is fitted by a sum of log-normal distributions to get a smooth interpolation curve. Fluorescence of all PNA strands exhibit progressions of three vibrational bands for all constructs, extending to the red by more than 4000 cm^{-1}. Figure 7.5.2-1 shows the absorption and stimulated emission spectra of TO labelled in single-stranded PNA (TOPNA), paired with counter strand DNA which is either matched (MDNA), mismatched (MMDNA), or abasic (ADNA) at the neighbouring site. The resultant duplexes are designated as *mds*, *mmds* and *ads* respectively. Differences in peak height are due to the fact that the total oscillator strengths are set equal while the band shapes may vary. Red enhancement is also calculated with respect to *mds*, by integrating the spectrum.

7.5.3 Comparison of spectral shift and broadening with matched double strand (*mds*)

The fitting results are tabulated in table 7.1 and observations are discussed as follows.

The absorption of TO in *mds* (which peaks at 19440 cm^{-1}) is prominent, and this is why the band shapes in *mds* are taken for reference. For example the absorption in *ads* requires no shift ($\Delta\tilde{\nu} = 0$) from the *mds* environment, only broadening by a Gaussian with fwhm $\tilde{\omega} = 400$ cm^{-1}. An initial estimate of the TO emission spectrum in *ads* can be made by applying the same parameters to the reference emission bandshape. It corresponds to the emission which would be observed if the environment were the same as in the *mds* reference. Instead the experimentally observed spectrum shows *less*

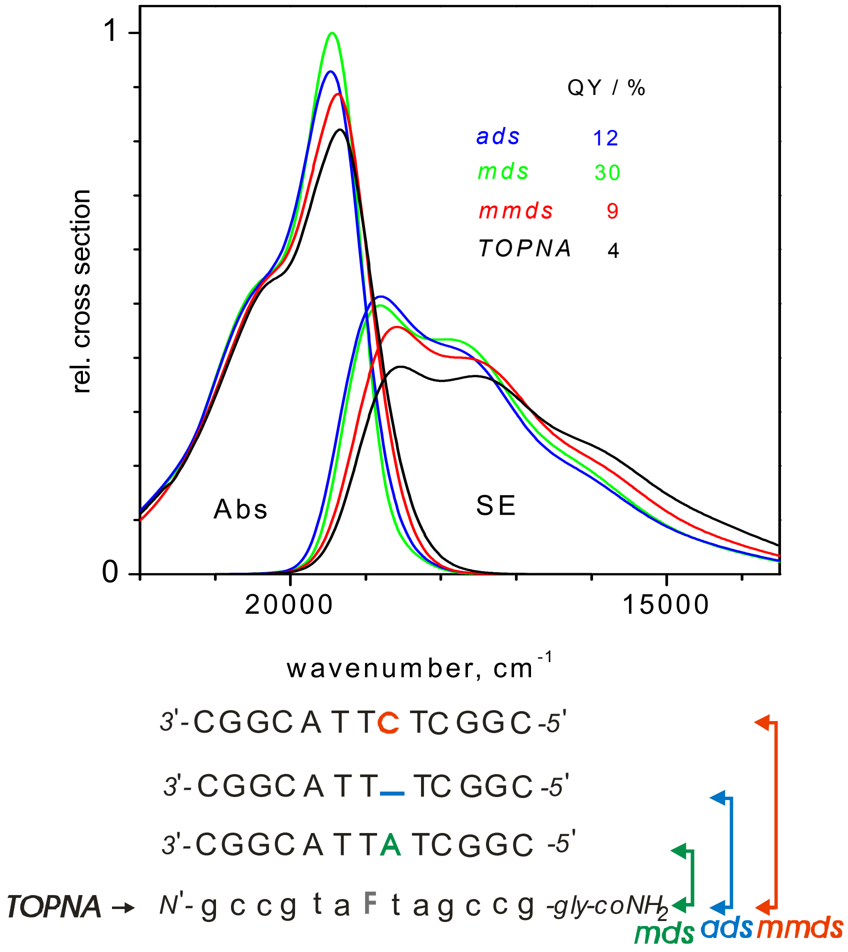

Figure 7.5.2.1 Stationary absorption and stimulated-emission spectra of TOPNA and of TOPNA/DNA duplexes. The spectra are normalized to equal oscillator strengths. The corresponding PNA, DNA base sequences and their fluorescence quantum yields are also given.

Table 7.1 The absorption and emission spectra of TOPNA and its duplex are fitted with line shape function and results are given.

Duplex	**Abs peak/broad cm^{-1}**	**Em shift from *mds* (rel)/broad cm^{-1}**	**red enhancement**
mds	19440 / n.a.	n.a.	n.a.
ads	19440 / 170	0 (0) / 170	-2.4 %
mmds	19350 / 220	-170 (-80) / 180	+2.7 %
TOPNA	19290 / 260	-250 (-100) / 180	+8.7 %

amplitude in the 2nd, 3rd vibronic band: it has the expected position but is actually sharper, less drawn out, than expected. Next consider emission from TO in *mmds*. From the absorption bandshape we find $\Delta\tilde{\nu} = $-90 cm^{-1} and $\tilde{\omega} = 520$ cm^{-1}. In reality the red-shift of emission is larger, $\Delta\tilde{\nu} \approx 170$-230 cm^{-1}, while broadening is clearly less. The main feature is an enhanced amplitude of the 2nd, "middle" vibronic band. The same qualitative behaviour is noted in *ss*DNA where the 2nd vibronic band is even more prominent.

The same fitting procedure is also followed for hybridised samples of TOAPNA with MDNA, MMDNA and ADNA and their resultant duplex are denoted as *mds-a, mmds-a,* and *ads-a* respectively. Figure. 7.5.2-2 shows absorption and stimulated emission spectra for respective above mentioned duplexes. Red enhancement has calculated with these duplexes as previous case and fitting results compared with *mds* are given in table 7.2 and observations are explained as follows.

Interestingly, the absorption band shape of TOAPNA appears to be independent of the counter strand, meaning that shift $\Delta\tilde{\nu} \approx$-200 cm^{-1} from, and broadening by $\tilde{\omega} \approx 400$-500 cm^{-1} of the TO absorption reference in *mds-a* is very similar for all constructs with TOAPNA. Let us now turn to the TOAPNA emission band shapes. Here the following is observed: in *mds-a* $\Delta\tilde{\nu} = $-200 cm^{-1}/ $\tilde{\omega} = 380$ cm^{-1} almost reproduces the measured spectrum. In *ads-a*, we find significantly smaller red-shift and broadening, -130/350 cm^{-1}, by which the 2nd vibronic band is almost simulated. The same holds for TOAPNA in *mmds-a* (-190/420 cm^{-1}). Only in TOAPNA is the 2nd vibronic band so prominent that the spectrum can no longer be described by the reference emission.

7.5.4 Quantum yields of double strands

Fluorescence quantum yield is obtained by comparing with the fluorescence spectrum of Fluorescein in 0.1 M NaOH. The values are represented in table 7.3. In practice, we can understand the quantum yield (QY) as it depends on base sequence and base paring. In TOPNA the increase of the QY is systematic whereas in TOAPNA it is not. In TOPNA the fluorescence QY of *ads* and *mmds* are less when

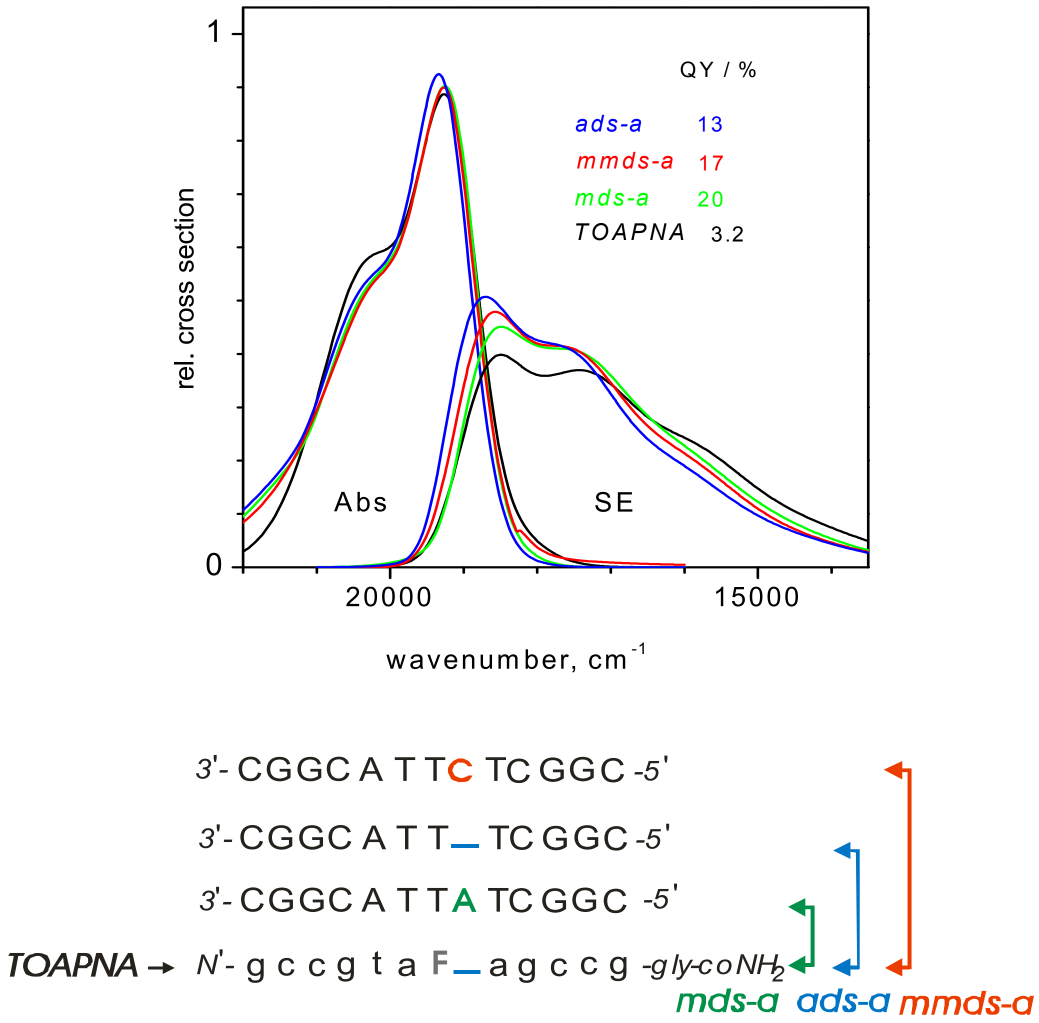

Figure 7.5.2.2 Optical spectra of TOAPNA containing an adjacent abasic site to TO, and of TOAPNA/DNA duplexes. The corresponding PNA, DNA base sequences and fluorescence quantum yields are given.

Table 7.2 The absorption and emission spectra of TOAPNA and its duplex are fitted with line shape function and results are given.

Duplex	Abs peak/broad cm^{-1}	Em shift from *mds* (rel)/broad cm^{-1}	red enhancement
mds-a	19240 / 160.	-270 (-70) / 160	+2.5 %
ads-a	19310 / 150	-90 (+40) / 100	-2.4 %
mmds-a	19250 / 180	-210 (-30) / 180	+0.5 %
TOAPNA	19220 / 220	-250 (-50) / 180	+8.8 %

compared to *mds*. The difference between *mmds* and *mds* could be used to distinguish the base mutant from the target DNA. In *mmds*, the TO moiety is probably twisted out of the stack because there is not sufficient room inside, and this is why the QY drops from 29% (*mds*) to 9 % (*mmds*). In case of TOAPNA there is always room for TO to be accommodated inside, independent of the base opposite to abasic site on the TOAPNA strand. Therefore the QY is always ≥ 13%.

Table 7.3 Relative fluorescence quantum yield of different duplexes are given. Fluorescein is used as standard.

DNA	with **TOPNA**	with **TOAPNA**
As such	**0.03925**	**0.03237**
MDNA	**0.29511** (*mds*)	**0.20078** (*mds-a*)
ADNA	**0.12026** (*ads*)	**0.13000** (*ads-a*)
MMDNA	**0.09017** (*mmds*)	**0.17100** (*mmds-a*)

The general view on the fluorescence increase of cyanines is that the extent of twisting or torsion between the heterocycle moieties is reduced, for example in highly viscous liquids or when near-range interactions are increased as in DNA [MBB00]. There are two aspects to this effect. (1) In an environment of higher viscosity, the motion is more damped and the process slowed even though the S_1 potential-energy surface may be unaffected. (2) On the other hand, stacked nucleobases on either side impede torsion directly; that is, they bend the S_1 surface upward along the twist coordinate. Hence, after optical excitation, the population remains in the vicinity of the FC point on the S_1 potential-energy surface and emission is observed. Because twisting is admitted to various degrees, different limiting energy gaps should be reached depending on the pairing of neighboring bases, which therefore sensitively influences the fluorescence quantum yield. Because of the extent of twisting and limiting energy gap show small variations in an unsystematic way, we did not find systematic behavior in the fluorescence quantum yield apart from the coarse rule mentioned above. Referring to the reaction path in figure 7.4-1, we identify the vibrational progression with asymmetric stretching of the methane bridge on the conrotary section of the path.

All optical spectra of hybridized solutions were also fitted with the Brownian oscillator model [BYM90]. This model characterizes the optical transition of an electronic two level system with a line shape function with the following three parameters. frequency ω, damping γ(t) and displacement *d.* The effective mode displacement *d*, is obviously different for the various constructs, whereas the vibrational frequency is constant. The pertinent parameters may be estimated by a description of the optical spectra through the fits, as shown in figure 7.5.4-1 for TO in single-stranded PNA (TOPNA).

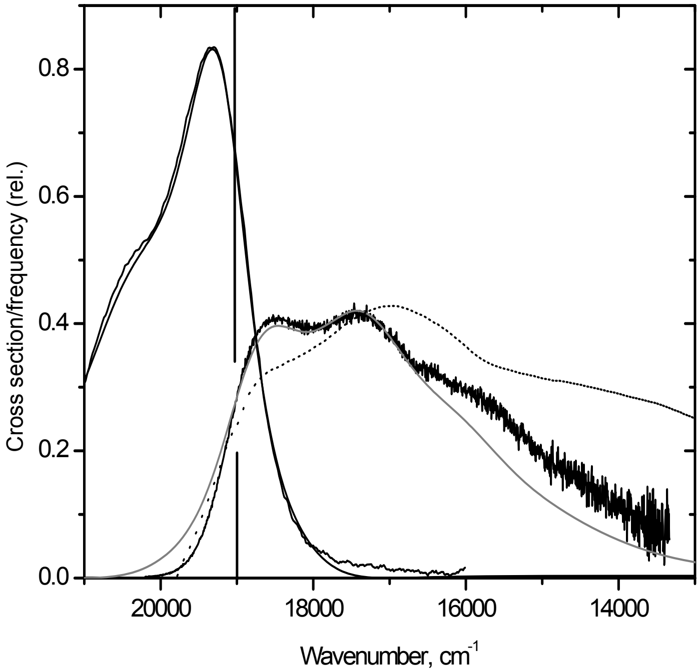

Figure 7.5.4-1 Bandshapes of TO in single-stranded PNA(TOPNA) (solid lines) described by the Brownian oscillator model (gray). The absorption shows an active mode in S_1 at 1350 cm^{-1} with dimensionless displacement d ≈1.11 from the S_0 geometry. The emission needs d ≈1.52 for broad vibronic structure and the vibrational frequency is estimated to be 1400 cm^{-1}. Transient absorption of TO in methanol at 300 fs is shown for comparison (spectrum L from figure 7.7.3-1a shifted by –480 cm^{-1} and scaled; dotted line. The absorption origin is marked by a vertical line.)

The absorption shows an active mode in S_1 at 1350 cm^{-1} with dimensionless displacement, $d \approx 1.11$, from the S_0 geometry. In emission, on the other hand, the active mode in S_0 has an estimated vibrational frequency of 1400 cm^{-1} and needs $d \approx 1.52$ from the S_1 geometry for broad vibronic structure. (Even a small change of *d* causes serious reshaping of the fluorescence spectrum; therefore *d* can be estimated to ± 0.02. For a quantitative description, the distribution of *d* along the twist coordinate must be included.) However, displacement and quantum yield are not related in a monotonic fashion, as the model reaction path alone would suggest. For example, by going from *mds* to *ads*, the quantum yield drops from 30 to 12%, while the displacement *decreases* slightly from d = 1.41, as can be seen by inspection of figure 7.5.4-1. This inversion becomes more pronounced when the next nucleobase to the TO in the labeled strand (t, thymine) is deleted to form abasic site (TOAPNA). The observations prove that neighboring nucleobases not only restrict torsional volume but also distort the S_1 potential-energy surface along high- frequency coordinates.

7.6 Time resolved measurements

7.6.1 Transient absorption spectra

Transient absorption spectra of thiazole orange in methanol were recorded with pump-super continuum probe spectroscopy. Thiazole Orange in methanol was excited by 40 fs pulses centered at 484 nm with repetition rate of 60 Hz with energy 0.5 μJ. The pathlength of sample cell was 0.35 mm, and the optical density was 0.65 at the absorption maximum corresponding to a concentration of 2.3×10^{-4} mol/L. The pump-induced transient absorption signal $\Delta OD(t, \lambda)$, was monitored by supercontinuum probe pulses covering the spectral range $340 \leq \lambda \leq 1000$ nm. Absorption spectra are shown in figure 7.6.1-1(a and b). Figure 7.6.1-1a represents their evolution from 50 fs to 1 ps after excitation. Positive induced optical density, $\Delta OD(t, \lambda)$, corresponds to excited-state absorption (ESA), while negative signal indicates bleach (BL) or stimulated emission (SE). At 1 ps, broad SE is observed from 10,000 to 18,000 cm^{-1}, there is no overlap with the absorption region, and the bleach contribution can be quantified by a negatively scaled absorption band. At 50 fs, because of overlapping the SE with the BL band, signal is most negative in between. Since pump is still present, the transient absorption spectrum at 50 fs also contains a coherent contribution of about ± 5 mOD, around the excitation frequency, which is centred at 20,690 cm^{-1}. But the pump has much lower intensity compared to its peak at $t = 0$.

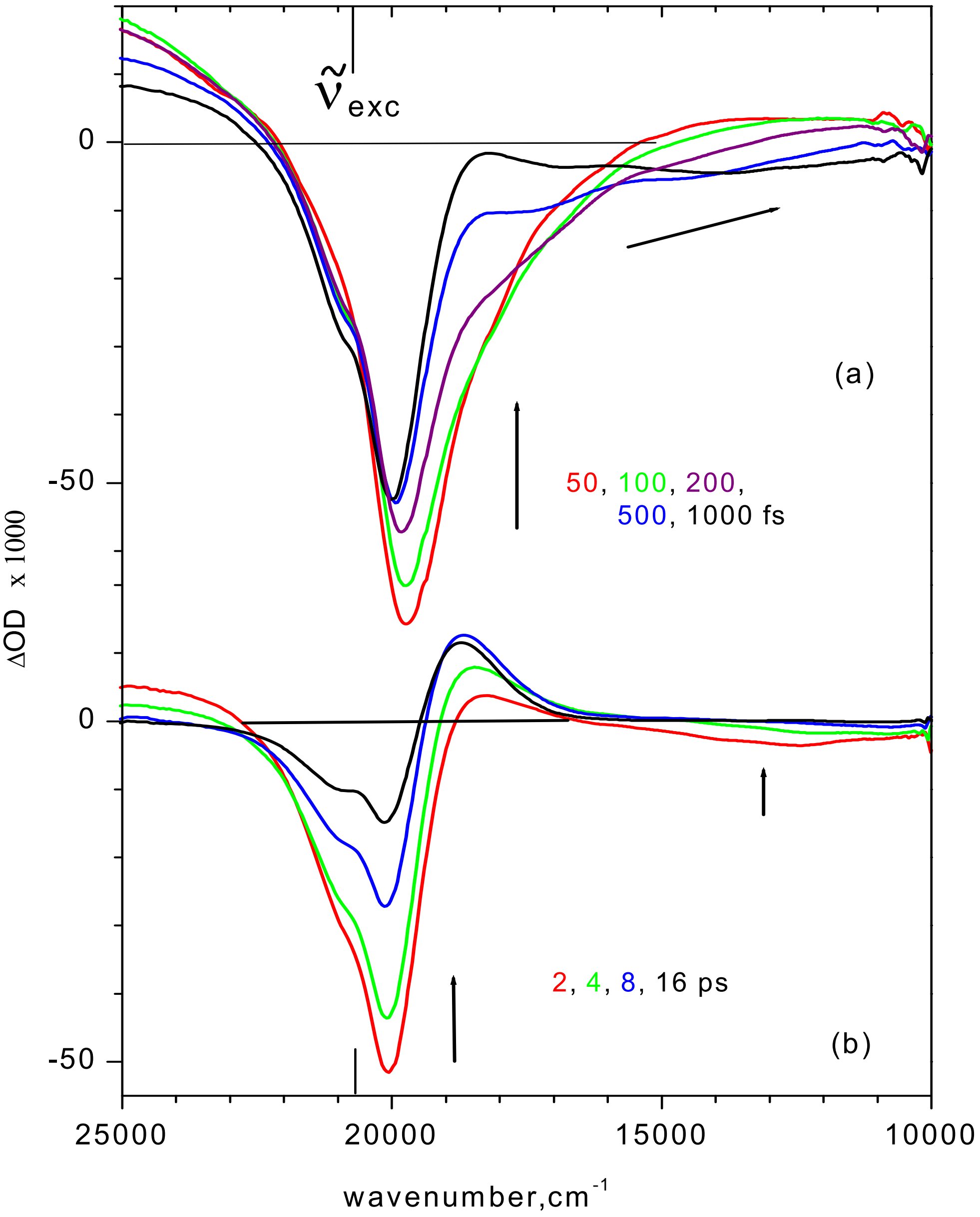

Figure 7.6.1-1 Transient absorption spectra of TO in methanol: (a) subpicosecond time scale showing bleach and red-shift of stimulated emission to the deep red, (b) picosecond scale on which internal conversion and cooling take place. Excitation at 484 nm, 65 fs time resolution fwhm and magic-angle polarizations.

Figure 7.6.1-1b represents the evolution from 2 ps to 16 ps. During this period, the deep red SE decays and the transient absorption spectrum gradually attains a dispersive shape. This indicates that the spectrum becomes broadened or shifted absorption spectrum. Separate measurements were performed with || and ⊥ polarizations of the pump light relative to that of the supercontinuum. The anisotropy is calculated during 1.5 ps with $\frac{I_{11} - I_{\perp}}{I_{11} + 2I_{\perp}}$. The value is 0.36 ± 0.01 for usable frequencies $\tilde{\nu} \leq 21{,}000$ cm^{-1}, that is in the BL and SE region and 0.26 ± 0.01 in the ESA range $\tilde{\nu} \geq 23{,}500$ cm^{-1}. Experiments done by varying the excitation energy yields no variation in the kinetics.

7.6.2 Transient fluorescence spectra

Time resolved fluorescence spectra of thiazole orange in methanol are recorded with fluorescence upconversion techniques. Thiazole orange was excited by 40 fs, 0.5 μJ pulses centered at 450 nm (500Hz). The path length of sample cell was 0.40 mm and the concentration 2 × 10^{-4} mol/L. Time resolved fluorescence spectra of TO are represented in figure 7.6.2-1 as quantum distributions over frequency. Emission from the narrow FC region can be observed directly. Here overlapping bands due to the other non linear optical processes which complicate the transient absorption are absent. At 50 fs, figure 7.6.2-1, the fluorescence band is a mirror image of the absorption. At 150 fs the band has shifted by 800 cm^{-1} to lower energy. Increasing the time up to1 ps, after this initial process, one observes strong broadening towards the red and decay in subpicosecond time scale. Finally the fluorescence disappears with about a 4 ps time constant (which is not shown).

7.7 Kinetic analysis

To analyse the data, the photoreaction is assumed to proceed through virtual excited states K, L and M for excited state and X and Y for ground state.

$$K(S_1) \xrightarrow{k_1} L(S_1) \xrightarrow{k_2} M(S_1) .... \xrightarrow{k_j} X(S_0) \xrightarrow{k_{j+1}} Y(S_0) .... \qquad 7.1$$

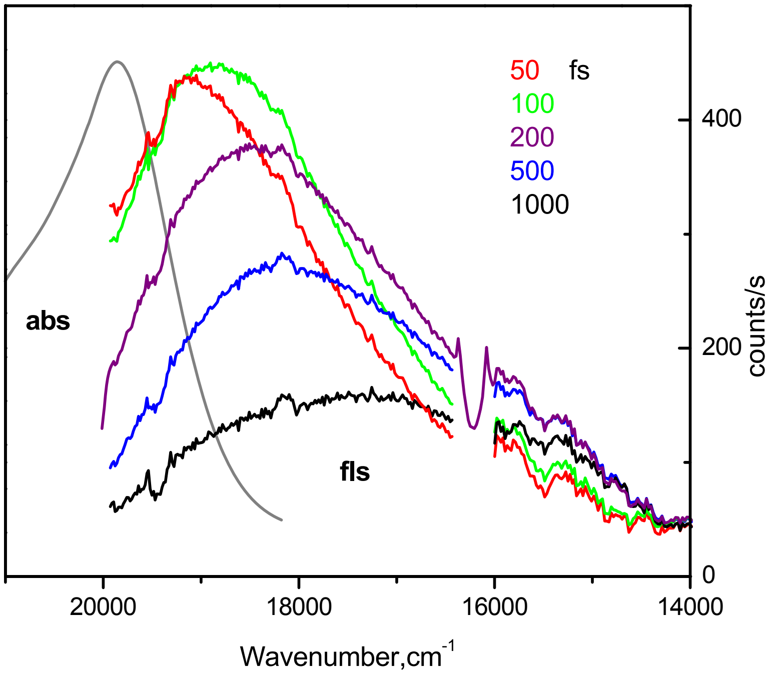

Figure 7.6.2-1 Transient fluorescence spectra of TO in methanol, from broadband upconversion with NIR gate pulses, show an initial red-shift over ~200 fs and subsequent broadening. Excitation at 450 nm, 80 fs time resolution and parallel polarizations. Signal is expressed as quantum distribution and scaled to the peak count rate. The absorption spectrum is also shown. (An artifact around 16200 cm^{-1} is due to scatter from the third-harmonic of the gate pulse.)

No physical meaning should be attached a priori to the characteristic intermediates, but of course, internal conversion to S_0 must be sketched in somewhere. For cyanines, the excited state relaxation involves no barrier and consists of continuous downhill motion along twist angles toward a perpendicular configuration of minimum energy, where internal conversion takes over. Evidence for internal conversion is (i) the disappearance of emission and (ii) the return to zero of the induced band-integral in transient absorption, as will be shown below. In principle, internal conversion may set in at stage L or earlier so that the kinetic approximation to the dynamics would have to contain a channel, $L(S_1) \rightarrow X(S_0)$. The limitations imposed by our scheme should be kept in mind later. Global analysis of time- and frequency-dependent data was done by singular-value decomposition [EKS01].

We seek characteristic fluorescence spectra along the way which would allow quantitative comparison with their counterparts from transient absorption. By combining both transient absorption spectra and fluorescence upconversion spectra, the characteristic transient emission spectra are extracted and related to the model reaction scheme of figure 7.4-1.

7.7.1 Analysis of transient fluorescence

The analysis starts with femtosecond fluorescence upconversion data. For transient fluorescence, we find that the three virtual states, K, L, and M are necessary and sufficient to describe the spectra and dynamics, with rate constants $k_1 = 4.97$, $k_2 = 1.44$, and $k_3 = 0.21$ ps^{-1}. A value for k_3 was obtained from transient absorption and kept fixed when fitting the fluorescence evolution. The total analysis was reiterated until consistency was achieved. Other sets of values for k_1 - k_3 are also possible. Transient emission spectra were analyzed for $t \geq 150$ fs because $t_0(\tilde{\nu})$ may smoothly deviate in a ± 15 fs band around the chosen function and because solvent Raman signal could not be uniquely separated from early fluorescence. Their time-dependent amplitudes are shown in figure 7.7.1-1; these curves describe the relative populations of the three states, convoluted with the apparatus function of the fluorescence experiment (Gaussian with 80 fs fwhm). The species-associated spectra are then expressed for stimulated emission, and we obtain the characteristic "pure" SE spectra which are shown in figure 7.7.3-1(b). The latter may be compared directly to the corresponding SE components from transient absorption. Deep-red emission around 12 000 cm^{-1} was not observed by our time resolved fluorescence experiment for technical reasons (vignetting in the spectrograph or input optics) nevertheless the kinetics of spectral change toward the red can be extracted reliably from the fluorescence data.

7.7.2 Analysis of transient absorption

For this purpose, we consider the initial period from -0.2 until 1.5 ps, which is largely shown in figure 7.6.1-1(a). The analysis of transient absorption spectra proceeds in two stages. First, the induced spectra, including coherence, are decomposed into species-associated spectra as described in ref. EKS01. The "species" in this case are the Gaussian pulse *G*(t) which describes the coherent contribution [DKE05] and the virtual states K, L, and M for the sequential contributions. Time derivatives *G', G''* were also included in the simulation of the coherent contribution. The time constants k_1 and k_2 are taken from the previous section. This treatment provides mainly the time resolution (65 fs fwhm) of the measurement. The amplitude of the bleach component is determined from the transient spectrum at 1.5 ps. With this information, the bleach $\mathrm{BL}(\tilde{\nu}, t)$ is simulated and subtracted from the data. The result is then reanalyzed in the second stage in order to obtain the ESA + SE spectra, which are shown in figure 7.7.3-1(a) for the three states. The associated amplitudes or kinetic traces are presented in figure 7.7.2-1. They represent the relative populations of K, L, and M as seen by transient absorption. Multiplying each of the traces with the corresponding spectrum, the temporal traces *G*(t), *G'*(t), and *G''*(t) with their associated spectra and summing the result, we obtain the observed transient spectra of figure 7.6.1-1 to within experimental noise of 0.6 mOD.

7.7.3 Comparison of transient absorption and fluorescence

Let us compare the characteristic spectra for transient absorption (figure 7.7.3-1 panel a) and pure stimulated emission obtained from upconverison (figure 7.7.3-1 panel b). The initial band K looks almost identical in the two observation modes: the peak for stimulated emission (i.e., the most negative value) occurs around 19 000 cm^{-1}, and the shape mirrors the absorption spectrum quite well. The peak from fluorescence upconversion occurs red-shifted by approximately 200 cm^{-1}, probably because of the

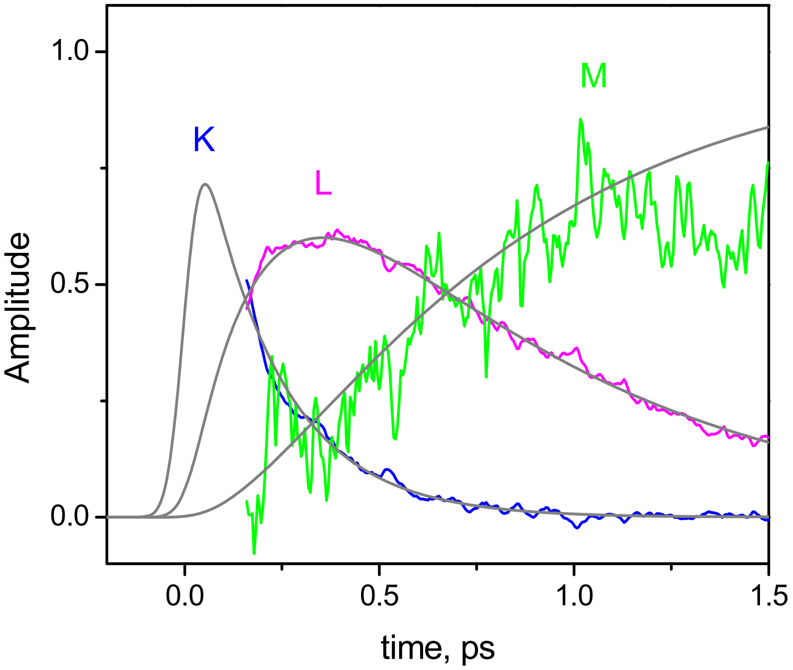

Figure 7.7.1-1 Joint decomposition of transient fluorescence spectra by global analysis. The evolution is described by a sequence K →L →M of virtual species in the excited state. Their time-dependent amplitudes are shown separately. These curves describe the relative populations of the three states, convoluted with the apparatus function of the fluorescence experiment. Pump and probe polarization were parallel for these measurements.

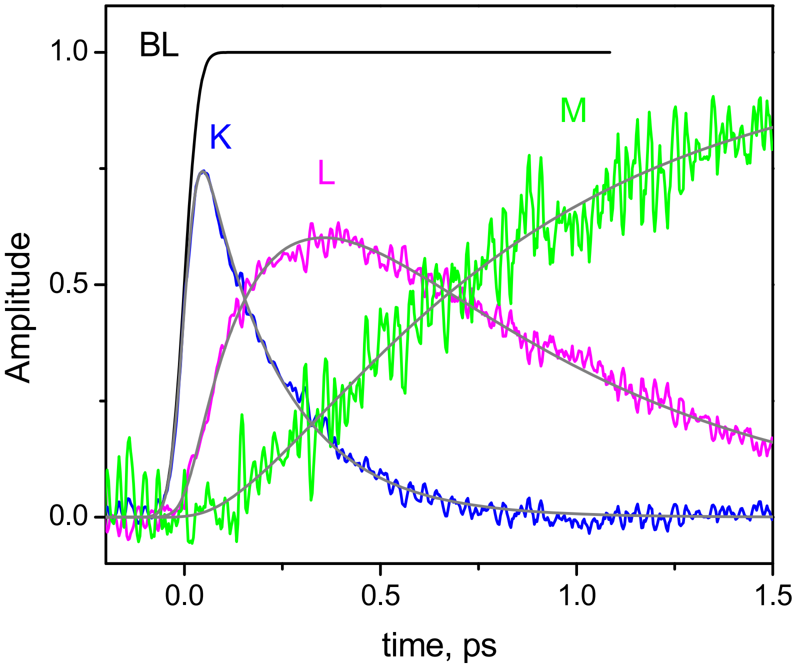

Figure 7.7.2-1 The analysis procedure is followed as transient fluorescence and results of the transient absorption are shown. Their relative populations are observed with different time-resolution and curve reflects their time-dependent amplitudes.

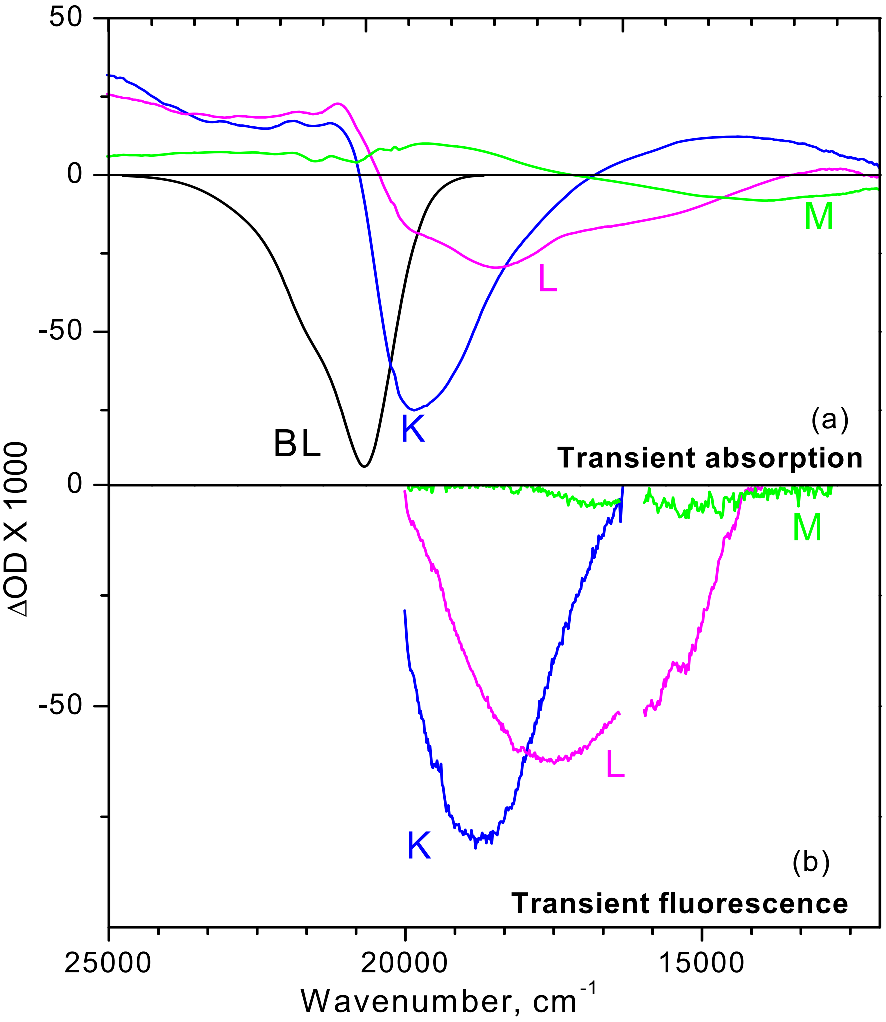

Figure 7.7.3-1 The associated spectra for the three states are shown in (a) for transient absorption and in (b) for transient fluorescence. Emission < 14000 cm^{-1} was not registered by time-resolved fluorescence for technical reasons. The associated spectra in (b) refer to stimulated emission rather than spontaneous fluorescence, to enable direct comparison with the absorption analogues in (a).

inner filter effect from ground-state absorption. From the figure 7.6.2-1, one finds that the fluorescence shifts to the red by 1000 cm^{-1} in 200 fs, and this observation is reflected in panel b by the second component L for pure stimulated emission, which has a broader peak at lower energy. (At 150 fs, the two are equally weighted (cf. figure 7.7.1-1), so that the corresponding Stokes shift is half of the peak separation). Turning to transient absorption in panel a, the peak values for K and L are more separated compared to their counterparts in panel b. This difference is explained by excited state absorption, which underlies transient absorption but does not contribute to fluorescence or pure stimulated emission derived from it. From a comparison, we conclude that excited state absorption rises in a broad band from 15 000 to19 000 cm^{-1} with the (nominal) time constant $1/k_1 \approx$ 200 fs. The observation of rising ESA in the bleach region of panel a, where SE is absent, supports this conclusion. The initial fluorescence occurs while the molecule twists away from the FC region, whereby radiative coupling to the ground state may diminish.

When and at which emission frequency does this effect set in? To approach the problem consider the band integral

$$BI_{fls}(t) = \int FQD(\tilde{\nu}, t)/\tilde{\nu}^3 d\tilde{\nu} \qquad 7.2$$

which may be calculated directly from the femtosecond fluorescence spectra; the result (after normalization, the band integral for the pure stimulated emission spectrum K (panel b) was set to that of the bleach BL (panel a), remember that the amplitudes in panels a and b were locked together in this way) is shown in figure 7.7.3-2. If the population stays constant, BI_{fls} is proportional to the oscillator strength or the square of the $S_1 \rightarrow S_0$ transition dipole moment. Our experiment shows a *rise* of BI_{fls}, reaching a maximum at 150 fs, clearly slower than the integrated apparatus function which was obtained from upconverted Raman scattering. Since the population in S_1 can only decrease after the pump pulse is over, several cases should be considered: radiative coupling may increase in the course of twisting or during brief nuclear coherence in another coordinate, or some artifact intervenes before 150 fs. The ambiguity can be reduced by the fluorescence analysis for $t \geq 150$ fs, which was summarized in figure 7.7.3.-1 panel b and figure 7.7.1-1. The band integrals are found to be nearly equal for the characteristic, empirical spectra K and L in panel b. In fact $BI_K < BI_L$ as observed, but spectrum K appears truncated at its blue side; equality should be achieved when the missing portion is reasonably appended. It follows that radiative coupling $S_1 \rightarrow S_0$ does not decrease for 200 fs, during which time the FC region is vacated and characteristic spectra L are assumed. This conclusion is supported by the band integral for transient absorption further below.

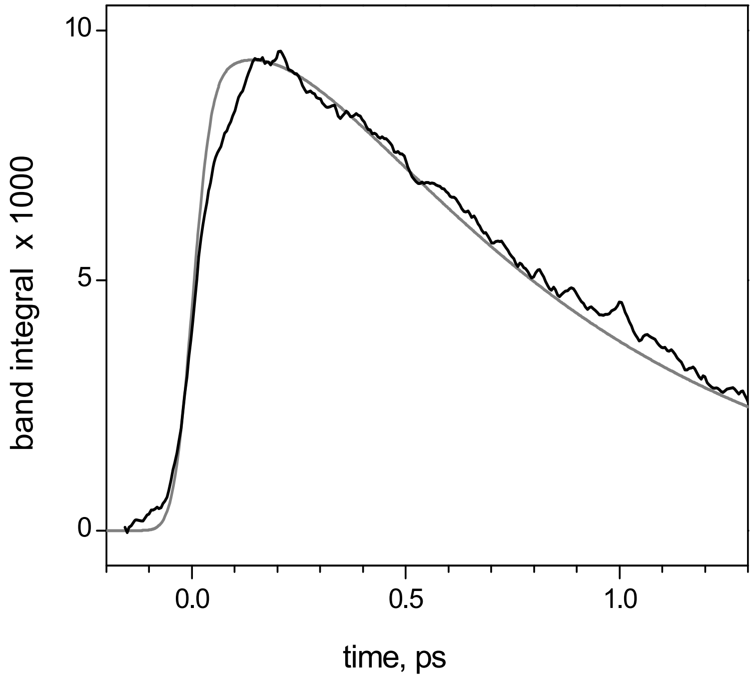

Figure 7.7.3-2 Band integral from femtosecond fluorescence spectra (figure 7.6.2-1), which suggests that radiative S_1–S_0 coupling is constant for the initial 200 fs – see text. The result from global analysis for t>150 fs is extrapolated to earlier time (gray curve).

A novel feature is presented by the broad SE band which is associated with transient state M. The band is directly observed by transient absorption (figure 7.6.1-1a) as the negative ΔOD across the range of 10 000-18 000 cm^{-1} at 1 ps delay. These measurements were often and well reproduced so that radiative coupling $S_1 \rightarrow S_0$ far below the initial emission frequency is certain. Fluorescence on a 4 ps time scale was also observed by upconversion. When the time constant k_3 = 0.21 ps^{-1} from transient absorption is used, a pure stimulated emission spectrum M is obtained, which is also shown in panel b of figure 7.7.3-1. Its blue flank matches the corresponding band in panel a quite well if allowance is made for underlying ESA. Below, we show that the deep-red emitting state M decays directly to the ground state so that no dark intermediate is populated on the S_1 energy surface; hence M can be identified with the minimum energy configuration there or with a wide region close to a conical intersection [HR005]. The oscillator strength for stimulated emission $M \rightarrow S_0$ can be estimated if the corresponding band is known completely.

In figure 7.7.3-1a, the transient absorption spectrum associated with M was shown, which consists of the SE and ESA contributions. Clearly, the part of the spectrum where OD < 0 is due to stimulated emission. If the integral is performed over this part only, one obtains a lower estimate of the oscillator strength, 20% relative to that of the BL band. More reasonable (but not certain) is the assumption that the ESA background extends linearly from its maximum around 19 000 cm^{-1} to zero at 10 000 cm^{-1}. In this case, the relative oscillator strength becomes 48%. We mentioned before that a conical intersection would be accidental with TO, which is why M probably corresponds to the global S_1 minimum. In this case the structure is essentially perpendicular and radiative coupling to the ground state should be significantly smaller than is actually observed. The observation therefore suggests that M is not perpendicular but instead represents a nonstationary, partly twisted region on the S_1 surface from where a conical intersection is accessed. The assignment should be decided by quantum-chemical calculations.

7.8 The emission lifetime

The emission time is generally determined by spectrally averaging over the fluorescence decay. When the emission shifts to the near infrared during the decay, late portions may be missed by conventional quantum yield or time-correlated photon-counting measurements. Likewise, our fluorescence upconversion measurements were not sufficiently sensitive for $\tilde{\nu} < 14\,000$ cm^{-1}. Therefore we turn to transient absorption because only this method could monitor the deep-red region. Under these conditions, SE + ESA are inseparable, and we treat all spectral change together by forming the band integral

$$\mathrm{BI}_{\mathrm{abs}}(t) \equiv \int \Delta\mathrm{OD}(\tilde{\nu}, t)\,/\tilde{\nu}\; d\tilde{\nu} \qquad 7.3$$

over the full observation range, that is, the (relative) induced oscillator strength. Solvation may shift ESA or SE bands within the range but should not affect the full integral. One finds

$$\mathrm{BI}_{\mathrm{abs}}(t) \propto n_1(t)\ \left[-f_{\mathrm{abs}} - f_{\mathrm{SE}}(t) + f_{\mathrm{ESA}}(t)\right] \qquad 7.4$$

The time dependence of oscillator strengths $f_{\mathrm{SE}}(t)$ and $f_{\mathrm{ESA}}(t)$ indicates electronic change, for example, while twisting around a central bond or along torsional motion of the thiazolyl moiety, and $n_1(t)$ is the population in the S_1 state. The full integral, which is shown in figure 7.8-1a, can therefore be considered as a measure of electronic change through optical excitation, weighted by population. By 15 ps it has returned to zero (a small deviation is attributed to the limited integration range) indicating complete ground-state recovery. The inset shows the initial period on an expanded time scale. Immediately after excitation, the full absorption integral stays constant until 0.4 ps while the spectral change is substantial during this time (cf. figure 7.6.1-1). An effective lifetime can be estimated as

$$\tau_{\text{eff}} = \int \mathrm{BI}_{\text{abs}}(t)\ dt / \mathrm{BI}_{\text{abs}}(0) = 4.7 \pm 0.1 \text{ ps} \qquad 7.5$$

with extrapolated $\mathrm{BI}_{\text{abs}}(t \rightarrow 0)$ for normalization, and the inferred quantum yield becomes $\tau_{\text{eff}} / \tau_{\text{rad}} = (7.6 \pm 0.4) \times 10^{-4}$. (By stationary fluorescence, we measure a quantum yield of 1.2×10^{-4} for TO in methanol. This value presents a lower limit because emission < 13 000 cm^{-1} was not registered; see figure 7.5.1-1.) At late time in the S_1 state, the effective lifetime shortens to 2.8 ps (dotted line in figure 7.8-1a). This type of nonexponentiality (if attributed to $n_1(t)$) is a hallmark of diffusional motion of the torsional coordinate toward a conversion funnel [BFO83].

7.9 Discussion

7.9.1 Summary

In summary, so far, the emission band mirrors the narrow absorption spectrum immediately after excitation and then experiences a dynamic Stokes shift of ~ 1000 cm^{-1} and broadening in the above 0.4 ps period. The radiative rate does not change significantly over this time. This phase appears to be similar to the relaxation to a shallow S_1 minimum which was calculated for symmetrical thiacarbocyanine [IS005]. The emission band shape in the intermediate time range is particularly interesting because model calculations predict asymmetric stretching activity [IS005, SHR00], after the FC region has been left (during process 2 in figure 7.4-1). Correspondingly, one expects

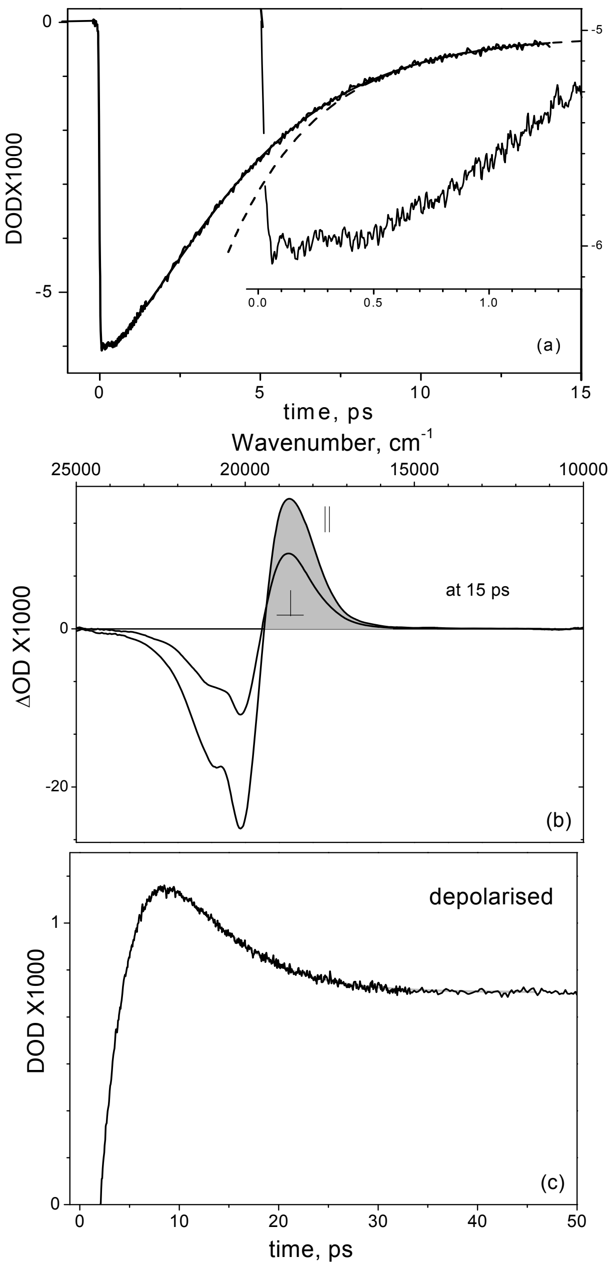

Figure 7.8-1 Picosecond dynamics of TO in methanol. (a) The full oscillator strength or band integral $\int \Delta\mathrm{OD}(\tilde{\nu},t)/\tilde{\nu}\ d\tilde{\nu}$ monitors electronic change. Initially constant (*cf.* inset), the effective decay time shortens to 2.8 ps late in S_1 (dotted exponential curve). Data refer to magic-angle detection. (b) Hot ground-state molecules / photoisomers are responsible for a dispersive shape of the transient spectrum when $t \geq 15\ \mathrm{ps}$, for example at t = 15 ps shown here for parallel and perpendicular polarizations. The partial band integrals from the lobes at lower energy (gray) are averaged to form the depolarized partial band integral (c) The latter measures the red-shift of the recovered ground-state absorption. It decays (time constant 4.6 ps) due to cooling and settles to a quasistationary value due to photoisomers.

vibronic structure of the emission around 0.3 ps, where the contribution by virtual species L is largest. Referring to figure 7.7.3-1, we indeed find vibronic structure for L, albeit with transient absorption only (panel a) because fluorescence upconversion did not extend sufficiently to the red (panel b). The L absorption spectrum is negative in the fluorescence range so that stimulated emission dominates here, and its structure may be considered reliable in view of the quality and reproducibility of the measurements. Simulations of the band shape with Brownian oscillators [BYM90] suggest a dimensionless displacement $d \approx 1.8$, but systematic deviation remains for large Stokes shifts, that is, for higher members, $k'' \geq 3$, of the vibrational progression, $0' \rightarrow k''$. Absorption of *mds* is described by the origin $\tilde{\nu}_{00}$ =19340 cm^{-1} and an underdamped mode with frequency $\tilde{\nu}$ =1350 cm^{-1}, dimensionless displacement d = 1.11, and friction constant γ= 135.6 ps^{-1}. Absorption of TOPNA is shifted to $\tilde{\nu}_{00}$ =19190 and broadened by an additional strongly-overdamped mode with reorganization energy $\lambda = 0$, spectral width Δ = 180 cm^{-1}, and damping constant Λ = 5 ps^{-1}; the model fluorescence band in figure 7.5.4-1 has $\tilde{\nu}$ = 1400 cm^{-1}, d = 1.52, γ =75.3 ps^{-1} and λ =450 cm^{-1}, Δ =300 cm^{-1}, Λ =5 ps^{-1}. The deviation may be caused by (i) excited-state absorption which contributes to the transient absorption spectrum, and (ii) the effect of torsional distribution in S_1 and the corresponding spectral convolution with the S_1-S_0 energy gap. Both complications were neglected in the simulations; we estimate that neglect of (ii) is the more serious of the two. Support for the existence of vibronic structure may be drawn from the emission in single stranded TOPNA, which was shown in figure 7.5.4.1 assuming that only intermediate twist angles are populated in this case. The transient absorption spectrum L is also represented in figure 7.5.4.1 (dotted line); note that direct comparison suffers equally from unknown (i) and to a lesser extents from unknown (ii). On balance, we conclude that TO emission in methanol exhibits high-frequency vibrational structure in the intermediate time range. The dynamic Stokes shift continues and slows gradually until, by about 2 ps, a broad quasi-stationary emission band is reached which is centered around 12 000 cm^{-1} and extends below 10 000 cm^{-1}. From here, internal conversion takes place, and the remainder deals with processes in the ground state. The following is therefore not relevant to the theme of this thesis, but it closes the photochemical cycle of

TO and, from a methodological point of view, shows further possibilities for the use of band integrals for condensed-phase spectroscopy.

7.9.2 Ground state reaction

The partial band integral is taken from dispersive $\Delta OD(\tilde{\nu},t)$, which dominates from 10 ps onward, by integrating $\Delta OD(\tilde{\nu}, t)$ over the red lobe only (figure 7.8-1b). It is a measure of broadening on the red flank of the recovered ground-state absorption, either because the molecular temperature has increased or because a photoisomer was created with a red-shifted absorption spectrum. The result is shown in figure 7.8-1c. The relaxation immediately after 10 ps is best described by 4.7 ps rise from internal conversion together with 4.6 ps exponential decay. The latter time constant is of the same order as that found for cooling of *p*-nitroaniline in methanol [KSH01] and is therefore ascribed to the same process. The remaining oscillator strength does not diminish until our last observation time of 125 ps; it should be due to the photoisomer. The asymmetry of the partial band integrals decays with a time constant of 124 ps due to rotational diffusion of the photoisomer. Referring to the scheme of intermediates, $X(S_0)$ and $Y(S_0)$ represent the hot and equilibrated photoisomer, respectively.

7.10 Conclusion

We conclude that a high-frequency mode (coordinate q) plays an important role in the structural reorganization of Thiazole Orange following $S_1 \leftarrow S_0$ optical excitation. The participation of another mode in the deactivation of cyanines has been described as a sequence of processes: fast vibrational relaxation followed by torsional motion [HCL02]. By observing vibronic structure of stationary emission in polynucleotides and of femtosecond transient emission in methanol solution, we showed instead that the high-frequency mode appears during torsion, which is taken to be the primary dynamical variable (coordinate τ). The observations are in agreement with recent model calculations [HR005, IS005, SHR00]. As the molecule twists away from the FC region, the mode becomes more displaced. In this way, better overlap between the lowest vibrational wave function, $\varphi_0^{S_1}(q)$, in S_1 with higher wave functions, $\varphi_k^{S_0}(q)$, in S_0 is achieved. Note that $\varphi_0^{S_1}(q)$ depends on τ as a parameter. Good vibrational overlap between S_1 and S_0 is a general condition for nonadiabatic coupling to become effective between the two electronic states. Even if the coupling coordinate Q is different from q, increasing mode displacement along q during torsion in S_1 helps provide ever higher accepting levels in S_0, in combined radiationless transitions

$$\psi_i^{S_1}(Q)\,\varphi_0^{S_1}(q) \rightarrow \psi_j^{S_0}(Q)\,\varphi_k^{S_0}(q) \qquad 7.6$$

In effect, the S_1-S_0 energy gap is reduced by the vibrational energy $E_k^{S_0}(\tau)$. Fast twisting motion along τ is thus leveraged into an even faster-shrinking effective energy gap, and internal conversion ensues.

8 Summary of the thesis

Stationary measurements on ANF derivatives

The solvatochromic behavior and photophysical properties of ANF and several derivatives in neat solvents and solvent mixtures were investigated. The absorption and fluorescence spectra of aliphatic ANF derivatives and of ANF nucleosides were measured in different solvents varying from non polar to polar. Using the absorption spectra of dBdP-ANF in 2-methyl butane together with Gaussian broadening, the mean band shift and width were obtained accurately. The polarity shift of dM-ANF was compared with the peak shift reported in the literature [CLP95]. A difference was due to the method of determining the relevant absorption frequency. Linear response theory was checked by relating the shift and broadening for all fluorene chromophore studied. Excited state dipole moments are also derived. Fluorescence lifetimes of ANF derivatives were measured depending on solvents. The lifetimes from fluorescence correspond to those from transient absorption measurements.

Solvation in aqueous mixtures (acetonitrile/water, dimethyl sulphoxide/water and acetonitrile/dimethyl sulfoxide) was monitored by optical absorption and by ^{1}H NMR spectroscopy (shift of amino proton). Preferential solvation refers to nonspecific effect whereby one component of the mixture is enriched around the solute. Part of the driving force may be entropic, for example the hydrophobicity of acetonitrile in water. For similar reason, the polar fluorenes are preferentially solvated by acetonitrile. In dM-ANF in almost pure water, a strong red shift of the absorption band with added cosolvent reflects cluster formation of the cosolvent or dimer formation of solutes.

The temperature dependence of ANF solubility was also measured in acetonitrile/water mixtures. From these data, the changes in enthalpy (ΔH) and in entropy (ΔS) upon transferring ANF from the solid to solution were obtained. The ΔS values are more negative for water-rich regions, which can be explained by preferential solvation.

In water-rich mixtures there is more contact with water so that the hydrogen bond network is more disturbed, hence ΔS is more negative.

Inclusion studies of a ANF riboside were performed with α, ß, and γ cyclodextrin as hosts in water. With increasing cyclodextrin concentration, an increase of optical absorbance and of fluorescence intensity and a change of shape together with a red shift of bands were observed. It can be concluded that the ANF riboside forms an "hydrophobic" complex in α CD, a "tight" complex with ß-CD, and both a "loose" and a "tight" complex with γ-CD. Binding constants are calculated by considering 1:1 complex at lower concentration and a 1:2 complex at higher concentration for ß-CD, as well as a 1:1 complex for γ-CD at all concentrations. ΔG is calculated and it related to the dissolving power of the mixture.

Femtosecond studies on ANF derivatives

Femtosecond transient absorption spectra of ANF derivatives and its glucosylated derivative (Gl-ANF) in a variety of solvents were measured with time resolution of 40 fs. The different transient spectral behavior of dM-ANF and of Gl-ANF in acetonitrile is discussed in detail. In Gl-ANF, the spectral signature due to stimulated emission decays very fast (within 300 fs); afterwards excited-state absorption dominates the transient spectra. The same is observed in methanol and dimethyl sulfoxide for both chromophores. On the other hand their transient behavior is similar in low-polarity solvents such as tetrahydrofuran, 1,4-dioxane, or ethyl acetate. It is believed that Gl-ANF undergoes *intra*-molecular processes other than solvation, probably intersystem crossing to a triplet state.

Solvation relaxation functions (C(t)) for ANF and dM-ANF in a variety of solvents were obtained by following the maximum of the stimulated emission band with time. For this purpose the transient spectra had to be decomposed into their ESA and BL parts. With Gl-ANF, C(t) could only be obtained by following the blue shift of the excited state absorption band. The solvation relaxation function is characterized by three time constants: the initial time constant, an average time constant, and the time required for to reach 1/e = 0.368. The relaxation curves of every solvent are compared with that of Coumarin 153. Differences between the curves from the two types of dye are described and discussed. In neat acetonitrile, an intermolecular solvent libration is seen more clearly by ANF and aliphatic derivatives than by Coumarin 153. In dimethyl sulfoxide the C(t) of fluorene derivatives deviate completely from that of the coumarin 153. In all other solvents the curves are partly matched. Differences probably reflect the different accuracy of the two types of measurements. Solvation relaxation curves obtained from the stimulated emission band and from the excited-state absorption band are compared.

Most importantly, femtosecond transient absorption spectra of the nucleoside Gl-ANF has been measured in water. A solvation relaxation function was obtained by following the blue shift of excited-state absorption. It shows an oscillation shoulder near 200 fs, identical to the one seen with methyl quinoline in water or obtained from the dielectric dispersion ε(ω) of pure water. This suggests that ANF, if made sufficiently water soluble, may serve as a faithful probe of local water dynamics. The observed dynamics is considerably faster than that calculated for ANF in DNA. This implies that the chromophore when stacked inside DNA can be distinguished from the chromophore when twisted around the sugar-phosphate backbone, extending into the aqueous boundary layer.

Stationary and femtosecond studies with Thiazole Orange (TO)

Excited state twisting dynamics of TO in methanol have been investigated in detail by comparing results from femtosecond transient absorption and fluorescence spectroscopy. Stimulated emission was observed up to 1000 nm for the first time. In transient fluorescence, the spectrum at 200 fs is the mirror image of the absorption spectrum. With time the emission band shifts dynamically to the red. At a Stokes shift of 1000 cm^{-1} a vibrational progression due to C = C asymmetric stretching is identified. The excited structural and electronic properties are discussed by reference to a simple symmetric cyanine. Twisting of the two moieties against each other is located on the conrotatory path, along which and a high frequency mode is displaced. This explains the observed vibronic structure around 690 fs. Vibronic spectra which are characteristic of different sections of the isomerisation path in S_1 are extracted by kinetic analysis. The dynamics of *cis*-isomer formation and subsequent cooling are also obtained.

Stationary optical spectra were measured for TO in PNA/DNA conjugates and their fluorescence quantum yields are compared. The quantum yield decreases from *matched* to *mis-matched* duplexes. The fluorescence spectra of duplexes show the vibrational progression of C=C asymmetric stretching. The fluorescence spectra are fitted with Brownian oscillator model, from which the vibrational displacement of the high-frequency mode was obtained. Hence, by connecting the vibronic structure of stationary emission in polynucleotides to femtosecond transient absorption spectra of TO in methanol solution, we conclude that high frequency modes are strongly coupled with torsion.

In this work oscillations were clearly seen in the solvation relaxation curves especially in water, obtained by following the dynamic fluorescence Stokes shift of the probe. This reflects the far-infrared spectra of the molecular solvent environment. In the literature, however, almost all solvation relaxation curves obtained until now were only nonexponential in behavior. The few exceptions were reported exclusively from our laboratory: N-Methyl-Quinolone in methanol and water [LKM05], and Amino-Nitro-Fluorene (ANF) in actonitrile [RKE98]. Here substituted ANFs are added to the list.

More research steps are needed to understand oscillatory relaxation behaviour of ANF linked into DNA. Therefore, the natural steps to be taken in continuation of this work are:

1. Melting temperatures studies of ANF-DNA duplexes – to obtain the thermal stability of duplex and binding constant when ANF is stacked between the nuclobases.
2. Femtosecond transient absorption studies of a number of ANF-DNA duplexes (because these were not synthesized yet at the conclusion of this work).
3. Femtosecond transient fluorescence of ANF-DNA duplexes.

4. NMR structure determination of the labeled duplexes.
5. Molecular dynamic simulations of the labeled duplexes.

Since the synthesis of ANF-labeled DNA oligomers has recently been successful, all of these points are presently under investigation.

9 References

[A0002] N. Agmon, *J. Phys. Chem. A* **2002,** 106, 7256.

[A0003] B. A. Armitage, *Drug Discovery Today* **2003**, 8, 222.

[A0090] N. Agmon, *J. Phys. Chem*. **1990**, 94, 2959.

[AD091] T. M. Alam, G. P. Drobny, *Chem. Rev.* **1991**, 91, 1545.

[AHW04] N. Amann, R. Huber, H. -A. Wagenknecht, *Angew. Chem. Int. Ed.* **2004**, 43, 1845.

[ALK05] D. Andreatta, J. L. P. Lustres, S. A. Kovalenko, N. P. Ernsting, C. J. Murphy, R. S. Coleman, M. A. Berg *J. Am .Chem. Soc.* **2005**, 127, 7270.

[AN005] R. A. I. Abou-Elkhair and T. L. Netzel, *Nucleosides, Nucleotides & Nucleic Acids* **2005**, 24, 85.

[ANR94] P. F. Aramendia, R. M. Negri, E. S. Roman, *J. Phys. Chem*. **1994**, 98, 3165.

[ASG86] E. Akesson, V. Sundström, T. Gillbro, *Chem. Phys.* **1986**, 106, 269.

[AW002] N. Amann, H. -A. Wagenknecht, *Synlett.* **2002**, 687.

[AYÅ98] J. -L. Alvarez, A. Yartsev, U. Åberg, E. Å kesson, V. Sundström, *J. Phys. Chem. B* **1998**, 102, 7651.

[AZM06] S. Arzhantsev, K. A. Zachariasse, M. Maroncelli, *J. Phys. Chem. A* **2006**, 110, 3454.

[ÅÅA94] U. Åberg, E. Åkesson, J. -L. Alvarez, I. Fedchenia, V. Sundström, *Chem. Phys*. **1994**, 183, 269.

[B0003] M. Bansal, *Curr. Sci.* **2003**, 85, 1556.

[B0064] N. G. Bakhshiev, *Opt. Spektrosk.* **1964**, 16, 821.

[B0070] J. B. Birks, *Photophysics of Aromatic Molecules*, Wiley-Interscience, New York, **1970**.

[B0082] J. -L. Brisset, *J. Chem. Eng. Data* **1982**, 27, 153.

[B0089] B. Bagchi, *Annu. Rev. Phys. Chem.* **1989**, 40, 115.

[BAE89] J. E. Bertie, K. M. Ahmed, H. H. Eysel, *J. Phys. Chem.* **1989**, 93, 2210.

[BB085] W. Baumann, H. Bischof, *J. Mol. Struct.* **1985**, 129, 125.

[BB099] B. Bagchi, R. Biswas, *Adv. Chem. Phys*. **1999**, 109, 207.

[BC089] J. S. Bader, D. Chandler, *Chem. Phys. Lett.* **1989**, 157, 501.

[BCH65] L. G. S. Brooker, A. C. Craig, D. W. Heseltine, P. W. Jenkins, L. L. Lincoln, *J. Am. Chem. Soc*. **1965**, 87, 2443.

[BFO83] B. Bagchi, G. R. Fleming, D. W. Oxtoby, *J. Chem. Phys*. **1983**, 78, 7375.

[BGL63] N. G. Bakshiev, O. P. Girin, V. S. Libov, *Opt. Spectroscopy* (U.S.S.R), **1963**, 14, 255395.

[BGM06] G. A. Burley, J. Gierlich, M. R. Mofid, H. Nir, S. Tal, Y. Eichen, T. Carell, *J. Am. Chem. Soc.* **2006**, 128, 1398.

[BGM92] J. M. Beechen, E. Gratton, O. M. Mantulin, *Globals Unlimited* **1992,** Urbana, Laboratory of Fluorescence Dynamics at the University of Illinois.

[BH049] H. A. Benesi, J. H. Hildebrand, *J. Am. Chem. Soc*. **1949**, 71, 2703.

[BJ090] P. F. Barbara, W. Jarzeba, *Adv. Photochem.* **1990**, 15, 1.

[BLK94] P. N. Borer, S. R. LaPlante, A. Kumar, N. Zanatta, A. Martin, A. Hakkinen, G. C. Levy, *Biochemistry* **1994**, 33, 2441.

[BMB98] E. B. Brauns, C. J. Murphy, M. A. Berg *J. Am. Chem. Soc*. **1998**, 120, 2449.

[BMC02] E. B. Brauns, M. L. Madaras, R. S. Coleman, C. J. Murphy, M. A. Berg **,** *Phys. Rev. Lett*. **2002**, 88, 158101.

[BMC99] E. B. Brauns, M. L. Madaras, R. S. Coleman, C. J. Murphy, M. A. Berg *J. Am. Chem. Soc.* **1999**, 121, 11644.

[BSB02] E. M. Boon, J. E. Salas, J. K. Barton, *Nat. Biotechnol*. **2002**, 20, 282.

[BSB03] C. Beuck, I. Singh, A. Bhattacharya, W. Hecker, V. S. Parmar, O. Seitz, E. Weinhold, *Angew. Chem. Int .Ed.* **2003,** 42, 3958.

[BYM90] B. W. Bosma, J. Y. Yan, S. Mukamel, *Phys. Rev. A* **1990**, 42, 6920.

[C0004] T. E. Cheatham, *Curr. Opin. Struct. Biol.* **2004**, 14, 360.

[CB091] A. Chandra, B. Bagchi, *J. Chem. Phys.* **1991**, 94, 3177.

[CBR97] A. Cupane, C. Bologna, O. Rizzo, E. Vitrano, L. Cordone, *Biophys. J.* **1997**, 73, 959.

[CBR99] F. Cichos, R. Brown, U. Rempel, C. von Borczyskowski, *J. Phys. Chem. A* **1999**,103, 2506.

[CCP05] A. Cuppoletti, Y. Cho, J. -S. Park, C. Strässler, E. T. Kool, *Bioconjugate Chem.* **2005**, 16, 528.

[CDG90] S. Chatterjee, P. D. Davis, P. Gottschalk, M. E. Kurz, B. Sauerwein, X. Yang, G. B. Schuster, *J. Am. Chem. Soc*. **1990**, 112, 6329.

[CFB88] Jr. W. E. Castner, G. R. Fleming, B. Bagchi, *Chem. Phys. Lett.,* **1988**, 143, 270.

[CFM00] G. Cosa, K. S. Focsaneanu, N. R. J. McLean, J. C. Scaiano, *Chem. Commun.* **2000**, 689.

[CG003] D. X. Cui, H. J. Gao, *Biotechnol. Prog.* **2003**, 19, 683.

[CLM63] J. Czekalla, W. Liptay, K. O. Meyer, *Z. Elektrochem.* **1963**, 67, 465.

[CLP95] J. Catalan, V. Lopez, P. Perez, R. M-Villamil, J-G. Rodriguez, *Liebigs Ann*. **1995**, 241.

[CM098] R. S. Coleman, M. L. Madaras, *J. Org. Chem*. **1998,** 63, 5700.

[CPC05] G. H. Clever, K. Polborn, T. Carell, *Angew. Chem. Int. Ed* **2005**, 44, 7204.

[CWP92] M. A. Carpenter, C. S. Willand, T. L. Penner, D. J. Williams, S. Mukamel, *J. Phys. Chem*. **1992**, 96, 2801.

[CWR97] F. Cichos, A. Willert, U. Rempel, C. vonBorczyskowski, *J. Phys. Chem. A* **1997**, 101, 8179.

[D0092] R. S. Drago, *J. Chem. Soc., Perkin Trans 2* **1992**, 1827.

[DC071] J. N. Demas, G. A. Crosby, *J. Phys. Chem*. **1971**, 75, 991.

[DEE86] R. M. C. Dawson, D. C. Elliott, W. H. Elliott, K. M. Jones, *Data for Biochemical Research*. Oxford, Clarendon Press, **1986**, p. 422.

[DGD95] T. G. Deligeorgiev, N. I. Gadjev, K. -H. Drexhage, R. W. Sabnis, *Dyes and Pigments* **1995**, 29, 315.

[DKE05] A. L. Dobryakov, S. A. Kovalenko, N. P. Ernsting, *J. Chem. Phys*. **2005**, 123, 044502.

[DM004] R. J. Desa, I. B. C. Matheson, *Methods Enzymol*. **2004**, 384, 1.

[DMS05] I. Dilek, M. Madrid, R. Singh, C. P. Urrea, B. A. Armitage, *J. Am. Chem. Soc*. **2005**, 127, 3339.

[DP099] T. J. F. Day, G. N. Patey, *J. Chem. Phys*. **1999**, 110, 10937.

[DSE89] G. L. Duveneck, E. V. Sitzmann, K. B. Eisenthal, N. J. Turro, *J. Phys. Chem*. **1989**, 93, 7166.

[DT080] T. J. Dougherty, R. E. Thoma, In Lasers in photomedicine and photobiology, Eds. R. Pratesi, C. A. Sachi., Springer-Verlag: Berlin, **1980**, p. 67.

[DW084] D. C. Dong, M. A. Winnik, *Can. J. Chem.* **1984**, 62, 2560.

[EBC93] M. Egholm, O. Buchardt, L. Christensen, C. Behrens, S. M. Freier, D. A. Driver, R. H Berg, S. K. Kim, B. Norde´n, P. E. Nielsen, *Nature* **1993**, 365, 566.

[ECR67] E. S. Emerson, M. A. Conlin, A. E. Rosenoff, K. S. Norland, H. Rodriguez, D. Chin, G. R. Bird, *J. Phys. Chem.* **1967**, 71, 2396.

[EKS01] N. P. Ernsting, S. A. Kovalenko, T. Senyushkina, J. Saam, V. Farztdinov, *J. Phys. Chem. A* **2001**, 105, 3443.

[EY039] C. Eckhart, G. Young, *Bull. Am. Math. Soc.* **1939**, 45, 118.

[F0089] G. D. Fasman, *Practical Handbook of Biochemistry and Molecular Biology*. Boca Raton, Florida, CRC Press, **1989**, pp. 536.

[FAR94] D. Figeys, E. Arriaga, A. Renborg, N. J. Dovichi, *J. Chromotogr.A* **1994,** 669, 205.

[FC096] G. R. Fleming, M. Cho, *Annu. Rev. Phys. Chem.*1996, 47, 109.

[FE0_ _] V. M. Farztdinov, N. P. Ernsting, *private communication.*

[FES_ _] V. M. Farztdinov, N. P. Ernsting, K.-H. Sklenar, *to be communicated.*

[FFP01] W. Fu, J. -K. Feng, G. -B. Pan, *J. Mol. Str (Theo).* **2001**, 545, 157.

[FL091] T. Fonseca, B. M. Ladanyi, *J. Phys. Chem*. **1991**, 95, 2116.

[FL094] T. Fonseca, B. M. Ladanyi, *J. Mol. Liq*, **1994**, 60, 1.

[FM094] R. S. Fee, M. Maroncelli, *Chem. Phys.* **1994**, 183, 235.

[FMM91] R. S. Fee, J. A. Milsom, M. Maroncelli, *J. Phys. Chem*. **1991**, 95, 5170.

[FWZ02] T. Fiebig, C. Wan, A. H. Zewail, *ChemPhysChem.* **2002**, 3, 781.

[G0091] B. Guillot, *J. Chem. Phys.* **1991**, 95, 1543.

[G0094] D. G. Gorenstein, *Chem. Rev*, **1994**, 94, 1315.

[G0098] Gaussian 98, Revision A 3, *Gaussian, Inc*., Pittsburgh PA, **1998.**

[GC000] P. L. Geissler, D. Chandler, *J. Chem. Phys*. **2000**, 113, 9759.

[GCG98] T. Gustavsson, L. Cassara, V. Gulbinas, G. Gurzadyan, J. -C. Mialocq, S. Pommeret, M. Sorgius, P. van der Meulen, *J. Phys. Chem. A* **1998**, 102, 4229.

[GCN05] S. T. Gaballah, G. Collier, T. L. Netzel, *J. Phys. Chem. B* **2005**, 109, 12175.

[GH070] E. v. Goldammer, H. G. Hertz, *J. Phys. Chem*. **1970**, 74, 3734.

[GH083] R. E. Grote, J. T. Hynes, *J. Chem. Phys*. **1983**, 77, 3736.

[GHA05] S. T. Gaballah, Y. H. A. Hussein, N. Anderson, T. T. Lian, T. L. Netzel, *J. Phys. Chem. A* **2005**, 109, 10832.

[GLK05] J. Gao, H. Liu, E. T. Kool, *Angew. Chem. Int. Ed.* **2005**, 44, 3118.

[GLT85] F. Grieser, M. Lay, P. J. Thistlethwaite, *J. Phys. Chem*. **1985**, 89, 2065.

[GK004] H. J. Gao, Y. Kong, *Annu. Rev. Mater. Res.* **2004**, 34, 123.

[GM098] J. A. Gardecki, M. Maroncelli, *Appl. Spectr*. **1998**, 52, 1179.

[GN005] S. T. Gaballah, T. L. Netzel, *Heterocyclic Commun*. **2005**, 11, 241.

[GNJ05] B. Giese, M. Napp, O. Jacques, H. Boudebous, A. M. Taylor, J. Wirz, *Angew. Chem. Int. Ed.* **2005**, 44, 4073.

[GR092] A. N. Glazer, S. H. Rye, *Nature* **1992**, 359, 859.

[GSR00] K. M. Guckian, B. A. Schweitzer, R. X.-F. Ren, C. J. Sheils, D. C. Tahmassebi, E. T. Kool, *J. Am. Chem. Soc.* **2000,** 122, 2213.

[GVE05] S. T. Gaballah, J. D. Vaught, B. E. Eaton, T. L. Netzel *J. Phys. Chem. B* **2005,** 109, 5927.

[GWW66] N. E. Good, G. D. Winget, W. Winter, T. N. Connolly, S. Izawa, R. M. M. Singh, *Biochem.* **1966**, 5, 467.

[H0073] J. B. Hasted, *Aqueous Dielectrics*; Chapman and Hall: London, 1973.

[H0085] J. T. Hynes, *In Theory of Chemical Reactions*; Chemical Ruber: New York, **1985**; p 171.

[HAW04] R. Huber, N. Amann, H. -A. Wagenknecht, *J. Org. Chem*. **2004**, 69, 744.

[HCL02] Y. Huang, T. Cheng, F. Li, C. –H. Hunag, S. Wang, W. Huang, Q. Gong, *J. Phys. Chem. B* **2002**, 106, 10041.

[HFC94] G. T. Hirons, J. J. Fawcett, H. A. Crissman, *Cytometry* **1994**, 15, 129.

[HFW03] R. Huber, T. Fiebig, H. -A. Wagenknecht, *Chem. Commun*. **2003**, 1878.

[HGP95] M. L. Horng, J. A. Gardecki, A. Papazyan, M. Maroncelli, *J. Phys. Chem*. **1995**, 99, 17311.

[HH092] E. R. Henry, J. R. Hofrichter, *Methods Enzymol*. **1992**, 210, 129.

[HHF87] J. B. Hasted, S. K. Hussain, F. A. M. Frescura, J. R. Birch, *Infrared Phys.* **1987**, 27, 11.

[HK084] S. R. Holbrook, S. -H. Kim, *J. Mol. Biol.* **1984**, 173, 361.

[HLS03] M. J. B -Hearn, R. E. Larsen, B. J. Schwartz, *J. Phys. Chem. A*, **2003**, 107, 4773.

[HMT96] W. J. Harrison, D. L. Mateer, G. J. T. Tiddy, *J. Phys. Chem.* **1996**, 100, 2310.

[HR005] P. A. Hunt, M. A. Robb, *J. Am. Chem. Soc*. **2005**, 127, 5720.

[HT078] L. A. Hallidy, M. R. Topp, *J. Phys. Chem*. **1978**, 82, 2415.

[IAH04] N. Ito, S. Arzhantsev, M. Heitz, M. Maroncelli, *J. Phys. Chem. B* **2004**, 108 , 5771.

[IS005] R. Improta, F. Santoro, *J. Chem. Theor. Comput*. **2005**, 1, 215.

[ITT05] F. Ingrosso, A. Tani, J. Tomasi, J. *Mol. Liq*. **2005**, 117, 85.

[J0086] P. Jacques, *J. Phys. Chem*. **1986**, 90, 5535.

[JFK94] R. Jimenez, G. R. Fleming, P. V. Kumar., M. Maroncelli, *Nature,* **1994**, 369, 471.

[JKS05] D. V. Jarikote, O. Köhler, E. Socher, O. Seitz, *Eur. J. Org. Chem.* **2005**, 3187.

[JWJ88] W. Jarzeba, G. C. Walker, A. E. Johnson, M. A. Kahlow, P. F. Barbara, *J. Phys. Chem*. **1988**, 92, 7039.

[K0058] E. M. Kosower, *J. Am. Chem. Soc*. **1958**, 80, 3253.

[K0062] R. Kubo, *J. Phys. Soc. Jpn.* **1962**, 17, 1100.

[KAT77] M. J. Kamlet, J. L. M. Abboud, R. W. Taft, *J. Am. Chem. Soc.* **1977,** 99, 6027.

[KEB98] A. Kummrow, M. F. Emde, A. Baltuska, M. S. Pshenichnikov, D. A. Wiersma, *J. Phys. Chem. A* **1998**, 102, 4172.

[KET02] P. Kaden, E. M -Enthart, A.Trifonov, T. Fiebig, H.-A.Wagenknecht, *Angew. Chem. Int. Ed*. **2005**, 44, 1636.

[KHS97] S. O. Kelley, R. E. Holmlin, E. D. A. Stemp, J. K. Barton, *J. Am. Chem. Soc.*, **1997,** 119, 9861.

[KIO97] T. Katoh, Y. Inagaki, R. Okazaki, *Bull. Chem. Soc. Jpn.* **1997**, 70, 2279.

[KJS04] O. Köhler, D.V. Jarikote, O. Seitz, *Chem. Commun.* **2004**, 2674.

[KK005] T. W. Kim, E. T. Kool, *J. Org. Chem*. **2005**, 70, 2048.

[KKS01] S. A. Kovalenko, N. E. -Konig, T. A. Senyshkina, N. P. Ernsting, *J. Phys. Chem. A* **2001**, 105, 4834.

[KM095] P. V. Kumar, M. Maroncelli, *J. Chem. Phys*. **1995**, 103, 3038.

[KMH00] C. E. Kerr, C. D. Mitchell, J. Headrick, B. E. Eaton, T. L. Netzel, *J. Phys. Chem. B* **2000**, 104*,* 1637.

[KR093] M. Krieg, R. W. Redmond, *Photochem. Photobiol*. **1993**, 57, 472.

[KRE97] S. A. Kovalenko, J. Ruthmann, N. P. Ernsting, *Chem. Phys. Lett*. 1997, 271, 40.

[KS003] O. Köhler, O. Seitz, *Chem. Commun*. **2003**, 2938.

[KS097] R. F. Khairutdinov, N. Serpone, *J. Phys. Chem. B* **1997**, 101, 2602.

[KSH01] S. A. Kovalenko, R. Schanz, H. Hennig, N. P. Ernsting, *J. Chem. Phys*. **2001**, 115, 3256.

[KTA93] C. V. Kumar, R. S. Turner, E .H. Asuncion *J. Photochem. Photobiol. A: Chem.* **1993**, 74, 231.

[L0005] Frederick D. Lewis, *Photochem. and Photobio.* **2005**, 81, 65.

[L0057] E. Lippert, *Z. Elektrochem*. **1957**, 61, 962.

[LB005] T. Liu, J. K. Barton, *J. Am. Chem. Soc.* **2005**, 127, 10160.

[LCC86] L. G. Lee, C. –H. Chen, L. A. Chiu, *Cytometry* **1986**, 7, 508.

[LJS99] M. J. Lang, X. J. Jordanides, X. Song, G. R. Fleming, *J. Chem. Phys*. **1999**, 110, 5884.

[LKL02] B. M. Luther, J. R. Kimmel, N. E. Levinger, *J. Chem. Phys.* **2002**, 116, 3370.

[LKM05] J. L. P. Lustres, S. A. Kovalenko, M. Mosquera, T. Senyushkina, W. Flasche, N. P. Ernsting, *Angew. Chem. Int. Ed.* **2005**, 44, 5635.

[LM098] B. M. Ladanyi, M. Maroncelli, *J. Chem. Phys.* **1998**, 109, 3204.

[LM098a] J. E. Lewis, M. Maroncelli, *Chem. Phys. Lett.* **1998**, 282, 197.

[LNA85] M. Levitus, R. M. Negri, P. F. Aramendia, *J. Phys. Chem*. **1995**, 99, 14231.

[LOF99] D. S. Larsen, K. Ohta, G. R. Fleming, *J. Chem. Phys*. **1999**, 111, 8970.

[LP002] B. M. Ladanyi, B. C. Perng, *J. Phys. Chem. A* **2002**,106, 6922.

[LS099] D. Laria, M. S. Skaf, *J. Chem. Phys*. **1999**, 111, 300.

[LWZ04] F. D. Lewis, Y. Wu, L. Zhang, X. Zuo, R. T. Hayes, M. R. Wasielewski, *J. Am. Chem. Soc.* **2004**, 126, 8206.

[LZR87] J. Lee, S. –B. Zhu, G. W. Robinson, *J. Phys. Chem*. **1987**, 91, 4273.

[M0057] E. G. McRae, *J. Phys. Chem.* **1957**, 61, 562.

[M0090] F. Matsui, Optical recording systems, Plenum. New York, **1990**.

[M0091] M. Maroncelli, *J. Chem. Phys.* **1991**, 94, 2084.

[M0093] M. Maroncelli, *J. Mol. Liq*. **1993**, 57, 1.

[M0096] D. P. Millar, *Curr. Opin. Struct. Biol.* **1996**, 6, 322

[M0002] Y. Marcus, *Solvent mixtures−properties and selective solvation*, Marcel Dekker Inc, New York, **2002**, p73, Table 2.16

[MBB00] A. Mishra, R. K. Behera, P. K. Behera, B. K. Mishra, G. B. Behera, *Chem. Rev*. **2000**, 100, 1973.

[MC094] P. L. Muino, P. R. Callis, *J. Chem. Phys.* **1994**, 100, 4093.

[MCS05] L. Mikelsons, C. Carra, M. Shaw, C. Schweitzer, J. C. Scaiano, *Photochem. Photobiol. Sci.* **2005**, 4, 798.

[ME0_ _] R. Mahrwald, N. P. Ernsting, *private communication.*

[MF087] M. Maroncelli, G. R. Fleming, *J. Chem. Phys.* **1987,** 86, 6221.

[MF088] M. Maroncelli, G. R. Fleming, *J. Chem. Phys.* **1988,** 89, 875.

[MF088a] M. Maroncelli, G. R. Fleming, *J. Chem. Phys.* **1988**, 89, 5044.

[MGA79] J. C. Mialocq, P. Goujon, M. Arvis, *J. Chem. Phys*. **1979**, 76, 1067.

[MMF89] M. Maroncelli, J. MacInnis, G. R. Fleming, *Science* **1989**, 243, 1674.

[MNT89] M. Minuro, T. Nozawa, N. Tamai, K. Shimada, I. Yamazaki, S. Lin, R. S Knox, B. P. Wittmershaus, D. C. Brune, R. E. Blankenship, *J. Phys. Chem*. **1989**, 93, 7503.

[MPP98] Y. H. Meyer, M. Pittman, P. Plaza, *J. Photochem. Photobio. A Chem*. **1998**, 114, 1.

[MSL97] D. V. Matyushov, R. Schmid, B. M. Ladanyi, *J. Phys. Chem. B* **1997**, 101, 1035.

[MSS04] P. K. Mandal, M. Sarkar, A. Samanta, *J. Phys. Chem. A* **2004**, 108, 9048.

[NB002] M. A. O'Neill, J. K. Barton, *J. Am. Chem. Soc.* **2002**, 124, 13053.

[ND096] S. Nigam, G. Durocher, *J. Phys. Chem*. **1996**, 100, 7135.

[NNB91] E. Neria, A. Nitzan, R. B. Barnett, U. Landman, *Phys. Rev. Lett.* **1991**, 67, 1011.

[NNZ95] T. L. Netzel, K. Nafisi, M. Zhao, J. R. Lenhard, I. Johnson, *J. Phys. Chem.* **1995**, 99, 17936.

[NSK98] J. Nygren, N. Svanvik, M. Kubista, *Biopolymers* **1998**, 46, 39.

[O0077] L. Onsager, *Can. J. Chem.* **1977**, 55, 1819.

[OJS05] O. Köhler, D. V. Jarikote, O. Seitz, *ChemBioChem* **2005**, 6, 69.

[OLK01] T. Yu. Ogul'chansky, M. Yu. Losytskyy, V. B. Kovalska, V. M. Yashchuk, S. M. Yarmoluk, *Spectrochim. Acta. A*, **2001**, 57, 1525.

[ORA99] T. Okonogi, A. W. Reese, S. C. Alley, P. B. Hopkins, B. H. Robinson, *Biophys. J.* **1999**, 77, 3256.

[ÖV006] T. A. Özal , N. F. A. v. der Vegt, *J. Phys. Chem B* **2006**, 110*,* 12104.

[P0002] M. C. Pirrung, *Angew. Chem. Int. Ed.* **2002**, 41, 1276.

[PBR00] T. J. Petty, A. J. Bordelon, E. M. Robertson, *J. Phys. Chem. B* **2000**, 104, 7221.

[PDV99] S. Prodhomme, J. -P. Demaret, S. Vinogradov, U. Asseline, L. M. -Allory, P. Vigny, *J. Photochem. Photobiol. B: Biol*. **1999**, 53, 60.

[PLK98] P. L. Paris, J. M. Langenhan, E. T. Kool, *Nucleic Acids Res.* **1998**, 26, 3789.

[PM093] A. Papazyan, M. Maroncelli, *J. Chem. Phys*. **1993**, 98, 6431.

[PMM02] E. Privat, T. Melvin, F. Merola, G. Schweizer, S. Prodhomme, U. Asseline, P. Vigny, *Photochem. Photobiol.* **2002**, 75, 201.

[PNJ97] S. A. Passino, Y. Nagasawa, T. Joo, G. R. Fleming, *J. Phys. Chem. A* **1997**, 101, 725.

[PNF97] S. A. Passino, Y. Nagasawa, G. R. Fleming, *J. Chem. Phys*. **1997**, 107, 6094.

[PSC94] T. T. Perkins, D. E. Smith, S. Chu, *Science* **1994**, 264, 819.

[PTV92] W. H. Press, S. A. Teukolsky, W. T. Vetterling, B. P. Flannery, *Numerical Recipes in Fortan*, 2nd ed.; Cambridge University press: New York, **1992**.

[PWS98] N. K. Petrov, A. Wiessner, H. Staerk, *J. Chem. Phys.* **1998**, 108, 2326.

[PWS01] N. K. Petrov, A. Weissner, H. Staerk, *Chem. Phys. Lett*. **2001**, 349, 517.

[PZ004] S. K. Pal, A. H. Zewail, *Chem. Rev*. **2004**, 104, 2099.

[R0088] C. Reichardt, *Solvents and Solvent effects in Organic Chemistry*, 2nd edn, VCH Publishers, Weinheim, **1988**, and references therin.

[R0094] C. Reichardt, *Chem. Rev*. **1994**, 94, 2319.

[RD095] B. H. Robinson, G. P. Drobny *Annu. Rev. Biophys. Biomol. Struct.* **1995**, 24, 523.

[RG095] H. S. Rye, A. N. Glazer, *Nucleic Acids Res*. **1995**, 23, 1215.

[RHM97] S. Rüdisser, A. Hallbrucker, E. Mayer, G. P. Johari, *J. Phys. Chem. B* **1997**, 101, 266.

[RHT00] T. Ratilainen, A. Holmen, E. Tuite, P. E. Nielsen, B. Norden, *Biochem.* **2000**, 39, 7781.

[RKE98] J. Ruthmann, S. A. Kovalenko, N. P. Ernsting, D. Ouw, *J. Chem. Phys*. **1998**, 109, 5466.

[RKJ88] I. Rips, J. Klafter, J. Jortner, *J. Chem. Phys.* **1988**, 89, 4288.

[RM003] N. Robertson, C. A. McGowan, *Chem. Soc. Rev.* **2003**, 32, 96.

[RQP90] H. S. Rye, M. A. Quesada, K. Peck, R. A. Matheis, A. N. Glazer, *Nucleic Acids Res*. **1990**, 19, 327.

[RS094] P. J. Rossky, J. D. Simon, *Nature*, **1994**, 370, 263.

[S0000] G. B. Schuster, *Acc. Chem. Res.* **2000**, 33, 253.

[S0077] D. M Sturmer, Synthesis and properties of cyanine and related dyes. Special topics in heterocyclic chemistry; Ed. A. Weissberger, E. C. Taylor, John Wiley & Sons. **1977**. (b) D. M. Sturmer, D. W. Heseltine, The theory of the photographic process, 4th ed., Ed. T. H. James; Macmillan Publishing Co.; NewYork, **1977**; Chapter8 (Sensitizing and desensitizing dyes).

[S0084] Y. R. Shen, *The Principles of Nonlinear Optics*, J. Wiley and Sons, New York, **1984**, p. 76.

[S0088] J. D. Simon, *Acc. Chem. Res.* **1988**, 21, 128.

[S0098] J. Szejtli, *Chem. Rev.* **1998**, 98, 1743.

[SAM04] M. M. Somoza, D. Andreatta, C. J. Murphy, R. S. Coleman, and M. A. Berg, *Nucleic Acids Res.* **2004**, 32, 2494.

[SAS98] L. D. Simon, K. H. Abramo, K. J. Sell, B. L. McGown, *Biospectroscopy* **1998**, 4, 17.

[SB095] A. Staib, D. Borgis, *J. Chem. Phys.* **1995**, 103, 2642.

[SC000] H. Shirota, E.W. Castner, *J. Chem. Phys.* **2000**, 112, 2367.

[SG082] A. Sundström, T. Gillbro, *J. Phys. Chem*. **1982**, 86, 1788.

[SGS88] R. K. Saiki, D. H. Gelfand, S. Stoffel, S. Scharf, R. Higuchi, G. T. Horn, K. B. Mullis, H. A. Erlich, *Science* **1988**, 239, 487.

[SHR00] A. Sanchez-Galvez, P. Hunt, A. M. Robb, M. Olivucci, T. Vreven, B. H. Schlegel, *J. Am. Chem. Soc*. **2000**, 122, 2911.

[SL096] M. S. Skaf, B. M. Ladanyi, *J. Phys. Chem*. **1996**, 100, 18258.

[SKK01] R. Schanz, S. A. Kovalenko, V. Kharlanov, N. P. Ernsting, *Appl. Phys. Lett*. **2001**, 79, 566.

[SM069] D. B. Siano, D. E. Metzler, *J. Chem. Phys*. **1969**, 51, 1856.

[SM096] R. M. Stratt, M. Maroncelli, *J. Phys. Chem.* **1996,** 100, 12981.

[SN006] A. Sen, P. E. Nielsen, *Biophys. J*. **2006**, 90, 1329.

[SOA99] J. O. Smith, D. A. Olson, B. A. Armitage, *J. Am. Chem. Soc*. **1999**, 121, 2686.

[SPE04] G. Saroja, Z. Pingzhu, N. P. Ernsting, J. Liebscher, *J. Org. Chem.* **2004**, 69, 987.

[SPK04] M. K. Singh, H. Pal, A. S. R. Koti, A. V. Sapre, *J. Phys. Chem. A* **2004**, 108, 1465.

[SR094] B. J. Schwartz, P. J. Rossky, *J. Chem. Phys.* **1994**, 101, 6917.

[SRB99] F. P. Schwarz, S. Robinson, J. M. Butler, *Nucleic Acids Res*. **1999**, 27, 4792.

[SS003] C. Schweitzer, J. C. Scaiano, *Phys. Chem. Chem. Phys*. **2003**, 5, 4911.

[SS092] H. M. Sevian, J. L. Skinner, *J. Chem. Phys.* **1992**, 97, 8.

[SSF85] R. K. Saiki, S. Scharf, F. Faloona, K. B. Mullis, G. T. Horn, H. A. Erlich, N. Arnheim, *Science* **1985**, 230, 1350.

[SSS00] N. Svanvik, A. Ståhlberg, U. Sehlstedt, R. Sjöback, M. Kubista, *Anal. Biochem.* **2000**, 287, 179.

[SW001] A. N. Shipway, I. Willner, *Chem. Commun.* **2001**, 2035.

[SWE02] D. N. Shin, J. W.Wijnen, J. B. F. N. Engberts, A. Wakisaka, *J. Phys. Chem. B* **2002**, 106, 6014.

[SWY98] C. Silva, P. K. Walhout, K. Yokoyama, P. Barbara, *Phys. Rev. Lett.* **1998**, 80, 1086.

[TDB94] T. Tassaing, Y. Danten, M. Besnard, E. Zoidis, J. Yarwood, *Chem. Phys*. **1994**, 184, 225.

[TRB05] A. Trifonov, M. Raytchev, I. Buchvarov, M. Rist, J. Barbaric, H. -A. Wagenknecht, T. Fiebig, *J. Phys. Chem. B.* **2005**, 109, 19490.

[VAW05] L. Valis, N. Amann, H.-A. Wagenknecht, *Org. Biomol. Chem*. **2005**, 3, 36.

[VR087] M. Vogel, W. Rettig, *Ber. Bunsen-Ges. Phys. Chem.* **1987**, 91, 1241.

[VS098] D. S. Venables, C. A. Schmuttenmaer, *J. Chem. Phys*. **1998**, 108, 4935

[VWF83] S. P. Velsko, D. H. Waldeck, G. R. Fleming, *J. Chem. Phys.* **1983**, 78, 249.

[W0056] C. H. G. Williams, *Trans. R. Soc. Edinburg,* **1856**, 21, 377.

[W0076] (a) A. Waggoner, *J. Membrane Biol*. **1976**, 27, 317. (b) A. Waggoner, A. Grinvald, *Ann .N. Y. Acad. Sci*. **1977**, 303, 217. (c) F. Grieser, M. Lay, P. J. Thistlethwaite, *J. Phys. Chem*. **1985**, 89, 2065.

[WJK90] G. C. Walker, W. Jarzeba, T. J. Kang, A. E. Johnson, P. F. Barbara, *J. Opt. Soc. Am. B.* **1990**, 7, 1521.

[WP065] W. West, S. Pearce, *J. Phys. Chem.* **1965**, 69, 1894.

[WRD03] W.Weigel, W. Rettig, M. Dekhtyar, C. Modrakowski, M. Beinhoff, A. D. Schlueter, *J. Phys .Chem. A* **2003**, 107, 5941.

[WXB05] C. Wan, T. Xia, H. -C. Becker, A. H. Zewail, *Chem. Phys. Lett.* **2005**, 412, 158.

[YAÅ95] A. Yartsev, J. -L Alvarez, U. Åberg, V. Sundström, *Chem. Phys. Lett.* **1995**, 243, 281.

[YDP98] A. Yoshimori, T. J. F. Day, G. N. Patey, *J. Chem. Phys*. **1998**, 109, 3222.

[YJB97] M. A. Young, B. Jayaram, D. L. Beveridge, *J. Am. Chem. Soc.* **1997**, 119, 59.

[YTN95] K. Yoshihara, K. Tominaga, Y. Nagasawa, *Bull. Chem. Soc. Jpn*. **1995**, 68, 696.

[ZB006] B. M. Zeglis, J. K. Barton, *J. Am. Chem. Soc.* **2006**, 128, 5654.

[ZCB94] H. Zhu, S. M. Clark, S. C. Benson, H. S. Rye, A. N. Glazer, R. A. Mathies, *Anal. Chem*. **1994**, 66, 1941.

[ZGF97] B. Zolotov, A. Gan, B. D. Fainberg, D. Huppert, *Chem. Phys. Lett.* **1997**, 265, 418.

[ZKL99] L. Zimanyi, A. Kulcsar, J. K. Lanyi, D. F. Sears, J. Saltiel, *Proc. Natl. Acad. Sci. U. S. A.* **1999**, 96, 4414.

[ZLF05] L. Zhao, J. L. P. Lustres, V. Farztdinov, N. P. Ernsting, *Phys. Chem. Chem. Phys.*, **2005**, 7, 1716.

10 Appendix

10.1 Crystal structure data for ANF

Empirical formula	$C_{13} H_{10} N_2 O_2$
Formula weight	226.23
Temperature	180(2) K
Wavelength	0.71073 Å
Crystal system, space group	Monoclinic, p 21/n
Unit cell dimensions	a = 10.7858 (19)Å alpha = 90 deg.
	b = 7.3930 (9) Å beta = 95.07(2) deg.
	c = 12.964 (3) Å gamma = 90 deg.
Volume	1029.7 (3) Å ^{3}
Z, Calculated density	4, 1.459 Mg/m^3
Absorption coefficient	0.101 mm^{-1}
F(000)	472
Crystal size	0.52 x 0.40 x 0.06 mm
Theta range for data collection	2.36 to 25.25 deg.
Limiting indices	$-12 \le h \le 12, -8 \le k \le 8, -15 \le l \le 15$
Reflections collected / unique	6463 / 1851 [R(int) = 0.0388]
Completeness to theta = 25.25	99.7 %
Max. and min. transmission	0.9940 and 0.9494
Refinement method	Full-matrix least-squares on F^2
Data / restraints / parameters	1851 / 0 / 195
Goodness-of-fit on F^2	1.009
Final R indices [I>2sigma(I)]	R1 = 0.0395, wR2 = 0.1035
R indices (all data)	R1 = 0.0504, wR2 = 0.1084
Extinction coefficient	0.014(9)
Largest diff. peak and hole	0.214 and -0.173 e. Å^{-3}

10.2 Stationary absorption and fluorescence spectra of Gl-ANF

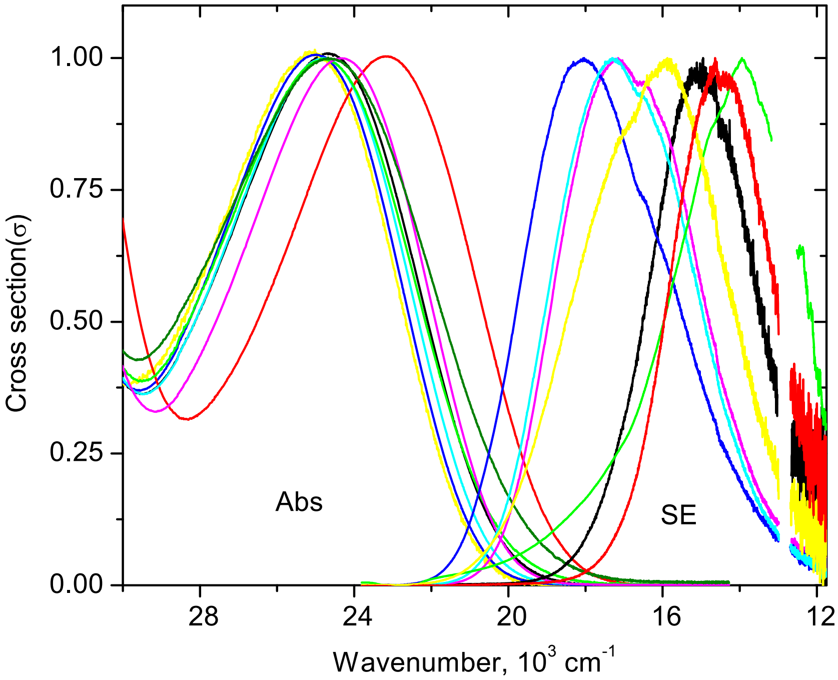

Figure 10.2 Absorption and emission spectra of Gl-ANF in varying solvents. Absorbance and fluorescence quantum distribution were converted into respective cross section and normalized.

Solvents	Abs peak maximum cm^{-1}	Band width cm^{-1}	Flurescence maximum cm^{-1}
Acetonitrile (black)	24550	1800	15149
Dimethyl sulphoxide (red)	23020	1770	14546
Methanol (green)	24660	1880	13943
Ethyl acetate (cyan)	24710	1700	17313
Diethyl ether (yellow)	25020	1670	16018
1,4-dioxane (blue)	24900	1650	18064
Tetrahydrofuran (magenta)	24230	1650	17195
Cyclohexane (orange)	20630	-	-
Water (olive)	24440	2230	-

10.3 Stationary absorption and fluorescence spectra of Ri-ANF

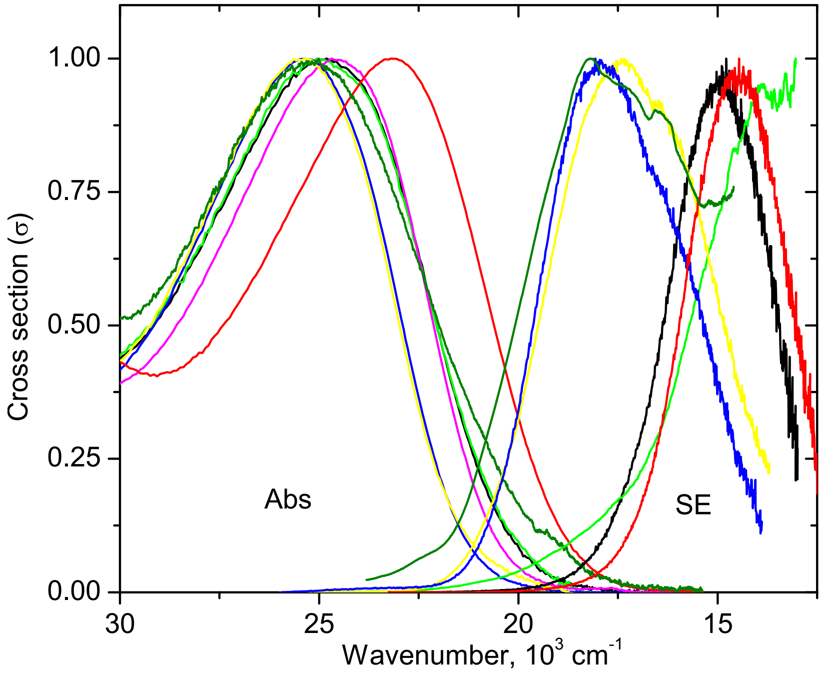

Figure 10.3 Absorption and emission spectra of Ri-ANF in varying solvents. Absorbance and fluorescence quantum distribution were converted into respective cross section and normalized.

Solvents	Abs peak maximum cm^{-1}	Band width cm^{-1}	Flurescence maximum cm^{-1}
Acetonitrile (black)	24740	2220	14897
Dimethyl sulphoxide (red)	23160	2060	14459
Methanol (green)	24760	2250	-
Diethyl ether (yellow)	25410	1890	17451
1,4-dioxane (blue)	25340	1860	17930
Tetrahydrofuran (magenta)	24590	1910	-
Water (olive)	23520	2170	17961

10.4 Lognormal description of ANF optical spectra (represented as oscillator distributions $M^2(\tilde{\nu})$) in various solvents

Solvent		**Absorption**	ν_p **/cm^{-1}, Δ/cm^{-1}, γ, h**	**Stat. fluorescence**
		$S_n \leftarrow S_0$	$S_1 \leftarrow S_0$	ν_p**/cm^{-1}, Δ/cm^{-1}, γ, h=1**
2-methyl-butane	mb	38115, 3080, 0.3674, 0.1237	25380, 854, 0.0048, 0.1225	
		41668, 6435, 0.1362, 0.4203	27309, 4072, 0.4053, 1.0000	*nm*
			34850, 4263, 0.2502, 0.0410	
n-pentane	Pen	38006, 3006, 0.3785, 0.1231	25351, 831, 0.0107, 0.1295	
		41196, 5463, 0.0688, 0.3334	27277, 4057, 0.4165, 1.0000	*nm*
			34817, 3560, 0.1300, 0.0349	
n-hexane	hex	38055, 3113, 0.3333, 0.1594	25245, 858, 0.0071, 0.1381	
		41213, 4967, 0.1350, 0.3179	27175, 4048, 0.4179, 1.0000	*nm*
			34715, 4200, 0.3227, 0.0354	
n-heptane	hep	37785, 2656, 0.3568, 0.0985	25156, 850, 0.0070, 0.1357	
		40881, 5694, 0.1268, 0.3405	27090, 4056, 0.4203 1.0000	*nm*
			34630, 3850, 0.2835, 0.0288	
n-octane	oct	37816, 2695, 0.3793, 0.0923	25094, 862, 0.0201, 0.1458	
		40820, 5603, 0.0587, 0.3427	27027, 4030, 0.4229, 1.0000	*nm*
			34568, 4020, 0.2895, 0.0272	
cyclohexane	ch	37668, 2444, 0.4009, 0.0722	24908, 773, 0.0260, 0.1564	
		40628, 6009, 0.0831, 0.3511	26858, 4019, 0.4331, 1.0000	*nm*
			34399, 3529, 02285, 0.0216	
carbon-tetrachloride [a]	ctc	38842, 6485, 0.3570, 0.3062	26299, 4455, 0.3654, 1.0035	20200, 4496, -0.3615
			33840, 4080, 0.2795, 0.0526	
chloroform	chl	38698, 7284, 0.545, 0.4033	25416, 5068, 0.2184, 0.9930	16013, 3749, -0.1016
			32976, 6191, 0.1101, 0.0650	
1,1,1 trichloro-trifluoro-ethane	tctf	40148, 8641, 0.6782, 0.3713	26885, 4571, 0.3326, 0.9962	*nm*
			34425 , 4200, 0.1859, 0.0527	
diethyl ether	dee	38541, 6760, 0.4811, 0.3633	25217, 4757, 0.3000, 0.9982	17191, 4169, -0.0921
			32757, 7144, 0.6462, 0.0329	
dipropyl ether	dpe	38520, 7036, 0.4892, 0.3769	25237, 4746, 0.2726, 0.9984	16856, 4478, -0.0319
			32777, 7198, 0.1107, 0.0494	
dibutyl ether	dbe	38702, 6820, 0.4629, 0.3880	25603, 4845, 0.3451, 1.0029	18835, 3939, -0.1810

			33143, 3710, 0.0581, 0.0358	
tetrahydrofuran	thf	37763, 6180, 0.4159, 0.3880	24414, 4802, 0.2719, 1.0014 31954, 5928, 0.2018, 0.0570	16908, 3582, -0.1537
tetrahydropyran	thp	37876, 6306, 0.4157, 0.3918	24484, 4795, 0.2774, 0.9999 32024, 5744, 0.2222, 0.0540	16406, 4077, -0.0722
1,4-dioxane	dio	38384, 6582, 0.5137, 0.4057	25169, 4745, 0.2954, 0.9976 32710, 5394, 0.1580, 0.0531	17864, 3690, -0.1769
methyl acetate	mac	38166, 6160, 0.4207, 0.3942	24932, 4906, 0.2512, 0.9997 32472, 6080, 0.0293, 0.0615	16532, 3606, -0.1281
ethyl acetate	eac	38140, 6125, 0.4288, 0.3784	24898, 4800, 0.2597, 0.9942 32430, 7885, 0.0021, 0.0600	16900, 3658, -0.1457
dimethylformamide	dmf	36716, 5058, 0.1887, 0.4132	23395, 5120, 0.2195, 0.9985 30935, 5540, 0.4666, 0.0678	14466, 3357, -0.1496
hexamethylphosphoramide	hmpa	*nm*	*nm*	15206, 3612, -0.1818
dimethylsulfoxide	dmso	36520, 5660, 0.2450, 0.4411	22916, 5165, 0.2237, 0.9999 30456, 4620, 0.3101, 0.0788	13997, 3203, -0.0898
acetonitrile	acn	38027, 6148, 0.4240, 0.3894	24813, 5134, 0.1878, 0.9957 32353, 6919, 0.1805, 0.0755	14475, 3717, -0.1977
propionitrile	prn	38100, 6612, 0.4980, 0.3897	24680, 4989, 0.2027, 0.9911 32220, 8708, 0.0120, 0.0713	14225, 3017, -0.1159
methanol	meoh	38491, 7107, 0.3951, 0.4234	24962, 5584, 0.1224, 0.9637 30597, 9090, 0.0451, 0.1069	13055, 3339, 0.4083
ethanol	etoh	38261, 7072, 0.3875, 0.4218	24670, 5420, 0.1176, 0.9511 29845, 9415, 0.0531, 0.1107	13755, 3938, 0.2979
propanol	proh	38301, 7096, 0.3766, 0.4233	24783, 5578, 0.1050, 0.9983 30943, 7332, 0.4132, 0.1004	14145, 3871, 0.3328
butanol	buoh	38272, 6963, 0.3765, 0.4076	24793, 5541, 0.0936, 0.9990 30774, 7584, 0.5131, 0.0951	14360, 4205, 0.2582
benzene [a]	bz	38356, 6550, 0.5130, 0.2935	25520, 4616, 0.3288, 0.9981 33060, 4853, 0.2602, 0.0494	18992, 3712,-0.1795
toluene [a]	tol	36793, 3332 , 0.0011, 0.121	25554, 4575, 0.3403, 1.0013 33094, 4936, 0.2968, 0.0431	19167, 3780, -0.1792

nm- not measured, [a] absorption analysis beyond S_0-S_1 limited by solvent.

10.5 Lognormal description of dM-ANF optical spectra (represented as oscillator distributions $M^2(\tilde{\nu})$) in various solvents

Solvent		Absorption $S_n \leftarrow S_0$	ν_p/cm^{-1}, Δ/cm^{-1}, γ, h $S_1 \leftarrow S_0$	Stat. fluorescence ν_p/cm^{-1}, Δ/cm^{-1}, γ, h=1
2-methyl butane	mb	36999, 3275, 0.0978, 0.2803	23910, 1016, 0.0024, 0.5906	*nm*
		40035, 4694, 0.4557, 0.2762	24902, 1174, 0.0047, 0.3560	
			25986, 3252, 0.6165, 0.8322	
			26491, 2199, 0.0117, 0.0583	
n-pentane	pen	36925, 3164, 0.0921, 0.2780	23866, 996, 0.0024, 0.5901	*nm*
		39899, 4630, 0.4830, 0.2811	24865, 1199, 0.0047, 0.3708	
			25968, 3312, 0.6154, 0.8066	
			26925, 2169, 0.0120, 0.0761	
n-hexane	hex	36818, 3135, 0.0968, 0.2800	23776, 1019, 0.0024, 0.6376	*nm*
		39771, 4593, 0.4803, 0.2788	24808, 1107, 0.0047, 0.3007	
			25707, 3223, 0.6583, 0.8026	
			26374, 2319, 0.0150, 0.0861	
n-heptane	hep	36814, 3121, 0.0735, 0.2855	23706, 1039, 0.0038, 0.6102	*nm*
		39777, 4612, 0.4802, 0.2936	24727, 1092, 0.0052, 0.2887	
			25706, 3356, 0.6635, 0.8464	
			26227, 2275, 0.0150, 0.0570	
n-octane	oct	36675, 2991, 0.0581, 0.2798	23636, 1026, 0.0040, 0.6447	*nm*
		39554, 4486, 0.5067, 0.2893	24710, 1040, 0.0053, 0.2539	
			25469, 3205, 0.6867, 0.8043	
			26291, 2271, 0.0240, 0.0966	
cyclohexane	ch	36564, 2959, 0.0597, 0.2854	23493, 1002, 0.0046, 0.6516	*nm*
		39408, 4472, 0.5067, 0.2933	24551, 1044, 0.0048, 0.2709	
			25361, 3193, 0.6724, 0.7978	
			26157, 2559, 0.0273, 0.0978	
carbon-tetrachloride [a]	ctc	36156, 4535, 0.1880, 0.2730	22617, 1571, 0.0000, 0.2315	18995, 3630, -0.1817
			24798, 4461, 0.5853, 0.9954	
			32210, 3336, 0.0000, 0.0261	
chloroform	chl	36116, 6441, 0.5042, 0.4256	23157, 4878, 0.2286, 0.9962	14714, 3371, -0.1749
			30387, 3970, 0.1210, 0.0552	

1,1,1-trichloro-trifluoro-ethane	tctf	37931, 7242, 0.5261, 0.3787	24999, 4449, 0.3614, 0.9957 31932, 4357, 0.2109, 0.0278	18816, 3683, -0.1623
diethyl ether	dee	37353, 6644, 0.5552, 0.3910	24303, 4423, 0.3126, 1.0034 31060, 3852, 0.1832, 0.0252	16284, 4192, -0.0607
dipropyl ether	dpe	37194, 6298, 0.5363, 0.3983	24306, 4356, 0.3237, 1.0023 31678, 4470, 0.1521, 0.0323	16034, 4649, -0.0230
dibutyl ether	dbe	37439, 6498, 0.5516, 0.3902	24457, 4266, 0.3706, 0.9990 32181, 4579, 0.1234, 0.0363	18369, 4031, -0.1565
tetrahydrofurane	thf	36436, 5927, 0.5463, 0.4383	23507, 4595, 0.2792, 1.0017 30909, 5121, 0.4168, 0.0514	16050, 3513, -0.1491
tetrahydropyrane	thp	36665, 6063, 0.4639, 0.4190	23661, 4535, 0.2964, 1.0022 30979, 3752, 0.1529, 0.0378	15480, 4152, -0.0955
1,4-dioxane	dio	36896, 6357, 0.5432, 0.4304	23942, 4559, 0.2954, 1.0031 31369, 4229, 0.1867, 0.0436	16986, 3603, -0.1454
methyl acetate	mac	36692, 5843, 0.4059, 0.4155	23765, 4733, 0.2593, 1.0011 30880, 4088, 0.1805, 0.0424	15511, 3572, -0.1484
ethyl acetate	eac	36757, 5883, 0.4367, 0.4183	23831, 4670, 0.2650, 1.0010 31168, 4893, 0.1366, 0.0473	15970, 3577, -0.1526
dimethylformamide	dmf	35763, 5029, 0.2301, 0.4500	22755, 4990, 0.2175, 0.9991 30255, 3706, 0.1196, 0.0572	13557, 3369, -0.1308
hexamethyl-[a] phosphoramide	hmpa	36849, 7357, 0.1329, 0.6747	22629, 4842, 0.2522, 0.9977 30013, 3474, 0.1184, 0.0759	14308, 3496, -0.0944
dimethylsulfoxide	dmso	35580, 5404, 0.3531, 0.4593	22375, 5057, 0.2153, 0.9981 30492, 4599, 0.3294, 0.0718	13033, 3171, -0.0612
acetonitrile	acn	36377, 6010, 0.4785, 0.4241	23328, 5019, 0.1801, 0.9980 31111, 6611, 0.0833, 0.619	13285, 3440, -0.1460
propionitrilea	prn	36477, 5585, 0.2752, 0.5306	23335, 4961, 0.1984, 0.9994 30968, 5648, 0.1249, 0.0821	13866, 3416, -0.1462
methanol	meoh	36756, 6507, 0.5072, 0.4432	23597, 5051, 0.1634, 0.9776 30050, 8584, 0.0000, 0.0928	*nm*
ethanol	etoh	36719, 6247, 0.4909, 0.4245	23635, 4803, 0.1478, 0.9660 28895, 9070, 0.0000, 0.0834	12890, 3394,-0.4824
propanol	proh	36719, 6264, 0.4829, 0.4362	23659, 4797, 0.1363, 0.9727 29110, 8426, 0.0000, 0.0832	13258, 3906, -0.4032

butanol	buoh	36732, 6291, 0.4800, 0.4315	23674, 4706, 0.1157, 0.9461	13439, 4312, -0.3256
			28170, 8927, 0.0000, 0.1032	
benzene [a]	bz	36078,4551, 0.2717, 0.4059	23680, 4353, 0.3359, 0.0439	17660, 3618, -0.1776
			30973, 3976, 0.1818, 0.0439	
toluene[a]	tol	36312, 4102, 0.0544, 0.4339	23768, 4292, 0.3479, 1.0042	18016, 3616, -0.1872
			30566, 3118, 0.2976, 0.0372	

nm- not measured, [a] absorption analysis beyond S_0-S_1 limited by solvent.

10.6 Lognormal description of dBdP-ANF optical spectra (represented as oscillator distributions $M^2(\tilde{\nu})$) in various solvents

Solvent		Absorption	ν_p /cm^{-1}, Δ/cm^{-1}, γ, h	Stat. fluorescence
		$S_n \leftarrow S_0$	$S_1 \leftarrow S_0$	ν_p/cm^{-1}, Δ/cm^{-1}, γ h (=1)
perfluoro-n-hexane	pfh	35758, 2464, 0.0034, 0.0905	23729, 832, 0.1110, 0.6219	23287, 945, -0.0024, 0.1081
		38638, 5757, 0.4981, 0.2560	25018, 1212, -0.2440, 0.7410	21759, 1317, -0.0123, 0.5472
			26114, 1287, 0.3676, 0.3221	20545, 1197, -0.1048, 0.7598
			26519, 3032, -0.1814, 0.4351	19200, 1599, 0.0000, 0.9373
			28744, 3172, 0.7791, 0.1396	18043, 1041, 0.0000, 0.4148
				17113, 1746, -0.6582, 0.3322
2-methyl-butane	mb	35969, 3271, 0.1124, 0.2347	23021, 996, 0.0024, 0.7066	22212, 1001, -0.0024, 0.6355
		39007, 4579, 0.4709, 0.2165	24292, 1416, 0.0084, 0.8190	20965, 1225, -0.1020, 0.9629
			25611, 1095, 0.0000, 0.2149	19621, 1235, 0.0000, 0.7261
			25996, 2759, 0.0023, 0.3668	18513, 969, -0.0000, 0.3412
			28050, 5745, 0.0159, 0.0934	17663, 1473, -0.6582, 0.1847
n-pentane	pen	35994, 3285, 0.0673, 0.2431	22999, 977, 0.0052, 0.7123	22205, 993, -0.0019, 0.6534
		39035, 4620, 0.5123, 0.2203	24270, 1410, 0.0127,0.8136	20960, 1185, -0.1137, 0.9764
			25594, 1087, 0.0000, 0.2097	19661, 1111, 0.0000, 0.6684
			25971, 2811, 0.0028, 0.3705	18584, 1106, -0.0001, 0.3286
			28289, 5981, 0.0116, 0.0994	17606, 1603, -0.5148, 0.1421
n-hexane	hex	35907, 3248, 0.0654, 0.2482	22896, 982, 0.0068, 0.7119	22130, 981, -0.0164, 0.6206
		38950, 4643, 0.5129, 0.2247	24175, 1436, 0.0126, 0.8343	20878, 1138, -0.0135, 0.9555
			25505, 1100, 0.0000, 0.2187	19566, 1247, -0.0000, 0.7479
			25939, 2758, 0.0028, 0.3660	18452, 924, -0.0002, 0.3023
			28389, 5957, 0.0105, 0.1011	17688, 1462, -0.7215, 0.1803
n-heptane	hep	35828, 3177, 0.0650, 0.2448	22824, 988, 0.0083, 0.7138	22045, 987, -0.0031, 0.6369
		38807, 4508, 0.4894, 0.2206	24105, 1445, 0.0114, 0.8430	20817, 1096, -0.0019, 0.9428
			25437, 1115, 0.0000, 0.2272	19527, 1287, 0.0000, 0.7390
			25894, 2769, 0.0030, 0.3613	18403, 1003, -0.0000, 0.2662
			28348, 5756, 0.0096, 0.0860	17632, 1619, -0.6210, 0.1731
n-octane	oct	35886, 3367, 0.0545, 0.2535	22769, 992, 0.0150, 0.7108	21957, 1016, -0.0024, 0.6367
		38950, 4610, 0.4914, 0.2113	24055, 1454, 0.0127, 0.8462	20738, 1112, -0.1020, 0.9415
			25388, 1130, 0.0000, 0.2317	19416, 1241, 0.0000, 0.7031

			25875, 2777, 0.0027, 0.3588	18263, 969, -0.0000, 0.3041
			28468, 5837, 0.0087, 0.0884	17413, 1473, -0.6582, 0.1529
cyclohexane	ch	35539, 2923, 0.0462, 0.2445	22621, 972, 0.0341, 0.7257	21892, 947, -0.0035, 0.6343
		38425, 4525, 0.5134, 0.2448	23912, 1425, 0.0084, 0.8512	20631, 1152, -0.0027, 0.9698
			25229, 1115, 0.0000, 0.2434	19343, 1161, 0.0000, 0.7322
			25758, 2700, 0.0016, 0.3436	18243, 999, -0.0000, 0.3129
			28188, 6351, 0.0004, 0.0943	17398, 1545, -0.5994, 0.1581
carbon-tetrachloride[a]	ctc	36384, 6972, 0.1746, 0.3512	22091, 959, 0.0030, 0.0831	19825, 1749, -0.0035, 0.4410
			23415, 3992, 0.3935, 0.9944	18594, 1793, -0.0027, 0.7293
			30046, 3691, 0.0665, 0.1298	17233, 1973, 0, 0.5677
				16223, 901, 0, 0.1237
				15378, 1360, -0.5994, 0.1381
chloroform	chl	34921, 6163, 0.5834, 0.3696	21826, 4487, 0.2482, 1.0009	14379, 3201, -0.1662
			29793, 3584, 0.1166, 0.0761	
1,1,1-trichlorotrifluoroethane	tct	36062, 4932, 0.3246, 0.3056	22549, 1150, 0.0079, 0.0802	19640, 1927, -0.0035, 0.4442
			23818, 3917, 0.2892, 0.9933	18409, 1887, -0.0027, 0.6981
			30372, 4399, 0.0293, 0.0554	17048, 1979, 0. 0.5761
				16038, 903, 0, 0.1279
				15193,1360, -0.5994, 0.1426
diethyl ether	dee	36252, 6297, 0.5004, 0.3382	23268, 4082, 0.3357, 1.0065	17890, 2439, 0.0931, 0.2633
			30490, 3488, 0.1194, 0.0531	16618, 2387, 0.2357, 0.6406
				15098, 2350, -0.0667, 0.5414
				13243, 6581, -0.2, 0.1260
dipropyl ether	dpe	36228, 6117, 0.5498, 0.3583	22130, 1187, 0.0023, 0.0717	17440, 3286, 0.0599, 0.3898
			23380, 3993, 0.2869, 0.9918	16168, 2453, 0.2534, 0.5091
			30487, 4799, 0.1156, 0.0572	14648, 2350, -0.0667, 0.4873
				12793, 6581, -0.2, 0.1567
dibutyl ether	dbe	36416, 6361, 0.5475, 0.3325	22125, 1080, 0.0024, 0.1043	19701, 2467, -0.2547, 0.4499
			23494, 3806, 0.3464, 0.9971	18588, 1971, -0.0255, 0.4788
			30539, 3861, 0.0891, 0.0488	17098, 2432, 0, 0.6112
				15243, 2270, -0.3075, 0.1308
tetrahydrofuran	thf	35710, 6634, 0.6128, 0.3635	22497, 4255, 0.3130, 1.0015	17530, 1911, -0.0035, 0.3583
			30063, 3802, 0.2720, 0.0618	16299, 2065, -0.0027, 0.6593
				14938, 2410, 0, 0.5029

				13083, 2254, -0.5994, 0.0755
tetrahydropyran	thp	35762, 6047, 0.4752, 0.4417	22634, 4213, 0.3152, 1.0034	16910, 2795, -0.0035, 0.4245
			30194, 4029, 0.3042, 0.0628	15679, 2411, -0.0027, 0.5363
				14318, 2360, 0, 0.5097
				12463, 3144, -0.5994, 0.1367
1,4-dioxane	dio	35888, 6181, 0.5618, 0.3637	22889, 4223, 0.3152, 1.0030	18290, 1889, -0.0035, 0.4014
			30344, 3980, 0.2585, 0.0615	17059, 2078, -0.0027, 0.6451
				15698, 2410, 0. 0.5445
				13843, 2254, -0.5994, 0.0758
methyl acetate	mac	35637, 6089, 0.5150, 0.3660	22727, 4381, 0.2771, 1.0012	16053, 3511, -0.1535
			30217, 3942, 0.1279, 0.0695	
ethyl acetate	eac	35795, 6075, 0.5031, 0.3557	22766, 4291, 0.3041, 1.0022	15648, 3456, -0.1576
			30191, 3650, 0.1767, 0.0604	
dimethylformamide	dmf	34881, 5471, 0.3744, 0.3989	21667, 4646, 0.2423, 0.9981	13634, 3162, -0.07
			29666, 3432, 0.1117, 0.0740	
hexamethylphosphoramide[a]	hmpa	34503, 5895, 0.4545, 0.3362	21613, 4558, 0.2695, 0.9994	14501, 3299, -0.1659
			29858, 3810, 0.0764, 0.0966	
dimethylsulfoxide	dmso	34880, 5892, 0.4439, 0.5030	21333, 4686, 0.2410, 0.9994	13140, 3053, -0.07
			29720, 3757, 0.0904, 0.0852	
acetonitrile	acn	35191,6085, 0.4764, 0.3731	22160, 4673, 0.2197, 0.9986	13339, 3105, -0.07
			29585, 3427, 0.1602, 0.0743	
propionitrile	prn	35246, 5927, 0.5140, 0.3651	22142, 4590, 0.2310, 09987	13812, 3226, -0.07
			29987, 4114, 0.1840,0.0697	
methanol	meoh	35734, 6480, 0.4710, 0.4957	22461, 4878, 0.1760, 0.9909	12290, 3061, 0.3840
			29890, 3898, 0.0001, 0.0836	
ethanol	etoh	35689, 6399, 0.5250, 0.4157	22558, 4699, 0.1869, 0.9887	12884, 3640, 0.3843
			29958, 4711, 0.0000, 0.0833	
propanol	proh	35741, 6423, 0.5121, 0.4629	22580, 4735, 0.1839, 0.9855	13317, 3999, 0.3093
			30005, 4309, 0.0000, 0.0858	
butanol	buoh	35710, 6245 0.4911, 0.3823	22665, 4748, 0.1553, 0.9829	13618, 4193, 0.2631
			30090, 4374, 0.0000, 0.0835	
benzene[a]	bz	35346, 4601, 0.2902, 0.3541	22684, 3994, 0.3566, 1.0081	19015, 1618, -0.0035, 0.4684
			30059, 3190, 0.2362, 0.0538	17775, 1692, -0.0027, 0.7871
				16455, 1713, 0, 0.5977

				15393, 1073 ,0, 0.1807
				14548, 1360, -0.5994, 0.1397
toluene[a]	tol	35032, 3545, 0.1529, 0.3116	22785, 3916, 0.3805, 1.0118	19292, 1615, -0.0035, 0.5170
			30202, 3103, 0.2483, 0.0430	18031, 1575, -0.0027, 0.7842
				16743, 1650, 0, 0.6334
				15643, 1039, 0, 0.2219
				14798, 1360,-0.5994, 0.1474

nm- not measured, [a] absorption analysis beyond S_0-S_1 limited by solvent. Underlined: parameter was fixed during fitting.

10.7 Chemical shift of different protons of ANF in CD_3CN / H_2O mixtures - calibrated by 0.5% of Hexamethyldisiloxane in CCl_4. The numbering of the proton is given as in the figure

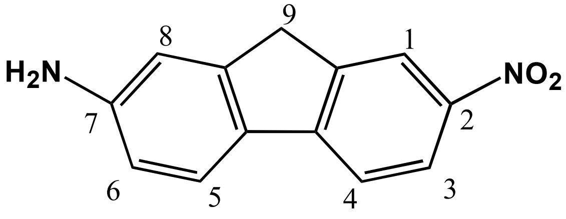

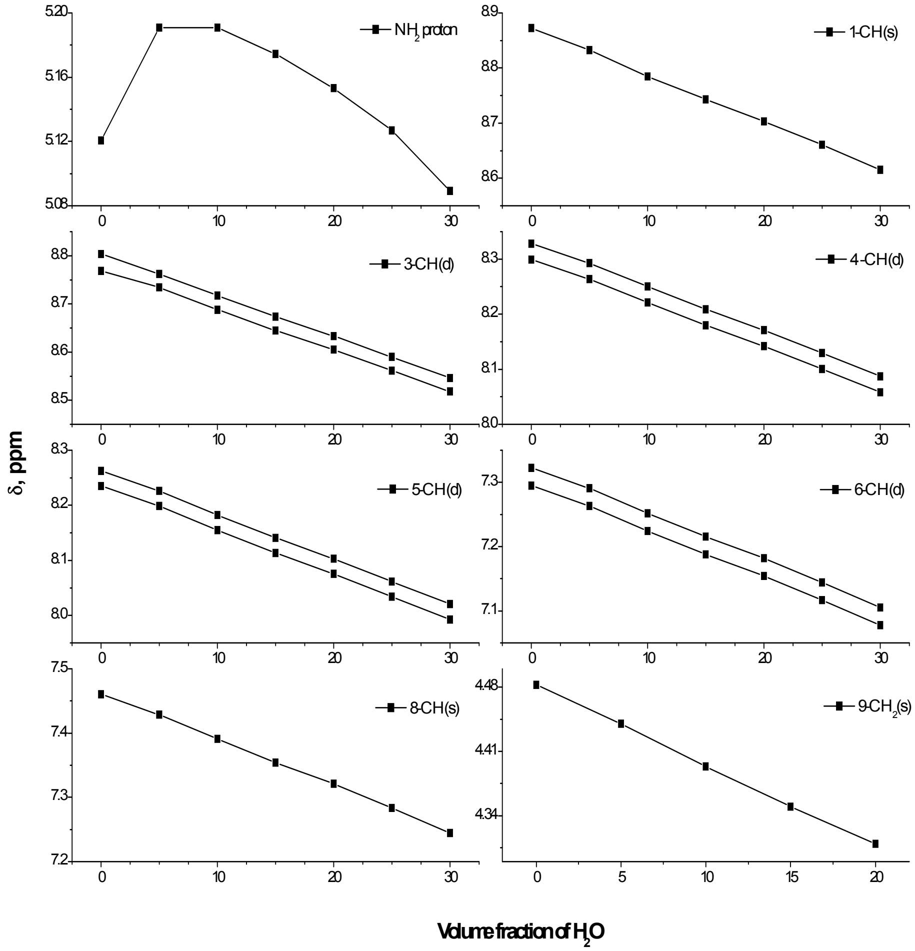

Except amino proton, all other protons are moving regularly towards lower chemical shift with increase of the volume fraction of water. (s – singlet, d – doublet).

10.8 Chemical shift of different protons of ANF in $(CD_3)_2SO$ / H_2O mixtures

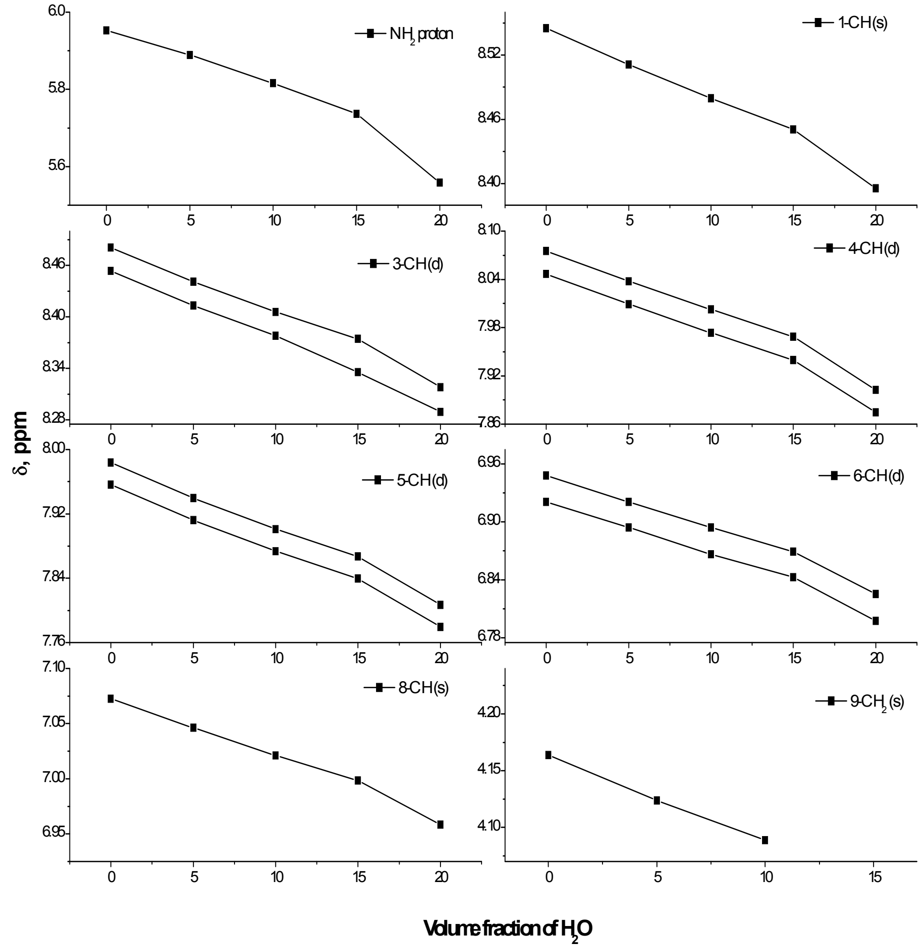

All protons are moving regularly towards lower chemical shift with increase of the volume fraction of water.

10.9 Fluorescence lifetimes of ANF, dM-ANF and Ri-ANF in different solvents

Solvents	ANF, ns	dM-ANF, ns	Ri-ANF, ns
Monoexponential			
Acetonitrile	< 0.050	< 0.050	0.104
Methanol	< 0.050	< 0.050	< 0.050
Dimethyl sulphoxide	0.119	0.309	0.113
Ethyl Acetate	1.717	3.022	2.399
1,4-Dioxane	2.158	3.090	2.564
Diethyl ether	0.738	1.151	0.983
Biexponential			
Carbon tetrachloride	1.523 (τ_1), 0.075 (τ_2)	2.152 (τ_1), 0.338 (τ_2)	1.453 (τ_1), 0.213 (τ_2)
Cyclohexane	2.121 (τ_1), 0.195 (τ_2)	1.375 (τ_1), 0.026 (τ_2)	1.989 (τ_1), 0.140 (τ_2)
2-methyl butane	2.112 (τ_1), 0.084 (τ_2)	3.592 (τ_1), 0.081 (τ_2)	1.636 (τ_1), 0.100 (τ_2)

The value of χ^2 was ≤ 1.2 for fitting of all fluorescence decays.

10.10 **Transient absorption spectra of dM-ANF in acetonitrile** - spectral range from 360 nm to 775 nm

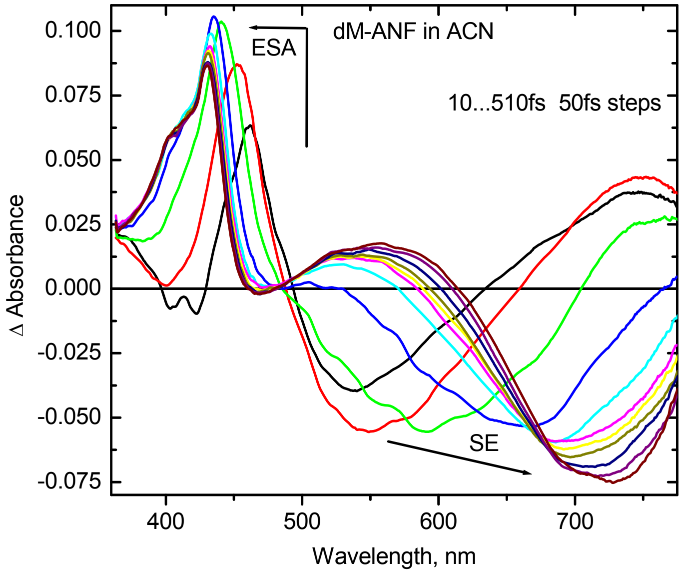

Figure 10.10.1 Transient absorption spectra of dM-ANF in acetonitrile from 10 fs to 510 fs in time steps of 50 fs after excitation at 400 nm. Negative ΔOD corresponds to Stimulated Emission (SE), and positive ΔOD corresponds to Excited State Absorption(ESA). Arrows indicate the direction of the spectral evolution.

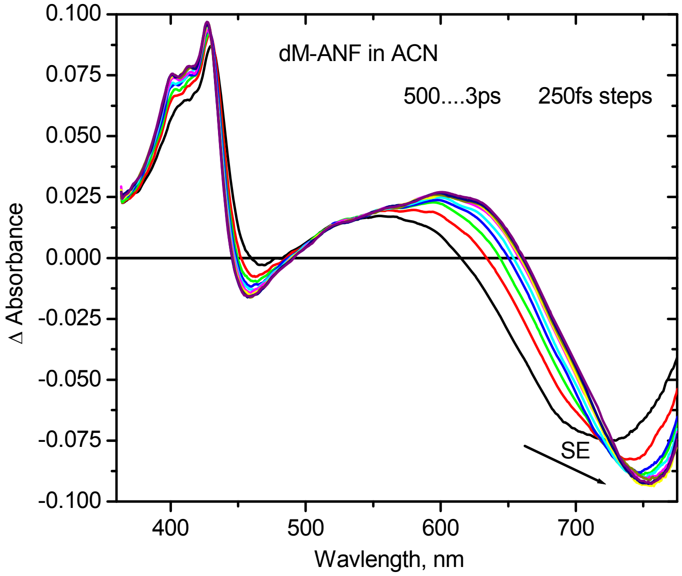

Figure 10.10.2 Transient absorption spectra of dM-ANF in acetonitrile from 500 fs to 3 ps, in time steps of 250 fs. Thus SE maximum is covered and it attains stationary emission spectrum at 2 ps.

10.11 Melting studies

Knowledge of the thermodynamics of polynucleic acids is always useful when designing a base sequences. This is particularly true when a solvatochromic probe is linked into the sequence. The following are our target strands with ANF (the fluorophore F) in the middle position. Note that the complementary strand must have an abasic site opposite at the 7th position.

1 **5’-G C G C A A F T T C G C G-3’** TS1
3’-C G C G T T _ A A G C G C-5’ TS1-a

2 **5’-G C T G C A F A C G T C G-3’** TS2
3’-C G A C G T _ T G C A G C-5’ TS2-a

Spectroscopic and calorimetric measurements are widely used to determine the thermodynamic parameter of polynucleic acids. The stability of a DNA duplex is reflected by its melting temperature. The procedure for measuring the melting temperature (T_m) were explained in the experimental section 3.3. The following DNA-duplex were studied as a background for our required modified base sequences. The melting temperature is also included. The examined solution contains individual strands of 1:1 ratio of 1µmoles/lit concentration.

	Base Sequences		T_m, °C
a.	**5’-G C G C A A G T T C G C G-3’**	TS1-S13	60.4
	3’-C G C G T T C A A G C G C-5’	TS1-SC13	
b.	**5’-G C G C A A T T C G C G-3’**	TS1-S12	53.0
	3’-C G C G T T A A G C G C-5’	TS1-SC12	
b.	**5’-G C T G C A A C G T C G-3’**	TS2-S12	57.0
	3’-C G A C G T T G C A G C-5’	TS2-SC12	

The relative stability of a DNA duplex structure depends on its base sequence. The 6th and 8th base position seems to be more important for stability than the positions nearer the end of a strand.

11 Acknowledgement

I would like to thank in the first place Prof. Dr. Nikolaus P. Ernsting for given me this great opportunity to enter the femtosecond world by calling from India. He continued his support, careful supervision, scientific inspiration, and many decisive scientific contributions from the beginning. With out his help, this thesis could not be made.

Dr. S. Kovelenko with his tremendous experience on using femtosecond laser system and its technique, taught and helped with all of my measurements. Dr. Tamara Senyushkina helped me to get solvation curves which she can do by looking of data at a glance of her eyes. Dr. Vadim Farztdinov simulated the solvation curve of DNA duplex which was used as a starting point for my work. I would also like to thank Dr. Luis Pérez Lustres for his constant support and providing S(t) curves for comparison. I would like to thank specially to Dr. Alexander Dobryakov for always discussing the mathematical aspect of scientific problems, for example the Genetic Algorithm. About the synthetic side, I thank to Dr. Rainer Mahrwald for teaching me from the beginning to the complicated level of nucleoside synthesis. I would also sincerely thank Prof. Oliver Seitz for my exposure of PNA's, and to his student D. V. Jarikote for providing Thiazole Orange PNA and for teaching me DNA hybridization. I am also thankful to Dr. Wilfried Weigel (Prof. W. Rettig lab) for helping me to measure fluorescence lifetimes. I thank heartily Mrs. Heiderose Steingräber for her kind, timely and constant help for tackling my problems with the German language *viz.*, accommodation, hospital and so many. I would like to thank my colleagues Dr. Horst Hennig, Dr. Lijuan Zhao, Dr. Saroja Ginagunta (for preparatory work for my study), Mr. Alexander Weigel, Mr. André Dallmann, Mrs. Iris Suter, Mr. Jens Breffke and Mr. Manoel Veiga. I am very thankful to Prof. P. Natarajan, Prof. P. Ramamurthy and to all of my colleagues in the National Centre for Ultrafast Processes, University of Madras. I consider this a great opportunity strictly to thank all of my teachers, starting from my village school to my college. I would like to thank all of my friends who are in India and Berlin.

At this point, I have to be not only thankful, but greatful in my whole soul to my Amma (although she is uneducated, she made me to this level), Appa, Annan, Anni, Thambi, Jr. Jai Krishnan, and Miss. Bhuvaneswari for allowing me to stay in Germany to do my PhD, and for their encouragement, support, blessing and with love greater than the amount of the sea.

List of Publications

1. **V. Karunakaran,** P. Ramamurthy, T. Josephrajan, V. T. Ramamkrishnan, “Solvent effects and photophysical studies of a new class of Acridine(1,8)dione dyes”, *Spectrochimica Acta Part A: Chemistry* **2002**, 58, 1443–1451.

2. V. Raghukumar, D. Thirumalai, V. T. Ramakrishnan, **V. Karunakaran**, P. Ramamurthy, “Synthesis of nicotinonitrile derivatives as a new class of NLO materials”, *Tetrahedron* **2003**, 59, 3761–3768.

3. V. A. Galievsky, S. I. Druzhinin, A. Demeter, Y.-B. Jiang, S. A. Kovalenko, L. P. Lustres, **K. Venugopal**, N. P. Ernsting, X. Allonas, M. Noltemeyer, R. Machinek, K. A. Zachariasse, “Ultrafast intramolecular charge transfer and internal conversion with tetrafluoroaminobenzonitriles”, *Chem. Phys. Chem* **2005**, 6, 2307-2323.

4. **K. Venugopal**, J. L. P. Lustres, L. Zhao, N. P. Ernsting, O. Seitz, “Large dynamic Stokes shift of DNA intercalation dye Thiazole Orange has contribution from a high-frequency mode” *J. Am. Chem. Soc.* **2006**, 128, 2954-2962.

5. D. Löwenich, K. Kleinermanns, S. Kovalenko, **K. Venugopal**, “Photoreduction of Cytochrome C Revisited: Wavelength and time dependence of the quantum yields”, *Photochem. Photobio.* (submitted on December **2006**).

6. **K. Venugopal**, T. Senyushkina, G. Saroja, J. Liebscher, N. P. Ernsting. “Solvatochromism and specific solvation of substituted 2-amino-7-nitro-fluorenes”, *J. Phys. Chem. A* (submitted on January **2007**).

7. M. Ostermeier, C. Limberg, B. Ziemer, **K. Venugopal** “Solvent dependent, exhaustive oxidation of an amino(methylpyridyl) ligand by $FeCl_3$ to give a water-soluble blue fluorophore”, *Angew. Chem. Int. Ed.* (submitted on January **2007**).

8. **K. Venugopal**, S. A. Kovalenko, T. Senyushkina, G. Saroja, N. P. Ernsting, “Femtosecond solvation dynamics of ANF derivatives and its nucleosides” (to be submitted).

9. **K. Venugopal,** N. P. Ernsting, “Inclusion studies of ANF nucleoside in different cyclodextrins” (to be submitted).

10. **K. Venugopal**, S. A. Kovelenko, N. P. Ernsitng, K. Kleinermanns, “Charge transfer in DNA bases – a study of Guanosine mono phosphate with various pH” (to be submitted).

Oral presentations

1. **K. Venugopal, "**Large dynamic Stokes shift of DNA intercalation dye Thiazole Orange has contribution from a high-frequency mode", XXIst IUPAC Symposium on photochemistry, Kyoto, *Japan,* 2-7 April **2006**.

2 **K. Venugopal,** "Large dynamic Stokes shift of DNA intercalation dye Thiazole Orange has contribution from a high-frequency mode", Sfb 450 Analyse und Steuerung ultraschneller photoinduzierter Reaktionen, Berlin*, Germany,*1 October **2005.**

Poster presented in conference

1. **K. Venugopal**, V. M. Farztdinov, N. P. Ernsting, R Mahrwald, H. Sklenar "A fluorescent probe of DNA dynamics: from ultrafast polar solvation to the local IR spectrum", XXIst IUPAC Symposium on photochemistry, Kyoto, *Japan*, 2-7 April **2006**.

Lebenslauf

Name	Karunakaran VENUGOPAL
Geburtsdatum:	15. April 1974
Geburtsort:	Chennai, Tamil Nadu (Indien)
Familienstand:	Ledig
1991:	Abschluss: Allgemeine Hochschulreife an der Singaram pillai higher secondary school, Chennai, Indien
Juni 1991 - März1994:	Grundstudium der Chemie [B.Sc. (Chemistry)] am D.G.Vaishnav College, University of Madras, Indien
August 1994 - Juni 1996	Hauptstudium Chemie [M.Sc.(General Chemistry)] am D.G.Vaishnav College, University of Madras, Indien.
Sept.1996 - März1997	Angestellt als Chemiker bei Akshaya Chemicals, Ayyapakkam, Ambattur Industrial Estate, Chennai, Indien
April 1997 - Mai 1998	Angestellt als “Quality Control Chemist” bei Tetrahedron Public Limited, Ambattur Industrial Estate, Chennai, Indien
Mai1998 - März 2003	Wissenschaftlicher “Project Assistant” am National Centre for Ultrafast Processes, University of Madras, Chennai, Indien
Seit April 2003	Wissenschaftlicher Mitarbeiter am Institut für Chemie der Humboldt-Universität zu Berlin.

Hiermit versichere ich, Karunakaran Venugopal, die vorliegende Arbeit selbstständig und ohne unerlaubte Hilfe angefertigt zu haben.

கற்க கசடற கற்பவை கற்றபின்
நிற்க அதற்குத் தக -குறள் 391

(Learn perfectly all that you learn, and thereafter keep your conduct worthy of that learning. ~ Thirukural)